

# Machine Learning of Atmospheric Turbulence in a Variational Multiscale Model

MSc Thesis

Martin Janssens





# Machine Learning of Atmospheric Turbulence in a Variational Multiscale Model

MSc Thesis

by

Martin Janssens

to obtain the degree of Master of Science  
at the Delft University of Technology,  
to be defended publicly on Tuesday August 27, 2019 at 10:00 AM.

Student number: 4275780  
Project duration: September 16, 2018 – August 28, 2019  
Supervisor: Dr. S. J. Hulshoff, TU Delft  
Thesis committee: Dr. R. P. Dwight, TU Delft  
Dr. B. Chen, TU Delft

An electronic version of this thesis is available at <http://repository.tudelft.nl/>.

Cover image: *The Starry Night*, Vincent van Gogh



# Abstract

Today's leading projections of climate change predicate on atmospheric General Circulation Models (GCMs). Since the atmosphere consists of a staggering range of scales that impact global trends, but computational constraints prevent many of these scales from being directly represented in numerical simulations, GCMs require "parameterisations" - models for the influence of unresolved processes on the resolved scales. State-of-the-art parameterisations are commonly based on combinations of phenomenological arguments and physics, and are of considerably lower fidelity than the resolved simulation. In particular, the parameterisation of low-altitude stratocumulus clouds that result from small-scale processes in sub-tropical marine boundary layers is widely considered the largest source of uncertainty that remains in contemporary GCMs' prediction of the temperature response to a global increase in CO<sub>2</sub>.

Improvements in the capacity of machine learning algorithms and the increasing availability of high-fidelity datasets from global satellite data and local Large Eddy Simulations (LES) have identified data-driven parameterisations as a high-potential option to break the deadlock. However, early contributions in this field still rely on inconsistent multiscale model formulations and are plagued by instability. To sketch a clearer picture on the sources of the accuracy and instability of data-driven parameterisations, this work proposes a framework in which no assumptions on the model form are made, building on a recent MSc thesis by Michel Robijns at the TU Delft. It uses Artificial Neural Networks (ANNs) to infer exact projections of the unresolved scales processes on the resolved degrees of freedom. These "interaction terms" naturally arise from Variational Multiscale (VMS) model formulations. The resulting VMM-ANN framework limits error to the data-driven interaction term approximations, offering explicit insight into their functioning.

The model is assessed in the context of a statistically stationary convective boundary layer turbulence problem, which is further reduced to a one-dimensional, forced inviscid Burgers' equation. Simple, feedforward ANNs with relatively local input stencils that are trained on error-free data a priori to inserting them in forward simulations (offline) are capable of predicting the interaction terms of this problem much better than traditional, algebraic VMS closures in offline settings at various levels of discretisation; they also generalise well to uncorrelated instances of the turbulence. However, this performance does not translate to simulations of forward problems. It is shown that the model suffers from instability due to i) ill-posed nonlinear solution procedures and ii) self-inflicted error accumulation. These correspond to two dimensions of forward simulations that are not accounted for by offline training on error-free data. The first instability mode can in some situations be dealt with by reformulating the VMM-ANN model architecture; the second is conjectured to demand training strategies that account for the self-induced errors. Finally, despite scaling well, the framework is still found to be computationally expensive compared to a state-of-the-art model. In all, appreciable challenges therefore remain in order to capitalise on the promise offered by ANNs to improve the parameterisation of clouds in GCMs in particular and turbulence in general.



# Preface

This thesis is the culmination of my MSc with the Aerodynamics group at the faculty of Aerospace Engineering at Delft University of Technology. It also brings me to a juncture where I conclude my engineering aspirations and continue on the path of atmospheric research. The document you are currently reading lives on this juncture. It attempts to marry recent progress on data-driven models intended for simulating turbulent flows encountered in engineering to the modelling of processes that drive the large scales of the atmosphere. In this context, I have endeavoured to contribute the thoughts of an educated engineer to the development of the atmospheric models upon which the prediction of climate change, one of the defining challenges of my generation, rests. I am grateful to be able to continue to devote my time to the understanding of and the solutions to this challenge in the coming years.

This study would never have been possible without the considerable insight, vision, numerical modelling expertise and skillful supervision of Dr. Steven J. Hulshoff. Steve, I am incredibly privileged to have been the beneficiary of uncountable one-liners and animated discussions that ran way over the time you had for them, but also of your solely constructive support, expedient feedback and remarkable investment in the work. The successful completion of this thesis would also not have been possible without Prof. Harm J.J. Jonker and Prof. Pier Siebesma of the Geosciences and Remote Sensing group at the TU Delft, who initially gave the right perspective for this work and very kindly provided both a test case and its data. I am truly thankful to you both. Thanks also to Michel Robijns for building the foundation upon which this work rests, and for our interesting conversations in the early stages of the project.

There are many more people to whom I am deeply indebted. First and foremost, I would like to thank my parents for their unconditional love and support throughout this journey. The values you instilled in me and the conditions you provided for me to succeed are the single most important reason for my successful completion of this work. A special thanks goes to my father, who committed to proofread every single word of this document. Carol, thank you, thank you for not only sticking with me through the long nights and weekends I should have spent with you rather than working, but for keeping me sane and grounded. I cannot wait to take on the world with you. Finally, I am profoundly thankful to all my friends and family; you gave colour to my years as a student. Rens, thanks for turning each of the long, dark hours of our MSc into a lively experience, you are a truly remarkable friend and probably the only person who knows what finishing this work means. Robin, thank you for being a guiding force and inspiration since the very first day of my studies; Max, thank you for making the Fellowship bearable and for teaching me how to enjoy life outside it. I cannot wait to continue to spend good times together with you in the future. Thanks also to Arent, Joël, Joris, the “Belgies” and everyone else who made the basement a slightly warmer place.

*Martin Janssens  
Delft, August 2019*



# Contents

<b>List of Figures</b>	<b>xi</b>
<b>List of Tables</b>	<b>xv</b>
<b>Acronyms</b>	<b>xvii</b>
<b>List of Symbols</b>	<b>xix</b>
<b>1 Introduction</b>	<b>1</b>
1.1 Background . . . . .	1
1.2 Research Objective and Research Questions . . . . .	2
1.3 Thesis Outline . . . . .	2
<b>2 Atmospheric Modelling</b>	<b>3</b>
2.1 Problem Formulation . . . . .	3
2.1.1 Mathematical Model . . . . .	3
2.1.2 Energy Spectrum of Atmospheric Turbulence . . . . .	4
2.2 General circulation models . . . . .	6
2.2.1 Modelling Approach . . . . .	6
2.2.2 Applications . . . . .	6
2.2.3 Assumptions and Approximations . . . . .	7
2.2.4 Discussion . . . . .	8
2.3 Global Cloud-Resolving Models . . . . .	9
2.3.1 Modelling Approach . . . . .	10
2.3.2 Applications . . . . .	10
2.3.3 Assumptions and Approximations . . . . .	10
2.3.4 Discussion . . . . .	11
2.4 Superparameterisation: The Multiscale Modelling Approach . . . . .	11
2.4.1 Heterogeneous Multiscale Methods . . . . .	12
2.4.2 Modelling Approach . . . . .	12
2.4.3 Applications . . . . .	14
2.4.4 Assumptions and Approximations . . . . .	14
2.5 Four Improvement Areas for SP . . . . .	14
2.5.1 Model Consistency . . . . .	15
2.5.2 Low Cloud Simulation Accuracy . . . . .	17
2.5.3 Computational Cost . . . . .	17
2.5.4 Scale Separation . . . . .	18
2.6 Summary and Outlook . . . . .	19
<b>3 A Variational Multiscale and Machine Learning Modelling Framework</b>	<b>21</b>
3.1 Conceptual Modelling Framework . . . . .	21
3.2 Variational Multiscale Methods . . . . .	22
3.2.1 Modelling Approach . . . . .	23
3.2.2 Model Equations . . . . .	24
3.2.3 Assumptions and Approximations . . . . .	26
3.2.4 Traditional VMS Closure Schemes . . . . .	28
3.2.5 Applications . . . . .	28

3.3	Potential of VMS Formulations as an Improved GCM . . . . .	29
3.3.1	Model consistency . . . . .	29
3.3.2	Low Cloud Accuracy and Computational Cost . . . . .	29
3.3.3	Scale Separation . . . . .	29
3.3.4	Potential High-fidelity Closure Integration . . . . .	30
3.3.5	Conclusion. . . . .	31
3.4	Data-driven Unresolved Scales Modelling. . . . .	32
3.4.1	Classes of Data-driven Unresolved Scales Models . . . . .	32
3.5	Artificial Neural Networks. . . . .	33
3.5.1	Brief Introduction . . . . .	34
3.5.2	State of the Art in Fluid and Atmospheric Dynamics . . . . .	35
3.5.3	The challenges and opportunities of ANNs as atmospheric models . . . . .	36
3.6	A VMM-ANN . . . . .	37
3.6.1	Outlook . . . . .	38
3.6.2	Verification and Validation. . . . .	40
<b>4</b>	<b>Simplified Test Cases</b> . . . . .	<b>41</b>
4.1	Simplified Test Cases for Atmospheric Modelling . . . . .	41
4.2	Statistically Stationary Convective Boundary Layer . . . . .	41
4.2.1	Mathematical Model. . . . .	42
4.2.2	Free, Dry Boundary Layer Turbulence . . . . .	42
4.2.3	Statistically Stationary Model . . . . .	44
4.3	Forced Inviscid Burgers' Problem . . . . .	45
4.3.1	Dimensionality Reduction . . . . .	45
4.3.2	VMS Problem . . . . .	45
4.4	Manufactured Solution Problem . . . . .	47
<b>5</b>	<b>Methodology</b> . . . . .	<b>49</b>
5.1	Model Framework. . . . .	49
5.2	Data Generation . . . . .	50
5.2.1	LES Model of the CBL . . . . .	50
5.2.2	1D Burgers' Problem . . . . .	52
5.2.3	Verification . . . . .	53
5.3	Identification Problem . . . . .	53
5.3.1	Approach . . . . .	54
5.3.2	Verification . . . . .	55
5.4	Machine Learning. . . . .	56
5.4.1	Approach . . . . .	56
5.4.2	Input Features . . . . .	57
5.4.3	Architecture . . . . .	59
5.4.4	Validation Approach . . . . .	61
5.4.5	Verification . . . . .	62
5.5	Forward Problem . . . . .	63
5.5.1	Approach . . . . .	63
5.5.2	Weak Residual Assembly . . . . .	65
5.5.3	ANN Evaluation . . . . .	67
5.5.4	Jacobian Assembly . . . . .	68
5.5.5	Time Marching. . . . .	69
5.5.6	Reference solutions . . . . .	70
5.5.7	Verification of full VMM-ANN . . . . .	71
<b>6</b>	<b>Exact Projections of Interaction Terms</b> . . . . .	<b>75</b>
6.1	Energy Spectra of the Model Problem . . . . .	75
6.2	Time-Averaged Spatial Profiles of Exact Interaction Terms . . . . .	76
6.3	Averaged Distributions of Interaction Terms . . . . .	78
6.4	Conclusions. . . . .	81

<b>7</b>	<b>Machine Learning</b>	<b>83</b>
7.1	Dataset size . . . . .	83
7.2	Input Features and Architecture. . . . .	84
7.2.1	Hyperparameter Sensitivity . . . . .	84
7.2.2	Optimised Architecture and Feature Sets. . . . .	86
7.3	Predictability as a Function of Discretisation Level . . . . .	88
7.3.1	Influence of the Stencil. . . . .	90
7.3.2	Influence of Structural Errors . . . . .	93
7.3.3	Inherent Predictability . . . . .	93
7.3.4	Outlook . . . . .	94
7.4	Conclusions. . . . .	94
<b>8</b>	<b>Properties of VMM-ANNs: Simple Problem</b>	<b>95</b>
8.1	Uniqueness . . . . .	96
8.2	Stability . . . . .	99
8.3	Improvement Attempts . . . . .	101
8.3.1	Adaptive Relaxation . . . . .	101
8.3.2	ANN Jacobian . . . . .	102
8.3.3	Limiting schemes . . . . .	103
8.3.4	Longer Temporal Input Stencils . . . . .	105
8.3.5	Training on CP Data . . . . .	106
8.3.6	A Quadratic Coefficient ANN Model . . . . .	107
8.3.7	Hybrid Algebraic-ANN Model . . . . .	108
8.4	Conclusions. . . . .	109
<b>9</b>	<b>Properties of VMM-ANNs: 1D Turbulence</b>	<b>111</b>
9.1	Stability . . . . .	111
9.2	Influence of Discretisation . . . . .	115
9.3	Aspects of Stability . . . . .	117
9.3.1	Artificial Viscosity Stabilisation . . . . .	117
9.3.2	Dataset Dependence. . . . .	119
9.3.3	Outlook . . . . .	119
9.4	Computational Cost. . . . .	120
9.4.1	ANN Training . . . . .	120
9.4.2	Weak Residual Assembly . . . . .	121
9.4.3	Jacobian Assembly . . . . .	121
9.4.4	Newton Iterations . . . . .	122
9.4.5	Overall Cost . . . . .	122
9.5	Conclusions. . . . .	122
<b>10</b>	<b>Conclusions and Recommendations</b>	<b>125</b>
10.1	Conclusions. . . . .	125
10.2	Recommendations . . . . .	127
<b>A</b>	<b>Atmospheric Scale Ranges and Models</b>	<b>131</b>
A.1	The Anelastic and Boussinesq Equations . . . . .	133
A.2	The hydrostatic primitive equations . . . . .	134
A.3	The SP Equations . . . . .	135
<b>B</b>	<b>A Bulk Model for the Statistically Stationary Convective Boundary Layer</b>	<b>137</b>
<b>C</b>	<b>Methodology Details</b>	<b>141</b>
C.1	Bi-Cubic Interpolation of DALES Data . . . . .	141
C.2	Finite Difference ANN Jacobian Assembly . . . . .	142
C.3	Adaptive Relaxation Scheme for Newton's Method . . . . .	143
	<b>Bibliography</b>	<b>145</b>



# List of Figures

2.1	Nastrom-Gage spectra of the variance in power of zonal velocity (left), meridional velocity (centre) and potential temperature (right), from GASP aircraft data [180]. . . . .	5
2.2	Climate system processes and their interactions [171]. . . . .	7
2.3	CO <sub>2</sub> concentration at which 2 K global temperature rise with respect to pre-industrial levels is reached as a function of ECS <sup>-1</sup> [221]. The circles represent climate models, in order of ascending ECS [33]. The spread in allowable CO <sub>2</sub> concentration corresponds to the spread in time, represented on the right axis, when the 2 K barrier will be broken. . . . .	9
3.1	Conceptual overview of the unresolved scales and resolved-scales coupling in a classical parameterisation, a SP and the approach taken here. . . . .	22
3.2	Nodal projection of $u$ onto piecewise linear bases $\bar{\psi}_i$ over finite elements with domain $\Omega_e$ and boundary $\Gamma_e$ , to construct $\bar{u}$ . This projection defines $u'$ as illustrated. . . . .	24
3.3	Schematic representation of an ANN with an input layer with 8 nodes, a single, densely connected hidden layer with 10 nodes and an output layer with 3 nodes. . . . .	34
4.1	Profiles of the mean variables in a statistically stationary, free CBL with vertical coordinate $z/z_i$ . From left to right: Mean potential temperature $\langle\theta\rangle$ , mean horizontal fluctuating momentum fluxes $\langle u''u''\rangle$ and $\langle v''v''\rangle$ , mean vertical fluctuating momentum flux $\langle w''w''\rangle$ and mean vertical heat flux $\langle w''\theta''\rangle$ . . . . .	44
4.2	A statistically stationary CBL can be attained by balancing the surface heat flux that produces free turbulence, $\langle w''\theta''\rangle_s$ with a radiative sink $S_\theta = \Gamma_s w_s$ . . . . .	45
4.3	Evolution of the manufactured solution for $w$ in Eq. (4.9) with the coefficients in Table 4.1, normalised with $w_A$ , over a half period of its oscillation. . . . .	47
5.1	High-level framework of the VMM-ANN. . . . .	49
5.2	Flowchart of the data generation procedure. The LES was run externally (grey background), while the subsequent data processing steps were performed locally with Python (green background). . . . .	50
5.3	Reprint of the mean variables in a statistically stationary, free Convective Boundary Layer (CBL) with vertical coordinate $z$ presented in Fig. 4.1. The blue lines include the effects of the unresolved scales and surface models; the orange lines represent the profiles constructed from the filtered variables. . . . .	51
5.4	Spatially averaged profiles of vertical velocity statistics of the mean and standard deviation of the last 3 hours of simulation and 3 instantaneous realisations of the profile around the 1hr mark	52
5.5	Verification of data extraction procedure . . . . .	53
5.6	Flowchart of the identification problem Mex app <code>getURTerms</code> . It is fully implemented in Mex (red background). . . . .	54
5.7	Individual terms and weak residual that build up the weak form for the manufactured solution problem on the domain $0 < z < 1$ , $0 < t < 6$ , discretised with $h = 0.25$ , $\Delta t = 1$ . . . . .	56
5.8	Flowchart of the machine learning stage's implementation. It is mostly comprised of a Python implementation (green fields) that wrap the <code>getURTerms</code> app described in Fig. 5.6 (red field). . . . .	57
5.9	Stencil of various ANN input features of the discretisation of space and time. Dashed lines indicate collocation in time, solid lines indicate piecewise linear finite element bases in space. $\frac{\partial \bar{w}}{\partial t}$ follows the distribution and logic of $\bar{w}$ . Curly braces denote integration over the appointed elements. . . . .	59
5.10	Cross-correlation $C(x + \delta x, y + \delta y)$ throughout $-\frac{L_x}{2} < x < \frac{L_x}{2}$ , $\frac{L_y}{2} < y < \frac{L_y}{2}$ when $t = 1hr$ , $\frac{z}{z_i} = 0.6$ .	61
5.11	Variation of $L_c$ with $\frac{z}{z_i}$ throughout the turbulent portion of the domain. . . . .	61
5.12	Training history of $J$ on training and validation data. . . . .	63
5.13	"Skill metric" $R^2$ of the trained ANN, evaluated on test data according to simple cross validation.	63

5.14	Flowchart of the numerical model that solves the forward problem. The solver is implemented in its own Mex app (red fields).	64
5.15	Contours of $\ \mathcal{R}_w\ _2$ over a range of its two degrees of freedom $a_1$ and $a_2$ at time levels $t = 6$ , $t = 7.5$ and $t = 9$ , approximating the extents of the manufacture solution's amplitude. The exact values of $a_1$ and $a_2$ of the manufactured solution are denoted by a square.	67
5.16	Order of accuracy test for the Implicit Euler (IE), Second Order Backwards (SOB) and Generalised Alpha (GA) time marches with the manufactured solution described in Section 4.4.	70
5.17	Discrete, instantaneous solutions of the Boussinesq-forced Burgers' problem at $\frac{h}{h_{DNS}} = [3, 6, 12]$ and single-column time-averaged statistics. All runs are with $\frac{\Delta t}{\Delta t_{DNS}} = 2$ , $t_f = 6$ hr and averaging is only over the last 5 hrs.	72
5.18	Space-time plots of the manufactured problem's solution and interaction terms predicted by the VMM-ANN (left), the exact model (right) and their difference (centre), for simulations where $h = 0.25$ , $\Delta t = 1$ .	73
6.1	Discrete, averaged energy spectra of a single column of the forced Boussinesq problem for projections on grids that are 3, 6 and 12 times the vertical spacing of the DALES simulation and 2 and 4 times the time step of the DALES simulation. Note that increasingly coarse discretisations of the same DALES solution do not reproduce the same resolved Fourier modes, since the problem is not periodic.	76
6.2	Spatial profiles of the squared weak form terms, averaged over 16 randomly sampled columns, varying with spatial discretisation $h/h_{DALES}$ , at $\Delta t/\Delta t_{DALES} = 2$ .	77
6.3	Spatial profiles of the squared weak form terms, averaged over 16 randomly sampled columns, varying with temporal discretisation $\Delta t/\Delta t_{DALES}$ , at $h/h_{DALES} = 6$ .	77
6.4	Temporally averaged modal decomposition of amplitudes of the Fourier-transformed Galerkin terms $G_F$ and Interaction terms $I_F$ over spatial wavenumbers, over the same number of columns as Fig. 6.2.	79
6.5	Spatially averaged modal decomposition of the amplitudes of the Fourier-transformed Galerkin terms $G_F$ and interaction terms $I_F$ over temporal wavenumbers, over the same number of columns as Fig. 6.3.	79
7.1	Scaling of predictive ability (Summed $R^2$ over $\hat{I}$ and $J$ ) and training time as a function of the number of samples used for ANN training, for FS2. For the present problem, the time cost of running a forward problem with 1024 elements is included as a dashed line.	83
7.2	Average impact on $J$ on the validation columns of varying the neurons/layer (subplots), learning rate (bar assemblies) and dropout (hue) in the ranges reported in Table 7.1. The extent of black bars denotes bootstrapped 95% confidence intervals, though the sampling rate is sufficiently low that these should be treated with care.	85
7.3	Average impact on $J$ on the validation columns of varying the optimiser between RMSProp, NAdam and Adam, for ReLU, ELU and Sigmoid activation functions. The black bars denotes bootstrapped 95% confidence intervals.	85
7.4	Training history on training and validation data and $R^2$ correlation on validation data (upper row) and test data (lower row) of each of the three interaction terms for the best set of hyperparameters, with FS3 as input.	86
7.5	Comparison of time-averaged spatial distributions of the $L_2$ norms of the interaction terms, as predicted by exact, ANN and algebraic models, at $h/h_{DALES} = 6$ and $\Delta t/\Delta t_{DALES} = 2$ , over 16 columns from a different DALES simulation than was trained on. The ANN is the best FS3 model in Table 7.3.	87
7.6	Contours of $R^2$ of an array of ANNs (top) and algebraic models (bottom) over a range of $h$ and $\Delta t$ . The ANNs use FS4 and the hyperparameters from Table 7.3, each trained and tested on data sampled with a different combination of $h$ and $\Delta t$ . All ANNs are trained on an equal number of samples, corresponding to the dimensions of the coarsest discretisation, randomly selected from 8x8 columns. They are evaluated on 16 different, full, uncorrelated columns from the same DALES simulation. Contour lines of constant Courant number $C$ are superimposed.	88
7.7	Amplitude distribution with $k_z$ of exact (circles), algebraic (squares) and ANN (pluses) predictions of the interaction terms at three levels of spatial discretisation, averaged over time, for a test column. $\Delta t/\Delta t_{DALES} = 2$ .	89

7.8	Amplitude distribution with $k_z$ of exact (filled circles) and ANN (pluses) predictions of the interaction terms at three levels of temporal discretisation, averaged over space for a test column, and with $k_t$ of the time derivative term at the two coarsest levels of $\Delta t$ . $h/h_{DALES} = 6$ . . . . .	89
7.9	Highest $w$ ( $w_{max}$ ) that can impact $\hat{I}_i^{n+1}$ on the stencil from Fig. 5.9 at a chosen combination of $\Delta t$ and $h$ (blue line), at $\Delta t/2$ (green line) and at $2h$ (red line), compared to a larger mode of length $L_l$ (orange line). The domains of dependence (DOD) of the stencil and the $L_l$ mode are shaded blue and orange, respectively. . . . .	90
7.10	Amplitude distributions with $k_z$ of the three interaction terms, predicted by ANNs with input stencil widths of $1-4h$ (pluses) compared to exact values (filled circles), averaged over the time dimension of a test column. $h/h_{DALES} = 3$ and $\Delta t/\Delta t_{DALES} = 2$ . . . . .	91
7.11	Amplitude distributions of the three interaction terms with $k_t$ , predicted by ANNs with $0-2\Delta t$ input history stencils (pluses) compared to exact values (filled circles), averaged over the space dimension of a test column. $h/h_{DALES} = 3$ and $\Delta t/\Delta t_{DALES} = 2$ . . . . .	92
8.1	Finite element discretisation of the manufactured solution problem with two degrees of freedom.	96
8.2	Response surfaces of $\ \mathcal{R}_{w_i}\ _2$ for a manufactured solution problem with two degrees of freedom $a_1$ and $a_2$ . They derive from simulations where $\Delta t = 2$ , $h = \frac{1}{3}$ and $C = 1.2$ . The ANN's structure is the same as that of the FS3 model in Table 7.3. . . . .	97
8.3	Response surfaces of $\ \mathcal{R}_{w_i}\ _2$ for a manufactured solution problem with two degrees of freedom $a_1$ and $a_2$ for ANN models with a linear activation function. They derive from simulations where $\Delta t = 3$ , $h = \frac{1}{3}$ and $C = 1.8$ . The ANNs have a single layer with varying numbers of neurons and take FS3 as input. . . . .	98
8.4	Response surfaces of $\ \mathcal{R}_{w_i}\ _2$ for a manufactured solution problem with two degrees of freedom $a_1$ and $a_2$ for $[2,2]$ ANN models with various degrees of nonlinearity. They derive from simulations where $\Delta t = 3$ , $h = \frac{1}{3}$ and $C = 1.8$ . The ANNs take FS3 as input. . . . .	98
8.5	Temporal evolution of the three degrees of freedom $a_1$ , $a_2$ and $a_3$ at increasing $\Delta t$ of simulations with $h = 0.25$ , closed by ANNs of shape $[512, 512]$ taking FS3 as input. $C = [1.2, 1.4, 1.6]$ for $\Delta t = [1.50, 1.75, 2.00]$ . . . . .	100
8.6	Response surfaces of $\ \mathcal{R}_{w_i}\ _2$ at the time step $n_e$ , when the solution's $E_{L_2} > 10^{-4}$ for the first time, for three increasing $\Delta t$ . The spatial grid spacing is $h = \frac{1}{3}$ , while the ANNs take FS3 as input and have a $[512, 512]$ structure. . . . .	100
8.7	The impact of adaptive relaxation on convergence of $\mathcal{R}_w$ for a $[2, 2]$ ANN model for $\hat{I}$ with ReLU activation functions and FS3 as input. Blue lines signify convergence without any relaxation, orange lines are adaptively relaxed with $\tau_r = 1 \cdot 10^{-3}$ and green lines with $\tau_r = 1 \cdot 10^{-4}$ . The simulations are run with $\Delta t = 3$ , $h = \frac{1}{3}$ , $C = 1.8$ , and the algebraic Jacobian. . . . .	102
8.8	The impact of the Jacobian implementation on convergence of $\mathcal{R}_w$ for a $[2, 2]$ ANN model for $\hat{I}$ with ReLU activation functions and FS3 as input. Blue lines signify convergence with an algebraic Jacobian (Eq. (5.28)), orange lines a ANN-based Jacobian that ignores the unresolved scales' time derivative and green lines the full ANN Jacobian. The simulations are run with $\Delta t = 3$ , $h = \frac{1}{3}$ , $C = 1.8$ , and $\tau_r = 10 \cdot 10^{-4}$ . . . . .	103
8.9	Temporal evolution of the three degrees of freedom $a_1$ , $a_2$ and $a_3$ when the components of $\hat{I}$ are nonlinearly limited, for simulations run with $h = 0.25$ , $\Delta t = 2$ , $C = 1.6$ . $\hat{I}$ is predicted by an ANNs of shape $[512, 512]$ , taking FS3 as input. . . . .	104
8.10	Temporal evolution of the three degrees of freedom $a_1$ , $a_2$ and $a_3$ of simulations with $h = 0.25$ , $\Delta t = 1.5$ , $C = 1.2$ , closed by ANNs of shape $[512, 512]$ that depend on $\bar{w}^{n+1, n, n-1}$ , $\bar{w}^{n+1, n}$ and $\bar{w}^n$ respectively. . . . .	106
8.11	Response surface of $\ \mathcal{R}_{w_i}\ _2$ for the ANN model trained on CP sequence data, for $\hat{I}$ at $t = 50$ s for a simulation with $\Delta t = 2$ , $h = 0.333$ , $C = 1.2$ . . . . .	106
8.12	Temporal evolution of the three degrees of freedom $a_1$ , $a_2$ and $a_3$ of simulations with $h = 0.25$ , $\Delta t = [1, 2]$ , $C = [0.8, 1.6]$ , for an ANN trained on data from the nonlinear Newton sequence of an exact-model forward problem . . . . .	106
8.13	Response surfaces of $\ \mathcal{R}_{w_i}\ _2$ for the direct (FS3 input, nonlinearly limited) and quadratic coefficient (FS2 input) ANN models for $\hat{I}$ . Black lines signify unrelaxed convergence with an ANN Jacobian (Eq. (5.28)), orange lines relaxed convergence ( $\tau_r = 1 \cdot 10^{-4}$ ) with an algebraic Jacobian, and green lines relaxed convergence ( $\tau_r = 1 \cdot 10^{-4}$ ) with an ANN Jacobian. The simulations are run with $\Delta t = 3$ , $h = \frac{1}{3}$ , $C = 1.8$ . . . . .	108

8.14	Response surface of $\ \mathcal{R}_{w_i}\ _2$ for the quadratic coefficient ANN model for $\hat{I}$ at $t = 12$ s for a simulation with $\Delta t = 3$ , $h = 0.333$ , $C = 1.8$ . . . . .	108
8.15	Temporal evolution of the three degrees of freedom $a_1$ , $a_2$ and $a_3$ of simulations with $h = 0.25$ , $\Delta t = [1, 2]$ , $C = [0.8, 1.6]$ , for the quadratic coefficient ANN model for $\hat{I}$ . . . . .	108
8.16	Response surface of $\ \mathcal{R}_w\ _2$ for the hybrid algebraic-ANN formulation, for simulations where $\Delta t = 1$ , at $t = 3$ . The ANNs are conditioned on input from the converged algebraic model (at the orange diamond). . . . .	109
9.1	Evolution of instability in $\bar{w}$ for the first model listed in Table 9.1, over four consecutive time steps due to subsequent mispredictions of the three, plotted interaction terms, for an excitation of the boundary-adjacent mode at $nDt = 20, 21$ , sudden growth of the mode at $nDt = 22$ and divergence at $nDt = 23$ . . . . .	113
9.2	Three instantaneous energy spectra corresponding to $w$ (blue), exact $\bar{w}$ (orange) and VMM-ANN predictions of $\bar{w}$ (green), separated by 5 time steps, over a period where energy accumulates in the smallest resolved modes of the VMM-ANN, run with the FS3 ANN from Table 7.3, on a discretisation with $h = 6h_{DALES}$ , $\Delta t = 2\Delta t_{DALES}$ and $C \approx 0.417$ . . . . .	114
9.3	Convergence paths of the first two modes and final profiles of the solution and interaction terms at $nDt = 23$ (failure) for simulations closed by exact and ANN predictions of the interaction terms. The models employ ANN and algebraic Jacobians (orange, green lines respectively) with nonlinear limiters active, and algebraic Jacobian without nonlinear limiting (red line). Note that the latter simulation diverges, such that its final profiles are not plotted. . . . .	114
9.4	Profiles of instantaneous and time-averaged norms of the interaction terms of a VMM-ANN run stabilised with additional artificial viscosity, $c_{a,1} = 1 \cdot 10^{-3}$ , $c_{a,2} = 1 \cdot 10^{-2}$ . The simulation runs at $\Delta t = 2\Delta t_{DALES}$ , $h = 3h_{DALES}$ , $C \approx 0.33$ , with a direct FS3 ANN interaction term model, using the hyperparameters from Table 7.3. . . . .	118
9.5	Time-averaged profiles of the $L_2$ norms of the sum of ANN-predicted interaction terms and “low” ( $c_{a,1} = 1 \cdot 10^{-4}$ , $c_{a,2} = 1 \cdot 10^{-3}$ ) and “high” ( $c_{a,1} = 1 \cdot 10^{-3}$ , $c_{a,2} = 1 \cdot 10^{-2}$ ) artificial viscosity terms, with their resulting vertical velocity statistics. Simulations are with the quadratic coefficient model at $\Delta t = 2\Delta t_{DALES}$ , $n_{el} = 32$ , $C = 0.33$ , closed by a [512,512] ANN, taking FS2 as input. . . . .	118
A.1	Particular mathematical models at various ranges of length and time scales compared to $h_{sc}$ and $u_0 = u_{th}$ . WTG is the weak temperature gradient model, HPE are the hydrostatic primitive equations, QG is quasi-geostrophic motion and PG is planetary geostrophic motion . . . . .	133

# List of Tables

4.1	Coefficients to describe the manufactured solution for $w$ in Eq. (4.9) and the resulting source term $S(z, t)$ in Eq. (4.10). . . . .	47
5.1	DALES settings and characteristics for the CBL model . . . . .	52
5.2	Feature sets used to define the ANN models' input. FS1 is an interpretation of Robijns' extended stencil [209], FS2 does not depend on unknowns at a new time level and FS3 extends FS1 backwards in time. . . . .	59
5.3	Parameters defining the verification ANN and its training. . . . .	63
5.4	Denormalised output of an ANN evaluated in Keras and Mex, for randomly chosen samples of each feature set. . . . .	67
5.5	Finite difference approximations of the element Jacobian terms in the second element of a 3-element implementation of the manufactured solution from the point $a_1 = a_2 = 0.17965$ . $\Delta t = 2$ , $h = \frac{1}{3}$ and $\delta a = 1 \cdot 10^{-5}$ . . . . .	69
5.6	$R^2$ coefficient of determination and $E_{L_2}$ for online VMM-ANN predictions of the components of $\hat{I}$ and $\bar{w}$ , compared to their offline counterparts. . . . .	72
7.1	Ranges of free hyperparameters sampled by random grid search, resulting in a total of 984 combinations. . . . .	84
7.2	Pearson correlation ( $R$ ) of hyperparameters to $J$ on the 16 validation columns, ranked in terms of positive to negative impact on reducing $J$ over the ranges reported in Table 7.1. . . . .	85
7.3	Set of ANN architectures and hyperparameters that yield the best performance on all considered feature sets. $R^2$ and $J$ are listed on a test dataset of 16 columns from a different DALES dataset than was trained on. . . . .	87
8.1	Characteristics of computational cost, accuracy and stability of direct and quadratic ANNs for simulations with ANNs of shape [512,512]. nD is the number of successfully completed time steps without simulation divergence. The failure modes WR, Div, MG and Stag refer to wrong root prediction, divergence of the iterative procedure, mispredicted root growth, and stagnation of the Newton iterations. . . . .	110
9.1	Characteristics of accuracy and stability of direct and quadratic ANNs for simulations with $h = 6h_{DALES}$ , $\Delta t = 2\Delta t_{DALES}$ , $C \approx 0.417$ and ANNs from Table 7.3. "CP set" refers to ANNs trained on an exact model's convergence and hybrid refers to the algebraic-ANN models. nD is the number of successfully completed time steps without simulation divergence. The failure modes MG and Stag refer to mode growth-driven divergence and stagnated convergence of the iterative solution procedure. . . . .	112
9.2	Characteristics stability of simulations closed by direct and quadratic coefficient ANN models. The direct models down to $\Delta t / \Delta t_{DALES} = 1$ correspond to those in Fig. 7.6a, while the quadratic models, closed by FS2, are trained on the same dataset as the direct models. The simulations run with $\tau_r = 0.01$ , an ANN Jacobian and nonlinear limiting to $[-0.5, 0.5]$ (only for direct models). Online $R^2$ before mode growth is measured until the first instance where $\bar{w}$ in the domain exceeds the maximum value encountered in the exact simulation, and nD is the number of successfully completed time steps without simulation divergence. The failure modes Stag and MG refer to stagnation and mode-growth-driven divergence of the Newton scheme. . . . .	116
9.3	Characteristics of stability of direct ANNs with FS3 input and hyperparameters from Table 7.3 for simulations with $h = 6h_{DALES}$ , $\Delta t = 2\Delta t_{DALES}$ , $C \approx 0.417$ . The training sets are the default 8x8 set and a single, randomly chosen column, while inside and outside refer to whether they have been tested on a column that belongs to or is uncorrelated from their training set, respectively. nD is the number of successfully completed time steps without simulation divergence. The failure mode MG denotes mode growth-driven divergence of the iterative solution procedure. . . . .	119

9.4	Characteristics of computational cost of direct and quadratic ANNs for simulations corresponding to selected runs from Table 9.1. All time units are in seconds. The listed values are a run's mean $\pm$ its standard deviation . . . . .	120
A.1	Universal characteristics of atmospheric motion, adopted from Klein [131] . . . . .	131
A.2	Discernible length scales of atmospheric motion, adopted from Klein [131] . . . . .	132
A.3	Non-dimensional parameters in Eq. (2.1) and their value in terms of $\varepsilon$ at the discernible reference lengths of Table A.2, when $u_0 = u_{th}$ and $t_0 = \frac{l_0}{u_0}$ . . . . .	132
C.1	Perturbations of the amplitudes $a$ for the unknown input features of the ANN, used to construct finite difference approximations to the Jacobian contributions in the left column. $c_{t,1}$ is a factor for the time derivative's finite difference approximation (see Section 5.5.5). . . . .	142

# Acronyms

<b>ABL</b>	Atmospheric Boundary Layer
<b>ANN</b>	Artificial Neural Network
<b>BNN</b>	Bayesian Neural Networks
<b>CAM</b>	Community Atmosphere Model
<b>CBL</b>	Convective Boundary Layer
<b>CEM</b>	Cloud Ensemble Model
<b>CMC</b>	Conditional Markov Chain
<b>CNN</b>	Convolutional Neural Network
<b>CP</b>	Corrector Pass
<b>CRCP</b>	Cloud-Resolving Convection Parameterisation
<b>CRM</b>	Cloud-Resolving Model
<b>CSRM</b>	Cloud System-Resolving Model
<b>DALES</b>	Dutch Atmospheric Large Eddy Simulation
<b>DFT</b>	Discrete Fourier Transform
<b>DNN</b>	Deep Neural Network
<b>DNS</b>	Direct Numerical Simulation
<b>DOD</b>	Domain of Dependence
<b>DSS</b>	Dynamic Subscales
<b>ECMWF</b>	European Centre for Medium-Range Weather Forecasts
<b>ECS</b>	Equilibrium Climate Sensitivity
<b>ELU</b>	Exponential Linear Unit
<b>ES</b>	Early Stopping
<b>ESM</b>	Earth System Model
<b>FEM</b>	Finite Element Method
<b>GA</b>	Generalised Alpha
<b>GCM</b>	General Circulation Model
<b>GCRM</b>	Global Cloud-Resolving Model
<b>GLS</b>	Galerkin/Least Squares
<b>GMRES</b>	General Minimised Residual
<b>GOROM</b>	Goal-Oriented Reduced Order Model

---

**GPU** Graphical Processing Unit  
**HIT** Homogenous Isotropic Turbulence  
**HMM** Heterogeneous Multiscale Method  
**HPC** High-Performance Computing  
**HPEs** Hydrostatic Primitive Equations  
**IP** Integration Point  
**LAM** Limited Area Model  
**LES** Large Eddy Simulation  
**LHS** Left Hand Side  
**MMF** Multiscale Modelling Framework  
**MMS** Method of Manufactured Solutions  
**NWP** Numerical Weather Prediction  
**ODE** Ordinary Differential Equation  
**OSS** Orthogonal Subscales  
**PDE** Partial Differential Equation  
**PDF** Probability Density Function  
**PINN** Physics-Informed Neural Network  
**POD** Proper Orthogonal Decomposition  
**ReLU** Rectified Linear Unit  
**RF** Random Forest  
**RHS** Right Hand Side  
**RNN** Recurrent Neural Networks  
**ROM** Reduced-Order Model  
**RQ** Research Question  
**SGD** Stochastic Gradient Descent  
**SOB** Second Order Backwards  
**SP** Superparameterisation  
**SSP** Sparse Superparameterisation  
**SST** Sea Surface Temperature  
**SUPG** Streamline-upwind Petrov-Galerkin  
**UP** Ultraparameterisation  
**VMM** Variational Multiscale Method  
**VMS** Variational Multiscale  
**WTG** Weak Temperature Gradient

# List of Symbols

- $\alpha_l$  Learning rate for neural network training
- $a$  Scaling amplitude of a finite-element mode
- $b$  Neuron bias
- $C$  Courant number
- $\chi$  Generic transport variable
- $c_{int}$  Internal wave speed
- $c_N$  Calibrated constant for dissipation of  $k$  in DALES
- $c_s$  Sea-level speed of sound
- $\delta_d$  Dirac delta peak forcing
- $\delta_{ij}$  Kroenecker delta
- $\Delta t$  Time step
- $\varepsilon$  Factor of scale separation
- $\varepsilon_t$  Dissipation of turbulence kinetic energy
- $\epsilon_{ijk}$  Levi-Civita symbol
- $E$  Turbulence kinetic energy
- Fr Froude number
- $F_{SS}^\chi$  Large and small scale source terms in the small and large-scale equations for  $\psi$  in superparameterisation
- $f$  Generic forcing term
- $g$  Gravitational acceleration
- $g'_e$  Unresolved scales element Green's function
- $\gamma$  Dry ratio of specific heats
- $\Gamma$  Adiabatic lapse rate
- $\Gamma_\Omega$  Spatial boundary of domain  $\Omega$
- $g_\Gamma$  Generic boundary condition on boundary  $\Gamma_\Omega$
- $h$  Grid spacing
- $h_{sc}$  Density scale height
- $I$  Interaction term between resolved and unresolved scales
- $\lambda_{L_2}$  Weight regularisation parameter
- $\lambda_r$  Relaxation parameter of Newton scheme
- $\mathcal{L}^*$  Adjoint operator of  $\mathcal{L}$

- $L_c$  Horizontal correlation length of turbulence
- $\mathcal{L}$  Generic partial differential equation operator
- $k_c$  Number of modes directly represented on a discretised space
- $k_K$  Number of modes required to span the turbulent spectrum down to the Kolmogorov scales
- Ma Mach number
- $\nu_a$  Artificial viscosity
- $N$  Brunt-Väisälä frequency
- $n_{el}$  Number of elements in finite element discretisation
- $n_{ip}$  Number of quadrature integration points in a finite element
- $n_{lyrs}$  Number of layers in an ANN
- $n_{neur}$  Number of nodes in a layer of an ANN
- $\omega$  Weight of neuron connection
- $\Omega$  Domain of influence of a partial differential equation
- $p$  Pressure
- $\pi$  Pressure fluctuation normalised by reference density
- $\bar{\Pi}$  Projection operator onto a  $\bar{\cdot}$  space
- $\Pi'$  Projection operator onto a  $\cdot'$  space
- $\phi$  Modal basis function of a finite-element solution
- $\psi$  Weak form weighting function
- $\Omega$  Heterogeneous multiscale method compression operator
- $q$  Specific humidity
- $q_c$  Mixing ratio of condensed water
- $q_p$  Mixing ratio of precipitating water
- $q_v$  Mixing ratio of water vapour
- Re Reynolds number
- $R_g$  Dry air gas constant
- $\rho$  Density
- $\rho_0$  Sea-level reference density
- Ro Rossby number
- $\mathcal{R}_s$  Strong residual of the resolved-scales equations
- $\mathcal{R}_w$  Weak residual of the resolved-scales equations
- $\mathfrak{R}$  Heterogeneous multiscale method reconstruction operator
- $\sigma$  Nonlinear neuron activation function
- St Strouhal number

- 
- $S_\theta$  Thermal source
- $\mathcal{S}$  Infinite-dimensional trial function space
- $S$  Source term for 1D manufactured solution
- $\tau$  Proportionality constant of variational multiscale algebraic subgrid models
- $\tau_r$  Free parameter of adaptive relaxation scheme
- $\theta$  Potential temperature
- $\theta_0$  Sea-level potential temperature
- $u_i$  Velocity
- $u_{th}$  Thermal wind speed
- $V$  Artificial viscosity term
- $\mathcal{V}$  Infinite-dimensional weighting function space
- $w$  Vertical velocity
- $w_e$  Entrainment velocity
- $w_s$  Subsidence velocity
- $W_{ip}$  Quadrature weight at an integration point
- $z_i$  Inversion height of a well-mixed atmospheric boundary layer



# Introduction

## 1.1. Background

Atmospheric General Circulation Models (GCMs) are an essential component of the Earth System Models (ESMs) that establish the world's leading predictions on climate change [172]. However, intercomparison studies of existing GCMs exhibit a large spread in their predictions of atmospheric CO<sub>2</sub> concentration at which a 2 K temperature rise with respect to preindustrial times, agreed upon in the 2015 Paris Agreement [190], is reached [27]. In high-emission scenario simulations, this uncertainty means some models predict the threshold will be crossed in 2040; others predict it will be around 2060 [221]. These extremes mandate vastly different optimal policy approaches, with societal cost of the uncertainty estimated at \$10 trillion [99].

The largest contributor to this uncertainty concerns the response of cumulus and stratocumulus clouds to warming [67]. Such clouds have a rather large impact on top-of-the-atmosphere radiative balance [27]. However, the turbulent scales in the Atmospheric Boundary Layer (ABL) that drive the evolution of such clouds lie far below the resolutions that computational limits will allow GCMs to resolve in the coming decades. Hence, clouds are currently approximated with phenomenologically informed unresolved scales models, "parameterisations", of considerably lower fidelity than the resolved simulation.

In recent years, improvements in the capacity of machine learning frameworks [143], coupled with the increasing availability of high-fidelity datasets from global satellite data [144] and local Large Eddy Simulation (LES) of clouds [70], highlight that the deadlock might be broken by data-driven parameterisations [220]. In particular, Artificial Neural Networks (ANNs) have successfully closed state-of-the-art GCMs in the last year [29, 205]. However, ensuring that an ANN adheres to the laws of physics and therefore returns stable, generalisable simulations remains a challenge [79]. Additionally, embedding machine learning frameworks in GCMs does not resolve the conceptual inconsistencies of state-of-the-art GCM formulations. These prevent the correct interaction between the smaller scales of clouds and the larger scales of climate [161], an issue that is expected to move centre-stage as the resolutions of GCMs increase in the coming decades [160].

Recently, fluid flow solvers closed by ANN unresolved scales models in a manner that imposed no a priori model assumptions showed promise to begin resolving these issues in the context of simple, 1D problems [209]. Rather than advancing ill-posed models for the unresolved processes themselves, which in turn inform approximate, phenomenological closures for the resolved scales, this approach proposes to concentrate directly on the potentially better-posed unresolved processes that project onto the resolved scales, and bypass those that do not. These processes can be encapsulated in "interaction terms", which arise directly from the decomposition of the problem's governing equations into their resolved and unresolved scales spaces.

Variational Multiscale (VMS) formulations of spectral and finite element methods form a particularly natural and intuitive modelling framework for expressing these interactions [109]. The VMS framework subsumes the model and discretisation errors introduced to the resolved scales simulation by the unresolved scales under the interaction terms, where they belong. It demonstrates rather clearly that if the interaction terms were exactly predicted, exact, discrete solutions of the problem could be attained. Therefore, the framework forms a natural point of departure for assessing the capabilities of ANNs as unresolved scales models for the interaction terms themselves. In turn, such models have no inherent limitations on how well the resolved scales can be represented and are only constrained by an ANN's ability to learn the interaction terms from large sets of relevant data that satisfy the underlying, governing equations.

In this context, the contribution of this work is twofold. First, the study aims to test the absolute limits of the capabilities of ANNs as unresolved scales models when all model assumptions are removed and they are free to predict fully consistent interaction terms. It will assess the degree to which such interaction terms are predictable and whether the predictions generalise to previously unseen situations, for a model problem with a large range of multiscale dynamics that span long time periods and are discretised at coarse resolutions. This stands in contrast to initial studies in this direction, which only considered sinusoidal solutions [209] or rapidly decaying turbulence [21] at comparatively fine resolutions. Second, this work will attempt to extend and deepen the understanding of the performance, limitations and opportunities of these unconstrained ANN closures, by investigating the numerical behaviour of Variational Multiscale Method (VMM)-ANN models in highly simplified settings and assessing their fundamental properties and performance in more complex situations. While this study is oriented towards atmospheric turbulence and is conducted within the VMS framework, it is likely that its conclusions generalise to other multiscale problems with complex, nonlinear scale interaction, such as turbulent flows in engineering applications, and to other discrete modelling frameworks than the VMMs in which the ANNs are here contained.

## 1.2. Research Objective and Research Questions

The research objective of this work is succinctly put,

*“To investigate the well-posedness, generalisability, and computational cost of machine-learned approximations of the exact interaction terms of a VMM, for proxies of the atmospheric model equations at relevant levels of discretisation, in offline and online settings.”*

Three main Research Questions (RQs) and their subquestions follow from this research objective.

- RQ1 What are the characteristic scales, spatial distributions and relevance to the global problem of the amplitudes of the interaction terms of a VMS formulation for the model problem, over a range of time and space discretisation levels?
- RQ2 What is the ability of feed-forward ANNs trained on error-free data to make generalised offline predictions of the model problem’s exact interaction terms, compared to state-of-the-art models?
  - RQ2.1 Which combinations of ANN input variables, output variables and architecture ensure that the ANN accurately represents the interaction terms?
  - RQ2.2 To what extent can an ANN predict the interaction terms over a range of increasingly coarse space and time discretisations?
- RQ3 To what extent does an ANN’s generalised offline predictive ability at coarse resolutions translate to online simulations?
  - RQ3.1 What are sources of the stability issues encountered by Robijns in [209]?
  - RQ3.2 To what extent can stability issues be abated by alternative formulations of the VMM-ANN model?
  - RQ3.3 What is the model’s computational cost compared to higher-fidelity simulations and algebraically stabilised VMM?

The research objective and research questions will be unpacked after a treatment of the literature that motivates their formulation, in Section 3.6.1.

## 1.3. Thesis Outline

The thesis is divided into three parts. First, two literature chapters more broadly develop the motivation for the study and the proposed model. Chapter 2 gives an overview over state of the art techniques for atmospheric modelling and poses criteria for a new generation of models. Chapter 3 builds upon this basis, arguing that consistent, data-driven multiscale modelling frameworks in general and VMM-ANNs in particular appear interesting candidates to begin meeting the criteria. Second, Chapter 4 identifies and describes an appropriate model problem for the numerical experiments that facilitate answering the research questions and Chapter 5 outlines the methodology that was developed to conduct the experiments. Finally, four chapters of results and discussion aim to answer the research questions in turn. Chapter 6 characterises exact interaction terms, Chapter 7 investigates aspects of offline machine learning of those interaction terms, Chapter 8 treats the numerical model’s properties in simple settings and Chapter 9 covers its performance in a more realistic setting of 1D turbulence. Conclusions and recommendations are presented in Chapter 10.

# 2

## Atmospheric Modelling

Accurate modelling of the atmosphere is essential to the utility of ESMs as predictors of large-scale dynamics of the earth system [172, 199]. However, posing direct numerical approximations of the fundamental laws of physics that govern the dynamic evolution of the atmosphere is extremely challenging, both in terms of establishing the laws that govern its interior [27] and spatio-temporal boundaries [80, 132, 193] as well as solving the resulting computational problems [221]. Contemporary numerical models of the atmosphere therefore necessarily predicate on sets of assumptions and approximations that ensure their tractability, but introduce errors. This chapter aims to give an overview over these models along with their central assumptions, approximations, and abilities, in order to establish a set of criteria for improving them.

The chapter opens by formulating the mathematical model of the atmosphere relevant to this study, before briefly characterising the dynamics it entails. Next, Section 2.2 and Section 2.3 will introduce the two main approaches traditionally taken to discretise the governing equations, GCMs and Cloud-Resolving Model (CRM)s, present their assumptions and approximations and discuss the resulting implications. In the emerging context, Section 2.4 discusses hybrid, multiscale approaches that attempt to leverage the advantages of each model class. Since these models embody the state of the art, they form a natural point of departure for posing criteria that future models must adhere to. This basis will be built upon in the subsequent chapters of this work.

### 2.1. Problem Formulation

Accurate modelling of the atmosphere is challenged by many of its particular features. First, the atmosphere's interfaces with other components of the earth system, primarily the hydrosphere, cryosphere, lithosphere, biosphere, and space [80], impose spatially and temporally varying boundary conditions on the simulation domain that are subject to the uncertainties in the models of these complex systems [132, 172]. Similar uncertainty exists in the initial conditions that atmospheric models are launched from [193]. Next, atmospheric models must represent the dynamics of interactions between aerosols and cloud moisture, both physically and chemically, at the molecular level. This is far beyond the capability of modern computing, and widely regarded as one of the major uncertainties in numerical simulations of climate response to anthropogenic emissions [27]. Finally, atmospheric motion exists on a truly massive range of scales, spanning more than ten decades in both spatial (from  $10^{-5}$  –  $10^5$ m) and temporal (from  $10^{-6}$  –  $10^5$ s) dimensions [131, 161] (To avoid common confusions elaborated on in [164], this text reserves the term "scales" for sizes of natural phenomena, grid cells and spatial and temporal modes building up a phenomenon, while "size" is used for physical dimensions). It is successfully simulating this scale range by tackling the challenges it imposes on a numerical model that lies at the foundation of this work.

#### 2.1.1. Mathematical Model

The central problem in this regard is to find a suitable discretised model of the problem dynamics' governing equations, the Navier-Stokes equations for a stratified flow on a rotating sphere, described in terms of its local velocity vector  $u_i$ , density  $\rho$ , pressure  $p$  and potential temperature  $\theta = \frac{p}{\rho}^{\frac{1}{\gamma}}$ , where  $\gamma$  is a reference ratio of dry

specific heats:

$$\text{St} \frac{\partial \rho}{\partial t} + \frac{\partial}{\partial x_j} (\rho u_j) = 0 \quad (2.1a)$$

$$\text{St} \frac{\partial u_i}{\partial t} + u_j \frac{\partial u_i}{\partial x_j} + \frac{1}{\text{Ro}} \epsilon_{ijk} \Omega_{ej} u_k + \frac{1}{\rho \text{Ma}^2} \frac{\partial p}{\partial x_i} + \frac{1}{\text{Fr}^2} \delta_{i3} = \frac{1}{\text{Re}} \frac{\partial}{\partial x_j} \left( \frac{\partial u_i}{\partial x_j} + \frac{\partial u_j}{\partial x_i} \right) \quad (2.1b)$$

$$\text{St} \frac{\partial \theta}{\partial t} + u_i \frac{\partial \theta}{\partial x_i} = S_\theta \quad (2.1c)$$

Equations such as Eq. (2.1) are referred to as conservation equations, transport equations, evolution equations or prognostic equations in the fluid dynamics, atmospheric dynamics and turbulence modelling communities. This text will reserve the term “conservation equations” for equation sets that directly reflect the basic conservation laws of nature, while “evolution equations” will be adopted for equations that describe the time-evolution of a quantity. Here, the conservation equations are non-dimensionalised such that the steady inertial term is of  $O(1)$ . This is achieved by employing a reference pressure, density, velocity, length and time to compute  $p$ ,  $\rho$ ,  $u_i$  and  $\theta$ . The Froude number  $\text{Fr}$  is the ratio of inertial to buoyant phenomena, the Mach number  $\text{Ma}$  the ratio of inertial to pressure-driven phenomena, the Rossby number  $\text{Ro}$  the ratio of inertial to Earth-rotational phenomena, the Strouhal number  $\text{St}$  the ratio of unsteady to steady inertial phenomena and the Reynolds number  $\text{Re}$  the ratio of inertial to viscous phenomena (these are defined in equation form in Eq. (A.2) in Appendix A).  $\delta_{ij}$  is the Kroenecker delta,  $\epsilon_{ijk}$  is the Levi-Civita symbol and  $S_\theta$  is a generic heat source. Conservation equations for various species of moisture and aerosols that influence the dynamic field quantities are readily added to this system to extend their representation to moist or chemical processes. Although these are of considerable importance, they do not affect the basic conclusions of this work and will therefore not be actively considered in this study.

Eq. (2.1) allows the evolution of a deterministic chaos in the form of turbulence that is extremely sensitive to its initial conditions across a wide range of scales [150–152]. In an extreme form, one might hypothesise that atmospheric dynamics are driven by *all* scales, leading one to consider situations such as the famous butterfly effect [61]. If its illustration of an arbitrary, very small scale that has the potential to affect very large scales is accurate, the deterministic predictability of the atmosphere should in fact probably be seriously questioned [12]. Not only would solving such problems numerically reach far beyond the computational resources that are expected to be available within the coming century [221], it would also be extremely challenging to find sufficiently accurate initial conditions for such simulations.

Therefore, the fundamental assumption that underlies any tractable model of the atmosphere’s large scales is that the model remains well-posed when the simulated scale range is necessarily truncated by a discretisation [202]. It is therefore made here at the outset of the document, and presupposes all subsequent discussion.

### 2.1.2. Energy Spectrum of Atmospheric Turbulence

The chaotic appearance of the turbulence that emerges from Eq. (2.1) can be somewhat organised by statistical analysis. Commonly, such analysis considers the distribution of covariances of the field variables over the spatial Fourier modes  $k_j$  that construct the solution to Eq. (2.1). For summed correlations of equal velocity field components  $u_i$ , this is an energy measure  $E$ :

$$E(k_j) = \frac{1}{2} \langle \hat{u}_i^*(k_j, t) \hat{u}_i(k_j, t) \rangle \quad (2.2)$$

Where  $\hat{u}_i$  denotes the Fourier-transformed  $u_i$ ,  $\hat{u}_i^*$  is  $\hat{u}_i$ ’s complex conjugate and  $\langle \cdot \rangle$  implies averaging over the temporal dimension. Nastrom and Gage [180, 181] famously report power spectra ( $u_i E$ ) with horizontal, spatial wavenumber  $k_h$  observed in the upper troposphere, reproduced in Fig. 2.1.

These observed spectra support the existence of a continuous atmospheric energy spectrum and oppose the hypothesis of a spectral gap in energy at intermediate wavenumber (as put forward e.g. in chapter 2 of [236]). However, the chaos of instantaneous observation gives way to two distinct regions of modes: A region at lower  $k_h$  (larger scales) with an approximate slope of  $-3$  and a region at higher  $k_h$  (smaller scales) with a slope of  $-5/3$ .

Several theories of various forms of turbulence have attempted to describe this spectrum, with varying degrees of success. Combinations of  $k^{-3}$  and  $k^{-5/3}$  spectra appear in inverse cascades of 2D turbulence [134],

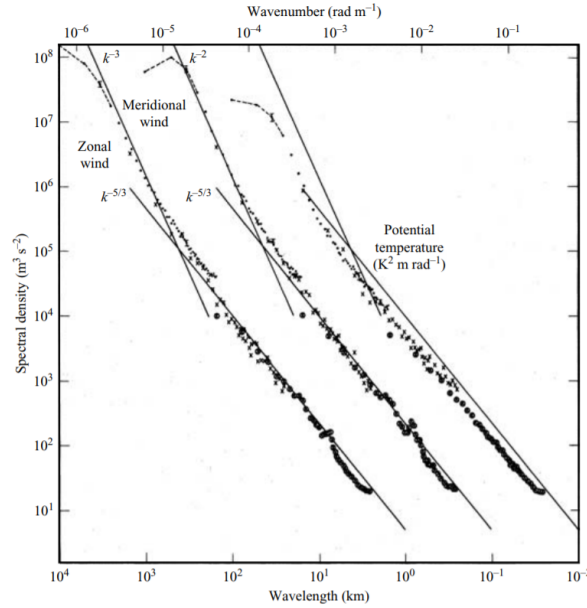


Figure 2.1: Nastrom-Gage spectra of the variance in power of zonal velocity (left), meridional velocity (centre) and potential temperature (right), from GASP aircraft data [180].

which could suggest the largest scales, which are often seen as quasi-2D, are forced by smaller scales [38]. Most observations and computations, however, indicate that a forward cascade is more likely (e.g. [245]).

A theory of forward cascading turbulence with a  $k^{-5/3}$  spectrum readily exists in the context of 3D Homogenous Isotropic Turbulence (HIT) [195]. Such theory assumes energy injection concentrated at large, integral scales and dissipation concentrated at small scales, where  $Re$  in Eq. (2.1) is sufficiently small for viscous dissipation to draw the kinetic energy from the flow. Kolmogorov identified these latter spatial ( $\eta$ ), temporal ( $\tau_\eta$ ) and velocity ( $u_\eta$ ) scales by dimensional analysis:

$$\eta = \left( \frac{\nu^3}{\varepsilon_t} \right)^{\frac{1}{4}} \quad (2.3a)$$

$$u_\eta = (\varepsilon_t \nu)^{\frac{1}{4}} \quad (2.3b)$$

$$\tau_\eta = \left( \frac{\nu}{\varepsilon_t} \right)^{\frac{1}{2}} \quad (2.3c)$$

Where  $\nu$  is kinematic viscosity and  $\varepsilon_t$  the dissipation rate of turbulence. When large-scale productive and small-scale dissipative forces balance and there is little stratification, they are separated by an “inertial” range of scales where energy is merely transferred between modes by the non-local wavenumber interactions that may be identified through the Fourier transform of the nonlinear, convective term in Eq. (2.1). In combination with Eq. (2.3), Kolmogorov deduced that this inertial range should decay with an exponent of  $-5/3$  [195]. Such models of energy spectra proficiently describe the situations that will be encountered later in this work.

However, it is rather remarkable that a  $k^{-5/3}$  spectrum is observed in Fig. 2.1, since this range of atmospheric turbulence is neither isotropic, homogeneous nor inertial, and many other processes than viscosity drain and add energy to the flow [160]. Rather, it appears to be predominantly anisotropic and inhomogeneous in the vertical coordinate [147] and is characterised by strong, intermittent, temporally unbalanced and backscattering energy injection with non-local interactions, for instance from gravity waves [153, 160, 203] or, at larger scales, baroclinic instability [12, 161, 252]. Hence, there is no theoretical consensus on what a physics-grounded, low-order model of this spectrum should be [147, 245]. Therefore, discretised solutions of Eq. (2.1) may yet be the best available tool to correctly capture the dynamics that compose Fig. 2.1 and the trends in its largest scales, even if such simulations must still capture an appreciable range of smaller scales to correctly predict these trends.

The scales defined by Eq. (2.3) are commonly associated with scales smaller than those in Fig. 2.1 [195]. In this context, the figure visually shows that a Direct Numerical Simulation (DNS) that captures the processes in the atmosphere down to these Kolmogorov scales must resolve a truly vast range of scales. To keep the computation of such discrete models tractable, it is necessary to augment them with an approximation for the scales that are *not* directly represented by the discretisation: An unresolved scales model. Such a model introduces assumptions, approximations and errors beyond those of the discretisation. It is an open question

which approaches to i) discretising Eq. (2.1) and ii) posing accompanying unresolved scales models yield the highest accuracy per degree of freedom [221]. Current methods lie spread over an interval that ranges from high-resolution, small in size and high in accuracy, to low-resolution, large in size and large in error; no models are currently equipped to simulate the range of scales in Fig. 2.1 in its entirety. The following sections aim to acquaint the reader with three traditional modelling approaches that sit on either end and in the middle of this interval. They will describe the assumptions and uncertainties these models must make and discuss how their respective drawbacks might inform a new generation of model frameworks.

These sections address the reader that is unfamiliar with the models and their qualities. Their treatment is therefore both introductory and high-level, merely aiming to develop the arguments that motivate the proposition of a new model in this study. Hence, these sections might not be of sufficient interest for each reader to cover in detail; such readers might skip directly ahead to Section 2.6.

## 2.2. General circulation models

GCMs are the class of models that aim at “numerically integrating the equations of fluid motion to simulate the evolution, maintenance, and variations of the [...] time-averaged, planetary scale motion representing the atmosphere’s long-term statistical behavior” [171]. While the class denotation GCM comprises both oceanic and atmospheric circulation models in many texts, it will be reserved for atmospheric circulation models, as these are the primary focus here.

A GCM is the top-down approach to numerical modelling of the atmosphere: Given a certain measure of computing power, its primary requirement is to return stable, long-term ( $O(1 - 10)$  years) simulations of the atmosphere, demanding concessions in discretisation resolution and modelling fidelity. This section will review the modelling approach, assumptions and approximations of the models that result from this trade-off and discuss their advantages and disadvantages.

### 2.2.1. Modelling Approach

To run long, stable calculations, GCMs feature relatively coarse grids. State of the art GCMs contain  $O(10^7)$  grid cells, resulting in horizontal spacings of  $O(10^1 - 10^2)$  km [85, 160, 220, 221] and vertical spacings in the boundary layer of  $O(10^{-1})$  km [85] that exponentially increase over 30-60 layers [171]. This reserves  $O(10^8)$  cells to discretise the oceans [220]. State of the art GCMs can explicitly resolve synoptic-scale processes or larger (see Appendix A for descriptions of these characteristic scales) [171]. This implies that internal gravity waves and small-scale processes cannot be directly resolved. Therefore, it is convenient to choose a mathematical model that does not include these processes. Such equation sets comprise variations of the Hydrostatic Primitive Equations (HPEs), derived in Appendix A.2, which are commonly chosen.

The HPEs retain fully compressible equations in the horizontal direction for length scales larger than the density scale height  $h_{sc}$  [131], while the vertical momentum equation is commonly reduced to hydrostatic balance [253]. This is justified by recognising that the characteristic length and time scales of global vertical motion are around  $10^{-3}$  and  $10^1$  times the characteristic scales of planetary-scale horizontal motion. This shallow-atmosphere approximation permits the omission of the time-varying component of vertical velocity  $w$  [253, 254]. This explicitly filters both vertical acoustic and internal waves by ignoring vertical mean velocity, allowing coarser, stable time discretisations.

### 2.2.2. Applications

Mechoso and Arakawa draw attention to two main applications of GCMs: i) Predictions of weather and climate and ii) climate system sensitivity and variability analysis. The former concerns itself with running ensembles of global simulations from a set of uncertain initial conditions. High resolutions and short time steps currently allow global weather forecasts of a week with greater than 60% correlation to observations, while lower resolution and longer time step simulations have documented several successful subseasonal predictions [171]. Most Numerical Weather Prediction (NWP) models today are based on models such as these [74].

The second application aims to better understand the climate system and its variability. Typically, such investigations run a control GCM until a “quasi-equilibrium” state is reached. A parameter in the simulation is then perturbed, for instance greenhouse gas concentration. The model is then rerun and compared to the unperturbed case. This is the common attitude to anthropogenic climate change assessments [27, 172]. More recently, this approach has been taken to investigate the sensitivity of the climate system to increased concentrations of stratospheric sulphuric aerosols [194, 242].

### 2.2.3. Assumptions and Approximations

GCMs directly represent only the dynamics of large scales of the conservation equations. These equations themselves only apply to part of the processes in the models' domains. Hence, GCMs rely rather heavily on assumptions and approximations associated with the impact of the processes they cannot represent. These are modelled by so-called parameterisations: Models informed by a mixture of physical, phenomenological and statistical arguments for processes that live below the resolved grid scales, are not yet fully understood, or both [101]. Fig. 2.2 is an example illustration of these processes.

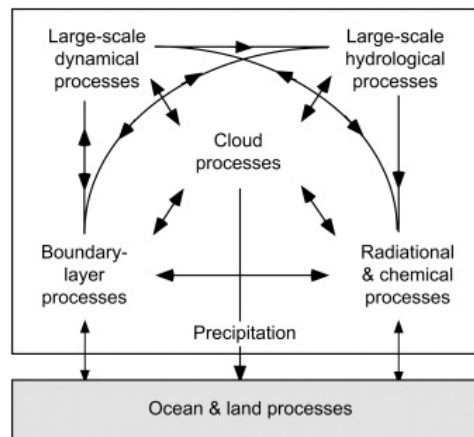


Figure 2.2: Climate system processes and their interactions [171].

A typical GCM contains parameterisations for almost all processes in Fig. 2.2: Radiation [171], planetary boundary layer processes [236], drag and momentum fluxes induced by orographic gravity waves [239], boundary conditions for moisture at the land surface, the influence of vegetation [171] and the dynamic and radiative effects of chemical and aerosol-related processes [175]. While all these processes are important, cloud processes (interchangeable with moist convection in most texts) form an especially crucial part of this interaction cycle. Arakawa emphasises that on the synoptic scales, clouds couple i) dynamic and hydrological processes through condensation, evaporation and redistribution of sensible and latent heat and ii) radiational, hydrological and dynamical processes by reflecting, absorbing and emitting radiation [12]. Furthermore, they influence ground-hydrological processes through precipitation and the atmosphere-ocean interface by interacting with the atmospheric boundary layer.

The appropriate parameterisation of clouds in general and cumulus clouds in particular is therefore broadly considered a primary driver for GCM performance [12, 61, 85, 86]. Arakawa defines cloud parameterisation as “the problem of formulating the statistical effects of moist convection to obtain a closed system for predicting weather and climate” [12]. To close the GCMs properly, the paper establishes six minimum target outputs of cloud parameterisations: i) cloud heating integrated over a vertical grid column, ii) vertical distributions of  $\theta = \theta(z)$  and specific humidity  $q = q(z)$ , iii) mass transport of momentum, temperature, moisture or generic aerosols by unresolved moist convection and the resulting impacts on atmospheric chemistry, planetary boundary layer interactions and the formation of liquid water and ice in the cloud (so-called cloud microphysics), iv) interactions with radiation on the unresolved and resolved scales, v) interactions between resolved and unresolved scale momentum and vi) stochastic effects that recognise the epistemic uncertainty of cloud parameterisation.

Historically, most cloud parameterisations rely on the assumption that the unresolved scales are in “quasi-equilibrium” [12, 71], such that the unresolved variable can be determined directly from other known quantities, independently from their history. Such variables are often referred to as diagnostic or deterministic variables. The quasi-equilibrium assumption is similar to the quasi-steady subscale assumption, which relies on the representative time scales of the processes below the grid resolution all being much smaller than the time step of the numerical model, such that on average, all unresolved scale phenomena have adjusted to the large scale conditions imposed on them. This is the explicit basis for early schemes such as the moist-convective adjustment scheme [163] and the celebrated Arakawa-Schubert parameterisation [14], upon which many modern models still build [178].

### 2.2.4. Discussion

The major advantage of GCMs is their ability to simulate, with relatively high fidelity, the atmosphere at climate-scale. They serve as the major informant for policy decisions regarding climate change projections [27, 172], as they are the current generation's unquestionable benchmark for predicting phenomena on such a scale. However, the assumptions required to close GCMs place important limitations on their utility. The drawbacks that follow can be broadly divided into those associated with the mathematical, physical and numerical modelling stages.

First, the HPEs underpinning most GCMs assume that the phenomena that can be resolved on the grid resolution of the simulation are such that the shallow atmosphere assumption is valid. However, horizontal grid spacings are expected to drop below  $O(10)$  km in the coming decade, such that organised Meso- $\beta$ -scale motion and deep convective clouds can be directly resolved by the model [221]. It is unreasonable to assume that the vertical velocity field can be diagnosed from hydrostatic equilibrium for such simulations [221]. In fact, use of the HPEs may cause numerical instabilities, because the horizontal perturbation pressure force is not hydrostatically balanced by the perturbation density field, leading to the generation of spurious, unstable modes [202]. This highlights the importance of posing *non*-hydrostatic models that are valid also for small-scale motion in the future [213].

Second, the physical modelling of the various parameterisation schemes introduces several problems. First, these parameterisations artificially separate processes on the unresolved scales level and are often inconsistent with respect to their discretisation, such that the modified equations do not reduce to the model equations as the grid resolution is increased [12]. Second, tuning their large number of free parameters i) unavoidably injects a dose of human subjectivity in the eventual model [101], ii) may give rise to strong, unexpected sensitivities of climate system response [261] and iii) makes their uncertainty difficult to quantify [220].

However, there is consensus in the community that the most concerning impact of parameterisation is its influence over the predictive quality of GCM solutions [12, 27, 118, 220]. Section 2.2.3 identified moist convection as an especially essential process that largely depends on dynamics that occur below the grid scale, but impacts the global circulation. The deficiencies of the parameterisations that attempt to capture these dynamics then yield GCMs that are unable to satisfactorily model clouds and contain substantial climate-scale uncertainties as a result [220, 221].

This is particularly true for low stratocumulus clouds. These cool the surface and lower troposphere, as their albedo is high, but their cloud tops are low [95]. For this reason, their accurate representation is vital for calculations of top-of-the-atmosphere radiative balance, upon which climate change assessments pivot. Stratocumulus clouds develop from turbulent updrafts that entrain the stable, free atmosphere into the atmospheric boundary layer. This entrainment takes place in the sharp cloud-top temperature inversion and essentially drives the cloud top height, the thickness of the cloud and much of its temporal evolution. Hence, it is key to many of its radiative and moist properties [57, 236] (this will be discussed further in Chapter 4). However, simulating these turbulent updrafts requires up to an order of magnitude higher vertical resolution than commonly achieved by GCMs [31], and up to three orders of magnitude higher horizontal resolution [221]. Therefore, they are currently placed entirely in the hands of the parameterisation schemes.

As GCM cloud simulations increase in resolution, they increasingly demand direct parameterisation of the microphysics that govern cloud behaviour at the smallest scales to be integrated in the moist convection parameterisation [82]. This includes simulation of a multitude of processes that are not necessarily well-understood, such as the growth of cloud droplets through condensation, growth of ice crystals through deposition, freezing and autoconversion of droplets, aggregation of ice crystals, depletion of cloud ice and droplets through snow and rain, evaporation of cloud water and sublimation and melting of ice and snow [171]. Their interaction with the cloud dynamics parameterisation, themselves subject to strong assumptions, yields a "parameterization squared conundrum, that is, parametrized microphysics in parametrized clouds" [85].

The implications of this deficiency are illustrated by Fig. 2.3. It shows how Equilibrium Climate Sensitivity (ECS) (the global surface temperature increase of a climate in equilibrium after a doubling of CO<sub>2</sub> concentrations), evaluated by a set of state-of-the-art GCMs, is scattered between 2-5 K [221]. This uncertainty range in turn corresponds to an interval of CO<sub>2</sub> concentrations of 480-600 ppm (parts per million) at which the average surface temperature difference with respect to preindustrial levels exceeds the 2 K threshold agreed upon in the 2015 Paris Agreement [190]. Under a high-emission scenario where no greenhouse gas emission reductions are implemented, these concentrations will be reached between 2040-2060 [220]. The extremes of this uncertainty interval mandate a completely different set of optimal policies to approach the problem, an uncertainty that is estimated to cost global society in excess of 10 trillion 2015 USD [99] in the coming

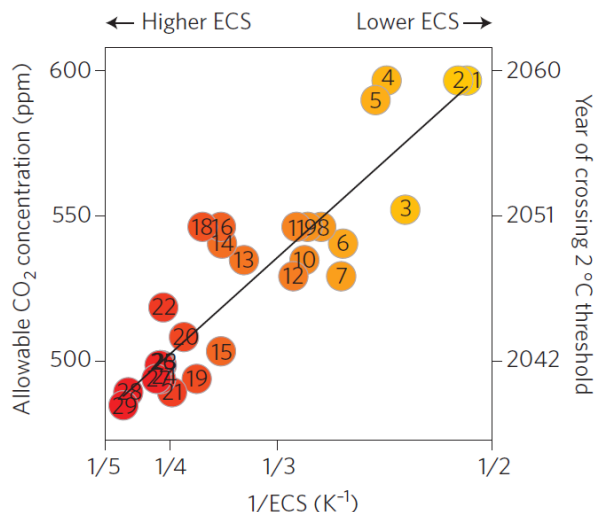


Figure 2.3: CO<sub>2</sub> concentration at which 2 K global temperature rise with respect to pre-industrial levels is reached as a function of ECS<sup>-1</sup> [221]. The circles represent climate models, in order of ascending ECS [33]. The spread in allowable CO<sub>2</sub> concentration corresponds to the spread in time, represented on the right axis, when the 2 K barrier will be broken.

decade if it is not reduced. By far the largest contribution to this uncertainty margin is the unknown response of low stratocumulus clouds over sea to warming [27, 67]: If there are more such clouds in a warmer climate, the 2 K threshold will be crossed later, if there are fewer, the barrier will be broken earlier. There is therefore unquestionably a need to improve parameterisation strategies for moist convective processes that exist far below the grid size, but play a central role in the climate system.

State of the art parameterisations are also criticised for their reliance on the quasi-equilibrium assumption. As the GCMs' horizontal grid resolution will approach  $O(10\text{km})$  in the coming decade, their time steps will come down in proportion. Just as deep convection then demands unsteadiness in the vertical direction to be accounted for in the governing equations, it is also likely that convective events will begin spanning multiple time steps [61]. The quasi-equilibrium assumption will then increasingly break down, such that unsteady unresolved scale models will be required.

A third point of criticism on GCMs pertains to their numerical models, in particular the measures taken to ensure the numerical stability of the GCM. Commonly, this is done by introducing artificial diffusion-like terms based on eddy-viscosity or hyper-viscosity assumptions (see [113] for an extensive review). Unsteady models in engineering turbulence may use arguments such as scale separation and characteristics such as turbulence isotropy and homogeneity on sufficiently small scales to assign physical meaning to eddy-viscosity models when a discretisation's cutoff wavelength resides in an inertial subrange [195]. However, Section 2.1.2 discussed how none of these arguments or characteristics are especially relevant for atmospheric turbulence. Still, GCM developers have traditionally rather focussed on minimising the harm done by these models at the resolved scales and on damping modes that could destabilise the simulation [113] than on formulating accurate models for unresolved turbulence directly. Since better turbulence closure models exist [168] and measurably improve the simulations [92], this is an area where improvements are still often found (e.g. [228]).

In all, it is clear that lacking mathematical, physical and numerical modelling assumptions lie at the foundation of the challenges faced by GCMs. A range of models exist that attempt to remedy these deficiencies by directly simulating the processes that GCMs parameterise. To demonstrate that these models are limited in their own sense and that the future of climate modelling likely still demands GCMs, these models will be reviewed presently.

## 2.3. Global Cloud-Resolving Models

CRMs refer to the class of models “whose grid-spacing is fine enough to allow explicit simulations of individual clouds, throughout their whole life cycle or over part of it [92].” CRMs are often referred to in literature as Cloud Ensemble Model (CEM)s or Cloud System-Resolving Model (CSRMs); this text adopts the first. In the atmospheric sciences, one traditionally further distinguishes CRMs from LES, with the former target-

ing phenomena of larger physical extent such as deep convection [92] and the latter the phenomena that could be simulated down to an inertial subrange, such as atmospheric boundary layers [235]. However, the overwhelming similarity between the approaches has practically reduced the differences to whether finer ( $< O(100)$  m) or coarser ( $< O(1)$  km) grids are being targeted. Hence, this text will mostly treat CRMs as the main class of models, but it implicitly covers almost all aspects of atmospheric LES while doing so.

While sharing many elements with their GCM cousins, the motivation-oriented definition given above indicates that its approach to atmospheric modelling is very much the opposite of that of GCMs. It is a bottom-up approach to numerical modelling, orienting its computing resources towards simulating the physical processes with as high fidelity as possible, trading off spatial and temporal coverage of the simulation. This section discusses the modelling approach, applications, approximations, advantages and disadvantages of CRMs in similar fashion as for GCMs, and presents contrasts and similarities between the approaches that are relevant to the rest of the text.

### 2.3.1. Modelling Approach

Specific small-scale phenomena such as updraft core velocity in deep convective clouds (which is essential for cloud microphysics and microphysics-dynamics interactions) display numerical convergence around 100m horizontal grid resolutions [124], while the simulation of cloud-top entrainment, which is vital for realistic simulations of low clouds [31], requires vertical grid-spacings of the order 25m [192]. These resolutions are several orders of magnitude lower than those achieved by GCMs. However, they are overambitious even for practical applications of Global Cloud-Resolving Model (GCRM)s, where recent developments such as migrating CRM codes to multicore processors have allowed numerical weather predictions over an area with the size of the Netherlands at 100m horizontal grid spacing [215], while the highest resolution GCRM simulation to date ran a 12 hour case of the global atmosphere at 870 m horizontal grid spacing [176]. This global simulation contained  $6.8 \cdot 10^{10}$  grid cells and required full use of RIKEN's K-computer, which at the time held the best LINPACK benchmark performance in the world: 8.162 petaflops [37]. More commonly, GCRMs contain up to  $O(10^9)$  grid cells [85], with time steps of approximately 10s [203].

At these grid spacings, motion of the order  $h_{sc}$  can be directly resolved (see Table A.2), such that vertical accelerations, even in the form of fluctuations around a hydrostatic mean state, must be calculated [85, 92]. Hence, nonhydrostatic mathematical models form the basis of CRMs, varying from anelastic models for deep convection [137] and Boussinesq-approximated equation sets for boundary layer simulations [97], to the full compressible Euler equations necessary for global simulations [138, 213]. In addition, evolution equations are included for various moist species, usually at least comprising specific humidity (or water vapour ratio) and several hydrometeors, for instance liquid cloud water and ice and various forms of precipitation [92].

### 2.3.2. Applications

CRMs have traditionally had two major areas of application [92]. The first category of studies attempts to better understand the dynamics of clouds by resolving a large range of turbulent dynamics and studying how these interact with microphysical and radiative thermodynamical processes to govern moist convection, an area that remains poorly understood [92]. This category involves careful studies of deep convection [124], boundary layer processes [227, 247], organised meso- $\beta$ -scale convection ([92] and references therein) and initial studies on cloud feedback to climate sensitivity [30].

The second category involves developing modelling strategies that will improve weather and climate predictions. This involves model intercomparisons of a single case with different LES or CRM models, which are usually developed independently [97], in order to validate them, ascertain their consistency and highlight structural strengths and shortcomings [70]. Once this is established, the models may serve as inspiration for and verification of GCM parameterisations [92].

### 2.3.3. Assumptions and Approximations

The assumptions and approximations underlying CRMs come significantly closer to the numerical and physical approximations encountered in engineering flows than those encountered in GCMs. As for GCMs, these assumptions and approximations primarily concern what cannot be resolved by the discretisation. However, only parameterisations of radiation, microphysics, and turbulence are normally required [203], because a much larger range of scales is directly resolved compared to GCMs.

CRMs solve evolution equations for a priori separated hydrometeor species and their size distributions, with microphysics parameterisations governing the various sources and sinks that drive the conversion of one species into another. This still invokes many assumptions on hydrometeor formation, conversion to

other species and dissipation. However, attempting to directly simulate the concentration of these species already much improves the parameterisation squared conundrum between radiation and microphysics, in spite of similar simple radiation schemes being employed as in GCMs. An excellent, more in-depth overview over the radiative and microphysics parameterisations that close CRMs is given by Guichard and Couvreur [92].

Approximating the unresolved turbulent dynamics also remains a defining challenge of CRMs and especially LES. As for GCMs, the most common approach to this end is to formulate an artificial diffusion-like model, both for finite volume methods and spectral and finite element approaches [7, 97, 121, 165, 213]. It is traditionally argued that this is a convenient formulation, since it robustly and cheaply drains sufficient turbulent energy from the resolved simulation to sustain a stable simulation [145, 229]. In state-of-the-art LES codes, the original, algebraic schemes have mostly given way to methods that pose one or multiple evolution equations for turbulence kinetic energy  $E$  and its derivatives, which contain interactions with the resolved moist convection, its parameterisation as well as radiation [59, 97].

### 2.3.4. Discussion

High-resolution CRMs are without doubt the highest fidelity models of the atmosphere that exist [92]. This is their great advantage over GCMs: Their higher resolution, lower number of approximations and increased consistency with respect to the processes they simulate make them the ideal for a unified framework for atmospheric simulation.

This is most prevalent in the much improved representation of moist convection by GCRMs that curtail the accuracy of climate predictions of GCMs. Because the turbulent processes in the atmosphere are highly energetic, anisotropic and interactive with respect to radiative and microphysical effects in such a way that intermittent backscatter of energy between continuous scales can directly force large-scale trends, GCRMs predict intra-seasonally varying climate phenomena driven by deep convection much better than GCMs [176, 243]. They also depict convective cloud processes with much less variability between models in model intercomparison projects [70, 92]. In fact, it is often argued that GCRMs that directly resolve phenomena all the way down to stratocumulus clouds and even further down the scale range in Fig. 2.1 may be the only way to properly simulate global atmospheric flow [160, 203]. The endgame of such argumentation is the hope that GCRMs will replace GCMs as the primary framework for global atmospheric simulations up to the climate scale [12, 203].

12 hour simulations of the entire atmosphere at sub-kilometer resolution are without doubt impressive [176]. However, along with LES simulations that highlight that another order of magnitude in grid resolution must be gained before one can reasonably begin resolving low clouds [124], they also immediately point to the intractability of GCRMs for long-term climate simulations. Schneider et al. estimate that computing power must increase by a factor  $10^{11}$  compared to the state of the art to achieve direct resolution of low clouds in these models [221]. Even under the very naïve assumption that computing power will continue doubling every 1.2 years, with every added FLOP devoted to perfectly scaling grid resolution, this would only become possible around 2060. By that time, the climate system will itself have unveiled its sensitivity to the emission experiment humanity is conducting on it [27, 221]. This sentiment is uniformly corroborated throughout the climate system modelling community [160, 214, 220].

Finally, even this picture may be overly optimistic. Early visions of global LES often suggest employing a single CPU per grid column, which at GCM resolution would demand  $O(10^6)$  horizontal “tiles” [85]. The large amount of CPU interfacing required between these cells at runtime renders the computational scaling of CRMs very inefficient [60, 85]. Similarly, the storage of a field quantity on a grid with  $10^9$  cells exceeds 1 TB for a single time step, requiring online post-processing to contain the storage requirements [203]. The state of the art has already encountered the limit at which adding CPUs is becoming energy inefficient, such that a priority in the field is porting existing codes to GPUs [7, 60]. This will likely demand a more specific focus on developing numerical methods that are conducive to “massively parallel” discretisation [85].

## 2.4. Superparameterisation: The Multiscale Modelling Approach

From the previous two sections, three specific characteristics emerge that might improve the GCM and GCRM approaches to atmospheric modelling. First, such models should employ non-hydrostatic equations that remain valid for the entirety of scales that meaningfully impact the resolved-scale atmospheric trends, including deep and shallow convection. Second, they should aim at running at the computational cost of GCMs, given the intractability of GCRMs for long-term global atmospheric simulations. Third, the impact of unre-

solved moist convection on the resolved scales should be strongly inspired by the lessons learned from CRMs to improve the consistency and fidelity of traditional parameterisations.

A promising avenue that leads in this direction is a hybrid strategy that harnesses both the cheapness of a GCM and the accuracy of CRMs on the scales associated with moist convection. Such a framework emerged in the late 90s through research on deep convective phenomena in the tropics. At the time, these were among the largest-scale moist convective systems that remained unresolved by GCMs [221], but were suffering from their traditional hydrostatic equations and quasi-steady, ensemble-averaging parameterisations. Simultaneously, CRM predictions over spatial domains of similar horizontal extent as GCM grid cells, driven by boundary conditions extracted from GCM simulations, began to show good resemblance to experimentally gathered evidence [87]. Based on these observations, it became apparent that a multiscale modelling framework that employs a conventional GCM, but replaces the traditional parameterisation with local CRMs, might offer substantial benefits for a GCM's accuracy. Such a framework emerged in 1999 as Cloud-Resolving Convection Parameterisation (CRCP), later referred to as the Multiscale Modelling Framework (MMF) or SP in the atmospheric modelling literature [83, 86].

This section will review SP. It will place it in the framework of Heterogeneous Multiscale Methods (HMMs), highlight the improvements that SP offers and identify four areas where further progress might be made. Based on these, a set of requirements for improved multiscale GCMs is defined. From this discussion, the next chapter will propose a novel modelling framework as an alternative to SP, and establish the additional conditions under which such a model could be beneficial.

### 2.4.1. Heterogeneous Multiscale Methods

Multiscale modelling arises in a great number of fields, ranging from Car-Parrinello molecular dynamics to composite material analysis and fluid flow simulations [8]. Hence, it might not be surprising that relatively general frameworks have been proposed to understand the fundamentals of such models. An abstract, generalised umbrella for these exists in the mathematical literature as HMMs [251].

HMMs refer to all methods that fall under a mathematical framework that systematically describes multiscale modelling, valid across disciplines [8, 251]. Therefore, it is instructive to introduce its principles here. Its goal is to capture “macro-scale” behaviour (similar to large-scale behaviour of the atmosphere) at a lower cost than employing a “micro-scale” model throughout the domain one attempts to simulate, by making either of two compromises: i) Extracting only the “gross behaviour” of the micro-scale model or ii) exploiting scale separations or self-similarities in the solutions of the mathematical models [158, 251]. While ideas in these directions have coexisted in many fields for decades, the HMM formulation ties them all up to these underlying principles.

HMMs engage a compression operator  $\mathfrak{Q}$ , which compresses the exact solution into a reduced number of states  $u_D = \mathfrak{Q}u$  and a reconstruction operator  $\mathfrak{R}$ , which, if exact, reconstructs the full solution  $u = \mathfrak{R}u_D$ , i.e. the identity  $\mathfrak{Q}(\mathfrak{R}(u_D)) = u_D$  holds. HMM assumes an incomplete macroscale model exists as Eq. (2.4a), where  $\mathcal{D}(u)$  denotes the model's missing part due to its reduced dimensionality. HMM then evaluates the microscale model only where it is needed to find  $\mathcal{D}(u)$  on the macroscale. The microscale model Eq. (2.4b) is therefore subject to the constraint  $d(u_D)$  that makes it reproduce the *macrostate* of interest:  $l(u, d(u_D))$ . A coupled multiscale model ensues:

$$\mathcal{L}(u_D, \mathcal{D}(u)) = 0 \quad (2.4a)$$

$$l(u, d(u_D)) = 0 \quad (2.4b)$$

### 2.4.2. Modelling Approach

Interpreted as a HMM, the premise of SP is to consider a traditional GCM as the macroscale model and replace its entire parameterisation suite with a CRM that operates as a microscale model within a single grid column of the GCM (these will be referred to as the outer and inner models respectively). The CRM can be any of those discussed in Section 2.3 and therefore couples radiation, microphysics and convection on the scales it resolves [83]. It traditionally operates on a 2D grid on a longitude-height plane in the column, sharing vertical grid nodes with the outer model, but retaining sufficient horizontal resolution for CRMs to function adequately [123]. It is run in several sub-time steps within a single time step of the outer GCM, forced by the (constant) GCM tendency on the outer scales. Each CRM is traditionally contained in the grid column of the GCM by imposing periodic boundary conditions on the horizontal edges of the CRM grid, allowing a

fully parallel computation of the unresolved scales model within a single time step of the GCM. In all, this approach reduces its computational cost by up to three orders of magnitude, compared to a GCRM [85].

Grabowski originally presents the coupling between outer and inner models by considering an evolution equation in conservative form of a generic variable  $\chi$ , advected with velocity  $u$  and forced by linear terms  $f$  (for instance, a pressure gradient, Coriolis force, buoyancy or phase change) around an ambient density  $\rho_0$  [87]. It is given by Eq. (2.5):

$$\frac{\partial(\rho_0\chi)}{\partial t} + \frac{\partial}{\partial x_j}(\rho_0 u_j \chi) = \rho_0 f \quad (2.5)$$

Explicitly decomposing these variables into a “large-scale” and a “small-scale” portion (which will correspond to the resolved and unresolved scale portions) yields:

$$\chi = \bar{\chi} + \chi' \quad (2.6a)$$

$$u = \bar{u} + u' \quad (2.6b)$$

$$f = \bar{f} + f' \quad (2.6c)$$

Such that the evolution equation can be written as:

$$\underbrace{\frac{\partial(\rho_0\bar{\chi})}{\partial t} + \frac{\partial}{\partial x_j}(\rho_0\bar{u}_j\bar{\chi})}_{\text{i}} = \rho_0\bar{f} + \underbrace{\rho_0 f' - \frac{\partial(\rho_0\chi')}{\partial t} - \frac{\partial}{\partial x_j}(\rho_0 u'_j \chi')}_{\text{ii}} - \underbrace{\frac{\partial}{\partial x_j}(\rho_0(\bar{u}_j \chi' + u'_j \bar{\chi}))}_{\text{iii}} \quad (2.7)$$

The terms grouped under i represent the interactions of large-scale dynamics, those grouped under ii the interactions of small-scale dynamics, and the terms under iii the interactions of small-scale and large-scale dynamics. Under an explicit assumption of scale separation, Grabowski proposes that when averaged over a large enough horizontal area, the interactions between small-scale perturbations and large-scale perturbations is comparatively small [87]. This would justify setting term iii to 0, which is discussed at some length in Section 2.5.1 and Section 2.5.4. The notation  $F_{SS}^\chi$  is now introduced to define:

$$F_{SS}^\chi = \rho_0 f' - \frac{\partial(\rho_0\chi')}{\partial t} - \frac{\partial}{\partial x_j}(\rho_0 u'_j \chi') \quad (2.8)$$

From this, two equations can be written in terms of the large-scale and small-scale variables explicitly, coupled to each other through  $F_{SS}^\chi$ :

$$\frac{\partial(\rho_0\bar{\chi})}{\partial t} + \frac{\partial}{\partial x_j}(\rho_0\bar{u}_j\bar{\chi}) = \rho_0\bar{f} + F_{SS}^\chi \quad (2.9a)$$

$$\frac{\partial(\rho_0\chi')}{\partial t} + \frac{\partial}{\partial x_j}(\rho_0 u'_j \chi') = \rho_0 f' - F_{SS}^\chi \quad (2.9b)$$

In the context of SP, Eq. (2.9a) is an example of the equation sets that are solved by the GCM. They will only account for large-scale phenomena, and defer processes such as latent heat release, phase changes, surface fluxes, radiative transfer and cloud microphysics to Eq. (2.9b), which feeds the overall impact this has on the large-scale variables back through  $F_{SS}^\chi$  [86]. The original proposal for SP casts the general form Eq. (2.9) as a set of “anelastic equations”. These equations are scale-dependent, but non-hydrostatic; the interested reader is referred to Appendix A.1 for their derivation from Eq. (2.1). The anelastic equations are augmented with three species of moisture. This results in seven large scale and small scale anelastic equations for moist dynamics, such that  $\chi = [u_i, \theta, q_v, q_c, q_p]^T$ , where  $q_v$ ,  $q_c$  and  $q_p$  are the mixing ratios of water vapour, condensed water and precipitation (condensed water that falls relative to the flow) [83]. The equations and their development are included in Appendix A.3.

The equations are numerically coupled in a two-phase time-stepping procedure to advance the solution from time level  $t^n$  to  $t^{n+1} = t^n + \Delta t$ :

1. The large-scale equations are solved to estimate  $\bar{\chi}^{n+1}$ . This provides equations for the large-to-small scale forcings  $F_{SS}^{\chi'}$ . It is common to relax the momentum coupling, whereas thermal coupling is usually immediate [83].

2. With these source terms, the small-scale equations are propagated on the small-scale grid to estimate  $\chi'^{m+1}$ . This requires several interior time steps smaller than that of the outer simulation to maintain stability on the smaller grid, where  $F_{SS}^{\chi'}$  is kept constant. By averaging the resulting small-scale state over a large-scale grid cell, this yields updated estimates for the small-to-large scale forcing  $\bar{F}_{SS}^{\chi}$ . Both large-scale and small-scale fields are then available for the next time step.

### 2.4.3. Applications

SP has garnered acclaim within the atmospheric modelling community [12]. This stems from three main advances that largely meet all the criteria for improved atmospheric models presented at the outset of this section.

First, it poses the most unified framework for integrating physics at the scales where it matters so far seen [85]. The framework is flexible in which microphysics and radiation schemes, as well as phenomenological source terms, are to be employed in the small-scales equations. The large-scale equations are kept consistent and free of subjectively-tuned, uncertain closures.

Second, from the perspective of traditional GCMs, SP provides a significant fidelity increase compared to classical parameterisation schemes, by actually attempting to resolve the parameterisation (hence the original, slightly self-conflicting name “cloud-resolving convection parameterisation”). This remedies the “parameterisation squared” problem [85] and allows SP to benefit from the advantages that CRMs hold in convection modelling.

Third, it achieves this at a significantly reduced cost compared to GCRMs by leveraging the scale separation assumption, which to the highest possible degree decouples the large-scale and small-scale equations. This allows solving the relatively cheap large-scale model on its own in each time step and solving each grid column’s embedded CRM in fully parallel fashion [85], making the model conducive to massively parallel High-Performance Computing (HPC) architectures that do not require the CPU interfacing of GCRMs.

For all these reasons, SP has been extensively applied since its development and it has improved the simulation of many phenomena. Extensive reviews of these can for instance be found in [85, 160] and references therein.

### 2.4.4. Assumptions and Approximations

The main modelling assumption underpinning the original SP formulation is that of scale separation. This manifests itself in four ways. First, as discussed above, the model’s definition assumes that the direct interaction between unresolved (“small-scale”) variables and resolved (“large-scale”) variables is small when averaging over a large enough area [87]. A large area in this sense is denoted by a length scale of  $O(10^2)$  km, such that the small scales incorporate both cloud system convection and meso- $\beta$ -scale dynamics [160]. At the time of its conception, this length scale was commensurable with the resolution achieved by state of the art GCMs, such that the assumption was generally considered reasonable when it was properly applied [84].

Second, the scale separation assumption contends that it is reasonable to expect the temporal and spatial extents of the unresolved scales to be small in comparison to the resolved scales. Hence, it assumes that it is sufficient to predict the unresolved scale quantity averaged over a GCM grid cell, as discussed in Section 2.2.3. Similarly, it assumes that the time-scales of individual, unresolved events are sufficiently small that the large-scale and small-scale velocity fields relax to each other with a time-scale comparable to the large-scale time step, while the large and small-scale thermodynamic fields are estimated to converge immediately [83].

The third assumption pertains to the periodic boundary conditions applied at each grid column’s horizontal boundaries. Such boundary conditions assume the perfect locality of each individual CRM to its own grid column. In terms of scale separation, the small-scales are assumed to be sufficiently small that they are local to each large-scale grid cell, such that all large-scale advection occurs only at the large scales.

Finally, the scale separation assumption often is interpreted to be strong enough that the large-scale model may solve HP equations, while the small-scale model turns to anelastic [85] or pseudo-incompressible equations [137, 138].

As these points form the foundation upon which SP is built, their validity will be discussed in the following sections.

## 2.5. Four Improvement Areas for SP

Despite being a substantial leap forward, traditional SP has several flaws that have ushered in new research. In particular, its original formulation is still somewhat lacking in four areas. The following subsections will

review these shortcomings and place them in the larger context of the direction in which global atmospheric model development appears to be headed, to outline model strategies that might help remedy them.

### 2.5.1. Model Consistency

So far, the discussion on SP has colloquially employed the terms “small scale” and “large scale”, without being rigorous about what is small and large. This is because the original derivation of SP is not very rigorous in its treatment of these terms. In fact, none of the early publications on the development of SP provide any mathematical justification of the terms that should be included in the model or under which circumstances the scale separation assumption is valid [83, 86, 87]. Its particular form is instead based on empirical observation and ad hoc arguments that follow from this [160].

For instance, the use of periodic boundary conditions in each column’s grid cell demands that the mean vertical large-scale velocity is 0 in order to conserve mass [84], which is therefore promptly assumed without justifying why the adoption of periodic boundary conditions was an appropriate choice in the first place. Similarly, it was assumed that term iii in Eq. (2.7) is 0 if the column’s spatial extent is sufficiently large, without indicating how large is large enough.

Practically speaking, the lack of a formal framework to assess the validity of the assumptions underpinning the method means that changing the model’s grid resolution might yield unpleasant surprises. This is especially true for the grid-dependent scale separation assumptions introduced in Section 2.4.4. Additionally, the early instances of SP only featured a 2D CRM in each grid column, aligned with Earth’s latitude bands, as this is the plane in which tropical convection primarily is observed [87]. This is obviously artificial, and leads to formulation intricacies that have proven difficult to handle naturally for 3D simulations on a rotating earth [85].

Several studies in the last decade have remedied these deficiencies. First, it was ascertained that replacing the 2D CRMs with 3D models removes the problems introduced by the former [122]. More generally, Majda [158] formally developed the SP framework by using the method of multiscale asymptotics [259], which is briefly outlined in Appendix A. The main points of Majda’s derivation are presented here, since they expose SP’s underlying assumptions somewhat better.

Letting the small parameter  $\varepsilon$  denote the ratio of two scales and substituting this into the system’s governing equations creates a hierarchy of equations at various orders. Majda considers the model in its limited area mode, which only cover parts of the globe. For these models, the resolved scales are  $O(10^2)$  km (meso- $\beta$ -scales) and the unresolved scales are  $O(10^1)$  km, such that  $\varepsilon = O(10^{-1})$  [158]. This is likely a good proxy for the labour division of global models in the coming decade [221]. Similar relations exist between characteristic time scales of the motion on these spatial scales, typically ranging from 2 hr at the meso- $\beta$  scale and 15 min at the microscale, such that the relations also hold for velocities. Defining

$$X_i = \varepsilon x_i \quad (2.10a)$$

$$T = \varepsilon t \quad (2.10b)$$

for the *horizontal* coordinate and for time then separates the scales. An ansatz for asymptotic expansions can be constructed from this:

$$u_{h,i} = \bar{u}_{h,i}(\varepsilon \mathbf{x}, z, \varepsilon t) + \varepsilon \bar{u}'_{h1,i}(\varepsilon \mathbf{x}, z, t) + u'_{h,i}(\varepsilon \mathbf{x}, \mathbf{x}, z, \varepsilon t, t) + O(\varepsilon^2) \quad (2.11)$$

In Eq. (2.11), the horizontal velocity is decomposed in a large-scale mean ( $\bar{u}_{h,i}$ ), a large-scale fluctuation of  $O(\varepsilon)$  ( $\bar{u}'_{h1,i}$ ) and a small-scale perturbation  $u'_{h,i}$ . The former two both depend only on  $X_i$  and  $T$ , while the latter also depends on  $x_i$  and  $t$ . Similar decompositions are proposed for the wet thermodynamic fields and are inserted in the governing equations. To give an idea of the procedure, consider how this reformulates the averaged continuity equation from Eq. (2.1) ( $u_h$  denotes horizontal velocities,  $w$  the vertical velocity):

$$\frac{\partial}{\partial x_j} u_{h,j} + \frac{\partial}{\partial z} w = 0 \quad (2.12a)$$

$$\frac{\partial}{\partial x_j} u_{h,j} + \varepsilon \frac{\partial}{\partial X_j} u_{h,j} + \frac{\partial}{\partial z} w = 0 \quad (2.12b)$$

$$\frac{\partial}{\partial x_j} \left( \bar{u}_{h,i} + \varepsilon \bar{u}'_{h1,i} + u'_{h,i} \right) + \varepsilon \frac{\partial}{\partial X_j} u_{h,j} \left( \bar{u}_{h,i} + \varepsilon \bar{u}'_{h1,i} + u'_{h,i} \right) + \frac{\partial}{\partial z} (\bar{w} + \varepsilon \bar{w}'_1 + w') = 0 \quad (2.12c)$$

Due to the scale separation,  $\tau$  quantities do not depend on  $x_i$  and terms such as  $\frac{\partial \bar{u}_{h,i}}{\partial x_i} = 0$ . Hierarchical reordering of Eq. (2.12c) at the various orders of  $\varepsilon$  then yields:

$$\varepsilon^0: \frac{\partial}{\partial z} \bar{w} = 0 \quad (2.13a)$$

$$\varepsilon^1: \frac{\partial}{\partial x_j} u_{h,j} + \frac{\partial}{\partial z} \bar{w}_1 = 0 \quad (2.13b)$$

$$\varepsilon^2: \frac{\partial}{\partial X_j} u_{h1,j} = 0 \quad (2.13c)$$

First, Eq. (2.13) clarifies that to leading order, continuity reduces to the self-consistent constraint that  $w = 0$  by a systematic analysis. This implies that on the meso- $\beta$ -scales, the vertical velocity has a leading-order term of  $O(\varepsilon^1)$ , while the horizontal velocities have a leading order of  $O(\varepsilon^0)$ , which is corroborated by observations [160].

Subjecting the momentum, thermodynamic and moisture equations to similar treatments likewise extracts their respective leading-order components. From this, the leading order vertical momentum balance is hydrostatic, whereas the averaged horizontal equation reduces to:

$$\frac{\partial \bar{u}_{h,i}}{\partial t} = - \frac{\partial}{\partial z} \left( \overline{w' u'_{h,i}} \right) \quad (2.14)$$

Let  $\langle \cdot \rangle$  denote a time-averaged quantity. If Eq. (2.14) and its thermodynamic and moisture counterparts are bounded in time, i.e.  $\langle \frac{\partial \bar{u}}{\partial t} \rangle = 0$ , then in an averaged sense:

$$\left\langle - \frac{\partial}{\partial z} \left( \overline{w' u'_{h,i}} \right) \right\rangle = \varepsilon \langle \bar{S}_i \rangle (\varepsilon \mathbf{x}, z, T) \quad (2.15)$$

Eq. (2.15) captures the essence of formally derived SP: The local, resolved-scale, space-time-averaged leading order terms must be balanced by source terms of  $O(\varepsilon)$ . For Eq. (2.15), this implies that the vertical flux of horizontal momentum on the scales resolved by the GCM must be sufficiently small. Practically, this means that the space-time fraction of deep convection (the most vigorous unresolved-scale phenomenon on the meso- $\beta$  scale) on the GCM-resolved scales can only be small or spatiotemporally decorrelated [158]. Similar constraints again exist for the thermodynamic and moisture equations.

The small-scale equations are derived by subtracting the leading-order terms from the original equations. Contrary to the original derivation, this does not assume that all interactions between resolved and unresolved scales are zero, but it retains the horizontal derivatives of large-scale values in the small scale equations [160]. In Limited Area Models (LAMs), these terms are critical for representing several important eddy instability types, such as the baroclinic instability [90]. They are, however, precluded from Eqs. (2.9a) and (2.9b), once again highlighting the need of this formal treatment.

The introduction of multiscale asymptotics to more formally define SP therefore confirms original ad hoc assumptions, highlights the model's regime of validity and improves its predictive ability. In a bid to generalise the approach to SP in a more meticulous manner, Majda therefore suggests a four-step approach to systematic SP [160]:

1. Formulation of multiscale method
2. Definition of small-scale model
3. Justified error introduction and subsequent model simplification
4. A posteriori validations of the SP approximations, particularly focussing on the capability of capturing multiscale interactions

These criteria will therefore be employed as guidelines for the following chapters, which propose and implement further improved multiscale formulations.

### 2.5.2. Low Cloud Simulation Accuracy

While SP substantially enhances the accurate simulation of deep convection, it still is unable to properly represent low clouds [192]. As discussed in Section 2.2.4, the uncertainty of the response of marine boundary layer low clouds to warming is arguably the largest outstanding uncertainty in the atmospheric component of climate and earth system models [67, 221]. Simultaneously, SP is becoming increasingly important for assessing the role of clouds in a warmer climate [15, 32]. It is at present not fully clear if SP is proficient enough for this responsibility, mandating rapid improvement.

The persistence of the low cloud simulation problem even for SP comes from the tradeoff that SP makes between computational cost and accuracy: The resolution of the embedded CRMs is simply not high enough to properly resolve the portions of the atmospheric boundary layer's turbulence that forms cumulus and stratocumulus clouds [192]. The models share the coarse vertical grid resolution of the outer GCM, employing 30-50 stretched layers with a spacing in the boundary layer of  $O(10^{-1})$  km [85]. Consequently, they cannot simulate stratocumulus cloud-top entrainment much better than traditional GCMs.

Similarly, the horizontal resolution of CRMs in global-size SP is typically still  $O(10^0)$  km [160]. This also cannot properly resolve the horizontal extent of individual clouds, which are typically  $O(10^{-1})$  km [236]. As a result of the CRM's coarseness, the models produce unrealistically low levels of cloud turbulence in the subtropics [192]. In this portion of the Hadley circulation, dry, descending air ("subsidence") balances the boundary layer turbulence to yield coherent, stable stratocumulus decks. However, the lack of accurate boundary layer turbulence in SP and other GCMs means that the presence of low clouds is "too little in the cool subtropical ocean regions in which stratocumulus clouds prevail" [258], leading to overprediction of ocean irradiation and temperature [234]. On the larger scales, the mispredictions manifest themselves in so-called "model biases", which are systemic mispredictions of the global climate [179].

Several studies have attempted to improve the boundary layer turbulence representation of SP over the last few years, broadly divided into two categories. The first attempts to improve the CRM's turbulence closure models to better represent their unresolved portions [228]. Such higher-order closure schemes improve the vertical structure of boundary layer clouds and subsequently their radiative balance [41, 258]. However, fourth-order models double the computational expense of the total simulation. More importantly, they remain philosophically similar to traditional GCM parameterisations, posing intricate closure relations with many uncertain, tunable parameters that prohibit the numerical convergence of the approach [258] and render the correlation between turbulence and microphysics especially sensitive [192].

The second strategy is to resolve the eddies directly in the superparameterisation. This could be through increasing the resolution of the CRM in the boundary layer such that the eddies fall within the resolved portion of the 2D CRM [192], or by directly employing high-fidelity 3D models such as LES [61, 85, 115, 221]. The original publication on high-resolution 2D CRM models increased the resolution of the SP-Community Atmosphere Model (CAM) to  $250 \times 20$  m, and coined this Ultraparameterisation (UP) [192]. This managed to improve the vertical boundary layer depth and stratocumulus structure by allowing stronger, more realistic boundary layer turbulence to balance subtropical subsidence. In turn, this yielded better estimates of liquid water content in the offshore diurnal cycle. Nevertheless, UP also suffers from misrepresentation of cloud thickness and albedo, an issue that is currently not fully understood. It is potentially a limitation of the 2D nature of the CRM, as subtropical stratocumulus clouds are much less directionally aligned than tropical convection [85].

The second approach was advocated by Grabowski [85] and very recently implemented [115], by coupling Dutch Atmospheric Large Eddy Simulation (DALES) [97] to the European Centre for Medium-Range Weather Forecasts (ECMWF)'s OpenIFS GCM [19]. Tests over an area representing the Netherlands over a diurnal cycle display promise that the stratocumulus deck is much better predicted with such a model than with the original model, based on a sparse vertical measurement profile.

Operationalising these models for climate simulations might therefore demand extension of the 2D CRMs in UP to 3D, while the current, high-fidelity 3D approach must be upscaled a from LAM to a GCM. However, these computations already run at exascale computing cost [192], which will make the extensions very difficult in the near future if they are to be achieved by a conventional resolution increase or scaling. This brings the discussion to the third drawback of SP: Its high computational cost.

### 2.5.3. Computational Cost

The bulk of the computational cost of SP is carried by evaluating the inner CRMs [160, 205]. Given SP's lack of low-cloud representation and the anticipated push to remedy this through high-resolution models, the computational cost of these CRMs might only become more of a hard limit in the future. However, recent

research has suggested that representing *all* scales below the large-scale model's grid resolution might also not be necessary when the large-scale model becomes fine enough to simulate much of the meso- $\beta$ -scales directly [159]. The concern of the small-scale CRMs is then mainly to simulate accurately the moist convective modes that drive the large-scale simulation [160]. The large-scale grid-resolutions required to resolve the meso- $\beta$ -scales in climate-scale computations will become increasingly standard for classical, cheaper GCMs in the coming decade [221]. Therefore, if the cost of the CRMs in SP can be reduced and reinvested in the outer model's grid resolution, the overall model accuracy may actually increase, as more scales are allowed to consistently interact within the outer model.

Pursuits of CRM cost reduction have been successfully investigated in traditional LAMs, which already operate at the grid resolutions of future GCMs. The first such study proposed Sparse Superparameterisation (SSP) [257]. This model runs the inner CRM in a fractional subdomain of the outer model's grid cell for a fraction of the outer model's time step. Similar reductions of the integrated CRM time step could later be achieved by mean state acceleration [117]. While obviously an artificial construct, reducing the space-time dimensions by a factor  $\frac{1}{3}$  will yield an efficiency gain of almost an order of magnitude for a 2D CRM. Nevertheless, pattern correlations with original, high-resolution versions of the model have been observed to remain over 0.75 [257]. The cost reduction is even more significant if the spatiotemporal extent of 3D CRMs is reduced by the same order. Such reductions similarly appear to have only little impact on the solution accuracy [115]. This is very encouraging, because it suggests that these models have arrived at a resolution stage where they could be represented by even cheaper, systematic models based on deterministic or stochastic arguments [160]. It might then not be necessary to run full 3D LES; if there are finite sets of scales at this level that dominate the unresolved scale projection onto the resolved scales, it might only be necessary to appropriately model these. This motivates one to focus only on representing these impactful scales' projections, rather than the full set of unresolved scales. Substituting the CRMs for such models would permit further resolution increases of the outer model, or push the cost of SP down to the order of conventional GCMs.

#### 2.5.4. Scale Separation

As introduced in Sections 2.4.4 and 2.5.1, the validity of the SP formulation hinges on the validity of the underlying scale separation assumption. The implications of this assumption are threefold: First, the spatiotemporal average of the outer model characteristic scale's fluctuating dynamics must be sufficiently small that it can be balanced by source terms at the inner model's characteristic scale (see Eq. (2.15)). Second, the terms predicted by the inner model may be represented in an averaged sense on the outer model's grid and will adjust to the large-scale state within an outer model time step. Third, the largest scales in the inner model are assumed to be sufficiently local that they only interact with neighbouring outer model cells through the scales represented by the outer model, facilitating the use of periodic boundary conditions and parallelised computation for the inner models.

Practically speaking, the assumption has been observed to work well when the outer model only resolves scales larger than the synoptic scale (100-200 km grid cells), which was state of the art when SP was first developed [123]. In this situation, most meso- $\beta$ -scale dynamics, which are highly anisotropic and organised along scales up to  $O(10^2)$  km [102], are deferred to the CRM. The cross-interactions between the GCM and CRM (term iii in Eq. (2.9)) will then be small, while the effects of pure, unresolved scales effects on the resolved scales dominate (terms ii in Eq. (2.9)), justifying the original model assumptions. However, introducing the grid scale break somewhere in the middle of the meso- $\beta$ -scales (15-100 km grid cells) means that an organised convective meso- $\beta$ -scale system cannot i) interact fully with itself, as it is *missing* the direct interactions between its resolved and unresolved scales contributions (term iii in Eq. (2.9)), or ii) coherently propagate quantities from one outer model grid cell to another, as those quantities are assumed to be fully local to a grid cell. It has been repeatedly observed that this leads to their misrepresentation [84, 115, 119]. Similar arguments pertain to the time step of the model [160]. As current GCMs operate with cells in the 50-100 km range, this could curtail the performance of the model.

Therefore, it is crucial to further assess the validity of the scale separation argument as the grid resolutions of GCMs reduce. Classical GCMs will increasingly resolve the meso- $\beta$ -scales on their grids [221] if cheap parameterisations are employed [220]. Hence, it is interesting that the model reestablishes its accuracy somewhat when the outer model of LAM SP is allowed to simulate down to *below* the meso- $\beta$ -scales (10-50 km grid cells), such that organised meso- $\beta$ -scale convection can be consistently represented on the resolved scales [84, 85]. The time step is in such situations also less ( $O(10^2)$  s) than the typical lifetime of a single convective meso- $\beta$ -scale event ( $O(10^3)$  s) [36]. Could this be a physical scale break that might be exploited? If so, these are the circumstances where SP algorithms might actually be made cheaper [257]. In

turn, that might facilitate representing the meso- $\beta$  scales fully on the outer model's grids in global SP.

Each of the implications of the scale separation assumption can be analysed in this context. First, as highlighted in Section 2.5.1, the vertical flux of horizontal momentum must be small to satisfy the asymptotic analysis, such that the spatiotemporal fraction of deep convection within an outer model grid cell and time step must also be small, or at least decorrelated [158]. As the grid spacing reduces, this increasingly breaks down [159, 161]. Hence, models constructed with this approximation are prevented from describing “the interaction between scales immediately above and immediately below the grid scale” [160], i.e the importance of term iii in Eq. (2.9) reappears. This dismisses the question posed above and mirrors Fig. 2.1's evidence for the non-existence of a meaningful gap in the atmospheric energy spectrum: The inaccuracies from introducing a scale break quickly rematerialise when the break migrates further down the scale range below the meso- $\beta$  scales and different scales begin contributing to term iii in Eq. (2.9).

Second, the effects of scale separation materialise in SP's ensemble averaging and time relaxation. Once the outer model's grid resolution and time step approach the sizes of single convective events, these assumptions break down: The ensemble gives a spatially fluctuating response to the mean state and individual convective events can span several time steps [61, 161], requiring consistent temporal coupling.

Third, the periodic CRM domains can prohibit small-scale instabilities from developing properly, causing mispredictions of their impact on the outer model's scales [161]. One could avoid this by embedding large, open, finite domains in the columns, though no studies employ these outside 1D test problems [88, 160].

In all, it is therefore unclear whether SP and other traditional HMMs are suitable models for GCMs operating at increasingly high resolution. While these methods gain their computational advantages by exploiting wide scale separations, self-similarities and quasi-steady time equilibration of the small scale models [55, 73, 251], they cannot do so for small scales that intermittently backscatter evolving, highly energetic vortices, jets, waves and latent heat release to the large scales, without statistical equilibration [158–160, 220, 248]. Similarly, traditional GCM parameterisations based on ensemble averaging and quasi-equilibrium will also have to navigate this hurdle, as touched upon in Section 2.2.4. This generalises the challenge beyond SP.

## 2.6. Summary and Outlook

In summary, this chapter has discussed the appreciable challenge of modelling the atmospheric dynamic scale range. It has identified parameterisation of low clouds as a primary issue for GCMs. While this could be remedied by non-hydrostatic GCRMs that directly represent the convection, these models will remain too computationally expensive for service. Therefore, improved models must engage non-hydrostatic equations, run at the cost of GCMs, but attempt to incorporate the accuracy of CRMs as best they can.

The chapter presented SP as an atmospheric multiscale method that broadly achieves these goals, rendering it the best currently available candidate for improving our current estimates of the future of Earth's climate. However, the method was originally very loosely and informally defined, is still unable to adequately represent low clouds, is limited by the computational cost of its CRM inner models and suffers from the consequences of its underlying scale separation assumption. While the first point has been addressed by the introduction of multiscale asymptotics as a formal framework to pose the method in, the remaining three points are likely to shift increasingly into focus as the resolution of GCMs increases in the coming decade.

In the light of these four challenges, four criteria for future-proof, improved climate-scale multiscale models of the atmosphere may be formulated as extensions to those that first ushered in the multiscale models:

1. The models must rest on a firm, consistent, mathematical foundation to assess their ranges of validity.
2. They must represent low clouds in an improved manner with less degrees of freedom than GCRMs.
3. They must fully and consistently couple the resolved scales model to the most impactful scales below it, to circumvent increasingly invalid scale separation assumptions at higher GCM grid resolutions.
4. They should be closed by high-fidelity inspired unresolved scales models that aim to capture all phenomena below the resolved scales that contribute to intermittent, highly energetic, non-equilibrated backscatter to the resolved scales.

These requirements form the conclusion of this chapter and provide the direct motivation for the remainder of this thesis. Proceeding along Majda's proposed four-step approach for systematic SP, the next chapter will formulate a multiscale method and a small-scale method, which have the potential to improve the four points presented above. The subsequent chapters will seek to validate the model's approximations and assess the model's capability to represent multiscale interactions, as well as its stability.



# 3

## A Variational Multiscale and Machine Learning Modelling Framework

The set of requirements for improved multiscale atmospheric models outlined at the end of the previous chapter poses two clear directions that will be treated presently. First, models derived within the framework of multiscale asymptotics explicitly predicate on the scale separation assumption. Hence, they are vulnerable when this assumption breaks down. There are, however, multiscale modelling frameworks that may be consistently derived on a firm mathematical basis *without* imposing any scale separation assumptions. For this reason, Section 3.2 will introduce such Variational Multiscale (VMS) formulations, outline their derivations and traditional closure approximations, and briefly review the scope of their application to atmospheric flow simulation. Section 3.3 scrutinises them against the set of requirements presented in Section 2.6.

The second important finding of Chapter 2 is that any unresolved scales model must handle moderate to no scale separation. As a consequence, the unresolved scales model must predict intermittent, highly energetic backscatter and cannot be in statistical equilibrium with the resolved scales. The success of an improved formulation of the GCM will therefore hinge on a convincing model for the unresolved scales. Section 3.4 will propose that such an unresolved scales model might derive from the data of scale-consistent simulations and observations, and Section 3.5 will nominate ANNs as especially promising candidates. This will result in the formulation of an entirely novel model that attempts to meet all requirements considered here in Section 3.6, which will outline a roadmap for its initial testing in the second part of this thesis. Readers that are familiar with VMS and data-driven parameterisation could skip straight to this section. However, all readers are encouraged to read Section 3.1, which offers a conceptual overview over the proposed modelling framework.

### 3.1. Conceptual Modelling Framework

A conceptual illustration of a modelling framework that attempts to meet the criteria posed in Section 2.6 is presented in Fig. 3.1, with its contrasts to classical parameterisation and SP. Classical parameterisations pose process-level parameterisations based on the resolved solution field  $\bar{u}$  for each component of their unresolved mechanisms, interface these parameterisations and use the combined estimates to pose source terms  $\hat{I}$  that enter the evolution equations of the resolved scales. SP replaces the individual parameterisations and their interfacing by solving scale-separated inner evolution equations, which again yield estimates for source terms that affect the resolved-scales at the next time level.

What is proposed here, however, is to acknowledge that one can only really measure what one resolves. Taking this perspective, the only aspect of interest of the unresolved scales is correctly representing their impact on the resolved scales. In the language of the HMMs introduced in Section 2.4.1, one would only be interested in representing the missing portion of the macroscale model. Hence, this study proposes to i) avoid individual, process-level parameterisations and scale separation entirely, by reanalysing the conservation equations of the problem and isolating the *exact* “interaction terms”  $I$  that couple the resolved and unresolved scales, ii) directly propose models for  $I - \hat{I}$  – rather than the unresolved scales variables themselves and iii) solve for the resolved scales in conjunction with the unresolved scales’ impact on them.

Conceptually, this proposal is very general and not particularly new: It is very similar to the first steps of traditional LES and CRM formulations reviewed in Section 2.3. The resolved-scales model’s role in this figure

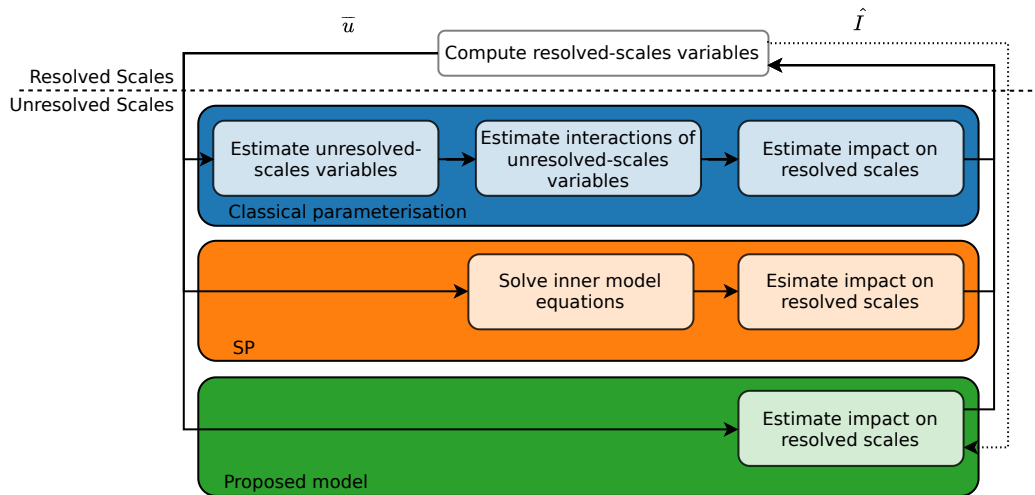


Figure 3.1: Conceptual overview of the unresolved scales and resolved-scales coupling in a classical parameterisation, a SP and the approach taken here.

would then be to meet criteria 1 and 3 from Section 2.6. They must find mathematical formulations of  $\hat{I}$  that fully and consistently couple the resolved and unresolved scales of the discretised model. Hence, any set of numerical approximations that respect these criteria are suitable outer model candidates, be they finite difference, finite volume or finite-element oriented.

In this work, this conceptual model is interpreted in terms of the VMS formulation of finite element and spectral methods, as will be extensively outlined below. This model is chosen because i) it lies very close to SP in terms of modelling philosophy, ii) it is essentially an LES and therefore comparable to those models also and iii) it is explicitly clear in where modelling and discretisation errors enter the equations, which cleanly facilitates the inclusion of high-fidelity models for  $\hat{I}$ . However, by appropriately modifying the analysis and resolved-unresolved scales interactions, similar methods such as filtered finite volume discretisations could be used as a resolved-scales model.

The notable difference between the proposed model and classical LES lies in their division of their work. While Section 2.3 established that such models are intractable for global computation when they must *resolve* the scales that drive shallow convective processes and satisfy criterion 2 from Section 2.6, there is nothing inherently limiting in their formulation if improved, scale-consistent unresolved scales models are used to close them at a coarser level of discretisation.

Therefore, the main novelty in this framework is the approach it takes to requirement 4 from Section 2.6: It attempts to leverage machine learning to condition fully coupled models for the unified physics of the unresolved scales on data from models and observations that satisfy the governing equations of the problem. If such closure schemes have sufficient skill at coarse resolutions, and manageable computational cost, models could be posed that meet all criteria in Section 2.6. It is the assessment of such models that is the central topic of this work. In the light of the above discussion, the study's conclusions are likely to translate to any numerical, scale-consistent resolved-scales model that facilitates the exact representation of  $I$ , such that the thesis also applies to traditional atmospheric or engineering finite volume approaches to turbulent flows.

## 3.2. Variational Multiscale Methods

The VMS framework is an alternative approach to multiscale modelling, grounded in the field of stabilised spectral and finite element discretisations for fluid dynamical problems. In this context, its development was motivated by the failure of traditional Galerkin methods for problems comprising multiscale phenomena [109]. Such discretisations tend to produce spurious, high frequency oscillations in their representations of advective phenomena that can destabilise computations, in a similar manner as central-difference type discretisations [116]. Schemes that address this issue are therefore traditionally called “stabilisation schemes” in the finite element community. While stabilisation could be achieved with artificial viscosity-type models, it was soon discovered that a more steerable technique was modifying the weighting functions of the Galerkin methods. For instance, biasing the weighting functions in the upwind direction with so-called “bubble func-

tions” gives the discretisation an increasing character of first order, numerically diffusive methods [16], but prevents the excessive cross-wind diffusion associated with artificial viscosity methods [104]. However, these “streamline-upwind” methods are still inconsistent, a drawback that was amended by introducing perturbations to the stabilisation term that were proportional to the residual of the resolved-scales equations. This idea gave rise to two popular residual-driven methods: Streamline-upwind Petrov-Galerkin (SUPG) methods for advection-diffusion equations [34] and its generalisation to problems where the basis functions are not piecewise-linear and the simulated process not predominantly advective, Galerkin/Least Squares (GLS) [106]. Petrov-Galerkin methods stand in contrast to Bubnov-Galerkin methods, where the weighting functions and basis functions are the same. These ideas were further conceptually generalised throughout the 90s, when Hughes cast the problem on a multiscale form [105], leading to the framework considered here.

### 3.2.1. Modelling Approach

The VMS formulation arises relatively naturally when one considers the decomposition of a field  $u$  as a linear superposition of an infinite number of orthogonal modes  $\phi_i$  with amplitude  $a_i$  (see Eq. (3.1)). If one requires  $k_K$  modes for a DNS ( $k_K$  denoting the wavenumber of the Kolmogorov length scale defined in Eq. (2.3a)), but employs a grid where  $k_c < k_K$  modes can be resolved, this implies that a natural way of separating which portions of  $u$  can be resolved directly and which must be approximated is the application of a linear projection operator that decomposes  $u$  into the resolved solution  $\bar{u}$  and the unresolved solution  $u'$ :  $u = \bar{u} + u'$ :

$$u = \sum_i^{\infty} a_i(t) \phi_i(\mathbf{x}) \approx \sum_{i=0}^{i=k_c} a_i(t) \phi_i(\mathbf{x}) + \sum_{i=k_c+1}^{i=k_K} a_i(t) \phi_i(\mathbf{x}) = \bar{u} + u' \quad (3.1)$$

It is immediately clear from this definition that  $u'$  is formally infinite-dimensional for nonlinear problems, and that it is significant up to  $k_K$  at least. Furthermore, its content depends on where  $\bar{u}$  is truncated. In multiscale LES, the goal is then to find approximations for  $u'$  that facilitate the accurate computation of  $\bar{u}$ , rather than  $u$  itself. Assuming one chooses a set of  $k_c$  bases to construct  $\bar{u}$ , this may be achieved by variational methods, setting this loose argumentation on a solid mathematical foundation.

Consider, for this discussion, a differential operator  $\mathcal{L}$  for a general Partial Differential Equation (PDE) of second order, valid on domain  $\Omega \in \mathbb{R}^d$ , where  $d \geq 1$  is the number of spatial dimensions. When this domain is bounded by a smooth boundary  $\Gamma_\Omega$  on which a Dirichlet condition is imposed, one may represent the abstract, continuous, boundary value problem as: Find  $u \in \Omega$  such that Eq. (3.2) is satisfied, where  $f \in \Omega$  is a generic forcing and  $g_\Gamma \in \Omega$  is a generic Dirichlet boundary condition:

$$\mathcal{L}u = f, \quad u \in \Omega \quad (3.2a)$$

$$u = g_\Gamma, \quad u \in \Gamma_\Omega \quad (3.2b)$$

Galerkin methods consider weak forms (sometimes referred to as variational forms in literature [110]) of the continuous model equations, which are tested with trial solutions  $u$  and weighting functions  $\psi$ .  $u$  and  $\psi$  must span the trial solution space  $\mathcal{S} \in H^1(\Omega)$  and weighting function space  $\mathcal{V} \in H^1(\Omega)$ , respectively, where  $H^1(\Omega)$  is the Sobolev space of square integrable functions with square integrable derivatives (i.e. for an arbitrary  $f(x)$ ,  $\int_\Omega (f^2 + f_x^2) < \infty$ ). Assuming that:

$$u = g_\Gamma \quad \text{on} \quad \Gamma_\Omega \quad \forall u \in \mathcal{S} \quad (3.3a)$$

$$\psi = 0 \quad \text{on} \quad \Gamma_\Omega \quad \forall \psi \in \mathcal{V} \quad (3.3b)$$

The weak counterpart to Eq. (3.2) is: Find  $u \in \mathcal{S}$  such that for all  $\psi$  in  $\mathcal{V}$ :

$$\int_\Omega \psi (\mathcal{L}u - f) d\Omega = (\psi, \mathcal{L}u - f)_\Omega = 0 \quad (3.4)$$

Where compact notation  $(\cdot, \cdot)_\Omega$  is introduced for symmetric, bilinear forms [109]. The central idea of the VMS formulation is to split the infinite-dimensional spaces  $\mathcal{S}$  and  $\mathcal{V}$  according to the linear decomposition of  $u$  presented in Eq. (3.1), i.e. at the *level of the discretisation*:

$$\mathcal{S} = \bar{\mathcal{S}} + \mathcal{S}' \quad (3.5a)$$

$$\mathcal{V} = \bar{\mathcal{V}} + \mathcal{V}' \quad (3.5b)$$

Such that  $u = \bar{u} \in \bar{\mathcal{S}} + u' \in \mathcal{S}'$  and  $\psi = \bar{\psi} \in \bar{\mathcal{V}} + \psi' \in \mathcal{V}'$ , where  $\bar{\mathcal{S}}$  and  $\bar{\mathcal{V}}$  are the spaces resolved by a discretisation and  $\mathcal{S}'$  and  $\mathcal{V}'$  are infinite dimensional. More precisely, the space decomposition can be expressed in terms of the projectors  $\bar{\Pi}_{\mathcal{S}}$  and  $\bar{\Pi}_{\mathcal{V}}$ , that map  $u$  and  $\psi$  onto  $\bar{\mathcal{S}}$  and  $\bar{\mathcal{V}}$ :

$$\bar{u} = \bar{\Pi}_{\mathcal{S}} u \quad (3.6a) \quad \bar{\psi} = \bar{\Pi}_{\mathcal{V}} \psi \quad (3.6b)$$

The projectors on  $\mathcal{S}'$  and  $\mathcal{V}'$  are then necessarily:

$$\Pi'_{\mathcal{S}} = id - \bar{\Pi}_{\mathcal{S}} \quad (3.7a) \quad \Pi'_{\mathcal{V}} = id - \bar{\Pi}_{\mathcal{V}} \quad (3.7b)$$

Where  $id$  denotes identity [109].

Note that one may read  $\bar{\Pi}_{\mathcal{S}}$  as a linear version of the HMM reduction operator  $\Omega$ , allowing the interpretation of the VMS framework as a linear sub-framework of HMM. In fact, the two approaches are *equivalent* if the HMM is expressed in a variational form, the resolved scale spaces  $\bar{\mathcal{S}}$  and  $\bar{\mathcal{V}}$  correspond to the HMM's coarse space,  $\bar{\Pi}_{\mathcal{S}} = \Omega$  and the same models are employed for the unresolved scales [186]. This conceptually connects VMS to SP.

The linearity of the VMS projection is particularly insightful, however, as it reveals that one must pose a linearly independent set of resolved and unresolved scales weak forms if the problem is to be solved exactly:

$$(\bar{\psi}, \mathcal{L}(\bar{u} + u'))_{\Omega} = (\bar{\psi}, f)_{\Omega} \quad (3.8a)$$

$$(\psi', \mathcal{L}(\bar{u} + u'))_{\Omega} = (\psi', f)_{\Omega} \quad (3.8b)$$

If Eq. (3.8a) is discretised with a Finite Element Method (FEM),  $\Omega$  will be subdivided in  $n_{el}$  finite elements, each spanning the subdomains  $\Omega_e$ , bounded by element interfaces  $\Gamma_e$ .  $\bar{\mathcal{S}}$  and  $\bar{\mathcal{V}}$  then refer to a finite element space, characterised for instance by piecewise linear basis functions, such that  $\bar{\mathcal{S}}, \bar{\mathcal{V}} \in C^0(\sum_e^{n_{el}} \Omega_e) \cap H^1(\Omega)$ . For such a discretisation,  $\bar{u}$  and  $\bar{\psi}$  are smooth within elements, but discontinuous in their slope on element interfaces. For a Bubnov-Galerkin method,  $\bar{\psi}$  additionally represents the method's bases, such that  $\bar{\mathcal{V}} = \bar{\mathcal{S}}$ . This is illustrated in Fig. 3.2:

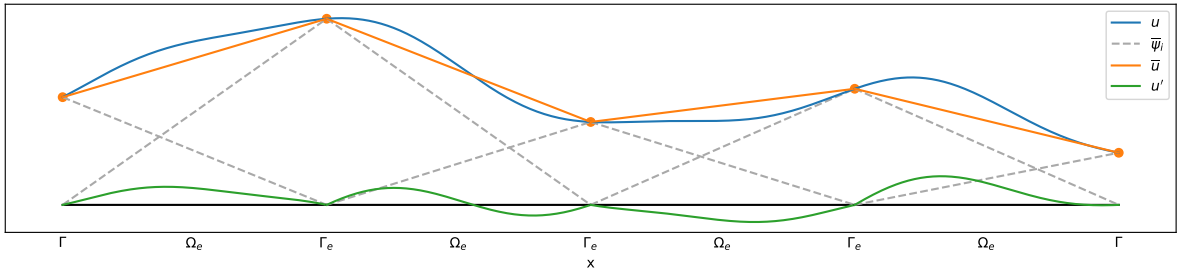


Figure 3.2: Nodal projection of  $u$  onto piecewise linear bases  $\bar{\psi}_i$  over finite elements with domain  $\Omega_e$  and boundary  $\Gamma_e$ , to construct  $\bar{u}$ . This projection defines  $u'$  as illustrated.

Fig. 3.2 assumes  $u$  is projected onto a piecewise linear basis in a manner that is nodally exact. However, it is also possible to employ projections that aim to minimise the  $L_2$  norm between  $u$  and  $\bar{u}$  either locally or globally [48, 50]. In this work, a nodally exact formulation such as presented in Fig. 3.2 is assumed, as it tends to promote the locality of the unresolved scales, although the argumentation is extendable to  $L_2$  projection-type discretisations if the appropriate adjustments are made (see [53] for a discussion). Furthermore, the piecewise linear bases illustrated by Fig. 3.2 will be employed throughout this thesis. While higher-order bases exist and might have benefits, these rapidly increase the expense of the method and, unless treated to explicitly represent unresolved processes, do not offer significantly broader insight on the conclusions drawn in subsequent chapters.

### 3.2.2. Model Equations

Section 2.6 concludes that it is likely necessary to let numerical models of the atmosphere depart from non-hydrostatic equations. Therefore, this thesis interprets  $\mathcal{L}$  as the operator for the Euler equations on a rotating sphere (Eq. (2.1) without momentum diffusion). To cast these equations in VMS form, weighting and solution functions are chosen in terms of density, velocity and potential temperature, diagnosing pressure through an

equation of state:  $\boldsymbol{\psi} = [\psi_\rho, \psi_{u_i}, \psi_\theta]$  and  $\mathbf{u} = [\rho, u_i, \theta]$ . This yields the following weak forms, where the time direction is yet to be discretised:

$$A(\boldsymbol{\psi}, \mathbf{u}) = 0 \quad (3.9a)$$

$$B_1(\boldsymbol{\psi}, \mathbf{u}) + B_2(\boldsymbol{\psi}, \mathbf{u}, \mathbf{u}) = 0 \quad (3.9b)$$

$$C_1(\boldsymbol{\psi}, \mathbf{u}) + C_2(\boldsymbol{\psi}, \mathbf{u}, \mathbf{u}) = 0 \quad (3.9c)$$

With:

$$\left\{ \begin{array}{l} A(\boldsymbol{\psi}, \mathbf{u}) = \left( \psi_\rho, \frac{\partial \rho}{\partial t} \right)_\Omega - \sum_{e=1}^{n_{el}} \left( \frac{\partial \psi_\rho}{\partial x_j}, \rho u_j \right)_{\Omega_e} \\ B_1(\boldsymbol{\psi}, \mathbf{u}) = \left( \psi_{u_i}, \frac{\partial u_i}{\partial t} \right)_\Omega - \sum_{e=1}^{n_{el}} \left( \frac{\partial \psi_{u_i}}{\partial x_i}, (\rho \theta^\gamma) \right)_{\Omega_e} - (\psi_{u_i}, g \theta \delta_{i,3})_\Omega + (\psi_{u_i}, 2 \varepsilon_{ijk} \Omega_{e,j} u_k)_\Omega \\ B_2(\boldsymbol{\psi}, \mathbf{u}, \mathbf{u}) = - \sum_{e=1}^{n_{el}} \left( \frac{\partial \psi_{u_i}}{\partial x_j}, \rho u_i, u_j \right)_{\Omega_e} \\ C_1(\boldsymbol{\psi}, \mathbf{u}) = \left( \psi_\theta, \frac{\partial \theta}{\partial t} \right)_\Omega \\ C_2(\boldsymbol{\psi}, \mathbf{u}, \mathbf{u}) = - \sum_{e=1}^{n_{el}} \left( \frac{\partial \psi_\theta}{\partial x_j}, u_j, \theta \right)_{\Omega_e} \end{array} \right.$$

Where the trilinear forms  $B(\cdot, \cdot, \cdot)$  are bilinear forms with a third multiplying variable in the integral. To reduce the derivative order to which  $u'$  must be approximated once the scales are split, Eq. (3.9) has been integrated by parts [53, 110]. For a second-order equation, this will yield non-vanishing boundary terms in Eq. (3.8a) to account for jumps in  $u'_x$ . As the second order terms associated with molecular viscosity do not participate in the Euler equations, however, these will be ignored in this study. This greatly simplifies the terms that must be carried along (they are commonly neglected at a later stage when  $u'$  is approximated locally [110]; the reader is referred to e.g. [53, 109] for texts where they are kept in the derivation). Summation over elements indicates how integration by parts is performed on a per-element basis.

It is now possible to split the scales according to the VMS decomposition Eq. (3.8). This gives rise to the following resolved-scales equations, which due to their linearity can be expanded and rearranged according to Eq. (3.10):

$$\underbrace{A(\overline{\boldsymbol{\psi}}, \overline{\mathbf{u}})}_i + \underbrace{A(\overline{\boldsymbol{\psi}}, \mathbf{u}')}_{iii} = 0 \quad (3.10a)$$

$$\underbrace{B_1(\overline{\boldsymbol{\psi}}, \overline{\mathbf{u}})}_i + \underbrace{B_2(\overline{\boldsymbol{\psi}}, \overline{\mathbf{u}}, \overline{\mathbf{u}})}_i + \underbrace{B_2(\overline{\boldsymbol{\psi}}, \overline{\mathbf{u}}, \mathbf{u}')}_ii + \underbrace{B_2(\overline{\boldsymbol{\psi}}, \mathbf{u}', \overline{\mathbf{u}})}_ii + \underbrace{B_1(\overline{\boldsymbol{\psi}}, \mathbf{u}')}_iii + \underbrace{B_2(\overline{\boldsymbol{\psi}}, \mathbf{u}', \mathbf{u}')}_iii = 0 \quad (3.10b)$$

$$\underbrace{C_1(\overline{\boldsymbol{\psi}}, \overline{\mathbf{u}})}_i + \underbrace{C_2(\overline{\boldsymbol{\psi}}, \overline{\mathbf{u}}, \overline{\mathbf{u}})}_i + \underbrace{C_2(\overline{\boldsymbol{\psi}}, \overline{\mathbf{u}}, \mathbf{u}')}_ii + \underbrace{C_2(\overline{\boldsymbol{\psi}}, \mathbf{u}', \overline{\mathbf{u}})}_ii + \underbrace{C_1(\overline{\boldsymbol{\psi}}, \mathbf{u}')}_iii + \underbrace{C_2(\overline{\boldsymbol{\psi}}, \mathbf{u}', \mathbf{u}')}_iii = 0 \quad (3.10c)$$

Eq. (3.10) contains three types of terms: i) The traditional Galerkin terms of unstabilised methods, ii) terms that represent the ‘‘cross’’ interactions between resolved and unresolved scales as they project on the resolved scales and iii) terms of pure unresolved scale projections onto the resolved scales. When projected onto an orthogonal basis, as for spectral methods, the linear portions of iii ( $A(\overline{\boldsymbol{\psi}}, \mathbf{u}')$ ,  $B_1(\overline{\boldsymbol{\psi}}, \mathbf{u}')$  and  $C_1(\overline{\boldsymbol{\psi}}, \mathbf{u}')$  in Eq. (3.10)) will disappear. However, for the non-orthogonal, piecewise linear finite element bases considered here, even these will contribute to couple the unresolved scales to the resolved scales.

The terms collected in brackets ii and iii exactly represent the impact of the unresolved scales  $\mathbf{u}'$  on set of resolved scales  $\overline{\mathbf{u}}$  in the finite element space  $\overline{\mathcal{V}}$ . Hence, these terms are the *exact* interaction terms of the discretisation,  $I$ , introduced in Section 3.1. Traditional Galerkin methods ignore these interaction terms, while traditional SP sets the terms in ii to 0 and only models the terms in iii with its inner CRMs. These are terms Majda proposes to keep and they appear in the asymptotic derivation of SP [160]. The VMS framework also retains all these terms. However, in contrast to any SP formulation, its focus is to find models of  $u'$  that optimally allow the representation of  $\overline{\mathbf{u}}$ , not  $u$  itself. Eq. (3.10) shows that this is achieved when the *projections* of

the terms that comprise  $u'$  onto  $\bar{\mathcal{V}}$  are modelled correctly, mathematically mirroring the conceptual approach outlined in Section 3.1. One can now write the unresolved scales equations as Eq. (3.11):

$$A(\boldsymbol{\psi}', \mathbf{u}') = -A(\boldsymbol{\psi}', \bar{\mathbf{u}}) = \left( \boldsymbol{\psi}', -\bar{\mathcal{R}}_{s,c} \right) \quad (3.11a)$$

$$B_1(\boldsymbol{\psi}', \mathbf{u}') + B_2(\boldsymbol{\psi}', \bar{\mathbf{u}}, \mathbf{u}') + B_2(\boldsymbol{\psi}', \mathbf{u}', \bar{\mathbf{u}}) + B_2(\boldsymbol{\psi}', \mathbf{u}', \mathbf{u}') = -(B_1(\boldsymbol{\psi}', \bar{\mathbf{u}}) + B_2(\boldsymbol{\psi}', \bar{\mathbf{u}}, \bar{\mathbf{u}})) = \left( \boldsymbol{\psi}', -\bar{\mathcal{R}}_{s,m,i} \right) \quad (3.11b)$$

$$C_1(\boldsymbol{\psi}', \mathbf{u}') + C_2(\boldsymbol{\psi}', \mathbf{u}', \mathbf{u}') + C_2(\boldsymbol{\psi}', \bar{\mathbf{u}}, \mathbf{u}') + C_2(\boldsymbol{\psi}', \mathbf{u}', \bar{\mathbf{u}}) = -(C_1(\boldsymbol{\psi}', \bar{\mathbf{u}}) + C_2(\boldsymbol{\psi}', \bar{\mathbf{u}}, \bar{\mathbf{u}})) = \left( \boldsymbol{\psi}', -\bar{\mathcal{R}}_{s,h} \right) \quad (3.11c)$$

They reveal that in  $S'$ , the direct unresolved and cross terms (left-hand sides in Eq. (3.11)), are forced by the negative projection of the strong residual of the resolved scales  $\bar{\mathcal{R}}_s = [\bar{\mathcal{R}}_{s,c}, \bar{\mathcal{R}}_{s,m,i}, \bar{\mathcal{R}}_{s,h}]$  onto the unresolved scales basis, which may provide some weaponry with which to attack the approximation of  $\mathbf{u}'$ .

### 3.2.3. Assumptions and Approximations

Even though Eq. (3.10) already exists in a finite space and therefore may be thought of as a discretisation, it remains an exact representation of Eq. (3.2) if Eq. (3.11) is exactly solved, in the sense that it might reconstruct correct projections of  $u$ , e.g. the nodally exact projection presented in Fig. 3.2. Still, the infinite-dimensional  $u'$  appears in Eq. (3.10). Hence, approximations must necessarily be made to reduce its effects to a manageable scope. However, splitting the scales *before* making approximations allows those approximations to be introduced to the portion of the problem that a discrete model will need to neglect: Eq. (3.11).

It is the goal of traditional VMS to solve Eq. (3.11) for  $u'$  approximately. This can be done directly for linear PDEs [105]. However, the presence of the nonlinear terms in Eq. (3.11b) and Eq. (3.11c) clearly clouds the picture. Scovazzi developed an appropriate analysis technique to interpret this [222], proposing to write an infinite asymptotic series expansion for  $u'$  in terms of  $\bar{\mathcal{R}}_s$ . This is reasonable if  $\bar{\mathcal{R}}_s$  is small, which Eq. (3.11) would lead one to expect to be true when i) Eq. (3.10) has provided a good estimate for  $\bar{u}$  and ii)  $\bar{u}$  makes up the larger part of  $u$ .  $u'$  is then small as a result, and the asymptotic series would be:

$$\mathbf{u}' = \sum_{n=1}^{\infty} \varepsilon^n \mathbf{u}'^n \quad (3.12)$$

In this context,  $\varepsilon = \|\bar{\mathcal{R}}_s\|_2$ , even if this is not the natural norm of the space in which the equations will be approximately inverted [222]. By separating Eq. (3.11b) and Eq. (3.11c) into their linear and nonlinear terms of  $\mathbf{u}'$  and inserting the expansion Eq. (3.12), one may write these two equations in terms of the perturbation series. This procedure is identical for Eq. (3.11b) and Eq. (3.11c). Therefore, for compactness, consider the following version of the unresolved scales equations:

$$\sum_{n=1}^{\infty} \varepsilon^n D_{\bar{\mathbf{u}}}(\boldsymbol{\psi}', \mathbf{u}'_n) + \sum_{n=2}^{\infty} \varepsilon^n \sum_{j=1}^{n-1} D_2(\boldsymbol{\psi}', \mathbf{u}'_j, \mathbf{u}'_{n-j}) = \varepsilon (\boldsymbol{\psi}', \hat{\mathcal{R}}_s) \quad (3.13)$$

Where:

$$D_{\bar{\mathbf{u}}}(\boldsymbol{\psi}', \mathbf{u}'_n) = \begin{bmatrix} B_1(\boldsymbol{\psi}', \mathbf{u}'_n) + B_2(\boldsymbol{\psi}', \bar{\mathbf{u}}, \mathbf{u}'_n) + B_2(\boldsymbol{\psi}', \mathbf{u}'_n, \bar{\mathbf{u}}) \\ C_1(\boldsymbol{\psi}', \mathbf{u}'_n) + C_2(\boldsymbol{\psi}', \bar{\mathbf{u}}, \mathbf{u}'_n) + C_2(\boldsymbol{\psi}', \mathbf{u}'_n, \bar{\mathbf{u}}) \end{bmatrix}$$

$$D_2(\boldsymbol{\psi}', \mathbf{u}'_j, \mathbf{u}'_{n-j}) = \begin{bmatrix} B_2(\boldsymbol{\psi}', \mathbf{u}'_j, \mathbf{u}'_{n-j}) \\ C_2(\boldsymbol{\psi}', \mathbf{u}'_j, \mathbf{u}'_{n-j}) \end{bmatrix}$$

$$\hat{\mathcal{R}}_s = \begin{bmatrix} \bar{\mathcal{R}}_{s,m,i} \\ \|\bar{\mathcal{R}}_{s,m,i}\| \\ \bar{\mathcal{R}}_{s,h} \\ \|\bar{\mathcal{R}}_{s,h}\| \end{bmatrix}$$

Similar to the asymptotic treatment of SP, this reveals a hierarchy of problems in  $\varepsilon$  by equating problems of equal order. However, this hierarchy can here be interpreted as a cascade of linear problems, forced by the sum of asymptotic interaction terms up to each level in the cascade:

$$D_{\bar{\mathbf{u}}}(\boldsymbol{\psi}', \mathbf{u}'_1) = \hat{\mathcal{R}}_s, \quad n = 1 \quad (3.14a)$$

$$D_{\bar{\mathbf{u}}}(\boldsymbol{\psi}', \mathbf{u}'_n) = - \sum_{j=1}^{n-1} D_2(\boldsymbol{\psi}', \mathbf{u}'_j, \mathbf{u}'_{n-j}), \quad n > 1 \quad (3.14b)$$

On this form, each of the bilinear operators  $D_{\bar{\mathbf{u}}}(\cdot, \cdot)$  can be separately inverted to estimate each of the perturbation series terms' contributions to  $\mathbf{u}'$ . The inversion of each linear problem in the cascade can now be achieved, by means of Green's functions. This can be understood by i) replacing the Right Hand Side (RHS) of each of the problems in Eq. (3.14) with a matching sequence of operators  $\mathcal{F}_n$ , ii) ensuring the integration by parts is carried out such that  $D_{\bar{\mathbf{u}}}(\boldsymbol{\psi}', \mathbf{u}'_n) = (\mathcal{L}^* \boldsymbol{\psi}', \mathbf{u}'_n)$  to isolate  $\mathbf{u}'$  from any derivatives and iii) projecting the equations onto  $(\mathcal{V}')^*$ , the dual space of  $\mathcal{V}'$ . At each level of the hierarchy, this leaves one to solve problems that are linear in  $\mathbf{u}'$  when  $\bar{\mathbf{u}}$  and  $\mathbf{u}'$  from previous levels in the hierarchy are known. With the notation of this paragraph, this can be written abstractly as:

$$(\mathcal{L}^* \boldsymbol{\psi}', \mathbf{u}'_n) = (\boldsymbol{\psi}', \mathcal{F}_n) \quad (3.15)$$

Because summation over elements is still implied, the Green's function problem to solve these can be posed separately in every single element, as  $\mathbf{u}' = 0$  on the element boundaries when the problem is solved exactly [53, 103, 107]. Thus, in  $(\mathcal{V}')^*$ , the Green's functions are "element Green's functions", which solve the problem:

$$\mathcal{L}^* \mathbf{g}'_e(\mathbf{x}, \mathbf{y}) = \delta_d(\mathbf{x} - \mathbf{y}), \quad \mathbf{g}'_e \in \Omega_e \quad (3.16a)$$

$$\mathbf{g}'_e(\mathbf{x}, \mathbf{y}) = 0, \quad \mathbf{g}'_e \in \Gamma_e \quad (3.16b)$$

Where  $\delta_d$  denotes Dirac's delta peak forcing. If the infinite-dimensional  $\mathbf{g}'_e$  is known exactly, substituting it for  $\boldsymbol{\psi}'$  in Eq. (3.15) then allows solving for  $\mathbf{u}'_n$  in  $\mathcal{V}'$  in every element:

$$\mathbf{u}'_n(\mathbf{y}) = - \int_{\Omega_e} \mathbf{g}'_e(\mathbf{x}, \mathbf{y}) \mathcal{F}_n(\mathbf{x}) d\Omega \quad (3.17)$$

In turn, this would yield expressions to be inserted in Eq. (3.12) for an estimate of  $\mathbf{u}'$ , which finally would yield expressions to be inserted in terms ii and iii in Eq. (3.10), closing these equations. For some homogeneous, linear PDEs and extensions thereof,  $\mathbf{g}'_e$  can be derived exactly [93]. This is not generally possible for forced, nonlinear PDEs such as those in the cascade of linear problems emerging from the Euler equations [133, 222], though they can be computed by hierarchical refinement in the polynomial order of the basis [109]. Nevertheless, entering a proposition such as Eq. (3.17) in the resolved scales equations is relatively costly, as it demands negotiating one integral to compute  $\mathbf{u}'$  at every integrated point in the integrals in Eq. (3.10). Therefore, approximations of the element Green's function are almost always necessary.

Fundamentally, these derivations then highlight the two properties of the unresolved scales equations that really require approximation:

1. Their nonlinearities, requiring an infinite perturbation series to write them as an infinite cascade of linear problems.
2. Their Green's functions for the linearised equations.

The design of unresolved scales models that spring from these approximations give rise to various VMMs that are instances of the VMS framework. They commonly begin by truncating the perturbation series to treat the nonlinearities. In conjunction with approximations of element Green's function at each level included in the perturbation series, this allows the design of an array of models.

### 3.2.4. Traditional VMS Closure Schemes

The most common unresolved scales models for solving both compressible and incompressible versions of the Navier-Stokes equations with VMMs stem from traditional stabilised methods [34, 106, 226]. These include only the first term of the perturbation series, fully linearising the unresolved scales equations. Second, they argue that when the resolved-scales basis is piecewise linear and  $\mathbf{u}' = 0$  on the element boundaries, element integrals that feature derivatives of the bases are essentially averaging operators on  $\mathbf{u}'$ , such that it is sufficient to correctly find an *average* element Green's function,  $\tau$  [105] (similar justifications for the functional form of  $\tau$  can be found with various approaches, e.g. those outlined in [47, 75, 105, 197]). Inserting these in Eq. (3.17) and using Eq. (3.14) and Eq. (3.12) truncated at  $n = 1$  then gives rise to traditional “algebraic” closure methods:

$$\mathbf{u}' \approx -\tau \overline{\mathcal{R}} \quad (3.18)$$

Where  $\tau$  can be derived exactly for several problems [109] and is approximated for many others [187]. Such approximations will be discussed in the context they appear in later in this thesis.

Three additional approximations are made by models on Eq. (3.18)'s form. First, they ignore the time derivatives of  $\mathbf{u}'$ , since the semi-discrete forms considered here do not march the unresolved scales model in time. This is a similar “quasi-steady” unresolved scales assumption as traditionally posed for GCMs, and must therefore be amended. This can be achieved with Codina's various Dynamic Subscales (DSS) approaches, that solve Ordinary Differential Equation (ODE) versions of Eq. (3.18) [48, 51, 52]:

$$\frac{\partial \mathbf{u}'}{\partial t} + \tau^{-1} \mathbf{u}' \approx -\overline{\mathcal{R}} \quad (3.19)$$

Second, in Eq. (3.18) and Eq. (3.19),  $\overline{\mathcal{R}}$  is not projected onto an orthogonal complement space of  $\overline{\mathcal{V}}$ , even though it is assumed that  $\mathbf{u}'$  is. This yields non-zero projections of the linear unresolved scale terms onto the resolved scales, such as the unresolved scales' time derivatives, exacerbating their neglect. It can be amended by Codina's Orthogonal Subscales (OSS) approach [48, 49], which first computes the portion of  $\overline{\mathcal{R}}$  that is not represented on the resolved scales  $\overline{\mathcal{R}} - \overline{\Pi_V} \overline{\mathcal{R}}$  and uses this quantity in favour of  $\overline{\mathcal{R}}$  in Eq. (3.18) or Eq. (3.19). Finally, it is common to decouple the computation of  $\tau$  associated with each of the PDEs from the other unresolved scales scale equations. This is justified when the unresolved scales variables are only weakly coupled.

In spite of its drawbacks, Eq. (3.18) already yields an improved accuracy per degree of freedom for many classes of problems, compared to traditional, ad-hoc closure schemes [10]. Three additional advantages to this formulation can be identified. First, models of  $\tau$  can be designed such that the stability of its time march is guaranteed [198, 226, 238]. Second,  $\mathbf{u}'$  is driven by the residual of the resolved scales and will therefore be zero exactly when the resolved-scales space is sufficiently inclusive to model *all* terms in it. Third, extra terms of the perturbation series, with their respective Green's function approximations, can readily be added to Eq. (3.18) [182, 222] for cases when the fully linear assumption is inadequate.

### 3.2.5. Applications

While the application of VMMs to LES simulation of the incompressible Navier-Stokes equations is relatively well-developed and has touched a broad number of problems [53], VMMs for the Euler equations with an unresolved scales model were introduced more recently by Rispoli [206], following initial steps by Koobus and Farhat [133]. They engage unresolved scales models such as Eq. (3.18), where  $\tau$  stems from element Green's functions for the full Navier-Stokes equations in the limit where  $\text{Re} \rightarrow \infty$ . In particular,  $\tau$  is here approximated by the largest eigenvalue in streamwise direction ( $\mathbf{u} + c_s$ ) of the wave-propagating portions of the Euler equations, extended to all three dimensions under the assumption that it is isotropic [206]. More recently, this VMS model was extended to atmospheric flow simulations. In particular, Marras et al. successfully solve an array of test cases based on non-hydrostatic, stratified, dry and moist convective versions of the Euler equations for the use in CRMs [165–167]. They achieve this without shock-capturing schemes and in spite of linearising the pressure-temperature interactions, neglecting several interaction terms in the resolved scales equations and using a particularly precarious time march. However, VMS formulations have yet to be posed at the scales of a GCM, despite various aspects of their formulation potentially being advantageous to such models. The next section aims to draw attention to these aspects and contrast them with SP, to confirm that they appropriately meet the requirements from Section 2.6.

### 3.3. Potential of VMS Formulations as an Improved GCM

To be a meaningful upgrade from state of the art SP, a VMM must hold immediate improvement potential in the three first requirements presented in Section 2.6, which correspond to the traditional weaknesses of SP. To also satisfy the fourth requirement, it must additionally be conducive to the inclusion of novel unresolved scales models that meet requirement four. Based on the theoretical development of VMS above, this section will review these points in turn.

#### 3.3.1. Model consistency

Viewing the multiscale formulation in the framework of VMS holds three conceptual advantages with practical implications. First, its a priori separation of the resolved and unresolved scales means that *all* interaction terms between the resolved and unresolved scales are present in both the resolved and unresolved scale equations. Therefore, the framework entirely avoids the ad-hoc nature of the original SP “formalism” [87], but also does not need additional constructions to represent large-scale variables on the small-scale grid, which are precluded even by the asymptotic multiscale derivation [88].

Second, the method is comparatively clear and flexible compared to SP, as interaction terms can be readily removed from the framework in situations where scale separation or the quasi-steadiness of the small scales can be assumed. The impact of neglecting the terms in question could be immediately quantified because they exist explicitly in all simulated equations, rather than as an unknown fraction of a single forcing term that couples the multiscale equations. As the models are increasingly headed into territory where scale separation breaks down, this might be a valuable asset of the model that traditional SP does not possess.

Finally, VMS associates the necessity of scale separation directly with its underlying reason: Its separation of  $u$  into a resolved-scales space with a discrete number of variables  $\bar{S}$  and an infinite-dimensional unresolved complement space  $S'$  illustrates that both discretisation and modelling errors derive from grappling with this infinite-dimensional space. Encouraging residual-driven closure formulations, this allows the models to be consistent with respect to both the grid resolution and the unresolved scales model. The residual-driven property stands in contrast to the traditional GCM formulation, where the parameterisation is traditionally independent of the number of modes included in the simulation [12], and SP, which will always simulate turbulent feedback from the unresolved scales [88, 89, 258]. This leads to inconsistencies when the grid size is not uniform or when stable flow regions (such as the stratosphere) are encountered. Residual-driven VMMs, however, inherently satisfy the consistency requirement for improved atmospheric models presented in Section 2.6.

#### 3.3.2. Low Cloud Accuracy and Computational Cost

Improving the representation of low clouds will fall to the small-scale model of either a VMS or SP formulation and is therefore less dependent on the framework it is formulated in, assuming that framework manages to backscatter their resolved-scale impacts effectively. As discussed in the next subsections, it is likely that the VMS formulation is more malleable to this end than SP, while specific closure schemes will be the topic of the next section.

Similarly, the computational cost at which VMS codes could resolve clouds is likely a function of its unresolved scales model, rather than the explicit model formulation. Unresolved scales representations based on element-averaged Green’s functions (see Section 3.2.3) assume that the unresolved scales are fully local in similar fashion as SP’s small-scale model. Such models are therefore equally favourable for running on massively parallel architectures as SP and likely to similarly enjoy the benefits of the development of GPU computing as advertised for SP [85]. However, as will be discussed in Section 7.3, higher-fidelity closures are likely to benefit from non-local information. As long as this non-locality does not exceed the information required by the resolved scales model to construct its spatial derivatives, this will not add an extra cost penalty. In such cases, direct comparisons of the computational cost of SP’s CRMs and the unresolved scales models introduced in the following section will be necessary.

#### 3.3.3. Scale Separation

Majda contends that when “intermittent strongly unstable fluctuations and only moderate scale separation without statistical equilibration” dominate, “more traditional numerical closure methods such as HMM cannot be applied” [160], reflecting the conclusion of Section 2.5.4. One might therefore be tempted to conclude that VMS, as a subclass of HMM, is not a suitable framework for global-scale atmospheric modelling. However, this criticism misses the point that HMMs are in fact not limited to only simulating processes with

explicit scale separation [251].

This was shown in Section 3.2.1. The formal linear projection of the full problem onto a finite-dimensional resolved-scales space and an infinite-dimensional unresolved scales space yields two equation sets in two variables that are *exact*. This implies that if the unresolved scales quantity  $u'$  can be exactly represented from Eq. (3.11), the resolved scales equations Eq. (3.10) are exact in a discrete sense [109]. Hence, while the formulation cannot capitalise on the scale separation assumption to increase its simulation speed, no model assumptions have yet been made.

The formulation's limitations only arise once a tractable model is derived from the exact, nonlinear, infinite-dimensional unresolved scales equations. Indeed, element-averaging of unresolved scales projections in a VMM is essentially equivalent to averaging predictions from SP's inner-model over the outer model's cells [167]. Similarly, it is common to assume that the unresolved scales are quasi-steady [39, 53]. However, it is not necessary to pursue this route.

In all, one can actually readily retrieve a weak formulation for SP from the VMS framework by considering three sets of scales: Large scales  $\bar{u}_i$  that correspond to the GCM-scales of SP, small scales  $\tilde{u}_i$  corresponding to the CRM-scales of SP and unresolved scales  $u'_i$ . Again, these could be consistently projected onto three sets of solution spaces, as can their weighting functions:

$$\mathcal{S} = \bar{\mathcal{S}} + \tilde{\mathcal{S}} + \mathcal{S}' \quad (3.20a) \quad \mathcal{V} = \bar{\mathcal{V}} + \tilde{\mathcal{V}} + \mathcal{V}' \quad (3.20b)$$

$$u_i = \bar{u}_i + \tilde{u}_i + u'_i \quad (3.21a) \quad \psi = \bar{\psi} + \tilde{\psi} + \psi' \quad (3.21b)$$

This would yield a set of three consistently coupled, exact, discretised equations of similar form as Eq. (3.8), where the goal is to find  $\bar{u}_i \in \bar{\mathcal{V}}$ ,  $\tilde{u}_i \in \tilde{\mathcal{V}}$  and  $u' \in \mathcal{V}'$ , such that:

$$(\bar{\psi}, \mathcal{L}(\bar{u} + \tilde{u} + u'))_{\Omega} = (\bar{\psi}, f)_{\Omega} \quad \forall \bar{\psi} \in \bar{\mathcal{V}} \quad (3.22a)$$

$$(\tilde{\psi}, \mathcal{L}(\bar{u} + \tilde{u} + u'))_{\Omega} = (\tilde{\psi}, f)_{\Omega} \quad \forall \tilde{\psi} \in \tilde{\mathcal{V}} \quad (3.22b)$$

$$(\psi', \mathcal{L}(\bar{u} + \tilde{u} + u'))_{\Omega} = (\psi', f)_{\Omega} \quad \forall \psi' \in \mathcal{V}' \quad (3.22c)$$

In this three-scale approach, Eq. (3.22a) corresponds to SP's outer model equations Eq. (2.9a), Eq. (3.22b) to SP's inner model equations Eq. (2.9b) and Eq. (3.22c) still consistently makes the reader aware of an infinite-dimensional unresolved scales space below the CRM's resolution. However, while explicit scale separation underpins Eq. (2.9a) and Eq. (2.9b), all interaction terms between Eq. (3.22a) and Eq. (3.22b) of the *discretised* equations follow naturally from the VMS decomposition, and can all be carried along on the discretisation. There is no need to introduce "point approximation" formalisms [160] to represent large-scale variables on small-scale grids: These are here well-defined as prolongation operators inherent to the framework [141]. If the cross-terms in the discretised equations are explicitly set to 0 and the appropriate terms inserted for the generic operator  $\mathcal{L}$  and forcing  $f$ , weak forms of the traditional SP equations Eq. (2.9a) and Eq. (2.9b) can be recovered.

This type of decomposition highlights a flexibility of the VMS framework that would allow it to rather naturally enforce the scale separation assumption to various degrees, when this is desired. While it may not exploit the HMM-type benefits that usually drive one to employ VMMs, it therefore offers an upgrade over the more rigid SP formulation in this regard.

### 3.3.4. Potential High-fidelity Closure Integration

This discussion has aimed to show that VMMs might hold some conceptual advantages over traditional SP and are likely at least equally proficient in all other areas. Yet, the discussion of SP made explicitly clear that the model's eventual performance will likely be dominated by the unresolved scales formulation that closes it. Therefore, the most important question of all might be how conducive models such as SP and VMMs are to the integration of high-fidelity closure models.

Section 3.2.4 showed that within the VMS framework, approximations are only really necessary for the nonlinear terms in Eq. (3.11) and for the Green's functions that invert linearised problems at each level of an asymptotic expansion for  $u'$ . While truncating the expansion beyond its linear term is successful for many fluid-dynamical applications, it is unlikely that such algebraic unresolved scales models will suffice when they must simulate the large, strongly interactive, backscattering extent of unresolved scales encountered by GCMs [160]. Similarly, assuming that the unresolved scales contributions of each variable is uncoupled from

the others is restrictive for a GCM; especially for moist atmospheric processes and their model equations, the unresolved scales interaction of moisture variables, microphysics, radiation and turbulence has a defining character for the large-scale flow. For these reasons, it will be necessary to find an improved unresolved scales model for the VMS formulation of atmospheric-scale flow.

First and most naïvely, one could attempt to formulate more optimal representations of  $\tau$ 's model coefficients within the confines of the algebraic model. Much research exists in this vein already [22, 68, 197] which shows promise for extracting more performance from the formulation, while remaining relatively robust [136]. However, Eq. (3.12) shows that in the presence of strong nonlinearity, as will be the case for atmospheric problems, these fully linearised models are likely insufficient.

Logically, an improved model could be based on including more terms in the perturbation series Eq. (3.12) and formulating models for each of the perturbation series' coefficients from Eq. (3.14). Such approaches measurably improve the fidelity of traditional algebraic closure when conditioned on DNS data [182], and if these models are posed for the entire remainder of the scale range, they have the advantages of additional modelling only acting as corrections to well-understood linear theory and retaining the residual-driven property. If posed as an OSS model, the impact of the unresolved scales time derivatives in semi-discrete formulations would furthermore drop, such that if the model is inferred well enough, it *only* needs to assume that the asymptotic formulation is an appropriate one.

However, it is unclear if the perturbation series approach to writing  $\mathbf{u}'$  is valid for GCMs. That formulation predicates on  $\mathbf{u}'$  being small compared to  $\bar{\mathbf{u}}$ , i.e. that most of the problem's energy resides in the large, resolved scales. If this is not the case, it is unlikely that the perturbation series, expanded in  $\bar{\mathcal{R}}_s$ , will converge. In fact if it would, one could solve the Navier-Stokes equations analytically with such an approach [222]. A GCM's  $k_c$  lies far above an inertial subrange. Hence, it is questionable whether a perturbation series approach holds water for such models.

Therefore, the higher-level analysis in Section 3.2.2 will form the basis for the novel models posed here. It identifies the terms that must be predicted by such a model: The interaction terms grouped under ii and iii in Eq. (3.10), and the large-scale variables that these may be informed by, the strong residuals of Eq. (3.11). This is subtly different from the perturbation series approach. In fact, here the assumption is not that the unresolved scales can themselves be approximated from the resolved-scales, only that one can approximate the *projections* of the unresolved scales that contribute to the evolution of the resolved scales. Since these quantities are integrated to only vary in the resolved finite element space, it seems more likely that they are predictable than highly fluctuating, direct representations of  $\mathbf{u}'$  itself. Despite the lack of an explicitly residual-driven framework to ensure the consistency of such models, they appear to hold significant potential to reconstruct the exact resolved scales when closed by data-driven models of the interaction terms for a forced Burgers' problem [209].

In contrast, SP is limited by ignoring several of these terms during derivation and has to bring them back with provisional arguments. Thus, the consistency and flexibility of VMMs to include and exclude terms where their impact does and does not matter make them an ideal testbed for experimenting with new, higher-order closure schemes, rendering such models at worst a clearer, more consistent version of traditional SP.

### 3.3.5. Conclusion

Returning to SP's HMM roots and casting the model in the form of a VMS may yield advantages in the model's formulation that might be advantageous when it can no longer rely on the scale separation assumption. The framework encourages a unified treatment of discretisation and modelling errors, is similarly conducive to massively parallel computation as SP, does not require a scale-separation assumption in integrating its unresolved scales models, and provides clear directions for developing higher-fidelity closures. These arguments motivate this study to use VMS formulations as an alternative large-scale model to a traditional GCM.

This VMM will be closed by direct models for the interaction terms in Eq. (3.10). That choice in turn fundamentally removes many of the modelling and analysis traits that are specific to VMMs and generalises the comparison to SP conducted here to one with any numerical framework that can be consistently decomposed into a resolved and an unresolved scales space with interaction terms that contain the full unresolved scales contribution to the resolved scales. Conceptually, this again reveals that the model framework introduced in Section 3.1 attempts to be nothing but a scale-consistent numerical model, whose proficiency will hinge on its model for the interaction terms.

Since the data-driven approach to estimate these terms in [209] appears to hold promise, and this fits within a larger, promising shift towards data-driven unresolved scales modelling in the fluid dynamics and atmospheric modelling community, it will be pursued here also.

### 3.4. Data-driven Unresolved Scales Modelling

Data-driven reduced-order models may capture the essence of a dynamical problem at lower computational cost than discretised PDEs [154], yet they are versatile enough to be considered universal function approximators [100], such that given enough data, they have no inherent limitations. Although they are well-established in both the fluid dynamics [155] and atmospheric modelling [196] communities, improvements in the capacity of statistical machine learning frameworks [143], coupled with the increasing availability of large, high-fidelity datasets from global satellite data [144] and local LES [70] increasingly offer promise that data-driven parameterisations can break the unresolved scales modelling deadlock that is currently hampering the prediction of low clouds in climate in particular [29, 63, 79, 88, 126, 188, 205] and turbulence in general [39, 42, 139, 246, 255].

Nevertheless, it remains likely that discretised PDEs will form the core of such models for the foreseeable future, rather than being completely substituted for data-driven models [220]. Data-driven models have no inherent awareness of the governing equations they must satisfy unless trained to a sufficient level. Hence, they will likely require time to mature to the fidelity of traditional numerical models, although efforts in this direction are already underway [127, 255]. Since Section 2.6 identified GCMs' unresolved scales models as the area with the highest improvement potential for high-accuracy, low-degree-of-freedom models, it is here considered most promising to investigate the use of data-driven models to this end.

In terms of the second and fourth criterion posed by Section 2.6, data-driven models are particularly suitable. All models considered here are by definition inspired by high-fidelity unresolved scales models when taught by high-fidelity simulations and are significantly cheaper to run than the CRMs employed by traditional SP. Furthermore, they can be kept grid-consistent by being made aware of grid resolution. If data is available over the entire range of scales that is traditionally neglected, they also have the potential to capture all phenomena that meaningfully contribute at the resolved scales. Yet, even data-driven models are unable to represent the scale continuum if they are taught by models that assume an underlying scale gap. Hence, the only manner in which they can fully satisfy criterion four is if they are taught by actual observations or by GCRMs [79]. Since GCRMs can currently only operate over time windows much shorter than the climate scale, it is highly questionable whether a statistical model driven by GCRM data can be made aware of phenomena on that scale. However, many dedicated weather satellites have now been operational for over a decade [144]. These are increasingly providing climate-scale datasets that can be targeted for training as an alternative [220, 221]. Additionally, data-driven unresolved scales models must face many more direct challenges associated with their fundamentals before facing scale continuity. These challenges will be the topic of subsequent chapters.

The following sections will establish that an array of such models exists, and select an approach that, when used to predict the interaction terms in Eq. (3.10), appears particularly promising to engage the challenges posed by Section 2.6: Consistency, accuracy, cost and capability to represent the range of unresolved scales without assuming scale separation. From this discussion, a novel modelling approach for scale-consistent atmospheric modelling emerges: A VMM-ANN.

#### 3.4.1. Classes of Data-driven Unresolved Scales Models

Existing data-driven unresolved scales models can be broadly divided into three partially overlapping classes: Modal reduced order models, stochastic unresolved scales models and statistical learning models. These are very briefly discussed here, to motivate the choice of the latter class for the remainder of this study.

##### Modal Reduced Order Models

First, modal Reduced-Order Models (ROMs) here refer to unresolved scales models that simulate a truncated set of modes that are based on an existing dataset. The most celebrated and famous of these is the Proper Orthogonal Decomposition (POD), which decomposes an “ensemble of signals”, which here is a high-dimensional simulated or experimental dataset, into a set of modal bases [23]. As a data-assimilation tool in oceanographic [72, 156] and atmospheric [56] studies, the POD's attractiveness stems from the fact that it will return a set of modes that are i) orthonormal, making it a “safe haven” of linearity in the nonlinear sea of turbulence, ii) the best possible approximation of the signal in the  $L_2$  norm and iii) phenomenologically interpretable [23, 139]. This set of modes can then be used to construct a reduced-order model of the system, which could be embedded as an energy-optimal unresolved scales model in a higher fidelity model that itself only resolves a truncated set of modes [250]. In the context of a three-scale VMS that is further closed by an optimal algebraic unresolved scale model, this approach is very effective for approximating the small

scales present in wall layers even when only very few modes are considered, despite the unsteady nature of the problem [39, 40].

Several drawbacks to this approach exist: Optimality in the  $L_2$  norm is not guaranteed for simulations that differ from the data that informed the original decomposition [42], the most energetic, truncated modes from the POD are not the most interesting ones for atmospheric application [202], and the necessity to truncate the number of modes is in direct conflict with the requirement here to pose an unresolved scales model for the entire unresolved scale range. While recent advances have provided tools to remedy the first two of these problems by goal-orienting the ROM's selected modes towards the phenomena one is actually interested in reproducing [35], they still suffer from the last drawback and are observed to not always find the globally optimal decomposition [42].

### Stochastic Unresolved Scales Models

Research into systematic stochastic unresolved scales models for atmospheric applications has become increasingly popular over the last decade, as they i) could potentially increase GCM accuracy per degree of freedom once they reach  $O(10^1)$  km resolutions [160, 257], ii) can statistically match correct backscatter in shallow scale spectra [88, 89, 159, 161], iii) offer a straightforward extension of existing schemes to include statistics on the unresolved scales' variability [63], iv) are particularly well-positioned to leverage data assimilation techniques and benefit from the machine-learning revolution [220] and v) generally strike good balances between their costliness and accuracy [120, 125, 126]. A well-funded consortium is currently developing a largely data-driven GCM based on a variety of these closures [220].

This has led to the proposal of several interesting methods, a.o. the use of Conditional Markov Chains (CMCs) to infer closure properties of GCMs from high-resolution LES [61–63], Markov chain lattices to infer clouds states [120, 125, 126] or Ornstein-Uhlenbeck processes to replace the small scales of a scale-separated model [55, 248]. While all offer improvements and promise in their own regard, these models are restricted, as they are only very loosely and indirectly physics-informed [64, 160, 248]. Moreover, inferring classical closure schemes, cloud states or the small scales directly is philosophically different from attempting to predict the interaction terms directly; it is unclear whether these approaches are sufficiently general for this more challenging task.

More advanced models that attempt to remedy this are the diffusion forecast, a nonlinear method to approximate a set of bases that form spectral Galerkin representations of solutions to the Fokker-Planck PDEs [24, 54, 94] and Stochastic Superparameterisation, which replaces SP's nonlinear small-scale equations with quasi-linear equations, in which the non-linear convective terms are substituted for a Gaussian source [88, 91]. While both methods again represent significant steps forward, the first of these is subject to the same drawbacks as the POD and the second will always produce turbulence, also in stable regimes [89]. Moreover, replacing the exact interaction terms in Eq. (3.10) with linearised stochastic forcings from an approximate model limits the potential of the method already at the model formulation stage. Hence, it is not considered further in this work.

### Statistical Learning Methods

The highest untapped potential for research therefore is found in the field of statistical learning algorithms that have enriched the traditional approach over the last years. These have permeated the atmospheric modelling community in the last year and appear to show strong promise. First Random Forests (RFs) [28, 96] manage to reconstruct several classical parameterisation schemes with impressive accuracy and robustness [188]. However, this is superseded by the potential displayed by ANNs, which in short time have claimed a central role in the field [25, 29, 66, 135, 204, 205, 217]. They are therefore introduced separately in the following section.

## 3.5. Artificial Neural Networks

No method embodies the recent advances in machine learning as powerfully as deep learning with ANNs. Although they have existed in some form for almost four decades [77], they have benefited especially from the availability of very large datasets and the continued growth of computing power [139]. ANNs have enjoyed a rapid rise to prominence and currently dominate the skill metrics in the fields of computer vision and data mining [143].

It is today expected that deep, sophisticated ANN architectures will have a similarly transformative impact on the modelling of “high-dimensional, complex systems” [139], such as those characterised by turbulence. This is because ANNs excel in situations where i) a relation between input and output is present, ii)

the relation is nonlinear and/or not fully known, but iii) large datasets conducive to training as well as the computational power to conduct that training are present. ANNs are universal function approximators [100], such that they can approach such problems without having to make a priori assumptions on the structure of the input-output relationship [21].

### 3.5.1. Brief Introduction

The simplest form of an ANN consists of individual “neurons” or “nodes”, organised in “layers”, which are densely or sparsely interconnected with one another [183]. An example of a dense architecture is sketched in Fig. 3.3, which displays an ANN with 8 input nodes, a “hidden” layer with 10 nodes and an output layer with 3 nodes.

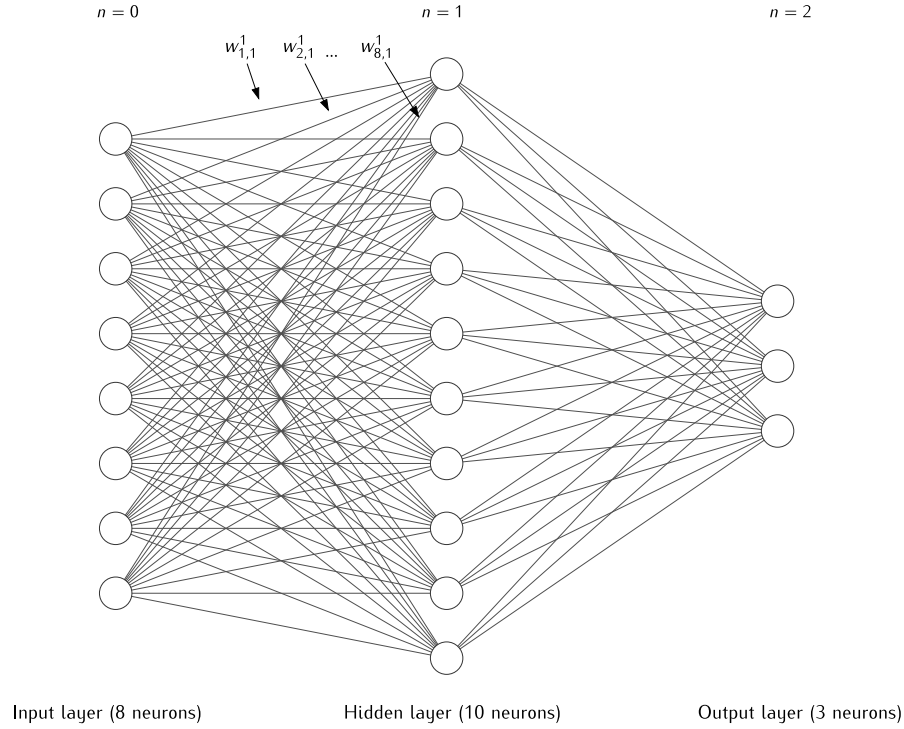


Figure 3.3: Schematic representation of an ANN with an input layer with 8 nodes, a single, densely connected hidden layer with 10 nodes and an output layer with 3 nodes.

The  $n + 1^{st}$  layer in the network accepts an input vector  $x_j^n$ , which in hidden or output layers are the outputs of  $n^{th}$  layer’s neurons. The output vector of the layer,  $x_i^{n+1}$  can be computed by first connecting it to the previous layer, linearly superimposing the products of the  $x_j^n$  inputs in each neuron with a weight  $\omega_{ij}^n$ . The individual connections with which these are associated are indicated in Fig. 3.3. Second, a “bias”  $b_i^{n+1}$  is added in each neuron and third, the output vector is constructed by passing the resulting value, the “activation”  $z_i^{n+1}$ , through a non-linear “activation function”  $\sigma$ :

$$x_i^{n+1} = \sigma \left( \omega_{ij}^n x_j^n + b_i^{n+1} \right) \quad (3.23)$$

By repeating this construction for several layers, a Deep Neural Network (DNN) is formed. Its function evaluations are therefore a series of full matrix-vector products ( $\omega_{ij}^n x_j^n$ ) and other matrix manipulations.

Its training is conducted by methods rooted in Stochastic Gradient Descent (SGD). By the ANN’s intent, its output is a function of some known data. The quality of the ANN’s prediction with respect to that data may be captured by a “loss function”  $J$ . This can, but does not need to be the  $L_2$  norm error of the output state [183]. The ANN is trained by minimising  $J$  with respect to the network’s free parameters: Its weights and biases. Under the assumption that  $J$  is convex, this is achieved when  $\frac{\partial J}{\partial z_i^n} = 0$ . Because the ANN consists of a recursive application of the known Eq. (3.23), the derivatives of the loss with respect to the weights and biases can readily be computed from the chain rule of calculus, offering a cheap method to compute  $\frac{\partial J}{\partial z_i^n}$  by

“backpropagating” through each of the network’s layers [210]:

$$\frac{\partial J}{\partial z_i^n} = \omega_{ji}^{n+1} \frac{\partial J}{\partial z_i^{n+1}} \delta_{ik} \frac{\partial \sigma}{\partial z_k^n} \quad (3.24)$$

Sequential application of Eq. (3.24) then returns the gradients to the individual weights and biases by invoking Eq. (3.23) and the chain rule once more:

$$\frac{\partial J}{\partial \omega_{ij}^n} = \frac{\partial J}{\partial z_i^n} x_j^{n-1} \quad (3.25a)$$

$$\frac{\partial J}{\partial b_i^n} = \frac{\partial J}{\partial z_i^n} \quad (3.25b)$$

This is sufficient information for a first order optimisation scheme to step the weights and biases along the computed gradient directions with a factor  $\alpha_l$ . In the  $t + 1^{\text{st}}$  training step, this updates the weights and biases as follows:

$$\omega_{ij}^{n,t+1} = \omega_{ij}^{n,t} - \alpha_l \frac{\partial J}{\partial \omega_{ij}^n} \quad (3.26a)$$

$$b_i^{n,t+1} = b_i^{n,t} - \alpha_l \frac{\partial J}{\partial b_i^n} \quad (3.26b)$$

The gradient descent steps are commonly performed sequentially on “batches” of a dataset, until the full set of training examples has been covered. A number of such “epochs” is commonly performed in a single training.

To gauge the progress and success of the training of an ANN as it cycles over training epochs, metrics of the model’s prediction accuracy or loss are commonly tracked throughout this process. To prevent the network from “overfitting” its data (the optimisation of the ANN’s weights and biases to reproduce specific, detailed patterns of the data that do not necessarily generalise to the underlying process they attempt to represent [211]), a common approach is to split the available dataset into training data, validation data and test data, with holdout and/or cross validation [170, 183]. Commonly, the dataset is first split into a set used during the training stage and a test set that will never be encountered during training, but is reserved for tests of the finalised model. Then, the first set is split into training data used in each training cycle over the ANN’s samples, and validation data, used to tune the model’s “hyperparameters” (free parameters). One commonly tracks progress during a training run with this validation data, to highlight the success or failure of ANNs to learn the desired data at an early stage [211].

Various subtle modifications can improve the learning of ANNs. One can manipulate the training strategy, the network architecture or the hyperparameters, all with potential benefits to improve the model’s accuracy and reduce its risk of overfitting. These are succinctly and comprehensively discussed in [143] and [183, 211] respectively and will be elaborated upon when necessary in the following chapters.

### 3.5.2. State of the Art in Fluid and Atmospheric Dynamics

DNNs today form an active research topic in the field of fluid dynamics [139]. Convolutional Neural Networks (CNNs) have been successfully applied to solving the pressure Poisson problem in divergence-free versions of the Navier Stokes equations [244], while hybrid convolutional-recurrent ANNs have been successfully employed to predict an arbitrary number of future states of the velocity or pressure given a time history in the context of multi-phase flows [255] and simplified representations of wall-bounded flows [232]. Simpler architectures have successfully modelled liquid splashes [246] and served as closure models for Reynolds Averaged Navier Stokes models, which Ling et al. managed to do in a rotationally Galilean invariant manner [148].

Finally, as is the focus here, ANNs have served as unresolved scales models in LES simulations, having learned Bardina’s scale similarity model [212], the cross and Reynolds stresses of HIT in the context of finite volume discretisations [21, 256], unresolved scales flame surface-density [142] and the approximate deconvolution method [170]. In the context of VMS, they have been used in several recent MSc theses at the TU Delft to optimise estimates of the free parameters of Shakib’s  $\tau$  [226] for the one-dimensional Burgers’ equation [22, 68], in the spirit of the first approach to improved modelling discussed in Section 3.3.4. These show

promise to yield better predictions than the classical model, especially when extended by DSS and OSS versions of the problem [136]. However, as noted previously, this is likely insufficiently general for the problem considered here, and is therefore not considered further.

Most relevant to this work is a recent MSc thesis study, conducted by Michel Robijns, which investigated in detail a VMM closed by interaction terms directly predicted by dense ANN architectures for a 1D Burgers' problem [209]. The study confirms that ANNs can learn these interaction terms well, generalise to new problems and outperform traditional algebraic VMS closure models at similar accuracy in “online”<sup>1</sup> simulations for a range of sinusoidal forcing terms. This highlights the potential of ANNs to close VMMs in the context of simple problems, though the methodology remains untested for actual turbulence, run at time and space discretisations that are more relevant for GCMs.

In the atmospheric community, Schneider et al. [220] note that teaching ANNs outside the structure of the governing equations might limit their predictive ability outside their training scope compared to unstructured parameterisations. This was indeed a feature of early investigations on the topic [135], which tested ensembles of ANNs, trained from CRMs, as stochastic closures in single-column models and simplified climate models. However, two studies conducted in the past year have firmly established the high potential held by ANN closures.

First, Brenowitz and Bretherton train ANNs with a single hidden layer to estimate the residual source terms of total water and liquid water static energy in a coarse-grained LAM simulation [29]. Minimising the accumulated error of the source terms over several time steps, these models reproduce the terms well and prevent divergence of the online simulation. However, the model does not ensure non-negative precipitation or top-of-the-atmosphere radiative balance, such that ad-hoc cutoffs are necessary. Second, Rasp et al. train dense, deep, feed-forward ANNs to directly replace the CRMs in the SP [205]. With this deep architecture and large datasets, the study manages to run stable online simulations with encouraging results; they represent the improved deep convective features of SP with respect to traditional GCMs very well. The model outperforms the traditional GCM, while speeding up the SP's inner model computation by a factor 8 and the total model (including training) by a factor 4. However, these predictions do not generalise well. Increasing the Sea Surface Temperature (SST) of the simplified aqua-planet setup in which the model ran by four degrees renders the model substantially worse than that of a classically parameterised GCM. This might be an inherent limitation as long as the constraints of physics are not imposed on the ANNs.

### 3.5.3. The challenges and opportunities of ANNs as atmospheric models

Recent reviews on the topic single out three concrete, major challenges for the future incorporation of ANNs as atmospheric unresolved scales models [66, 79]:

1. Ensuring sufficient generalisability outside their training scope, by harnessing existing knowledge.
2. Capturing variability as well as mean states, following modern stochastic parameterisations.
3. Conserving energy and moisture to guarantee stable simulations.

Since one of the premises of improved unresolved scales models is that they should improve accuracy per unit computational cost, one might add as a fourth challenge that ANN unresolved scales models must manage to achieve their stability and generalisability without relying on ever-increasing datasets; they must remain cheaper than simulating the unresolved scales directly.

In spite of these challenges, it might be advantageous to turn to ANNs rather than modal unresolved scales models. ANNs are generally thought to be better suited for multiscale feature extraction, handling transformations and to represent invariance [139, 148] than modal decompositions. Furthermore, a linear, single-layer ANN, trained to reconstruct a set of superimposed linear combinations, reduces to the POD when the loss function is the state error in the  $L_2$  norm [17, 174]. Hence, one might view the POD as a subset of the more general function space spanned by nonlinear ANNs, which can possess more richness as a consequence. Correspondingly, changing the cost function of an ANN to equation-constrained, goal-oriented versions might yield similar advantages over Goal-Oriented Reduced Order Models (GOROMs).

Such Physics-Informed Neural Networks (PINNs) have recently been proposed by regularising their cost function with the residual of the PDE they attempt to model, and show promise in learning the PDEs of

<sup>1</sup>The term “online” will be reserved for forward-in-time simulations of the space-time discretisation where the unresolved scales model is repeatedly evaluated in conjunction with the rest of the model, while “offline” simulations refer to simple evaluations of the unresolved scales model outside the context of a time march of the complete model

simple [200, 201] and complex flow problems [127]. It is therefore currently thought that grounding ANNs more firmly in physics may improve also the extent to which they generalise to new, unknown situations that must still adhere to the same physical principles, providing a direction that might satisfy the first challenge.

Correspondingly, it is possible to extend an ANN to a stochastic model form. Ensembles of slightly differently trained ANNs [135] and Bayesian Neural Networks (BNNs) with Probability Density Functions (PDFs) over each of the model's weights and biases [157] provide points of departure for such an approach. To formulate tractable models, one might turn to variational inference methods that optimise an assumed fit of the underlying PDFs [98, 129, 191] or dropout techniques that deactivate any given neuron in the network and its connections with a prescribed probability during both training *and* forward sweep to yield the equivalent to deep Gaussian processes [78, 260]. With such extensions, ANNs appear at least as capable as the traditional stochastic methods discussed above to meet the second challenge.

While constraining ANNs with physics during training is commendable, it does not guarantee that the models' predictions will satisfy those constraints, especially when subjected to data that is far removed from their training envelope. To contain deviations of the model to undesired regimes, one might therefore be inclined to impose constraints on the model based on prescribed trends of e.g. the energy evolution during online running, as proposed by Robijns [209]. However, while this could be successful for problems where the large-scale statistics are known, it is at direct odds with the goal of any model: It should correctly *predict* these large-scale statistical trends, rather than reproduce known ones.

Without such explicit constraints, an ANN is not guaranteed to be conservative and the model is not guaranteed to remain stable. While Rasp et al. managed to conserve energy [205], the traditional SP by which this model was taught retains artificial diffusion terms that likely lower the difficulty of achieving such stability. In contrast, fluid dynamics ANN models that targeted exact reconstructions of the entire flowfield [255] or the unresolved scales flowfield [21] remain unstable without further intervention. Even Robijns encounters instabilities in online simulations, arising from inexact ANN predictions of the exact interaction terms [209]. Hence, an atmospheric, 3D model that must handle significant backscatter may encounter similar instabilities without further online stability insurance. However, the mechanisms that drive such instabilities remain uninvestigated. Hence, potential cures could well be identified by exploring the construction of the models in more detail.

In fact, the net could be cast somewhat wider than the stability considered in these initial studies. The models that emerge from combining ANNs with numerical methods are not only subject to the physical aspects of that modelling, but also to their numerical component. Therefore, one should demand that such models satisfy all fundamental requirements traditionally imposed on the wider class of numerical models. In this context, a model's stability must account for the discretisation, which is defined to be stable if the numerical solution for a given number of degrees of freedom derives from a well-posed problem. In turn, a problem is well-posed if it has a solution, that solution is unique and the solution responds proportionally to small perturbations in the input data [111], allowing the unique solution to be continually found. This aspect of combining ANNs with standard numerical models has not received any attention in literature.

This is somewhat surprising, since well-posedness is a non-trivial aspect of the problem at hand. For instance, finding  $u'$  as a direct function of  $\bar{u}$  is an ill-posed problem: Since  $S'$  is infinite, a single state of  $\bar{u}$  presumably can give rise to many states of  $u'$ . The interaction terms  $\hat{I}$  depend directly on  $u'$ , but only appear on the well-posed resolved scales. Hence, it is unclear whether finding these interaction terms is also ill-posed, or whether they can be uniquely determined from features of the resolved scales, such as the strong residual or a time history.

Finally, even if the ANNs are proficient at learning these terms exactly, their inclusion in forward problems might give rise to new, unexpected manifestations of ill-posedness once they become involved in nonlinear solution procedures and are subject to their own model errors. All these aspects are relevant to the model's performance, but their impact is so far lacking from the literature.

### 3.6. A VMM-ANN

One overarching difference between ANN unresolved scales models and the other data-driven unresolved scales models emerges from this discussion. While ANN atmospheric unresolved scales models clearly have both large challenges and opportunities, the extent to which the challenges will be prohibitive or the opportunities will outshine the potential of other methods is largely unknown at the moment. The limitations of all other models are much easier to identify, because their fundamentals are better understood or because they have been investigated for some time. ANNs' statistical properties are in contrast not well understood [211];

neither are therefore their limits. Simultaneously, only a small number of very recent studies have so far been conducted on their application to atmospheric unresolved scales modelling. These have been exploratory in nature, yet have immediately underscored the ultimate promise of the method by conducting experiments at global scale.

An avalanche of research inspired by this success is now underway [25, 185, 204, 217]. However, the current literature misses insight into which aspects of atmospheric ANN unresolved scales models drive their performance. Therefore, these studies should be informed by a proper, systematic assessment of how well ANNs perform when nearly all assumptions on model structure are removed. To facilitate these insights, Section 3.3.4 and Section 3.5.3 introduced how a VMM is a particularly suitable model to embed the ANN in. The VMS structure yields a term-by-term decomposition of exact unresolved scales projections that can be learnt directly by an ANN, facilitating immediate investigation of which terms are well-predicted and which are not, where instabilities are sourced, what the skills and weaknesses of the ANN formulation are or whether the formulation is at all well-posed. This stands in contrast to implementations in the context of SP [29, 205]. To judge ANN unresolved scales models on their merit, it is therefore natural to begin studying them in the context a VMS framework.

In all, ANN unresolved scales models have demonstrated considerable ability compared to other data-driven parameterisations, while immediate potential for further improvement can be identified. Yet, they lack rigorous study on their driving parameters. Finally, they fit naturally within the VMS framework. For all these reasons, they are the most interesting data-driven unresolved scales model for this study. The future atmospheric model that meets all criteria established in Section 2.6 and will form the basis of the study will therefore be a VMM-ANN.

All the uncertainties that cloud the current judgement on an ANN unresolved scales model's potential also encourage taking a step back from the eventual global flow problem that a GCM targets, since the range of scales of the problem makes it exceptionally difficult to assess. Hence, if one is interested in understanding the potential of the model, it is prudent to incrementally build it up from the simplest, most well-understood, yet relevant problem. Therefore, this study will consider the VMM-ANN in the context of a highly simplified model problem. Describing a model problem that is suitable to this end will therefore be the goal of the next chapter.

### 3.6.1. Outlook

The discussions in this chapter finally set the context for unpacking the research objective and research questions that were posed at the outset of the document. From these, a roadmap for the remainder of this thesis emerges that closely follows the systematic procedure for multiscale model development proposed by Majda [160].

#### Research Objective

The VMM-ANN formulation outlined in this chapter offers two advantages over the state of the art. First, the framework removes all modelling assumptions and pushes the ANNs to the highest possible level they could operate at as unresolved scales models, allowing the complete model to theoretically meet all requirements from Section 2.6. Second, the formulation offers clarity for studying the model's properties in more detail. In the scope of this project, this allows filling three notable research gaps that emerge from the above review. First, to the best of the author's knowledge, no studies other than [21, 209] have systematically studied ANNs as direct models for exact interaction terms, while no study has assessed the ability of ANNs to predict the terms for turbulent atmospheric dynamics at levels of discretisation that are sufficiently coarse to inform on their ability to close global models. More broadly, no studies establish whether learning interaction terms with ANNs and running numerical simulations with the ANN predictions embedded are well-posed problems, or which aspects of the models govern this. Finally, another crucial performance attribute of such models – computational cost – has therefore also not been assessed for proxies of atmospheric turbulence. The synthesis of these three gaps defines the concrete research objective of this thesis:

*“To investigate the well-posedness, generalisability, and computational cost of machine-learned approximations of the exact interaction terms of a VMM, for proxies of the atmospheric model equations at relevant levels of discretisation, in offline and online settings.”*

#### RQ1

*What are the characteristic scales, spatial distributions and relevance to the global problem of the amplitudes of the interaction terms of a VMS formulation for the model problem, over a range of time and space discretisation levels?*

A characterisation of the turbulent dynamics of the model problem is mandatory to understand i) the spatial statistics and modal distributions that build up the terms that the ANNs must learn, ii) which resolutions are sufficiently coarse that the interaction terms must capture the impact of true, physical, unresolved turbulence, iii) the attributes of the problem that do and do not translate to the global problem and iv) which features of the problem are likely to drive the models themselves.

To make these assessments, high-fidelity data of the model problem must be available and the interaction terms must be identified from the data at several levels of discretisation. The framework developed to this end is outlined in Sections 5.2 and 5.3, while the analysis that attempts to answer the research question is conducted in Chapter 6.

## RQ2

*What is the ability of feed-forward ANNs trained on error-free data to make generalised offline predictions of the model problem's exact interaction terms, compared to state-of-the-art models?*

Armed with this knowledge, one may begin assessing the extent to which the ANNs can learn interaction terms derived from high-fidelity simulations of the model problem turbulence as a function of resolved scales variables. This assessment is conducted in terms of an ANN's ability to predict interaction term examples that are uncorrelated from those the model has been trained on in an offline setting, given error-free input data. This ability is termed "generalised offline predictive ability" from here on. The RQ is treated in Chapter 7.

### RQ2.1

*Which combinations of ANN input variables, output variables and architecture ensure that the ANN accurately represents the interaction terms?*

First, the study will aim to establish i) the extent to which the models are capable of generalising their interaction terms predictions outside their training envelope when instantaneously fed error-free data, in accordance with the first general challenge for ANNs from Section 3.5.3, ii) which hyperparameters govern their learning, iii) which features of the resolved-scales flow their predictive skill responds most favourably to and iv) how they compare to state-of-the-art algebraic VMM closures.

Section 5.4.1 outlines the machine learning framework let loose on the high-fidelity data, while the first part of Chapter 7 answers the various components of the RQ.

### RQ2.2

*To what extent can an ANN predict the interaction terms over a range of increasingly coarse space and time discretisations?*

To assess whether ANN unresolved scales models can really meet requirements 2 and 4 from Section 2.6, the study will next attempt to ascertain whether the predictive ability of the ANN drops off as resolutions become coarse. "Coarse" will in this work be used to describe discretisation levels that require the interaction terms to capture an appreciable extent of physical, unresolved-scales turbulence; these levels follow from answering RQ1. In answering RQ2.2, the study will i) assess the predictability over a range of spatio-temporal discretisations, ii) discuss how the ANNs err and how this changes with discretisation, iii) identify driving parameters for the terms' predictability and iv) examine the implications this has for solving forward problems with ANNs embedded as the unresolved scales model. These topics are treated in the second part of Chapter 7.

## RQ3

*To what extent does an ANN's generalised offline predictive ability at coarse resolutions translate to online simulations?*

The real motivation of the study is, of course, to establish whether more accurate forward simulations of a deterministic chaos can be conducted with the VMM-ANN. However, Section 3.5.3 outlined that many early studies have grappled with instability in their online simulations [21, 29, 135, 209]. Therefore, the third topic of the thesis is to assess the extent to which the characteristics and abilities displayed by the ANNs in offline settings translate to online simulations. This part of the work aims to identify the impact of aspects that distinguish the online problem from its offline counterpart, in a bid to i) better understand whether these underpin the observed instabilities and ii) find model configurations that better lend themselves to robust simulations. The investigation is conducted through methodology outlined in Section 5.5, and broken down into three sub-questions that are addressed in Chapters 8 and 9.

### RQ3.1

*What are sources of the stability issues encountered by Robijns in [209]?*

Section 3.5.3's final remark introduces the two factors that are different between offline training and on-line simulations: The ANNs' lack of exposure to examples that encapsulate the effects of i) the iterative solver of the nonlinear problems and ii) the errors that the ANNs themselves are likely to induce in a time march. These might lie at the root of the problems encountered by Robijns. In this light, RQ3.1 attempts to establish causes of the instabilities.

In particular, this part of the study aims to establish if the models are well-posed and therefore stable. As is common for numerical methods of nonlinear problems, the requirement is here relaxed to practical well-posedness: The problems that are solved can be non-unique, but only to the degree that the model never finds a spurious solution in practice. The model should possess this property regardless of the ANN's accuracy. Hence, the research question will study the model's stability in a highly simplified setting without significant ANN prediction error, but at coarser discretisation than considered by Robijns [209].

### **RQ3.2**

*To what extent can stability issues be abated by alternative formulations of the VMM-ANN model?*

The study next builds on the understanding that results from analysing RQ3.1 to search for model configurations that possess improved stability characteristics. This search can focus on configurations of the model or on the ANNs themselves. Here, the first approach is taken, to i) show that conventional model improvements are likely insufficient to contain the ANNs' unstable proclivities and ii) outline directions for the future development of successful models. To comprehensively answer RQ3.2, it is considered in the context of both a simple, understandable problem in the second part of Chapter 8 and the more complex, but realistic model problem in the first part of Chapter 9.

### **RQ3.3**

*What is the model's computational cost compared to higher-fidelity simulations and algebraically stabilised VMM?*

Finally, forward simulations of the model problem are gauged on a metric that strongly contributes to their potential: Computational cost. This is compared to algebraic VMS closures and the exact model problem over a range of discretisations at the end of the thesis, to assess whether the complete model has potential to satisfy criteria 2 and 4 from Section 2.6.

## **3.6.2. Verification and Validation**

The coming chapters will venture to implement the VMM-ANN model and thoroughly assess and discuss its proficiencies and drawbacks with respect to state of the art models. This discussion overlaps with many aspects of validation studies, which generally aim to gauge whether the right model of reality has been developed and to quantify and understand all error sources of the model with respect to that reality [111, 207]. However, for such discussions to be meaningful, the first criterion to be met by the modeller is that the model presented here is implemented correctly. Therefore, a verification effort that measures the errors and uncertainties in the output of the numerical model must first be conducted.

It is not so trivial to unentangle the traditional interpretation of verification and validation for the proposed method. Verification is commonly associated with investigating errors introduced by the discretisation, while validation also assesses modelling errors. However, because Eq. (3.10) is exact, modelling errors are only introduced *after* discretisation, yielding VMS' unified representation of discretisation and modelling errors. Since the only reason the eventual model will not be exact is because the ANNs that will be employed to model the closure terms of Eq. (3.10) are not perfect models of reality, this is in the author's opinion best described as "modelling error" that must be treated by validation. Therefore, the assessment of the model's uniqueness and stability, normally associated with solution verification, is here considered part of the validation effort. The term verification will therefore be reserved for code verification - efforts to assess whether the ideas presented here have actually been correctly implemented.

# 4

## Simplified Test Cases

To judge whether the conjectured improvements of the VMM-ANN model proposed in the previous chapter materialise, it must be subjected to a quantitative assessment. However, given the complexity of the global problem, Section 3.6 identifies that the assessment should begin in the context of highly simplified, yet relevant test cases as a proof of concept. From this point of departure, the VMM-ANN can be incrementally and systematically extended to build up the necessary understanding to judge its potential as a GCM.

This chapter outlines several simplified test cases that are common in the field in Section 4.1, before Section 4.2 settles on a case that is especially qualified for this study and details its most important aspects. Subsequently, Section 4.3 simplifies this test even further to arrive at a 1D, forced inviscid Burgers' problem that forms a bridge between the work of Robijns [209] and more complicated problems. Finally, Section 4.4 introduces an even simpler problem that will be used extensively to verify the model and give insight in its functioning.

### 4.1. Simplified Test Cases for Atmospheric Modelling

While many physical processes are not yet sufficiently represented in climate simulations, the previous chapters have highlighted that the inability to represent the impact of unresolved dynamics in GCMs is particularly detrimental. Hence, if the merit of atmospheric unresolved scales models is to be gauged in simplified test cases, these must at least feature a turbulent spectrum reminiscent of that encountered in the atmosphere [161]. Often, moisture, radiation and chemistry are added as subsequent modelling steps [166, 167].

Many test cases that comprise simplified versions of atmospheric turbulence therefore exist. For instance, Grooms and Majda investigate the merit of stochastic SP in a problem of 1D dispersive wave turbulence with shallow spectral decay [88], while the various formulations of Lorenz models [150, 152] embody an entire class of simplified deterministic, chaotic dynamic systems [94] that have been used for early model tests of several methods [24, 55, 63, 73].

An alternative approach is to attempt to capture an actual physical phenomenon on a reduced set of scales. This has as an advantage for a model under development that one may test the actual equations the eventual model will solve in a simplified sense, if a high-fidelity solution of the problem is readily available. This approach will be taken here.

For problems driven by buoyant convection in a stratified environment, such as convective cloud formation, a common test case is a bubble of warm air, rising into a large and small domain [208]. 2D versions of this model have been broadly used to verify dynamical cores of non-hydrostatic GCMs [9] and also existing VMS models [167]. Kelly tests a quasi-2D version of the problem [121], while fully 3D simulations are often conducted as a final step [7, 166].

### 4.2. Statistically Stationary Convective Boundary Layer

While the models presented above are a suitable testbed for VMM-ANNs, this study has particularly stressed the need to improve the simulation of stratocumulus clouds that top the atmospheric boundary layer. Since this is a phenomenon that occurs on the smallest scales of the atmospheric turbulence spectrum, it is a natural area to begin testing the proposed model: If the model cannot capture the simplest form of boundary

layer turbulence when all scales above it are not present, it will not improve moist convective parameterisation when they are.

Furthermore, a data-driven unresolved scales model will require data to learn from. For a global model, scale-continuous data could be sourced from observations or GCRM data. The most natural downscaled analogue of a GCRM is an LES, which is especially proficient in simulating boundary layer turbulence [92]. Hence, using an atmospheric boundary layer simulation as the test case in this study permits the use of LES to readily generate large quantities of high-fidelity training, validation and test data to train, verify and validate the VMM-ANN model. In turn, using LES as the high-fidelity model keeps the VMM-ANN conceptually similar to how it would approximate and learn from global, scale-consistent models.

The models presented above predict a mean state that evolves in time. However, convenient measures of turbulent statistics are often time-averaged. Therefore, a simulation that is statistically stationary in time is a particularly interesting starting point for validation studies. The large stratocumulus cloud decks of the sub-tropics that are susceptible to GCM and SP misprediction effectively behave as statistically stationary turbulent boundary layers on the time scales of days [236]. Hence, a statistically stationary atmospheric boundary layer test case is also especially relevant to the low-cloud parameterisation problem.

There are several other advantages to the statistically stationary CBL. First, it incorporates a sufficient range of scales that an increasingly coarse simulation allows an ANN to demonstrate its proficiency in a realistic setting [247]. Second, the CBL is an extensively researched topic [146, 231, 236, 240] with well-understood governing dynamics, for which LES has been extensively validated [70, 247]. Third, statistically stationary Boussinesq equation simulations are not an overly large departure from what has already been successfully modelled by traditional VMMs [167] or by a VMM-ANN model [209]. For all these reasons, this test case will be considered in this project as the performance yardstick of the model. The test case will be simulated by refined LES runs, generating a ground truth dataset to train ANNs on and to validate the model against.

#### 4.2.1. Mathematical Model

The model will be governed by the Boussinesq equations in a large, horizontal domain, which are derived from Eq. (2.1) in Appendix A.1, without Coriolis forces:

$$\frac{\partial u_j}{\partial x_j} = 0 \quad (4.1a)$$

$$\frac{\partial u_i}{\partial t} + \frac{\partial}{\partial x_j} (u_j u_i) + \frac{\partial \pi}{\partial x_i} + g \frac{\theta''}{\theta_0} \delta_{i3} = 0 \quad (4.1b)$$

$$\frac{\partial \theta}{\partial t} + \frac{\partial}{\partial x_j} (\theta u_j) = S_\theta \quad (4.1c)$$

The Boussinesq equations result from four assumptions, that are commonly only met in an atmospheric boundary layer experiencing shallow convection [202], i.e. at the smallest of atmospheric scales. First, all thermodynamic variables may only deviate slightly from their reference values, such that density, pressure and potential temperature fluctuations  $[\rho'', p'', \theta'']$  from a reference state  $[\rho_0, p_0, \theta_0]$ , defined as

$$\rho'' = \rho - \rho_0 \quad (4.2a)$$

$$p'' = p - p_0 \quad (4.2b)$$

$$\theta'' = \theta - \theta_0 \quad (4.2c)$$

are relevant unknowns. Second,  $\frac{\theta''}{\theta_0} \gg \frac{p''}{p_0}$  and  $\frac{\rho''}{\rho_0} \gg \frac{p''}{p_0}$  [131, 202] such that  $\rho''$  can be expressed only in terms of  $\pi = \frac{p''}{\rho_0}$  and  $\theta''$  and can be removed from the equations. Third, processes associated with advective and internal wave dynamics must be of equal magnitude and of sufficiently large time scale that they are far removed from processes at the time scales of the speed of sound  $c_s$ . This means the inertial and gravity terms balance, but sound waves may be ignored. Finally, the ‘‘aspect ratio’’ of the motions, or the ratio of characteristic vertical and horizontal length scales, must be sufficiently small. This justifies neglect of time-variations in the density fluctuations in Eq. (2.1a), while maintaining their influence in the gravity term in Eq. (2.1b), where they influence potential temperature fluctuations. A more rigorous treatment of this discussion is included in Appendix A.1.

#### 4.2.2. Free, Dry Boundary Layer Turbulence

A Reynolds averaging, denoted here by  $\langle \cdot \rangle$ , of the dry Boussinesq equations will introduce the Reynolds stress tensor in the mean momentum equations and turbulent potential temperature flux (or simply heat flux) in

the thermodynamic equation. One may derive exact transport equations for these variables, which facilitates a characterisation of the dynamics that drive the boundary layer turbulence<sup>1</sup>. The most commonly analysed variable is the turbulent kinetic energy  $E = \frac{1}{2}\langle u_i'' u_i'' \rangle$ , first encountered in Section 2.1.2, as it is a measure of turbulent intensity. The evolution equation for  $E$ , which follows directly from the Reynolds stress equations of the Boussinesq problem, is Eq. (4.3):

$$\underbrace{\frac{\partial E}{\partial t}}_i + \underbrace{\langle u_j \rangle \frac{\partial E}{\partial x_j}}_{ii} = \delta_{i,3} \underbrace{\frac{g}{\langle \theta \rangle} \langle u_i'' \theta'' \rangle}_{iii} - \underbrace{\langle u_i'' u_j'' \rangle \frac{\partial \langle u_i \rangle}{\partial x_j}}_{iv} - \underbrace{\frac{\partial}{\partial x_j} \langle u_j'' E \rangle}_{v} - \underbrace{\frac{\partial}{\partial x_i} \langle u_i'' \pi \rangle}_{vi} - \underbrace{\epsilon_t}_{vii} \quad (4.3)$$

The proposed test case allows several simplifications to be made to Eq. (4.3) [236]. Therefore, a short introduction to each term follows: Term i represents storage and might be neglected if the timescales of the turbulence are sufficiently short that the layer instantaneously adjusts over a length scale associated with the layer depth. This will not be assumed, as the layer is commonly too deep for such approximations [146]. Term ii represents advection of the turbulence with a mean flow and is zero in the absence of such mean flow. No horizontal mean flow will be imposed on the proposed model, while no vertical mean flow follows from the boundary conditions of the simulation (see Section 5.2.1). Therefore, this term will be neglected in the proposed, simple model.

Terms iii and iv are the main sources of turbulence production. In meteorological jargon, term iii denotes buoyant or free production (or consumption) of  $E$ . It is commonly associated with the diurnal cycle over land. When radiative solar influx on a surface raises the surface's potential temperature over that of the air layer directly above it, a positive vertical heat flux  $w''\theta''$  develops from the product of vertical velocity fluctuations  $w''$  and  $\theta''$ . In its temporally averaged form, this is written as  $\langle w''\theta'' \rangle$ . Eq. (4.3) reveals this as a source of  $E$ , allowing turbulence to develop. This is not the standard state of the lower troposphere, which is commonly characterised by a stable potential temperature gradient [169]. When  $\langle w''\theta'' \rangle < 0$ , air parcels are forced back to any starting height they are displaced from; a stable situation ensues that consumes turbulence. In boundary layer meteorology, term iii is sufficiently important that it is common to normalise all other terms in Eq. (4.3) with it. Since the term only acts in vertical direction, it is the main driver of anisotropy in the CBL [236]. In the test case considered here, a uniform  $\langle w''\theta'' \rangle > 0$  will be imposed on the lower boundary to drive the turbulence, resulting in a horizontally homogeneous and isotropic situation.

Term iv denotes inertial, or forced production by mean wind shear. It is often dominant only in horizontal direction at the very surface, where roughness induces a full “surface” layer. The term is often the only source of boundary layer turbulence at night. Commonly, shear due to mean vertical motion is insignificant in all situations but deep convection. As term ii, term iv is exactly zero for the proposed test case. This situation is called “free turbulence”, which is distinguished from “forced turbulence”, when the production is dominated by term iv.

Term v is termed flux divergence. Its role is heuristically to redistribute  $E$  through the layer. For a case where periodic boundary conditions may be assumed, this is made explicit by the fact that its integral over the boundary layer height is zero. As discussed in Section 5.2.1, such conditions are applied to this test case.

Term vi is a pressure correlation term. It is often small and difficult to measure in observational experiments, and is therefore regularly lumped with other unknowns to form a single residual term when one analyses datasets. Pressure fluctuations might also be associated with internal or acoustic waves. Such waves occur at the top of the layer, which is by definition neutrally stable, but excited by penetrating dynamic thermal structures.

The final term in Eq. (4.3) is dissipation: Molecular-level diffusion of turbulence to heat at the Kolmogorov scales. In boundary layer modelling, this is commonly treated to the LES assumption: If one filters the flow-field in the inertial subrange of the turbulent energy spectrum,  $\epsilon_t$  is directly related to the resolved-scale turbulence through a net forward energy cascade. Such an assumption is imposed also for the Boussinesq equations, which do not themselves possess a diffusion term. The resulting balance therefore simplifies to:

$$\frac{\partial E}{\partial t} = \delta_{i,3} \frac{g}{\langle \theta \rangle} \langle u_i'' \theta'' \rangle - \frac{\partial}{\partial x_j} \langle u_j'' E \rangle - \frac{\partial}{\partial x_i} \langle u_i'' \pi \rangle - \epsilon_t \quad (4.4)$$

Meteorological interpretation of such equations is often phenomenological. In this spirit, consider the following explanation of the development of a CBL that is averaged over a large, horizontal area and schema-

<sup>1</sup>Similar equations can be derived and analysis be conducted for moisture variables if they are included in the model. See chapter 4 in [236] for derivations and a comprehensive discussion.

tised in Fig. 4.1. When buoyant thermals, engendered by the heat flux at the surface, rise into a stable atmosphere with positive temperature gradient, they will become negatively buoyant [169, 236]. However, a turbulent “air parcel” will carry over its residual momentum and overshoot into this stable region; this is called “penetrative convection” [58] and results in dome-type turbulent structures. The atmosphere in these overshooting regions is stable and diffusion of the momentum only happens relatively slowly. Hence, the momentum “sinks” back into the convective layer, transporting with it “sheets” of warm air from the stable atmosphere that rapidly mix into the convective layer. Such entrainment results in a growing, well-mixed layer of relatively constant potential temperature and neutral stability. It is capped by a temperature inversion where  $\theta$  rises very rapidly with altitude, before transitioning into the free atmosphere. The vertical coordinate at which the entrainment occurs is therefore termed the inversion height  $z_i$ , which represents the boundary layer top (or cloud top in the case of the cloud-topped boundary layer). Note that no vertical mean motion is necessary for the layer to develop in time; it is purely driven by the entrainment. This is shown in the leftmost subfigure of Fig. 4.1.

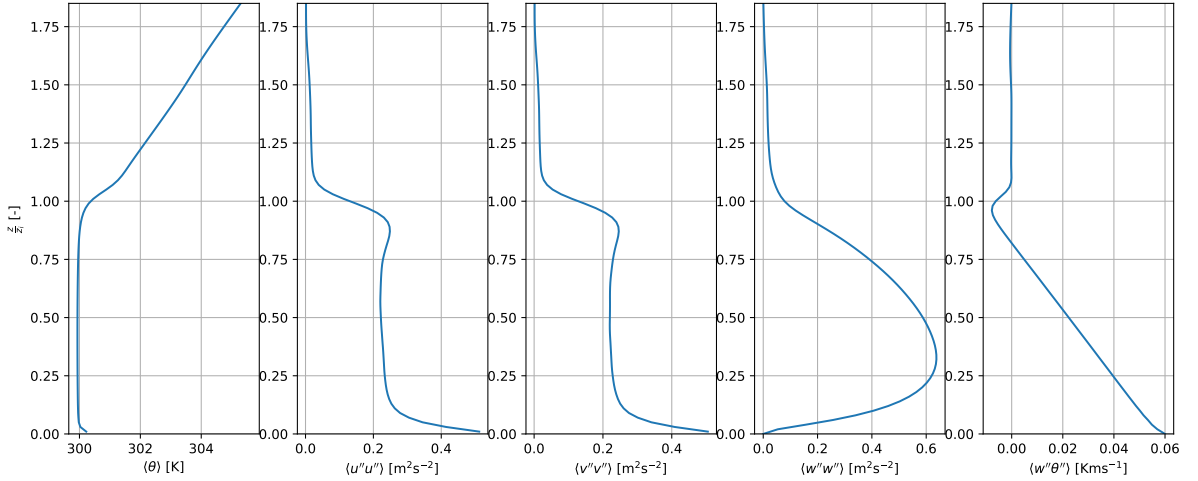


Figure 4.1: Profiles of the mean variables in a statistically stationary, free CBL with vertical coordinate  $z/z_i$ . From left to right: Mean potential temperature  $\langle \theta \rangle$ , mean horizontal fluctuating momentum fluxes  $\langle u''u'' \rangle$  and  $\langle v''v'' \rangle$ , mean vertical fluctuating momentum flux  $\langle w''w'' \rangle$  and mean vertical heat flux  $\langle w''\theta'' \rangle$ .

Several other aspects of this figure are instructive. First, note that both components of the horizontal momentum statistics are of equal magnitude. This highlights the horizontal isotropy of the proposed simulation. Furthermore, horizontal statistics have a vertical gradient only in the near-wall region and at the inversion, above which they reduce to 0. Conversely, the vertical momentum statistics peak around  $\frac{z}{z_i} \approx 0.3$ . Through term V in Eq. (4.4), these contribute to turbulence production when  $\frac{z}{z_i} > 0.3$  and to its dissipation when  $\frac{z}{z_i} < 0.3$ . In the literature, this is again commonly explained phenomenologically: The vertical momentum of rising thermals reduces through dilution with free atmospheric air, drag, and the warming and stabilising effect of the mixed layer top [236]. Finally and most importantly, turbulent heat flux reduces nearly linearly throughout the height of the layer, as depicted in the rightmost subfigure. To entrain air at the top of the layer, a certain amount of energy must be spent, yielding a negative turbulent heat flux towards the inversion height [240].

### 4.2.3. Statistically Stationary Model

While the turbulent profiles discussed so far are self-similar [231], they are not stationary in time. As long as a positive surface heat flux  $\langle w''\theta'' \rangle_s$  is imposed, the inversion height will keep growing. This is clearly visualised by considering a bulk model of the well-mixed CBL as proposed by Van Driel and Jonker [247] and sketched in Fig. 4.2. Van Driel and Jonker pose linear ODEs for the temporal evolution of  $z_i$  and the temperature inversion  $\Delta\langle \theta \rangle$ . Through analytical stability analysis, they find that despite imposing  $\langle w''\theta'' \rangle_s > 0$  at the surface,  $z_i$  in their model has stable stationary points when a uniform, radiative sink  $S_\theta = \langle w''\theta'' \rangle_e$  is imposed.  $S_\theta$  can be interpreted as a large-scale subsidence velocity  $w_s$  multiplied with the potential temperature gradient of the stable, free atmosphere above the layer  $\Gamma_s$ . Since this model shows surprisingly good agreement with high-fidelity LES for the development of  $z_i$  and  $\Delta\langle \theta \rangle$ , its findings prescribe an appropriate  $S_\theta$  that will be inserted

in Eq. (4.1c) to guarantee the statistically stationary nature also of the LES model that will solve Eq. (4.1) for this study. The derivation of the mixed layer model and its stationary points that inform the prescription of  $S_\theta$  are included in Appendix B.

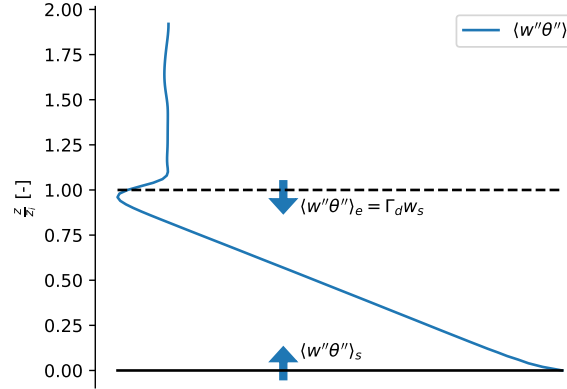


Figure 4.2: A statistically stationary CBL can be attained by balancing the surface heat flux that produces free turbulence,  $\langle w''\theta'' \rangle_s$  with a radiative sink  $S_\theta = \Gamma_s w_s$ .

### 4.3. Forced Inviscid Burgers' Problem

The Boussinesq problem consists of three spatial dimensions and a temporal dimension. It features five conservation equations [236]. However, previous work has verified and validated the VMM-ANN's capability in the context of a forced Burgers' equation, as a first 1D stepping stone for simulating turbulence [209]. Therefore, to ensure that the model can be understood, verified and validated at each stage of complexity, it is also sensible for this study to depart from a single equation in a single unknown. Compared to Robijns' initial study, the Boussinesq test case will i) subject the model to a significantly more realistic turbulent forcing and ii) challenge it to consider much coarser time and space discretisations. Therefore, such a 1D test case seems a particularly logical bridge from Robijns' initial tests to the prediction of the full 3D turbulence that the CBL simulation develops.

#### 4.3.1. Dimensionality Reduction

The vertical momentum equation is singled out as the best candidate for dimensionality reduction for two reasons. First, the momentum equations are targeted since they are the only equations that feature a nonlinear term that contributes to turbulent effects in a single variable. Second, as discussed in Section 4.2.2, the problem's turbulence is anisotropic in the vertical direction, such that  $w$  is the single variable that generates the most pronounced vertical statistics (see Fig. 4.1).

Therefore, the vertical momentum equation in Eq. (4.1) is rewritten on the form of an inviscid Burgers' equation:

$$\frac{\partial w}{\partial t} + \frac{\partial}{\partial z} (ww) = f \quad (4.5a)$$

$$f = -\frac{\partial}{\partial x} (uw) - \frac{\partial}{\partial y} (vw) - \frac{\partial \pi}{\partial z} - \frac{g}{\theta_0} (\theta - \theta_0) \quad (4.5b)$$

While obviously a significant simplification, this problem fundamentally contains the two most important aspects of the original problem: i) The prediction of a nonlinear convective term that allows shocks and energy transfer among a wide range of scales, punctuated by intermittent backscatter from high frequency to low frequency modes [173], and ii) the requirement to evolve these modes in time in a fully consistent manner. These aspects are challenged by the physical, turbulent forcing.

#### 4.3.2. VMS Problem

A VMS model is readily posed for Eq. (4.5) by following the procedure outlined in Section 3.2.1. The weak form of the equation, tested with the problem's basis  $\psi$  in the domain  $\Omega$  and in the infinite-dimensional

space  $\mathcal{V}$  is presented in Eq. (4.6), where it is assumed that the basis  $\psi$  respects the Dirichlet impermeability conditions of the original problem (this and the other boundary conditions that close the 3D simulation are further discussed with DALES itself in Section 5.2.1). Solving Eq. (4.6) will give the solution  $w$  in the likewise infinite-dimensional solution space  $\mathcal{S}$ .

$$\left(\psi, \frac{\partial w}{\partial t}\right)_{\Omega} + \left(\psi, \frac{\partial}{\partial z}(ww)\right)_{\Omega} = (\psi, f)_{\Omega} \quad (4.6)$$

The scale decomposition  $\psi = \bar{\psi} + \psi'$  and  $w = \bar{w} + w'$  into the respective spaces  $\bar{\mathcal{V}} + \mathcal{V}'$  and  $\bar{\mathcal{S}} + \mathcal{S}'$  then yields the resolved and unresolved scales equations.  $\bar{w}$  is still constructed by projecting  $w$  onto a piecewise linear finite element basis  $\bar{\psi}$  in a nodal manner, so integration by parts can be performed on the convective term without carrying along element boundary terms. In this work, a semi-discrete Bubnov-Galerkin discretisation will be employed, such that  $\bar{\mathcal{S}} = \bar{\mathcal{V}}$  and

$$\bar{w} = \sum_{i=0}^{i=n_{el}+1} a_i(t) \bar{\psi}_i(z) \quad (4.7)$$

Where  $\bar{\psi}_0$  and  $\bar{\psi}_{n_{el}+1}$  will be weighted by homogeneous amplitudes to reflect the enforcement of the strong Dirichlet condition. The goal of the method is then to find the amplitudes  $a_i(t)$  to construct  $\bar{w} \in \bar{\mathcal{S}}$ , satisfying Eq. (4.8a), leaving the influence of  $w' \in \mathcal{S}'$ , formally satisfying Eq. (4.8b), on Eq. (4.8a) subject to modelling:

$$\underbrace{\left(\bar{\psi}, \frac{\partial \bar{w}}{\partial t}\right)_{\Omega} - \left(\frac{\partial \bar{\psi}}{\partial z}, \bar{w}^2\right)_{\Omega}}_{\text{Galerkin terms}} + \underbrace{\left(\bar{\psi}, \frac{\partial w'}{\partial t}\right)_{\Omega}}_{w'_i \text{ projection}} - \underbrace{\left(\frac{\partial \bar{\psi}}{\partial z}, 2\bar{w}w'\right)_{\Omega}}_{\text{Cross term}} - \underbrace{\left(\frac{\partial \bar{\psi}}{\partial z}, w'^2\right)_{\Omega}}_{\text{Reynolds term}} = \underbrace{(\bar{\psi}, f)_{\Omega}}_{\text{Boussinesq forcing}}, \quad \forall \bar{\psi} \in \bar{\mathcal{V}} \quad (4.8a)$$

$$\left(\psi', \frac{\partial \bar{w}}{\partial t}\right)_{\Omega} - \left(\frac{\partial \psi'}{\partial z}, \bar{w}^2\right)_{\Omega} + \left(\psi', \frac{\partial w'}{\partial t}\right)_{\Omega} - \left(\frac{\partial \psi'}{\partial z}, 2\bar{w}w'\right)_{\Omega} - \left(\frac{\partial \psi'}{\partial z}, w'^2\right)_{\Omega} = (\psi', f)_{\Omega}, \quad \forall \psi' \in \mathcal{V}' \quad (4.8b)$$

The following chapters will attempt to model the three terms that close Eq. (4.8a) directly, through the use of ANNs that are directly informed by the resolved scales. Therefore, these interaction terms are given introductions below along with a brief motivation for the relevance of their inclusion in the model:

$\left(\bar{\psi}, \frac{\partial w'}{\partial t}\right)_{\Omega}$  Since the chosen finite element basis is not orthogonal to the unresolved scales space, linear terms of  $w'$  will have a nonzero projection on the resolved scales. The only such term in Eq. (4.8a) is the projection of the unresolved scales' time derivative  $\frac{\partial w'}{\partial t} = w'_t$ . Its "projection" along the time direction can be interpreted by viewing the finite-difference discretisation of the semi-discrete system that results from Eq. (4.8a) as a collocation scheme with a Dirac basis at the discrete time levels. While this is a somewhat inelegant formulation of this term, semi-discrete methods are significantly cheaper than space-time discretisations, whose matrices grow rapidly with degrees of freedom, while the main motivation for this project is the potential to save cost. The term's correct representation meets the criterion that future GCMs' unresolved scales models cannot rely on these being quasi-steady over the time steps of the resolved-scale model. Therefore, assessing its characteristics, predictability and impact in forward simulations is crucial.

$\left(\frac{\partial \bar{\psi}}{\partial z}, 2\bar{w}w'\right)_{\Omega}$  This term is traditionally labelled "cross stress" in the LES [249] and VMS-LES community [107, 222]. If  $w$  is interpreted as a spectral superposition of modes (as in Eq. (3.1)), this term represents the direct, non-local interactions between modes of sufficiently low wavenumber to be resolved and modes of such high wavenumber that they cannot be resolved, in the space of modes that *can* be resolved. As ignoring this term precluded the representation of several important phenomena on the resolved scales of SP, its character, predictability and impact will also be carefully assessed in the following chapters

$\left(\frac{\partial \bar{w}}{\partial z}, w'^2\right)_\Omega$  This ‘‘Reynolds stress’’ term is the last classical unresolved scales turbulent impact on the resolved scales. In a spectral sense, it represents pure interaction between modes of wavenumbers that exceed the grid cutoff, yet combine to form modes of a wavenumber that *can* be resolved. Since this is also traditionally significant [87], it will be analysed at a similar level as the other terms in the coming chapters.

In spite of its benefits, it is important to pause here to summarise the limits of this model problem. Contrary to the requirements of a global problem, it has i) used a mathematical model that only remains valid for shallow convection at very small scales, ii) ignored moist and radiative processes, iii) assumed a statistically stationary state and iv) reduced the problem to a 1D proxy. Hence, this problem is much too simple to systematically lay bare all the challenges the global problem faces. This might mean that the model is proficient for simple problems, but not necessarily suitable for more complex simulations. There is precedence for such development: While Dorrestijn concludes that CMCs are skilled at inferring turbulent fluxes to predict shallow convection [63], they were not as proficient for deep convection or in GCMs [64]. The latter study also finds that training the CMCs on global data is better than training them locally, such that eventual global models might not be able to exploit local high-resolution simulations to be successful, as suggested in [220].

The present study does not reject these challenges. In fact, its initial investigation in Chapter 6 attempts to outline in more detail the manner in which the model problem’s turbulent characteristics differ from the larger-scale problem. However, with these limits in mind, the study will merely attempt to ascertain whether the model can successfully handle this most simple of situations before moving to more complex cases.

#### 4.4. Manufactured Solution Problem

As discussed in Section 3.6.2, the first step in the process to assess the VMM-ANN is to verify that the ideas put forward here are implemented correctly. Subsequently, the model’s properties can be validated. As a reflection of the somewhat cloudy distinction between verification and validation in this project, a technique commonly associated with verification, the Method of Manufactured Solutions (MMS), will play a significant role in all these studies.

The MMS takes the inverse approach of solving the PDE of interest [207]. It prescribes a known solution for the PDE and its boundary and initial conditions and substitutes this in the PDE, yielding a forcing that is consistent with the ‘‘manufactured’’ solution. For the propagation of the Left Hand Side (LHS) of Eq. (4.5), the following manufactured solution is chosen:

$$w = w_S + w_A(c_z + \sin(\omega_{wz}z))(c_t + \sin^2(\omega_{wt}t)), \quad z \in [0, 1], \quad t > 0 \quad (4.9)$$

Where the coefficient values are summarised in Table 4.1. Eq. (4.9) represents the evolution of a standing wave in space with solely positive values. This is an appropriate manufactured solution, because such a wave cannot be exactly represented by a piecewise linear basis, while it remains well-defined and smooth throughout the domain it is tested on. A representation of its evolution over a half period is included in Fig. 4.3.

Coefficient	Value
$w_S$	0.1
$w_A$	0.1
$c_z$	0.0
$c_t$	0.0
$\omega_{wz}$	$\pi$
$\omega_{wt}$	0.5

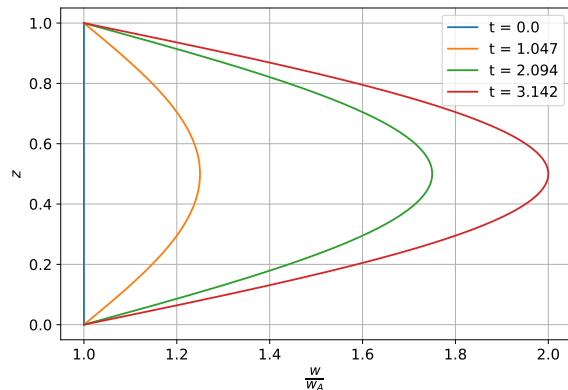


Table 4.1: Coefficients to describe the manufactured solution for  $w$  in Eq. (4.9) and the resulting source term  $S(z, t)$  in Eq. (4.10).

Figure 4.3: Evolution of the manufactured solution for  $w$  in Eq. (4.9) with the coefficients in Table 4.1, normalised with  $w_A$ , over a half period of its oscillation.

Inserting Eq. (4.9) in the LHS of Eq. (4.5) results in the following source term  $S$ :

$$S(z, t) = 2w_A(c_z + \sin(\omega_{wz}z)) \sin(\omega_{wt}t) \omega_{wt} \cos(\omega_{wt}t) + 2(w_S + w_A(c_z + \sin(\omega_{wz}z)))(c_t + \sin(\omega_{wt}t)^2) w_A \omega_{wz} \cos(\omega_{wz}z)(c_t + \sin(\omega_{wt}t)^2) \quad (4.10)$$

The problem that must satisfy the manufactured solution both in the interior and at the spatio-temporal boundaries is then:

$$\frac{\partial w}{\partial t} + \frac{\partial}{\partial z}(ww) = S(z, t), \quad z \in ]0, 1[, \quad t > 0 \quad (4.11)$$

$$w = u_A, \quad z = 0, z = 1 \quad (4.12)$$

$$w = 0, \quad t = 0 \quad (4.13)$$

Where the boundary and initial conditions are consistent with Eq. (4.9).

Traditionally, manufactured solution problems serve two purposes: To point out obvious implementation errors and to verify that various numerical discretisations are of the expected order [111]. Here, it is additionally extensively used in the validation process, as a simplest possible case that can highlight the model's stability characteristics. This problem will therefore return in each of the following chapters, fulfilling a slightly different role every time.

# 5

## Methodology

Section 4.3 introduced the 1D Boussinesq-forced Burgers' problem as this study's model problem. This chapter aims to cover the theory behind and setup of the numerical experiments that translate this particular model problem's formulation into results that facilitate answering the study's research questions. Since these aim to provide insight into the functioning of the model as much as they aim to maximise performance, the methodology outlined in this chapter is often chosen for its clarity rather than for merely maximising the performance of the algorithms. At every stage in the chapter, the implementation of the methodology is verified in the context of the manufactured solution problem introduced in Section 4.4.

The chapter is a rather lengthy, dense and detailed review of the methodology and its verification. This is in the interest of i) fully documenting the novel model and ii) ensuring verification is carried out properly so that uncertainty regarding the model's implementation will not cloud the results of failing models in the following chapters. To keep the chapter somewhat workable, several sections and algorithms of somewhat lesser impact have been deferred to Appendix C. However, readers might still find the reading experience more pleasant if they skip sections here that appear of limited immediate interest and rather return to them if discussions in the subsequent four chapters are found unclear.

### 5.1. Model Framework

The model framework broadly consists of four stages, illustrated by Fig. 5.1. First, data is drawn from the high-fidelity DALES simulations and formatted to appropriately drive the 1D Boussinesq-forced Burgers' problem. This is treated in Section 5.2.2. Second, "identification problems" are solved that compute exact versions of the interaction terms from coarsely discretised versions of the data. The procedure to solve these problems is explained in Section 5.3; its results will be the subject of Chapter 6 and provide the basis for answering RQ1. Third, a machine learning stage is encountered, in which ANNs are trained to represent the interaction terms and are evaluated on their performance. This is described in Section 5.4, while the results of this stage are treated in Chapter 7 to answer RQ2. Finally, forward problems are solved with ANNs embedded in a VMS framework. The aspects of this framework that were developed for this study are discussed in Section 5.5. In turn, the results that flow from the forward portion of the framework form the basis for answering RQ3 in Chapter 8 and Chapter 9.

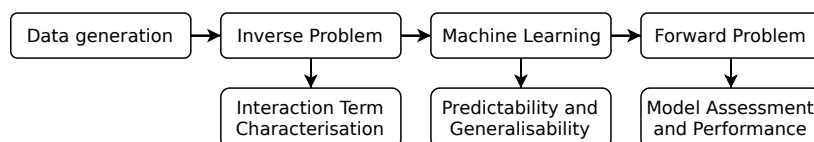


Figure 5.1: High-level framework of the VMM-ANN.

## 5.2. Data Generation

A data-driven unresolved scales model requires data to fit on and test against. The procedure for generating and preparing this data for the 1D forced Burgers' problem introduced in Section 4.3 is presented in Fig. 5.2. First, the statistically stationary CBL case elaborated on in the previous chapter will be simulated with a high-fidelity LES code, resulting in dense datasets of  $[u_i, \pi, \theta]$  in space and time that are approximate solutions to Eq. (4.1). This is explained in Section 5.2.1. Next, Section 5.2.2 will outline the reduction of the problem's dimensionality and illustrate how force terms are constructed to fit the Burgers' problem. Finally, the approach is verified in Section 5.2.3.

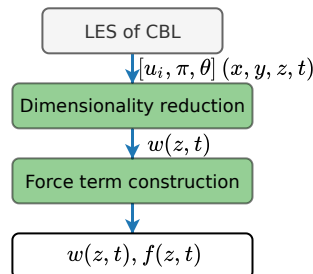


Figure 5.2: Flowchart of the data generation procedure. The LES was run externally (grey background), while the subsequent data processing steps were performed locally with Python (green background).

### 5.2.1. LES Model of the CBL

The model used to run high-fidelity simulations of the dry, statistically stationary CBL is DALES. DALES is a state of the art atmospheric LES code developed by a collaborating group of researchers at various institutes in the Netherlands and Germany [97] that has been extensively validated with observations and other atmospheric LES frameworks [70].

Heus et al. comprehensively introduce the model [97]. It is a finite-volume code that runs on a staggered grid, with velocity components located at the directional cell boundaries and scalars placed at the cell centres. It is only designed to solve the Boussinesq equations. The model solves filtered transport equations for  $\bar{u}_i$ , liquid water potential temperature  $\bar{\theta}_l$ ,  $\bar{\pi}$ , specific humidities of total water and rain water, rain droplet number concentration and up to 100 passive scalars. These equations may contain source terms for microphysics, radiation, chemistry, large-scale forcing and relaxation. For the dry CBL, the moist transport variables and source terms are all ignored, bypassing the complexities and uncertainties of these models, while a sink  $S_\theta$  is added to the  $\theta$ -equation as described in Section 4.2.3.

DALES solely models unresolved scales turbulence through eddy viscosity models. It has two methods for determining the required eddy viscosity coefficients: The conventional Smagorinsky model [229] and a one-equation approach that models and solves Eq. (4.3) [59]. The latter is default and requires several parameterisations. While most of these are necessary to handle moisture, it is most important to note the model for dissipation for the CBL:

$$\varepsilon_t \propto \frac{E^{\frac{3}{2}}}{\min\left(h, c_N \frac{E^{\frac{1}{2}}}{N}\right)} \quad (5.1)$$

Where  $N$  is the Brunt-Väisälä frequency<sup>1</sup>,  $h$  the grid spacing and  $c_N$  is a calibrated constant. The profiles presented in Fig. 4.1 are in fact DALES profiles for the statistically stationary convective boundary layer that have been subjected to this turbulence closure. The turbulent velocity statistics subfigures in Fig. 5.3 display that the model does not drain sufficient levels of turbulent energy without this closure:

<sup>1</sup>Brunt-Väisälä frequency  $N = \sqrt{\frac{g}{\theta} \frac{d\theta}{dz}}$ : The angular frequency at which a displaced parcel of air will oscillate in a statically stable environment [131, 169, 236]. It can be more generally interpreted as the eigenfrequency of the ordinary differential equation that emerges when the momentum equation in  $z$  reduces to a buoyancy-driven unsteadiness around an often hydrostatic reference condition. If  $N$  is real, or alternatively  $\frac{d\theta}{dz} > 0$ , oscillating solutions such as gravity waves ensue (i.e. the atmosphere is statically stable). If it is not real, or  $\frac{d\theta}{dz} < 0$ , instabilities grow exponentially, resulting in a statically unstable state) [236]

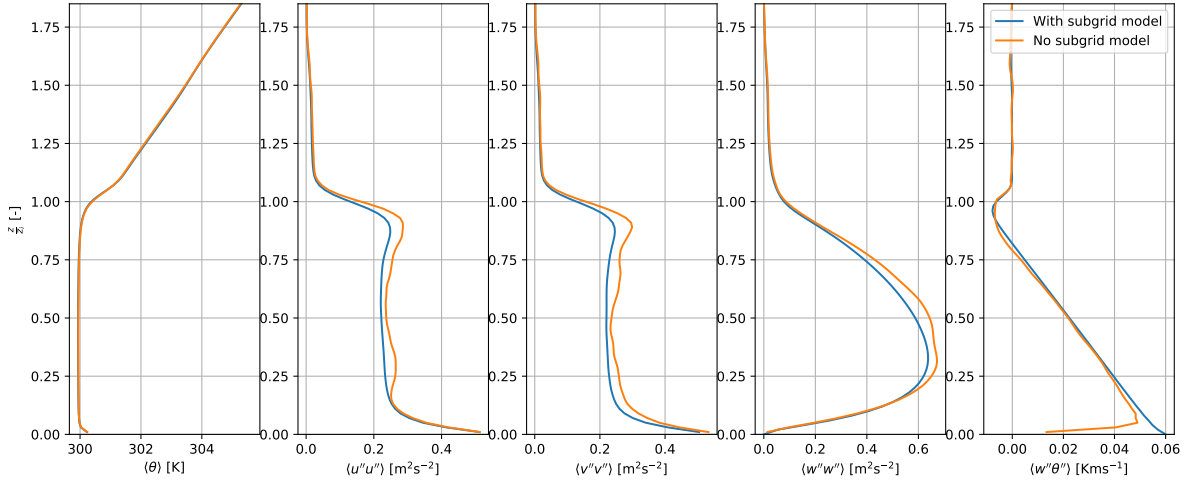


Figure 5.3: Reprint of the mean variables in a statistically stationary, free CBL with vertical coordinate  $z$  presented in Fig. 4.1. The blue lines include the effects of the unresolved scales and surface models; the orange lines represent the profiles constructed from the filtered variables.

The DALES fields extracted for training the ANN model are the filtered quantities that result in these over-predicted statistics. Combined with the fact that even an LES closed by artificial diffusion unresolved scales models may make significant errors in these profiles compared to a DNS, this is clearly not ideal. However, these filtered LES quantities will still be treated as ground truth for the VMM-ANN model. This can be justified by the fact that the VMM-ANN will only be gauged at discretisation levels that are much coarser than those DALES ran with, such that the large errors in the near-wall field will not strongly manifest themselves. It is then reasonable to expect that the errors in the LES compared to a DNS are of little influence when assessing the new model.

DALES imposes a no-slip condition at the lower boundary, where  $z = 0$  (Eq. (5.2a)). However, it does not resolve the flow down to the actual geometry of the surface or the associated relevant scales, requiring a “surface model” to represent the fluxes of scalars, such as heat, between the bottom boundary and the fluid. Here, the vertical heat flux  $\langle w''\theta'' \rangle$  is the only such interaction. It is imposed by the surface model to ensure that the heat flux profile in the rightmost subfigure in 5.3 more faithfully extends down to the surface boundary<sup>2</sup>:

$$z = 0: \quad u_i = 0 \quad (5.2a) \quad w\theta = (w\theta)_s \quad (5.2b)$$

DALES expects periodic boundary conditions to be imposed on the domain sides. No mean horizontal wind is prescribed. This has two implications. First, it allows the use of both spatially and temporally uncorrelated samples to be used to train the data-driven unresolved scales model of the same statistical turbulence. Second, it constrains  $\langle w \rangle = 0$  throughout the domain, since continuity of mean velocity requires that  $\frac{\partial \langle w \rangle}{\partial z} = 0$  and the surface boundary is impermeable. At the domain’s top, where  $z = L_z$ , Neumann conditions on horizontal velocity are demanded, impermeability is enforced, and the heat flux is kept constant:

$$z = L_z: \quad \frac{\partial u_{1,2}}{\partial z} = 0 \quad (5.3a) \quad w = 0 \quad (5.3b) \quad \frac{\partial \langle w''\theta'' \rangle}{\partial z} = \text{cst} \quad (5.3c)$$

Since penetrative convection produces gravity waves at  $z_i$  that are only lightly damped [169], it is common to impose an additional momentum sink that gradually activates above the inversion height. This prevents the gravity waves from reflecting off the domain boundary’s ceiling and artificially dominating the free atmosphere above the inversion. Such a “sponge layer” is standard in DALES, but since the convection in this problem is both stable and very shallow, it is turned off.

A DALES simulation is initialised with random fluctuations of velocity in an otherwise stably stratified en-

<sup>2</sup>For the VMS formulation, it is possible to impose the heat flux boundary condition that drives the 3D problem weakly [112], which may carry additional advantages in modelling the surface layer in an integrated sense. However, as the 1D problem considered here is merely a reflection of how the heat flux impacts the evolution of vertical momentum through the forcing  $f$ ,  $f$  will drive the turbulence of the problem and Dirichlet conditions will be imposed on  $w$  at the boundary. These Dirichlet conditions could also have been imposed weakly, as further discussed in Chapter 10

vironment. This allows the surface-driven turbulence to develop naturally, but it also means that a “spinup” time is necessary to allow the simulation to attain its statistically steady state. In [247], it is suggested that one hour is sufficient for the convective CBL at hand. Fig. 5.4 confirms this is a reasonable assumption: The spatially averaged vertical velocity statistics profiles beyond this point enter the (admittedly arbitrarily chosen) region sketched out by a single standard deviation from the mean of all realisations of the profile in the last 3 hours of simulation. Therefore, statistics will be averaged over the time span beyond the first hour of the simulation.

Time stepping is handled by a third order Runge-Kutta scheme, where the time step is adaptively constrained by the maximum Courant number  $C$  in the domain, while interpolation can be performed with a range of schemes, varying from common central differencing to nearly monotonic 5<sup>th</sup> order schemes, depending on the accuracy desired for each variable. Here, the second order scheme is used.

The parameters that permit the DALES simulation of the statistically stationary CBL are summarised in Table 5.1. In all, ten such runs are performed, all with a slightly different initial fluctuation field. This means that while all runs in this ensemble are statistically equivalent, they will provide individually different training examples for the machine learning stage that are uncorrelated from each other.

Parameter	Value
Domain size [ $N_x \times N_y \times N_z$ ]	128 × 128 × 96
Grid cell size [ $h_x \times h_y \times h_z$ ]	40m × 40m × 20m
Simulation time [hr]	6
Spin-up time [hr]	1
Average time step [s]	10
Lapse rate $\Gamma_s$ [ $\text{Km}^{-1}$ ]	0.005
Subsidence $w_s$ [ $\text{ms}^{-1}$ ]	0.015
Surface heat flux $\langle w''\theta'' \rangle_s$ [ $\text{Kms}^{-1}$ ]	0.06
Average inversion height $z_{i0}$ [m]	1000

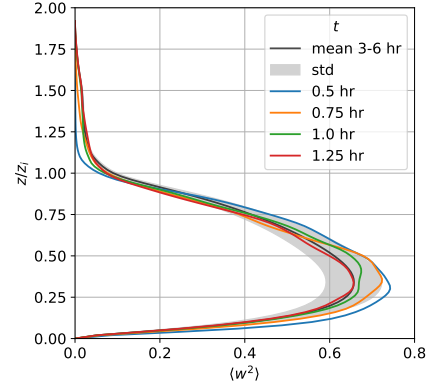


Table 5.1: DALES settings and characteristics for the CBL model

Figure 5.4: Spatially averaged profiles of vertical velocity statistics of the mean and standard deviation of the last 3 hours of simulation and 3 instantaneous realisations of the profile around the 1hr mark

### 5.2.2. 1D Burgers’ Problem

The dimensionality reduction of the DALES field is achieved by extracting individual “columns” of data in the vertical coordinate from the netCDF binary files that contain the simulation results. This maintains the time dimension of the problem, but splits each 3D simulation into  $128 \times 128$  columns in  $[z, t]$ , each associated with a different horizontal coordinate. These individual, reduced datasets are stored on disk and are manipulated in two stages.

First, to reduce the vertical momentum equation of the Boussinesq problem that gave rise to these fields to a Burgers’ problem, the forcing  $f$  as presented in Eq. (4.5) must be constructed. However, in reality the forcing will have to correspond to DALES’ approximation of the momentum equation Eq. (4.1b). In particular, as DALES solves filtered equations where the unresolved scales are approximated by an eddy viscosity model, this introduces a diffusion term, which is not present in the force term as it was introduced in Eq. (4.5b). Hence, the forcing term that will be used to drive the actual Burgers’ problem Eq. (4.5a) is somewhat different than presented in Chapter 4. The eddy-viscosity term can, however, implicitly accounted for in the by constructing  $f$  only from the LHS of the Burgers’ equation Eq. (4.5a):

$$f = \frac{\partial w_{DALES}}{\partial t} + \frac{\partial}{\partial z} (w_{DALES}^2) \quad (5.4)$$

As this also bypasses the necessity to reproduce DALES’ discretisation of each of the terms in Eq. (4.5b) and only requires loading a dense vertical velocity flowfield  $w_{DALES}$  in computer memory, this approach is taken here. The problem therefore reduces to posing suitable models for  $\frac{\partial w_{DALES}}{\partial t}$  and  $\frac{\partial}{\partial z} (w_{DALES}^2)$ .

Second, the data is sampled only every 6<sup>th</sup> time step of the LES simulation ( $\Delta t_{DALES} = 6\Delta t_{DNS}$ ), in order to avoid any spurious oscillations developed by its Runge-Kutta time march. This means that temporal dy-

namics of shorter time scales than  $6\Delta t_{DNS}$  cannot be captured; neither can therefore their impact on the LES solution. In general, the simulations that will be run here will be sampled at an even coarser level, such that it will often be assumed that neglecting the LES time scales below  $6\Delta t_{DNS}$  does not yield an unreasonable  $w$  and  $f$ . Exceptions will be addressed where they occur.

To construct the forcing anywhere in the spatio-temporal 1D domain of the Boussinesq-forced Burgers' problem, the discrete, sampled  $w$  in any column of the DALES data must be made a continuous function of  $z$  and  $t$  from its nodal definition at  $z_i$  and  $t^n$ :

$$w_i^n \rightarrow w(z, t) \quad (5.5)$$

To achieve this,  $w(z, t)$  is defined as a set of bi-cubic Hermite splines, following the methodology outlined in Appendix C.1. One final time, it is argued that the coarseness of the eventual simulations generally justifies using these splines as ground truth, as the ANN will be taught at space and time scales larger than these definitions. Therefore, it is assumed that the ANNs are learning characteristics of the actual underlying data, not merely the coefficients of local splines, unless otherwise stated.

This continuous version of  $w(z, t)$  is now used to generate the necessary derivatives to construct the force term. While it is possible to compute these derivatives analytically from the splines, they have here been constructed with first order backwards finite difference schemes:

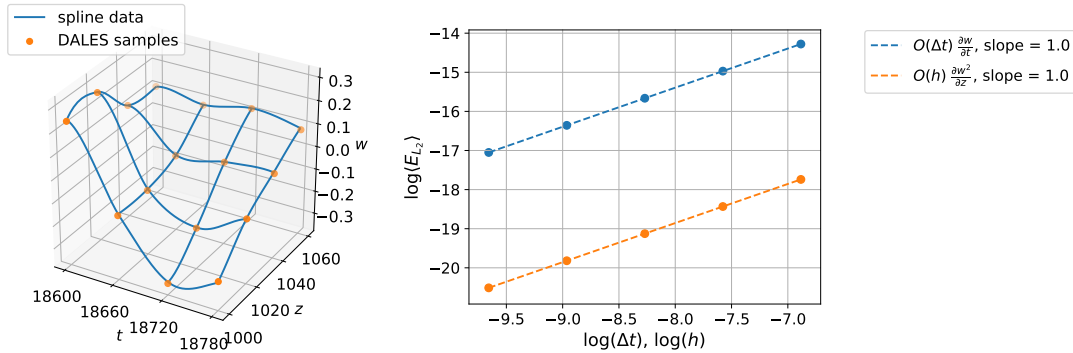
$$f(z, t) \approx \frac{w(z, t) - w(z, t - \Delta t_{DNS})}{\Delta t_{DNS}} + \frac{w(z, t)^2 - w(z - h_{DNS}, t)^2}{h_{DNS}} \quad (5.6)$$

Where  $h_{DNS} = 10^{-8}$ ,  $\Delta t_{DNS} = 10^{-8}$ .

### 5.2.3. Verification

The essential results of the data generation procedure are the splined  $w(z, t)$  and its finite-difference based forcing  $f(z, t)$ . Therefore, a verification of these terms is presented in Fig. 5.5. Fig. 5.5a illustrates the sampled  $w_{DALES}$  at an arbitrary section of the space-time surface, and a dense reconstruction of the four bi-cubic splines required to extract a value in the centre square. The figure shows that these splines coincide with the points, as required, and displays their  $C^1$  continuity, as expected.

Fig. 5.5b contains the order of accuracy test of the finite difference implementations that compose Eq. (5.6) with respect to the manufactured solution Eq. (4.9) over a range of fairly refined  $h$  and  $\Delta t$ . Located in their asymptotic regions, their  $L_2$  errors averaged over 1200 time steps and 4 elements converge at the expected order of 1. The chosen  $h_{DNS}$  and  $\Delta t_{DNS}$  lie at the bottom end of the asymptotic region, to minimise the error in this term. This leaves the framework verified.



(a) Verification and illustration of spline interpolation of DALES samples in  $z, t$ . (b) Order of accuracy tests of finite difference approximation of 1D forcing in  $h$  and  $\Delta t$ .

Figure 5.5: Verification of data extraction procedure

## 5.3. Identification Problem

The first meaningful stage of data manipulation is identifying the exact interaction terms of a coarsely discretised solution to the forced Burgers' problem. This is achieved by an application that leverages the code

framework “Mex”, written in C++ on top of the open source finite element library MFEM [2] and the large linear system-handling library HyPre [1]. Mex consists of a set of classes developed and maintained in-house at the aerodynamics group by Dr. Steven Hulshoff, and features almost all required tools for rapidly setting up and efficiently solving time-varying PDEs based on finite-element or spectral discretisations. Its modular, class-based structure allows for a relatively user-friendly implementation experience, where much of the numerical heavy lifting is handled by the backend and users are mainly subjected to the frontend implementation of their PDE of interest. It manages this while retaining sufficient generality that no essential limitations to its setup were found during the relatively adventurous excursions from regular finite element implementations attempted in this study. Several Mex implementations are outlined in more detail in Section 5.5, which describes the implementation of the forward problem. Here, the `getURTerms` app used to solve the identification problem is considered.

Section 5.3.1 aims to describe how Mex was leveraged to solve the identification problem. Its goal is to take individual columns of  $w$ ,  $f$  and  $\frac{\partial w}{\partial t}$  from the DALES simulations and construct instances of the weak form terms that solve the variational Burgers’ problem Eq. (4.6), given an exact nodal projection of  $w$  onto a piecewise linear finite element basis,  $\bar{w}$ . Later, it will be the goal of forward simulations to reconstruct this nodal projection  $\bar{w}$  based on estimates of the interaction terms extracted here. This section outlines the general approach of the implementation and discusses the implications of several design choices introduced at this stage. It is verified in Section 5.3.2.

### 5.3.1. Approach

Fig. 5.6 outlines the general structure of solving the identification problem. It begins by importing a column’s continuous  $w$ ,  $f$  and  $\frac{\partial w}{\partial t}$  fields as outlined above. It then steps through a time loop, which at most covers the time span of the LES simulation. At each of the time steps in this loop, the identification problem is solved to construct the weak form terms of Eq. (4.8a).

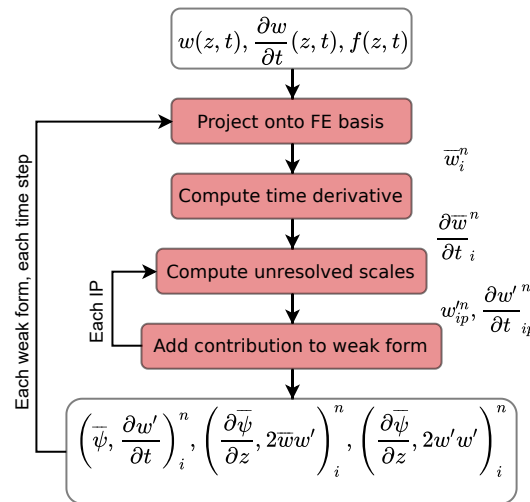


Figure 5.6: Flowchart of the identification problem Mex app `getURTerms`. It is fully implemented in Mex (red background).

Time marching is handled by the main application. Each time step commences with a nodal projection of  $w(z, t)$  onto the spatial discretisation’s finite element basis to construct an “exact” solution  $\bar{w}$  of less degrees of freedom than the original problem. Practically speaking,  $\bar{w}$  consists of a vector of amplitudes  $a_i$  that weights each of bases  $\bar{\psi}$  defined by the chosen finite element space. Note that  $\frac{\partial w'}{\partial t}$  depends on the chosen time march. Therefore, the training data is computed for the same time march to be used in forward simulations (this time march will be presented in Section 5.5.5).

Assembly of the weak forms is handled by a `DomainIntegrator` object. This object contains almost all necessary functions and variables for assembling weak forms, as well as access to a finite element database, where several relevant quantities associated with the finite element space are stored. Only two loops that construct the weak forms are therefore implemented here: A loop over elements and a nested loop over Integration Point (IP)s.

The former loop considers one finite element at a time. It prepares all properties associated with that element, such as its active  $a_i$  and  $\bar{\psi}$ , and integrates the weak forms over the element's domain. Each weak form is built as a sum over the domain where its weighting function is non-zero, for this study always two elements:

$$(\bar{\psi}, \cdot)_{\Omega} = \sum_{i=0}^{i=1} (\bar{\psi}, \cdot)_{\Omega_{e,i}} \quad (5.7)$$

Therefore, the variable to be predicted by the ANN can be either the per-element contribution to a weak form or the full weak form. Since the latter is somewhat easier to interpret and results in less cluttered codes, this unconventional approach is considered here. However, it precludes computing the contribution of the interaction terms to the resolved-scales energy balance: Such balances require the element-wise contributions to the weak forms, rather than the full weak forms (see e.g. Appendix B of [209] for a derivation). The implications of not being able to compute these balances are discussed in Section 8.2.

The nested loop in Fig. 5.6 performs most of the work. It must perform quadrature approximations to construct the integral weak form terms:

$$(\bar{\psi}, \cdot)_{\Omega_e} \approx \sum_{ip}^{n_{ip}} W_{ip} \bar{\psi}_{ip}(\cdot)_{ip} \quad (5.8)$$

Where  $W_{ip}$  are weights at the integration points of the quadrature scheme and  $n_{ip}$  are the number of integration points in an element. These two parameters govern the quadrature's standard integration rule: A sufficient number of points are chosen that exact integrals can be computed of a polynomial which order is equivalent to the highest degree polynomial that can be found by the basis functions multiplications that build up the various terms in the weak form in the element. The weights follow from the definition of that polynomial and the transformation properties of the element in assembly problems. However, the exact interaction terms multiply  $w'$ , which fluctuate to a much higher degree than  $\bar{w}(\bar{\psi})$ . Therefore, a relatively high number of integration points ( $3 \frac{h}{h_{DNS}}$ ) is required to satisfactorily determine these interaction terms, increasing the computation time somewhat.

To perform the quadrature,  $w'$  and  $\frac{\partial w'}{\partial t}$  are computed at each IP, for the  $i^{\text{th}}$  weak form, at the  $n^{\text{th}}$  time level through their definitions:

$$w'_{i,ip}{}^n = w(z_{ip}, t^n) - \bar{w}_i^n \quad (5.9a)$$

$$\frac{\partial w'}{\partial t}_{i,ip}{}^n = \frac{\partial w}{\partial t}(z_{ip}, t^n) - \frac{\partial \bar{w}}{\partial t}_i{}^n \quad (5.9b)$$

This procedure facilitates the computation of each of the interaction terms. Other terms that are to be used as input features to the machine learning stage as a function of the defined discretisation are also constructed in this app. These will be discussed further in Section 5.4.

### 5.3.2. Verification

The implementation of the `getURterms` app is verified in two stages. The first, outlined here, confirms that the individual weak form terms are implemented in such a manner that they close the full weak residual exactly, i.e.

$$\mathcal{R}_w = \left( \bar{\psi}, \frac{\partial \bar{w}}{\partial t} \right)_{\Omega} - \left( \frac{\partial \bar{\psi}}{\partial z}, \bar{w}^2 \right)_{\Omega} + \left( \bar{\psi}, \frac{\partial w'}{\partial t} \right)_{\Omega} - \left( \frac{\partial \bar{\psi}}{\partial z}, 2\bar{w}w' \right)_{\Omega} - \left( \frac{\partial \bar{\psi}}{\partial z}, w'^2 \right)_{\Omega} - (\bar{\psi}, f)_{\Omega} = 0, \quad \forall \bar{\psi} \in \bar{\mathcal{V}} \quad (5.10)$$

The requirement that  $\mathcal{R}_w = 0$  can be confirmed by considering the terms that build up the manufactured solution individually, as well as their sum. This is done in Fig. 5.7 for several time instances over an oscillation period of the problem.

The budget for  $\mathcal{R}_w$  closes up to  $10^{-7}$  for all instances in space and time. Since the major balance is between the externally computed  $(\bar{\psi}, f)$  and the terms constructed separately by the app, this indicates that the implementation is likely correct. However, this can only be fully verified once the interaction terms are inserted back into forward simulations and these manage to reproduce the correct  $\bar{w}$ . This is considered under the verification of the implementation of the forward problem in Section 5.5.6.

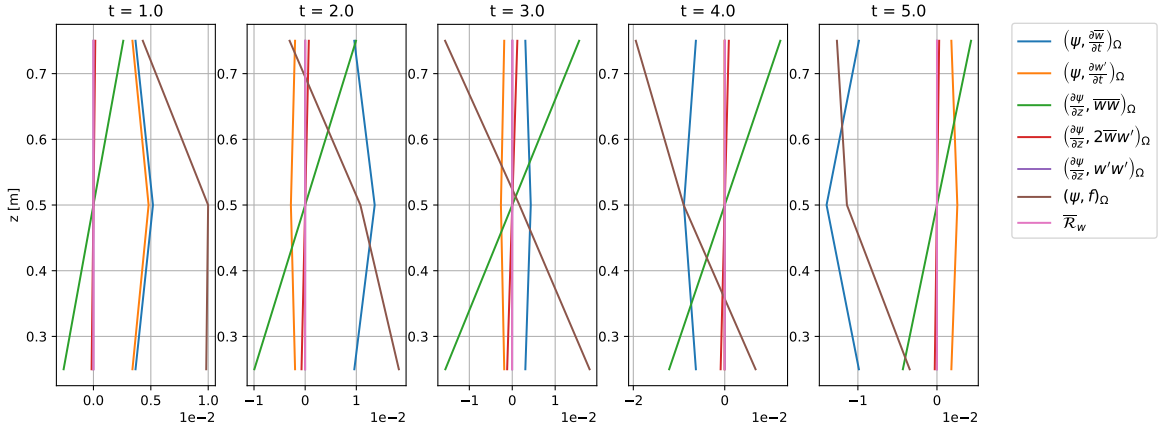


Figure 5.7: Individual terms and weak residual that build up the weak form for the manufactured solution problem on the domain  $0 < z < 1$ ,  $0 < t < 6$ , discretised with  $h = 0.25$ ,  $\Delta t = 1$ .

## 5.4. Machine Learning

The input features and exact interaction terms that result from solving the identification problem for a certain discretisation constitute a structured dataset. The function that maps the input features into interaction terms can then be approximated by a machine learning model. As introduced and discussed in Section 3.4 and Section 3.5, this model will be an ANN within the context of this study. The approach taken here to train ANNs to evaluate their impact on the study's RQs is outlined in the following sections: Section 5.4.1 gives a general description of the approach, before Sections 5.4.2 and 5.4.3 discuss the input feature sets and architectures considered here. Finally, Section 5.4.4 describes the validation strategy, before Section 5.4.5 conducts a verification.

### 5.4.1. Approach

Two broad distinctions can be made in how the model is fit to the data. The first approach only solves the identification problem once and trains the ANN a priori to its inclusion in the forward problem. The second performs the training of the ANN in conjunction with forward simulations of the problem, where each online prediction made by the ANN is followed by solving an identification problem and performing a step of ANN training. Such “online training” is commonly iterative, such that a number of predictions and training steps are performed for each weak form at each time step [136]. This allows the ANN to explore the spaces it would naturally enter in a simulation due to its inherent inferiority. It also extends the richness of the input feature dataset to which the ANN is subjected during training. However, since there is only a single correct set of interaction terms at every weak form and time step, each of these different, “wrong” features would still match a single output, which risks overconstraining the problem more than necessary. Furthermore, this adds a significant time penalty to the training phase, while confining the training to code frameworks that can easily be matched with Mex, such as OpenNN [4].

A priori training of the ANNs based on direct output from an identification problem, on the other hand, facilitates the use of well-developed, flexible Python-based frameworks for the design of ANN architecture and hyperparameter tuning, while only their forward passes must be evaluated online in the C++ solver. Online training is therefore not considered in the scope of this project. However, training with samples that have been generated by solving the forward problem a posteriori is considered in Section 8.3.5, and the potential of full, online training is revisited in Section 9.3.

Instead, the ANNs are trained *before* they are embedded in the forward problems, by exploiting the open source Python library Keras [44] as an API to Google's TensorFlow backend [6]. Keras is chosen for its flexibility, built-in capability to handle large input datasets and immediate suitability to run with the version of TensorFlow that was pre-installed on the hardware available in this project to leverage two NVIDIA Quadro K2200 CUDA-compatible graphics cards.

Fig. 5.8 illustrates the entire machine learning stage. It begins by selecting a set of input features that the ANN will attempt to map to the interaction terms, along with a discretisation to run the problem with. Subsequently, a tensor grid of data columns that will be part of the training phase is selected by specifying a

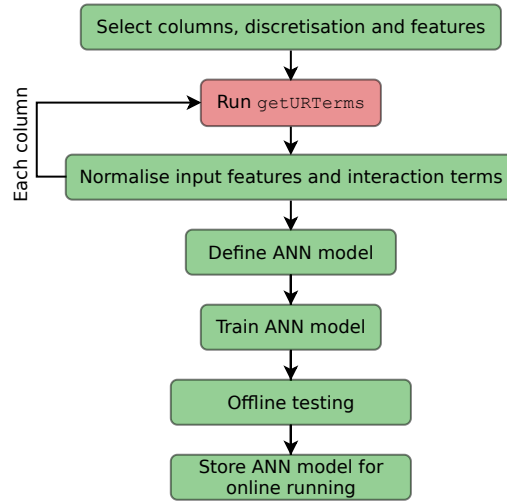


Figure 5.8: Flowchart of the machine learning stage's implementation. It is mostly comprised of a Python implementation (green fields) that wrap the `getURTerms` app described in Fig. 5.6 (red field).

constant spacing  $\Delta x$  between the columns that is a multiple of the DALES simulation's horizontal lengths  $L_x$  and  $L_y$ . The columns are extracted on this grid:

$$w(z, t)_{jk} = w(z, t)_j \otimes w(z, t)_k, \quad j \in [\Delta x, \dots, L_x], \quad k \in [\Delta x, \dots, L_y] \quad (5.11)$$

Each of the columns is subsequently propagated through `getURTerms` to compute their input feature and interaction term distributions. As the datasets that ensue rapidly outsize the memory of the hardware at hand, they are pre-processed before training. First, they are converted to binary files that can be quickly loaded. Second, each input feature or interaction term  $F$  in the total set of columns is normalised to the domain  $[-0.5, 0.5]$  with their respective minimum and maximum values encountered in the set:

$$F_n = \frac{F - F_{min}}{F_{max} - F_{min}} - 0.5 \quad (5.12)$$

Heuristically, normalising the input features aims to prevent any single weight in the ANN from becoming very large as a result of some inputs being numerically much larger than others. Models with large weights tend to become unstable or rapidly saturated during training [183], such that input mapping to an  $O(1)$  space is almost universal practice [26].

Similarly, large differences in ANN output, which form the basis of the method's loss function, may yield large gradients of that function. This can cause dramatic changes to the weights and also promote instabilities during training. Furthermore, this project's goal is to assess to which extent all interaction terms can be learned at various levels of discretisation. However, Chapter 6 will show that their magnitudes will vary as their discretisation changes. By always normalising them to the same domain, their individual contribution to the loss function is given equal weight in all scenarios.

The pre-processing stage is finalised by the implementation of custom `DataGenerator` classes in Keras, which organise samples into batches that are loaded onto the two graphics cards in cyclic fashion. Next, the ANN model is defined and trained, as will be discussed in the following two sections, before the trained models are stored as binaries. Separate programs then allow testing the trained models on a set of data from an arbitrary simulation of the identification problem. This framework allows assessing the generalisability of the problem. Finally, the ANN's weight matrices, bias vectors, structure and activation functions are stored separately for models that are to be embedded in forward simulations, such that they can be accessed from Mex.

### 5.4.2. Input Features

As discussed in Section 3.5, ANNs excel in situations where a relationship between desired outputs and a set of input features can be identified, but the direct evaluation of that relationship is unknown or impractical.

The discussions in Section 3.2 have established the theoretical link between the interaction terms and their resolved-scales drivers through the VMS analysis, setting the stage for this discussion.

To investigate RQ2.1, various ranges of input features are tested offline. The choice of these “feature sets” is motivated in the following paragraphs. They are summarised in Table 5.2, while several of the individual terms that compose the feature sets are positioned at multiple relevant spatio-temporal locations on a so-called “stencil”, shown in Fig. 5.9 along with their labelling logic.

The first input feature set consists purely of parameters that immediately follow from the VMS analysis. First, Section 3.2.4 shows that in many traditional LES settings, a decent model can be developed by assuming  $w' \propto \overline{\mathcal{R}}_s^m$ , where  $m$  is often only 1. Although it is unclear to what extent the expansion in  $\overline{\mathcal{R}}_s^m$  holds as the simulations become increasingly coarse, the unresolved scales equations from where the  $w'$  contributions to the interaction terms derive will always be forced by  $\overline{\mathcal{R}}_s$ . Therefore,  $\overline{\mathcal{R}}_s$  is the first feature upon which the ANN will depend.

However,  $\overline{\mathcal{R}}_s$  is defined at point-wise instances, while the interaction terms are integrals. Therefore, a first approximation to  $\overline{\mathcal{R}}_s$ 's effect on the element-integrated scale is attained by simply integrating it over single elements:

$$\overline{\mathcal{R}}_{s,I} = \int_{\Omega_e} \overline{\mathcal{R}}_s dz \quad (5.13)$$

A more sophisticated approach could attempt to fit a curve through individually evaluated points of  $\overline{\mathcal{R}}_s$ , of which the defining parameters could be ANN inputs. However, this has not been attempted here in the interest of keeping the ANN implementation straightforward. Assessing the effects of such improved formulations is thus left as a recommendation for future studies.

Next, the cross term explicitly depends on  $\overline{w}$  at the new time level  $t^{n+1}$  directly. All other terms depend on this  $\overline{w}^{n+1}$  implicitly through its influence on  $w'$  in the cross terms of the unresolved scales equations. Therefore,  $\overline{w}^{n+1}$  is also included. Similarly,  $\frac{\partial \overline{w}}{\partial t}^{n+1}$  directly influences the unresolved scales time derivative projection. It is the final contribution to this feature set.

Robijns investigated the spatial locality of the input features [209], finding accuracy gains in the prediction of the interaction terms when extending the feature set's stencil to cover information from elements adjacent to the element under consideration. Therefore, this study will also consider such extended stencils of the input features. However, as Robijns predicted element-wise contributions to the weak forms rather than the weak forms themselves, the stencil extension is implemented somewhat differently here. For the  $i^{\text{th}}$  weak form test, the feature set consists of i)  $\overline{\mathcal{R}}_{s,I}$  integrated over the two adjacent elements where the weak form is non-zero and ii)  $\overline{w}$  and  $\frac{\partial \overline{w}}{\partial t}$  that correspond to the adjacent weak forms. Their positions on the space-time stencil are illustrated at Fig. 5.9's  $t^{n+1}$  level.

This completes feature set 1 (FS1). It closely mirrors the feature set considered by Robijns, with the exception that the strong residual is included explicitly, rather than relying on the ANN to construct internal representations of such a term through a specified forcing.

Two categories of input features may now be distinguished: Those that depend on the problem's unknown  $\overline{w}^{n+1}$  and those that do not. This is of importance for integration of the ANNs in online simulations, where the nonlinear weak equations must be solved with an iterative procedure.  $\overline{w}$  will vary throughout that procedure, requiring these inputs to be continually available and to yield well-behaved convergence. Therefore, while feature sets in the first category are more clearly related to the VMS formulation, feature sets and models in the second category will also be considered.

The “explicit” feature sets in the second category are only based on a time history. Two versions could be considered: i) sets that consider *all* features at previous time levels and ii) sets that only extend some of the features backwards in time. For FS2, only  $\overline{w}$  and  $\frac{\partial \overline{w}}{\partial t}$  are considered at  $t^n$ , since including  $\overline{\mathcal{R}}_{s,I}^n$  is not found to add capability. Finally, the known force term at the current time level  $f^{n+1}$  is independent of  $\overline{w}^{n+1}$  and can still be used. The forcing is integrated over an element in a similar manner as for  $\overline{\mathcal{R}}_{s,I}$  in Eq. (5.13), resulting in  $f_I^{n+1}$  as displayed in Fig. 5.9. This term completes the second feature set.

Next, adding a time history to FS1 might be both beneficial for its learning and for maintaining its stability [29]. Furthermore, the minimum information that theoretically needs to be available to construct the highest frequency wave in temporal direction, the  $2\Delta t$  wave, is information from at least two time history steps. Therefore, FS3 extends FS1 by adding  $\overline{w}^{n,n-1}$  to the input set. Since the time marches considered here will explicitly base themselves on time histories of  $\overline{w}$  at  $t^n, t^{n-1}$ , it is somewhat redundant to consider  $\frac{\partial \overline{w}}{\partial t}$  at these time levels in addition to  $\overline{w}$ . Therefore, the time derivative terms remain unchanged.

Finally, other features might further enhance the relation between input and output. Such features could include the Galerkin terms  $\mathcal{R}_{w_g}$  in Eq. (4.8a), or their history:

$$\mathcal{R}_{w_g} = \left[ \left( \bar{\psi}, \frac{\partial \bar{w}}{\partial t} \right)_{\Omega}, \left( \frac{\partial \bar{\psi}}{\partial z}, \bar{w}^2 \right)_{\Omega} \right] \quad (5.14)$$

These features are added to FS3 at the current time level and only locally, resulting in FS4.

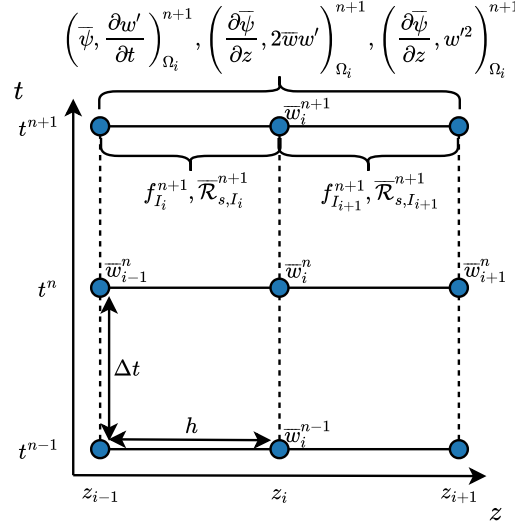


Figure 5.9: Stencil of various ANN input features of the discretisation of space and time. Dashed lines indicate collocation in time, solid lines indicate piecewise linear finite element bases in space.  $\frac{\partial \bar{w}}{\partial t}$  follows the distribution and logic of  $\bar{w}$ . Curly braces denote integration over the appointed elements.

Feature set	Features	Note
FS1	$\left[ \frac{\partial \bar{w}}{\partial t} \Big _{i-1,i,i+1}^{n+1}, \bar{w}_{i-1,i,i+1}^{n+1}, \bar{\mathcal{R}}_{s,I_i}^{n+1}, \bar{\mathcal{R}}_{s,I_{i+1}}^{n+1} \right]$	Base stencil
FS2	$\left[ \frac{\partial \bar{w}}{\partial t} \Big _{i-1,i,i+1}^{n-1}, \bar{w}_{i-1,i,i+1}^n, f_{I,i}^{n+1}, f_{I,i+1}^{n+1} \right]$	Explicit stencil
FS3	$\left[ \frac{\partial \bar{w}}{\partial t} \Big _{i-1,i,i+1}^{n+1}, \bar{w}_{i-1,i,i+1}^{n-1,n,n+1}, \bar{\mathcal{R}}_{s,I_i}^{n+1}, \bar{\mathcal{R}}_{s,I_{i+1}}^{n+1} \right]$	Time-history stencil
FS4	$\left[ \frac{\partial \bar{w}}{\partial t} \Big _{i-1,i,i+1}^{n+1}, \bar{w}_{i-1,i,i+1}^{n-1,n,n+1}, \bar{\mathcal{R}}_{s,I_i}^{n+1}, \bar{\mathcal{R}}_{s,I_{i+1}}^{n+1}, \mathcal{R}_{w_g}^{n+1} \right]$	Added feature stencil

Table 5.2: Feature sets used to define the ANN models' input. FS1 is an interpretation of Robijns' extended stencil [209], FS2 does not depend on unknowns at a new time level and FS3 extends FS1 backwards in time.

### 5.4.3. Architecture

A broad variety of ANN architectures exist. The strength of this property is the ability to design tailored ANN models that effectively treat a wide array of problems [183]. The drawback is that a large number of design choices must be made at this stage, without a systematic set of guidelines to ensure that globally optimal architectures are achieved. While this is not dissimilar to the tuning of free parameters in GCM parameterisations, it does not detract from the conceptual advantages ANNs hold over such models: It should in theory already be possible to model any function with a single-layer ANN with enough neurons [100].

Turbulence, though inherently non-local, is often predicted in an unresolved scales sense by various assumptions on the locality of those scales. In the spirit of such assumptions, CNNs and Recurrent Neural Networks (RNNs) might manage to capture local spatially and temporally varying features that are specific to the spatio-temporal domain under consideration here. However, in the interest of maintaining clarity in the approach, this study confines itself to dense, fully connected architectures such as presented in Fig. 3.3 that themselves are evaluated locally. The implications of this choice are extensively discussed in Chapter 7.

The network's loss function  $J$  is a comparatively important aspect of physics-oriented applications of ANNs. As discussed in Section 3.5.3, a broad range of studies show that "regularising" state output of an ANN

with physics-informed soft constraints can significantly improve their fidelity and behaviour when they are embedded in numerical methods [25, 127, 200]. Lumping the bases and the individual strong PDE terms they weight in integrated predictions of the interaction terms prevents the application of Raissi’s physics-informed approach [200] or Zhang’s extension thereof to weighted basis structures [260]. However, an attractive feature of learning direct weak form interaction terms is that the method is inherently physics-informed: For a given set of resolved-scales information, minimising the ANN output state’s  $L_2$  error minimises the error in  $I = \left[ \left( \bar{\psi}, \frac{\partial w'}{\partial t} \right)_{\Omega}, \left( \frac{\partial \bar{\psi}}{\partial z}, 2\bar{w}w' \right)_{\Omega}, \left( \frac{\partial \bar{\psi}}{\partial z}, w'w' \right)_{\Omega} \right]$ . When the Galerkin terms are correctly predicted, this is equivalent to minimising the exact weak residual as defined in Eq. (5.10). Therefore, the loss function that is employed throughout this study is merely the average  $L_2$  error of the interaction terms:

$$J = \frac{1}{3(n_{el} - 1)n_{\Delta t}n_c} \sum_{c=0}^{n_c} \sum_{n=0}^{n_{\Delta t}} \sum_{i=1}^{n_{el}} \sum_{t=0}^{t=2} (\hat{I}_{t,i,n,c} - I_{t,i,n,c})^2 \quad (5.15)$$

Where  $c$  denotes summation over the  $n_c$  columns of the training,  $n_{\Delta t}$  refers to the number of time steps in a column and  $n_{el} - 1$  is the number of weak form tests associated with the degrees of freedom at each time level.  $\hat{I}$  is the ANN approximation of  $I$ .

While  $J$  is presented as a relevant measure of ANN training performance, it clearly scales with the absolute order of magnitude of  $\hat{I}$ . Hence, a more general metric to assess how well various ANNs predict the terms they attempt to learn in different settings is the coefficient of determination for a linear fit between exact and predicted values,  $R^2$ . In the following chapters, this will therefore often be quoted as a main metric of ANN prediction skill alongside  $J$ .

Several other hyperparameters are aggregated into the model. Most obviously, the number of layers and number of neurons per layer are kept variable. Next, two classical tools to prevent overfitting will be carried along: A dropout probability [233] that applies to every neuron and a regularisation parameter  $\lambda_{L_2}$  that multiplies an  $L_2$  weight regularising term [183]. Finally, the learning rate  $\alpha_l$ , the activation function, the optimiser, the number of epochs and the mini-batch size are variable. Of these, the chosen set activation functions and optimisers demand a brief elaboration.

Three activation functions will be considered: Sigmoids, defined by Eq. (5.16), Rectified Linear Units (ReLUs), defined by Eq. (5.17) and Exponential Linear Units (ELUs), defined by Eq. (5.18).

$$\sigma_s(z) = \frac{1}{1 + e^{-z}} \quad (5.16) \quad \sigma_r(x) = \begin{cases} ax & x \geq 0 \\ 0 & x < 0 \end{cases} \quad (5.17) \quad \sigma_e(x) = \begin{cases} ax & x \geq 0 \\ a(e^z - 1) & x < 0 \end{cases} \quad (5.18)$$

The latter two functions’ gradients are constant for positive activations. This avoids the vanishing gradient problem associated with multi-layer networks of sigmoid activations. These functions’ derivatives are  $< 1$  and tend to zero for large positive or negative activations, meaning that sequential application of the backpropagation equation Eq. (3.24) through a network’s layers will decay the weights’ and biases’ gradients with exponent  $-n_{lyr}$ , preventing much progress to be made in learning for earlier layers. ReLUs, however, only pass positive activations. It has been observed that learning can be sped up by employing activation functions that do not return to zero for negative activations, and further by reducing the non-zero activations to a constant, deactivated state [46]. ELUs describe such states. Hence, these three choices span a relatively broad range of available options without increasing the size of the hyperparameter space prohibitively.

Three optimisers will also be considered. The first of these is RMSProp [241]. Its goal is to prevent large differences in the weights’ magnitudes, which hampers finding an appropriate, global learning rate for the algorithm. This can be achieved by normalising individual gradients with their magnitudes and increasing or reducing the individual weight’s learning rate by assessing whether it has been negative in consecutive steps. For an SGD method consisting of mini-batched gradient updates, each with a different gradient magnitude, this “Rprop” method can be adapted by normalising the gradients with a running average over multiple batches of the gradient’s root-mean-square. This changes the weight update equation Eq. (3.25a) to:

$$\omega_{ij}^{n^{t+1}} = \omega^{n^t} - \alpha_l \frac{\frac{\partial J}{\partial \omega_{ij}}^{n^{t+1}}}{\sqrt{\beta \left\langle \left( \frac{\partial J}{\partial \omega_{ij}}^n \right)^2 \right\rangle^t + (1 - \beta) \left( \frac{\partial J}{\partial \omega_{ij}} \right)^{2^{t+1}}}} \quad (5.19)$$

Where  $\beta$  is an adjustable relaxation parameter. While RMSProp effectively controls how far down a direction an update can proceed, one might also attempt to improve the estimate of the gradient direction

with respect to the global optimum in all parameters. So-called “momentum”-based approaches offer such improvements, by replacing the gradient in Eq. (3.25a) with a history of gradients, where each term in the history is scaled by a decay factor  $\mu$ , e.g.:

$$\omega_{ij}^{n^{t+1}} = \omega^{n^t} - \alpha_l \left( \mu \frac{\partial J}{\partial \omega_{ij}}^{n^t} + \frac{\partial J}{\partial \omega_{ij}}^{n^{t+1}} \right) \quad (5.20)$$

Combining such momentum approaches with RMSProp yields the “adaptive moment estimation” method Adam [128], which is extremely popular (note that the normalisation of Adam is somewhat more intricate than Eq. (5.19); this is not elaborated on here). Adam computes  $\frac{\partial J}{\partial \omega_{ij}}^{n^{t+1}}$  based on the current state. However, one might also add  $-\alpha_l \mu \frac{\partial J}{\partial \omega_{ij}}^{n^t}$  to  $\omega_{ij}^{n^t}$  *before* computing  $\frac{\partial J}{\partial \omega_{ij}}^{n^{t+1}}$ . This “Nesterov accelerated gradient” has theoretical benefits [237] and often improves performance further when built on top of Adam [65]. Therefore, such a “NAdam” scheme is also considered.

Common approaches to “optimise” high-dimensional hyperparameter set outlined above are downsampled grid searches. A vast array of sampling strategies, such as random selection, Latin Hypercube, or a Sobol sequence can be attempted, all of which are more systematic than trial-and-error and cheaper than full grid searches. In this work, the tool Talos is used to this end [5], working directly on top of the Keras models to perform a hyperparameter optimisation for a pre-selected dataset.

#### 5.4.4. Validation Approach

To ensure the ANN is not overfitting its data, a strong validation approach must be in place. As introduced in Section 3.5.1, it is common to do so with holdout and/or cross-validation strategies. Following common practice, a holdout strategy is pursued in this work for the relatively large datasets ( $> 10^5$  samples) encountered for the computation of the interaction terms from many columns of data [211]. However, when training on columns of data that derive from the same DALES simulation, there is a risk of holding out columns of data that are strongly correlated to the columns that were trained on. Testing the trained model with such data may give overly optimistic interpretations of the model’s generalisability. Therefore, the horizontal correlation length  $L_c$  of the vertical turbulence is established according to Eq. (5.21) [195]:

$$L_c = \int_0^{\frac{L_x}{2}} C(\delta x) d\delta x \quad (5.21a)$$

$$C(\delta x) = \frac{1}{w(x, y, z, t)^2} w(x, y, z, t) w(x + \delta x, y, z, t) \quad (5.21b)$$

Under the assumption that the turbulence is horizontally isotropic, traversing along  $x$  to establish  $C$  is equivalent to sampling along any other horizontal direction. This can be verified by evaluating Eq. (5.21b) in the domain at various  $\delta x$  and  $\delta y$  and ascertaining that it is approximately constant at equal  $r = \sqrt{\delta x^2 + \delta y^2}$ , as is illustrated at  $\frac{z}{z_i} = 0.6$  in Fig. 5.10.

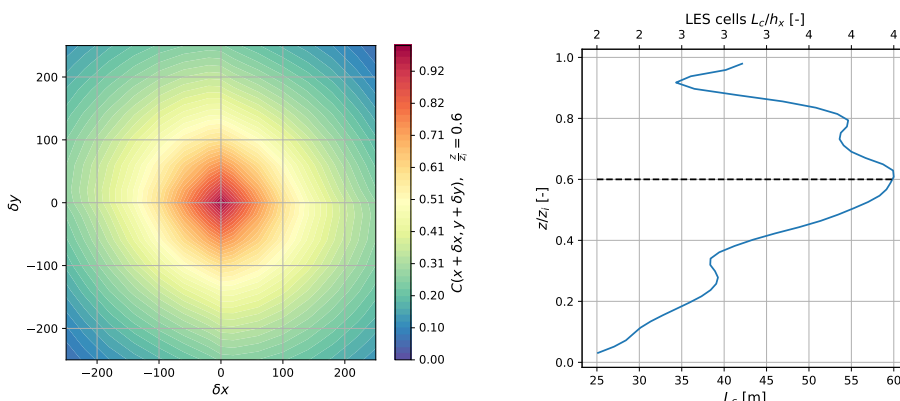


Figure 5.10: Cross-correlation  $C(x + \delta x, y + \delta y)$  throughout  $-\frac{L_x}{2} < x < \frac{L_x}{2}$ ,  $\frac{L_y}{2} < y < \frac{L_y}{2}$  when  $t = 1hr$ ,  $\frac{z}{z_i} = 0.6$ .

Figure 5.11: Variation of  $L_c$  with  $\frac{z}{z_i}$  throughout the turbulent portion of the domain.

While the horizontal isotropy is expected, Fig. 5.11 shows that  $L_c$  itself varies markedly throughout the domain, reaching its maximum  $L_c = 59.9\text{m}$  at  $\frac{z}{z_i} = 0.6$ , as indicated by the broken line. This corresponds to at least four columns' worth of spacing. It is then reasonable to treat data separated by more than four columns as validation data for hyperparameter tuning and test data for generalisation studies. Once  $\Delta x$  in the tensor grid sampling falls below 4 columns, a subset of columns from a differently initialised simulation of the statistically equivalent turbulence is considered for validation and testing purposes. In all cases, a minimum of 16 uncorrelated columns of data are used in both the validation and test sets, to ensure that a representative subset of the entire turbulent spectrum is sampled.

Note that even this validation strategy is not yet sufficient to gauge how well the models here generalise to *statistically* different situations, which is generally the largest problem encountered by ANN unresolved scales models in SP [25, 205]. However, learning any turbulence problem's statistics from individual examples is already a formidable challenge that should be tackled before problems with different statistics are introduced. As this framework has not yet passed the first test, it is prudent to ensure its skill in this regard before proceeding to the more challenging second test.

With this framework in place,  $J$  is evaluated on the validation set at the end of each epoch during training. To further prevent overfitting, an Early Stopping (ES) constraint is coupled to this evaluation. Based on a few trial runs for each problem, appropriate tolerances are set on  $J$ 's minimum required improvement over a specified number of epochs and on the number of epochs the training is allowed to continue for after the threshold has been crossed [183].

#### 5.4.5. Verification

The verification of the machine learning phase builds upon the verification of the identification problem presented in Section 5.3.2. The machine learning phase is verified by stepping through each of the steps in Fig. 5.8 with the manufactured solution problem. This problem is sufficiently simple that one would expect most ANNs to learn it almost perfectly. Therefore, the exact interaction terms of the manufactured solution problem are extracted from `getURTerms`, along with the features that define FS3. These correspond to the interaction terms considered in the verification of `getURTerms` in Section 5.3.2. The features and interaction terms are normalised according to Eq. (5.12).

Next, an ANN described by the parameters in Table 5.3 is trained on this data. For the verification problem, only a single run of `getURTerms` is performed. Hence, despite the efforts outlined above to find uncorrelated validation and test data, this problem employs cross-validation [211]: A different portion of the same training dataset is used as validation data in each epoch of the training, while a priori randomly extracted examples of the data are used for testing after training.

This is a somewhat abusive treatment of the traditional intention of a test set, as its individual samples are highly correlated to samples that feature in the training. Therefore, such training and testing of the problem cannot be ascertained to generalise well to situations outside its training domain. However, the intent of this training is also not to construct models that generalise outside the manufactured solution problem. Therefore, this practice is considered appropriate to verify the implementation of the training framework. It is also considered appropriate for assessing the basic impact of the ANN on the model form of the VMM-ANN, when only evaluated within the scope of the manufactured solution problem. Therefore, this implementation will return in Chapter 8.

Fig. 5.12 and Fig. 5.13 confirm the implementation. The simple manufactured solution converges monotonically over approximately 500 epochs, before ES ends the run. The training and validation losses follow each other closely, indicating that the network continues learning the interaction terms of the manufactured solution throughout the training. This is confirmed by testing the trained model on the previously unseen test data, shown in Fig. 5.13. In fact, plotting each of the normalised exact interaction terms against their corresponding ANN prediction reveals that the problem can be learned almost exactly. Here,  $R^2$  approximates 1 up to 5 significant figures, without much hyperparameter tuning.

Parameter	Value
Feature set	FS3
Number of examples	3600
Layers	[256,256]
Activation	ReLU
Testing fraction	0.2
Validation fraction	0.16
Dropout	0.0
$\lambda_{L_2}$	$1 \cdot 10^{-6}$
$\alpha_l$	$1 \cdot 10^{-4}$
ES tolerance	$1 \cdot 10^{-7}$
ES patience	50

Table 5.3: Parameters defining the verification ANN and its training.

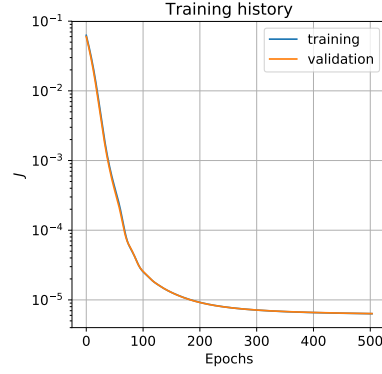


Figure 5.12: Training history of  $J$  on training and validation data.

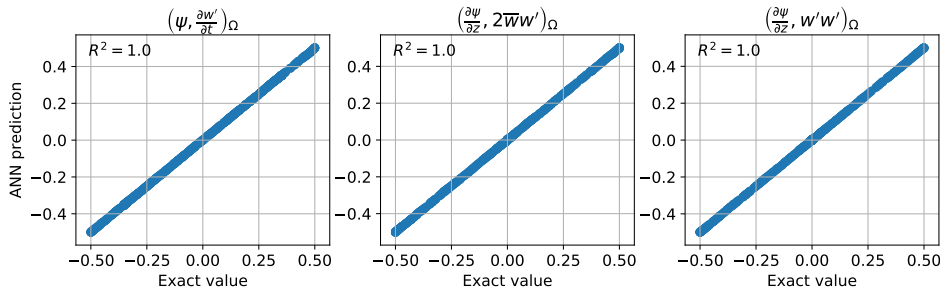


Figure 5.13: "Skill metric"  $R^2$  of the trained ANN, evaluated on test data according to simple cross validation.

## 5.5. Forward Problem

The final step of the modelling framework is simulating forward problems with a VMM closed by an ANN as the unresolved scales model. This framework will facilitate answering RQ3 and is broadly laid out in the following sections. It is constructed by overhauling an existing Mex app intended to run LES approximations of the incompressible Navier-Stokes equations (INS) to a suitable form for running ANN-embedded simulations. A general introduction to the framework is given in Section 5.5.1, before Sections 5.5.2 to 5.5.5 cover the new or refurbished objects that define the new model along with their verification. Finally, a set of reference solutions to be used for comparison in the following chapters is introduced.

### 5.5.1. Approach

As introduced in Section 4.3, a semi-discrete approach is taken here to solve the forced Burgers' problem Eq. (4.8a). Hence, the spatial discretisation precedes the time discretisation. The spatial weak form terms may then first be integrated by quadrature, such that a system of coupled, nonlinear ODEs results. The only unknowns in this system are functions of the nodal solution amplitudes  $a_i(t)$  and their time derivatives  $\frac{\partial a_i}{\partial t}$ :

$$M_{ij} \frac{\partial a_i}{\partial t} = \mathcal{N} \left( a_{ij}, \frac{\partial a_{ij}}{\partial t} \right) \quad (5.22)$$

Two design choices must be made to solve Eq. (5.22): First, a finite-difference based time discretisation must be posed, which relates  $\frac{\partial a_i}{\partial t}$  to the fully discrete unknowns at  $t^{n+1}$ ,  $a_i^{n+1}$ . This reduces Eq. (5.22) to a nonlinear system of algebraic equations for  $a_i^{n+1}$ . For the Burgers' problem, this is an equation for the weak residual  $\mathcal{R}_{w_i}^{n+1}$ , which will have the following dependence on  $a$ :

$$\mathcal{R}_{w_i}^{n+1} \left( \partial_t (a_{i-1,i,i+1}^{n+1}), a_{i-1,i,i+1}^{n+1}, a_{i-1,i,i+1}^{n+1,2}, \hat{I}(a_{i-1,i,i+1}^{n+1}) \right) = 0 \quad (5.23)$$

$\partial_t(a)$  is a general finite difference operator to compute the time derivative. The square terms in  $a$  result from the nonlinear convective term. Together with the ANN-predicted interaction terms  $\hat{I}$ , these constitute

the nonlinearity in the problem. Note that  $\hat{I}$  is *not* a function of  $a$  when the explicit feature set (FS2) is used to predict the interaction terms, in which case it also does not contribute to the problem's nonlinearity. In this project, Eq. (5.23) is solved with Newton's method, which will be frequently encountered in the following sections. The method expands  $\mathcal{R}_{w_i}$  to first order from a guessed state  $a_i^p$  and requires the approximation to satisfy the original problem:

$$\mathcal{R}_w(a_i) \approx \mathcal{R}_w(a_i^p) + \frac{\partial \mathcal{R}_w(a_i^p)}{\partial a_j} \Delta a_j^p = 0 \quad (5.24)$$

Solving the approximation Eq. (5.24) gives the blueprint for a corrector scheme to the prediction that in each Corrector Pass (CP) i) solves a linear system for a set of perturbations  $\Delta a_j^p$  to the current prediction along the gradient direction defined by the Jacobian matrix  $\frac{\partial \mathcal{R}_w(a_i^p)}{\partial a_j}$  (Eq. (5.25a)) and ii) updates the predicted state with the resulting  $\Delta a_j^p$  (Eq. (5.25b)).

$$\frac{\partial \mathcal{R}_w(a_i^p)}{\partial a_j} \Delta a_j^p = -\mathcal{R}_w(a_i^p) \quad (5.25a)$$

$$a_i^{p+1} = a_i^p + \Delta a_i^p \quad (5.25b)$$

Assuming that  $\mathcal{R}_w(a_i^p)$  resides in a basin of attraction which contains the root  $\mathcal{R}_w(a_i) = 0$ , that the Jacobian matrix  $\frac{\partial \mathcal{R}_w(a_i^p)}{\partial a_j}$  can be correctly predicted and that sufficiently small steps  $\Delta a_i^p$  are taken, this procedure will not only drive  $\mathcal{R}_w(a_i^p)$  to zero, but also converge to the *desired* root of  $\mathcal{R}_w(a_i)$  that solves Eq. (5.23) [219]. Therefore, it will in theory yield the correct degrees of freedom  $a_i^{n+1}$  and solution  $\bar{w}^{n+1}$ . This discussion gives rise to the general solution procedure illustrated by Fig. 5.14.

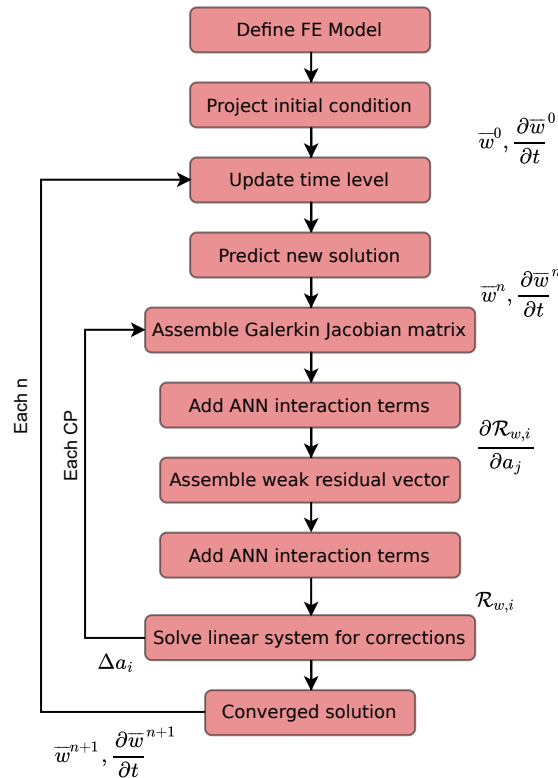


Figure 5.14: Flowchart of the numerical model that solves the forward problem. The solver is implemented in its own Mex app (red fields).

A simulation is initialised with a database of parameters that define the finite element model, such as the time march, finite element discretisation, unresolved scales model, force term and linear solver. After this initialisation, the (homogeneous) initial condition is projected onto the finite element space.

Next, the simulation steps through a time loop spanning the period for which the forcing is defined; this forcing derives directly from the data generation procedure described in Section 5.2.2. At each time level, a “same” predictor [114] gives an initial guess for  $\overline{w}_i^{n+1}$  and  $\frac{\partial \overline{w}}{\partial t}^{n+1}$ ; this predictor merely assumes  $\overline{w}_i^{n+1} \approx \overline{w}_i^n$  and  $\frac{\partial \overline{w}}{\partial t}^{n+1} \approx \frac{\partial \overline{w}}{\partial t}^n$ . This provides an initial condition for the Newton procedure’s corrector passes in Eq. (5.25).

At each time level, the iterative solution procedure must then be engaged. First,  $\frac{\partial \mathcal{R}_w(a_i^p)}{\partial a_j}$  and  $\mathcal{R}_w(a_i^p)$  are constructed. This is done by first assembling their respective Galerkin term contributions, before forward passes of the ANN evaluate  $\hat{I}$  to complete the linear system Eq. (5.25a). Eq. (5.25a) itself is solved with an iterative General Minimised Residual (GMRES) method. This Krylov subspace method is attractive because it guarantees minimisation of the linear system’s residual (not to be confused with the weak residual) in the  $L_2$  norm and scales better than direct solvers for very large linear systems [141]. Although the systems encountered in this work never exceed  $O(10^2) \times O(10^2)$  degrees of freedom, sizes for which direct methods are generally faster, the iterative method is retained in case the computation would be scaled. The method’s optimality obligates storing a growing number of residual vectors in memory. To contain this memory growth, the Krylov space is limited to 50 vectors. The system solve itself is allowed to run at most 100 iterations. However, it never encounters this limit for any cases in this study and converges to the specified tolerance on the residual’s  $L_2$  norm of  $10^{-10}$ . Potential preconditioning of the method is discussed in Section 5.5.4.

Finally, solution amplitudes are updated. Unless the  $L_2$  norm of the weak residual vector  $\|\mathcal{R}_{w_i}\|_2$  has converged to the relatively strict tolerance of  $10^{-10}$ , another corrector pass is taken in which the above assemblies and system solves must be performed again. When convergence is reached, the time level is finally updated and the entire procedure repeated.

### 5.5.2. Weak Residual Assembly

The weak residual vector  $\mathcal{R}_{w_i}$  is assembled within another `DomainIntegrator` object. However, while it features similar loops over elements and integration points as the method that solves the identification problem, several aspects of the weak residual assembly are different. These are covered here, aided by Algorithm 1.

---

#### Algorithm 1 Weak Residual Assembly

---

```

1: for  $i=0,1,\dots,n_{el}-1$  do ▷ Element loop
2:   Prepare local element and element vector
3:   if  $i=0$  then
4:     Assemble global strong residual vector  $\overline{\mathcal{R}}_{s,I_i}$ 
5:     for  $ip=0,1,\dots,n_{IP}-1$  do ▷ Integration point loop
6:       Load current guess of  $\overline{w}$ ,  $\frac{\partial \overline{w}}{\partial t}$  and known  $f$ 
7:       Add IP contribution to Galerkin terms of  $\mathcal{R}_{w_i}$ 
8:       if  $\hat{I}_\tau$  are needed then
9:         Add IP contribution to  $\hat{I}_{\tau,i}$ 
10:      if  $sgsType=exact$  then ▷ Unresolved scales model
11:        Add exact  $I_i$  from getURTerms to  $\mathcal{R}_{w_i}$ 
12:      else if  $sgsType=algebraic$  then
13:        Add  $\hat{I}_{\tau,i}$  to  $\mathcal{R}_{w_i}$ 
14:      else if  $sgsType=ANN$  then
15:        Assemble input feature vector from chosen FS
16:        Evaluate ANN
17:        Add ANN  $\hat{I}_i$  to  $\mathcal{R}_{w_i}$ 
18:      Store  $\hat{I}_i$ ,  $\overline{w}$ 

```

---

The routine’s loop over elements begins by transforming the weak forms to a master element, on which the assembly is performed [111]. This is not strictly necessary and does not add much benefit when solving 1D problems on a structured grid, but will be advantageous for higher-dimensional problems that might operate on unstructured grids. Therefore, this “isoparametric” implementation is maintained.

The Galerkin terms are assembled using the quadrature scheme outlined in Section 5.3.1. While the iden-

tification problem required a high number of IPs to ensure that the highly fluctuating interaction terms' integrals were well-predicted, here it is sufficient to use 3 IPs. This reflects that the polynomials that must be spatially integrated in this work are quadratics: They are products of linear basis functions,  $(\bar{\psi}, \frac{\partial \bar{w}}{\partial t})$ , and products of a linear basis function's derivative and a linear basis function squared,  $(\frac{\partial \bar{\psi}}{\partial z}, \bar{w}^2)$ .

The interaction terms are added after the quadrature loop, since they are direct predictions from the ANN. Therefore, they do not contribute to the quadrature or its integration order. This is potentially advantageous, since the quadrature can be a time-consuming element of the solution procedure of several classes of problems [218] and in higher dimensions. However, as forward passes of the ANNs demand the evaluation of several matrix-vector products, this will in fact render the assembly more expensive in cases where large ANN architectures are employed. This is further discussed in Section 9.4.

The interaction terms are processed in three stages. First, the necessary data to construct a feature set is gleaned from the integration database or constructed in position. Integrated strong residuals are globally computed before an element loop and are thus stored in memory, while solution amplitudes and their derivatives are accessed from pointers to their underlying solution vectors. Features that additionally require the evaluation of an algebraic unresolved scales model, such as those in FS4, require quadrature. They are therefore assembled in the IP loop and are computed and stored locally, i.e. in the current and previous element in a loop. Feature sets FS2-4 require information from two previous time levels to evaluate the ANN. As this data is not yet accessible in the first two time steps of a simulation, the routine bypasses the ANN evaluation for the interaction terms until the third time step. Instead, exact interaction terms are used from a corresponding `getURTerms` simulation, which pre-runs the forward problem simulation.

Second, the ANN is evaluated by accessing a custom `SubModel` class that is described in Section 5.5.3. Finally, this makes the interaction terms available, which are added to the relevant index in the element vector. As for the identification problem, this is done somewhat differently from what is conventional: Fully integrated weak forms are added to a single row in the weak residual vector, rather than element contributions to each of the rows in the residual vector that are non-zero within an element.

While the `DomainIntegrator` is primarily written to embed direct ANN predictions of the interaction terms, three other versions of the interaction terms can be added within the framework. First, as alluded to above, exact terms from pre-run `getURTerms` simulations can be included for verification purposes. Second, algebraic estimates of the spatial interaction terms can be separately constructed and added in similar fashion. Finally, explicit ANN models as well as hybrid models that switch between algebraic and ANN closure online are implemented; these will be discussed in more detail in Section 8.3.6 and Section 8.3.7, respectively. The `DomainIntegrator` is finalised by several storage routines that facilitate the post-processing of predicted  $\hat{I}$ ,  $\mathcal{R}_w$  and  $\bar{w}$ .

The implementation is again verified with the manufactured solution problem, reduced to very few degrees of freedom. At least two such degrees of freedom are required to separately test the handling of either boundary condition. Simultaneously, this number is sufficiently low that it is cheap to evaluate  $\|\mathcal{R}_w\|_2$  over a grid of the two unknown amplitudes  $a_1$  and  $a_2$  that can be visualised on a response surface. Three such response surfaces are shown in Fig. 5.15. They are constructed with exact interaction terms from the `getURTerms` simulation and the weak residual assembly routine outlined above. It is assumed for these response surfaces that the time derivative component of  $\mathcal{R}_w$  is constructed with an implicit Euler scheme, i.e.:

$$\frac{\partial \bar{w}}{\partial t} \approx \frac{\bar{w}^{n+1} - \bar{w}^n}{\Delta t} \quad (5.26)$$

Where the implicitness of the scheme with respect to the unknown  $\bar{w}^{n+1}$  is inherent to the predictor-corrector framework outlined at the start of this section.

Three notable conclusions can be drawn from Fig. 5.15. First, with the exact interaction terms in the vector,  $\|\mathcal{R}_w\|_2$  only has a single root over the ranges of  $a_1$  and  $a_2$  considered here, resulting in a map around this state. Second, this root is reached at a combination of  $a_1$  and  $a_2$  that corresponds exactly to the known, exact values of the manufactured solution, at three separate time steps that approximately span the amplitude range of the manufactured solution. This confirms the implementation of the weak residual assembly framework. Finally, this also completes the verification of the identification problem discussed in Section 5.3.2, which is here shown to predict interaction terms that reconstruct the manufactured solution exactly.

Clearly, the above verification only applies to the implementation of the general assembly routine and not yet to that of the ANN. These aspects of the code are, however, verified with the remainder of the ANN implementation in Section 5.5.3.

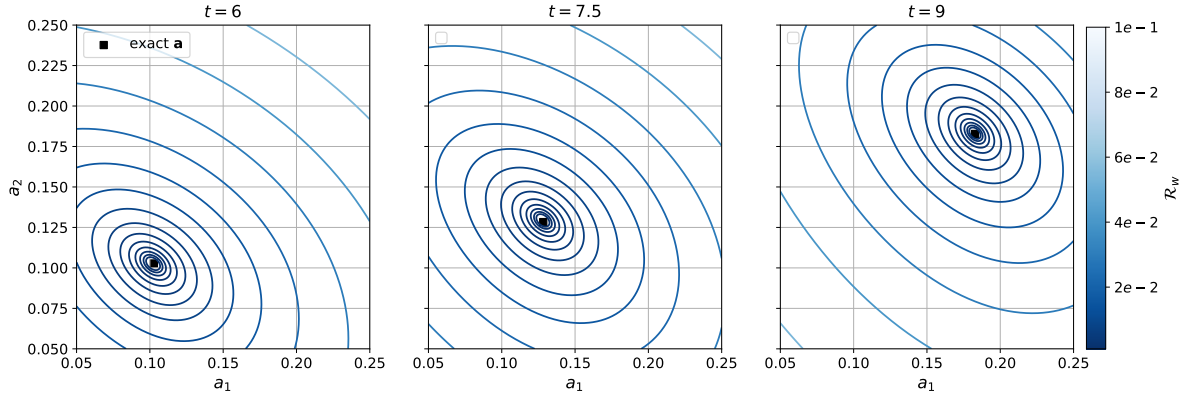


Figure 5.15: Contours of  $\|\mathcal{R}_w\|_2$  over a range of its two degrees of freedom  $a_1$  and  $a_2$  at time levels  $t = 6$ ,  $t = 7.5$  and  $t = 9$ , approximating the extents of the manufacture solution's amplitude. The exact values of  $a_1$  and  $a_2$  of the manufactured solution are denoted by a square.

### 5.5.3. ANN Evaluation

Since no online training of the ANN is performed, only forward ANN passes need to be evaluated for the forward problem. Interesting C++ libraries exist that specialise in forward evaluations of Keras models (e.g. [3]). However, to bypass the maintenance associated with rapidly updating external libraries, it is chosen to implement the forward passes of the ANN internally in Mex.

This is done in a dedicated `SubModel` class, which loads a trained and stored ANN's activation function, shape, normalisation parameters, weight matrices and bias vectors at the outset of a Mex run. Its evaluation function is called during assembly of the weak residual and Jacobian. The function normalises the input features and passes them through the network layers. In each layer, the activation is computed by i) multiplying a weight matrix and an input vector and ii) adding a bias vector. Activation functions, which are included as class methods, translate the activations to inputs to the next layer. Finally, the output is denormalised. If desired, it can then be limited to specified ranges (see Section 8.3.3). The procedure is recapped in Algorithm 2.

---

#### Algorithm 2 ANN Evaluation

---

- 1: Normalise input features  $x_i^0$
  - 2: **if** Limited **then**
  - 3:   Limit input
  - 4: **for**  $n=0,1,\dots,n_{l_{yrs}}-1$  **do**
  - 5:   Evaluate  $z_i^{n+1} = \omega_{ij}^{n+1} x_j^n + b_i^{n+1}$
  - 6:   Pass through activation function  $x_i^{n+1} = a(z_i^{n+1})$
  - 7: **if** Limited **then**
  - 8:   Limit output
  - 9: Denormalise output
- 

The ANN evaluation is verified for each feature set. By pushing the same known features through a verified Keras ANN and the implementation discussed here, Table 5.4 emerges. The errors in this table are on average  $O(10^{-7})$ , which is considered sufficient here for accepting the model as verified.

Feature set	$\left(\overline{\psi}, \frac{\partial w'}{\partial t}\right)_\Omega$		$\left(\frac{\partial \overline{\psi}}{\partial z}, 2\overline{w}w'\right)_\Omega$		$\left(\frac{\partial \overline{\psi}}{\partial z}, w'^2\right)_\Omega$	
	Keras	Mex	Keras	Mex	Keras	Mex
FS1	$1.82094 \cdot 10^{-3}$	$1.82095 \cdot 10^{-3}$	$2.82051 \cdot 10^{-3}$	$2.82050 \cdot 10^{-3}$	$2.32685 \cdot 10^{-6}$	$2.32795 \cdot 10^{-6}$
FS2	$1.81692 \cdot 10^{-3}$	$1.81694 \cdot 10^{-3}$	$2.82273 \cdot 10^{-3}$	$2.82272 \cdot 10^{-3}$	$2.34188 \cdot 10^{-6}$	$2.35256 \cdot 10^{-6}$
FS3	$3.19377 \cdot 10^{-3}$	$3.19378 \cdot 10^{-3}$	$6.32167 \cdot 10^{-3}$	$6.32166 \cdot 10^{-3}$	$7.94026 \cdot 10^{-6}$	$7.95026 \cdot 10^{-6}$
FS4	$1.45625 \cdot 10^{-4}$	$1.45625 \cdot 10^{-4}$	$6.65156 \cdot 10^{-4}$	$6.65148 \cdot 10^{-4}$	$8.7817 \cdot 10^{-6}$	$8.7854 \cdot 10^{-6}$

Table 5.4: Denormalised output of an ANN evaluated in Keras and Mex, for randomly chosen samples of each feature set.

### 5.5.4. Jacobian Assembly

The implementation of the weak residual must naturally be an exact representation of the problem one intends to solve. In contrast, the Jacobian  $\frac{\partial \mathcal{R}_{w_i}}{\partial a_j}$  in most cases only needs to be approximated, since every CP estimates  $\Delta a_i$  and not  $a_i$  itself. The weak residuals of many traditional VMMs for the Navier-Stokes equations and Burgers' problems are commonly at most quadratic in their unknowns (see Eq. (5.23)), since their unresolved scales models are also frequently at most quadratic [226]. More complex models possess added nonlinearity [238], but all these models are sufficiently smooth that the Newton procedure Eq. (5.25) usually converges in very few iterations, even with rough approximations of the Jacobian that are infrequently updated. As Jacobian assembly is at least as expensive as assembling the weak residual, it is then justifiable to subject the linear GMRES solver to an expensive ILU preconditioner, such that subsequent linear system solves are cheap [141, 224] and the overall Newton procedure takes less computation time.

However, Section 8.1 will identify that including highly nonlinear ANNs may make  $\mathcal{R}_{w_i}$  a much more complicated function of its degrees of freedom, for which the Jacobian must be accurate and updated frequently to successfully navigate  $\bar{w}$  through the nonlinear space. In the interest of attempting to find these correct solutions, higher-fidelity estimates of the Jacobian that are frequently updated are investigated here. Therefore, it is also not justified to apply preconditioning.

The Jacobian of the Burgers' problem is written out in Eq. (5.27):

$$\frac{\partial \mathcal{R}_{w_i}}{\partial a_j} = \left( \bar{\psi}_i, \frac{\partial}{\partial a_j} \left( \frac{\partial \bar{w}}{\partial t} \right) \right)_{\Omega} - \left( \frac{\partial \bar{\psi}_i}{\partial z}, \frac{\partial}{\partial a_j} (\bar{w}^2) \right)_{\Omega} + \frac{\partial}{\partial a_j} \left( \left( \bar{\psi}_i, \frac{\partial w'}{\partial t} \right)_{\Omega} \right) - \frac{\partial}{\partial a_j} \left( \left( \frac{\partial \bar{\psi}_i}{\partial z}, 2\bar{w}w' \right)_{\Omega} \right) - \frac{\partial}{\partial a_j} \left( \left( \frac{\partial \bar{\psi}_i}{\partial z}, w'^2 \right)_{\Omega} \right) \quad (5.27a)$$

$$\bar{w} = \sum_{j=0}^{n_{wf}} \bar{\psi}_j a_j \quad (5.27b)$$

The locality of the bases employed in this study ensures that only two weighting functions  $\bar{\psi}$  are non-zero in every element, such that two weak equation tests ( $n_{eq} = 2$ ) differentiated to two unknown  $a$  in every element ( $n_{wf} = 2$ ) contribute to the global matrix. Therefore, a  $2 \times 2$  element matrix must be assembled in every element, which can be inserted into the global system in an overlapping fashion. An algorithmic outline that describes this implementation is included in Appendix C.2.

Once again, the Galerkin terms and interaction terms require different treatment. Whereas the Jacobian contributions of the Galerkin terms can be directly estimated, those from the unresolved scales cannot, due to their dependence on an unknown  $w'$ . Here, two levels of complexity in the Jacobian estimate of the interaction terms are considered. The first is a simplified version of the derivatives of the interaction terms from the algebraic unresolved scales model described in Section 5.5.6. It is defined by Eq. (5.28).

$$\frac{\partial}{\partial a_j} \left( \left( \bar{\psi}_i, \frac{\partial w'}{\partial t} \right)_{\Omega} \right) \approx 0 \quad (5.28a)$$

$$\frac{\partial}{\partial a_j} \left( \left( \frac{\partial \bar{\psi}_i}{\partial z}, 2\bar{w}w' \right)_{\Omega} \right) \approx - \left( \frac{\partial \bar{\psi}_i}{\partial z}, 2 \frac{\partial \bar{w}}{\partial a_j} \tau \bar{\mathcal{R}}_s \right)_{\Omega} - \left( \frac{\partial \bar{\psi}_i}{\partial z}, 2\bar{w}\tau \frac{\partial \bar{\mathcal{R}}_s}{\partial a_j} \right)_{\Omega} \quad (5.28b)$$

$$\frac{\partial}{\partial a_j} \left( \left( \frac{\partial \bar{\psi}_i}{\partial z}, w'^2 \right)_{\Omega} \right) \approx \left( \frac{\partial \bar{\psi}_i}{\partial z}, 2\tau \bar{\mathcal{R}}_s \frac{\partial \bar{\mathcal{R}}_s}{\partial a_j} \right)_{\Omega} \quad (5.28c)$$

$$\frac{\partial \bar{\mathcal{R}}_s}{\partial a_j} = \frac{\partial}{\partial a_j} \left( \frac{\partial \bar{w}}{\partial t} + \frac{\partial \bar{w}^2}{\partial z} \right) \quad (5.28d)$$

Where the three main assumptions are that i) the contribution from  $\left( \bar{\psi}_i, \frac{\partial w'}{\partial t} \right)_{\Omega}$  is zero, since it is neglected by the traditional algebraic model, ii) the algebraic model provides a reasonable approximation to the convective unresolved scales projections and iii) the dependence of  $\tau$  on  $\bar{w}$  is sufficiently insignificant that it can be ignored.

A more commensurate Jacobian approximation for ANN interaction term models can be constructed by differentiating the ANN's output with respect to its relevant inputs:  $\frac{\partial \hat{I}}{\partial a_j}$ . Such an approximation would include a model for the time derivative and benefit from the potentially improved accuracy of the ANN's estimate for the interaction terms.

$\frac{\partial \hat{I}}{\partial a_j}$  can be computed for all implicit feature sets in Table 5.2. Sampling  $\overline{w}^{n+1}$  and  $\frac{\partial \overline{w}^{n+1}}{\partial t}$  at the element boundaries (where  $\psi = 1$ ) directly reduces them to the desired  $a$  and  $\frac{\partial a}{\partial t}$ . Computing  $\frac{\partial \overline{\mathcal{R}}_{s_i}}{\partial a_j}$  is somewhat more involved. Its assembly is therefore defined in algorithmic form (see Algorithm 4 in Appendix C.2), though it can still be compiled. Hence, a direct functional relationship exists between  $\hat{I}$  and the features of this study, paving the way for computing  $\frac{\partial \hat{I}}{\partial a_j}$ . The explicit feature set is reconsidered in Section 8.3.6.

As the ANNs considered here are continuous, differentiable functions of their input variables<sup>3</sup>,  $\frac{\partial \hat{I}}{\partial a_j}$  could in theory be computed by automatic differentiation [20]. However, not many C++ frameworks for automatic differentiation of a specified ANN exist. Furthermore, it would be nontrivial to couple these frameworks to Mex. Hence, it is likely that that an automatic differentiation procedure would have to be implemented. Although such an implementation is relatively straightforward (it comes close to backpropagation), it would require a finite difference counterpart to be available for verification. Therefore, this study has taken the finite difference approach to computing  $\frac{\partial \hat{I}}{\partial a_j}$ , although this option is clearly less satisfying.

The implementation of this Jacobian requires several steps of rather involved methodology that do not contribute to the present discussion. Hence, the interested reader is referred to Appendix C.2 for a more detailed outline of the algorithm.

Verification of the algorithm is conducted in two stages. First, perturbed variables are hand-checked on their correctness. Second, the Jacobian implementation itself can be checked by comparing the predicted finite difference approximations for  $\frac{\partial \hat{I}}{\partial a_j}$  to finite differences based on the weak residual assembly, which was outlined and verified in Section 5.5.2. These reference finite differences can be constructed by perturbing the relevant input  $a_i$  to the weak residual assembly routine. The approach is cumbersome and manual, and is therefore carried out only at a few points. The results at one of these points is presented in Table 5.5.

Element	Jacobian term	Assembly routine result	Perturbed $\mathcal{R}_w$ result
	$\frac{\partial}{\partial a_1}(\hat{I}_1)$	0.060185	0.060195
	$\frac{\partial}{\partial a_2}(\hat{I}_1)$	0.189449	0.188754
	$\frac{\partial}{\partial a_1}(\hat{I}_2)$	-0.118429	-0.118517

Table 5.5: Finite difference approximations of the element Jacobian terms in the second element of a 3-element implementation of the manufactured solution from the point  $a_1 = a_2 = 0.17965$ .  $\Delta t = 2$ ,  $h = \frac{1}{3}$  and  $\delta a = 1 \cdot 10^{-5}$

The table shows that the results agree up to  $O(10^{-3})$ . This is considered sufficient to proceed. Note that adding unconstrained terms from the ANNs to the Jacobian has the potential to negatively affect its conditioning. Still, no adverse impact from this was experienced in this study.

### 5.5.5. Time Marching

The last module that is modified for this work is the time march. Three algorithms are considered. The first of these is a Generalised Alpha (GA) scheme for the Navier-Stokes equations [45, 114]. It is formulated to achieve second-order accuracy with an adjustable amplification factor for high-frequency modes, such that these can be damped at will. However, it does so by carrying out the iterative solution procedure for a time step's degrees of freedom at an intermediate level  $t^{n+\alpha_f}$  and their time derivatives at  $t^{n+\alpha_m}$ . In the framework put forward here, this would require the prediction of "wrong" interaction terms at these time levels that only become correct once they are transformed to  $t^{n+1}$ . This is both questionable practice and unclear. Hence, in the interest of maintaining clarity in the approach, time stepping schemes that require intermediate time levels (including Runge-Kutta schemes) are left out from the study.

Rather, two backwards finite difference stencils are implemented. The first is the implicit Euler scheme presented in Eq. (5.26). However, as this scheme is first order and highly dissipative [111], it is found insuf-

<sup>3</sup> Technically, this is not true when discontinuous activation functions such as ReLUs are employed. For these functions,  $\frac{\partial a}{\partial x}(x=0)$  is undefined (see Eq. (5.17)). However, this is commonly overcome by assuming  $\frac{\partial a}{\partial x}(x=0) = 0$ , which turns out to have surprisingly little practical impact [81].

ficient for simulations with practically useful time steps. It is therefore only used here to initialise a Second Order Backwards (SOB) scheme:

$$\frac{\partial \bar{w}}{\partial t} \approx \frac{3\bar{w}^{n+1} - 4\bar{w}^n + \bar{w}^{n-1}}{2\Delta t} \quad (5.29)$$

All these time marches are monolithic and do not exploit the structure of the equations. The implementation of a Poisson solver might therefore feature in extensions of the framework to multiple dimensions, though it is not considered for the simple Burgers' problem.

To aid convergence in the presence of strong nonlinearities, an adaptive relaxation scheme has been implemented [11, 219]. This is described in some detail in Appendix C.3. The full implementation of the SOB time march is summarised in Algorithm 3.

---

**Algorithm 3** Time March
 

---

```

1: for n=0,1,...,n $\Delta$ t do ▷ Time loop
2:   if n <= 1 then
3:     Set time march coefficients to implicit Euler
4:   else
5:     Set time march coefficients to SOB
6:   Update  $\bar{w}^n, \bar{w}^{n-1}$ 
7:   "Same" predictor for  $\bar{w}^{n+1}, \frac{\partial \bar{w}}{\partial t}^{n+1}$ 
8:   while  $\|\Delta a_i\|_2 < \text{tol}$  do
9:     Update  $\frac{\partial \mathcal{R}_{w_i}}{\partial a_j}$  and  $\mathcal{R}_{w_i}$ 
10:    Solve for  $\Delta a_i$ 
11:    Compute relaxation parameter  $\lambda_r$ 
12:    Update  $\bar{w}^{n+1}, \frac{\partial \bar{w}}{\partial t}^{n+1}$ 

```

---

It is straightforward to verify the implementation of the time march, as it can be directly subjected to an order of accuracy test with the manufactured solution. It is tested with the algebraic unresolved scales model elaborated on in Section 5.5.6, which is known to behave consistently [226]. This results in Fig. 5.16, where the first order convergence of the implicit Euler scheme and the second order convergence of the SOB scheme are shown alongside the GA scheme's convergence.

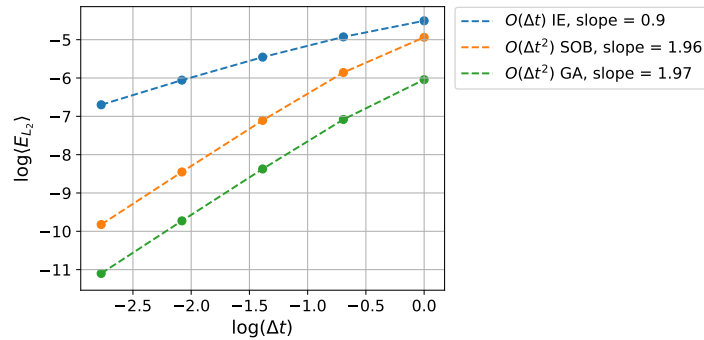


Figure 5.16: Order of accuracy test for the Implicit Euler (IE), Second Order Backwards (SOB) and Generalised Alpha (GA) time marches with the manufactured solution described in Section 4.4.

The GA scheme displays impressive error performance, even compared to the SOB scheme. The first order scheme is also verified, allowing its use as a startup method for the second order time march.

### 5.5.6. Reference solutions

In the following chapters, the VMM-ANN will be frequently compared to two VMMs with other unresolved scales models: An exact model for the interaction terms and an algebraic model. The exact model is attained by running the entire forward simulation with the exact interaction terms from the identification problem. This returns piecewise linear, nodally exact versions of  $w$  and, in a single column, corresponding vertical

statistics  $\langle w^2 \rangle$ . Spatial distributions of these quantities for the Boussinesq-forced Burgers' problem are shown in Fig. 5.17a for various  $h$ . It is the first clear illustration in this work of the ideas put forward in Chapter 3: While coarser resolutions result in less capture of detail, the structure of large, resolved scales might still be represented very accurately *if* the interaction terms can be represented exactly.

To facilitate comparisons against state of the art approximations of the interaction terms, a conventional algebraic unresolved scales model will be used. Its  $\tau$  is the nonlinear algebraic unresolved scales model proposed by Taylor, Hughes and Zarinis for the Navier-Stokes equations [238]. Here, it is reduced to apply only to the Burgers' problem:

$$w' = -\tau \overline{\mathcal{R}}_s \quad (5.30a)$$

$$\tau = \frac{1}{(2J_t^{-1} \overline{w})^2 + \left(\frac{2}{\Delta t}\right)^2} \quad (5.30b)$$

$J_t^{-1} = \frac{\partial \xi}{\partial z} = h^{-1}$  is the inverse Jacobian of the isoparametric finite element transformation from global coordinates  $z$  to the assembly's master element's coordinates  $\xi$  [111, 197]. The model is in this context essentially a modification of Shakib's original proposal [226] for problems where  $\text{Re} \rightarrow \infty$ , which informally and incompletely attempts to account for the time discretisation [52]. Eq. (5.30) is also the algebraic model that was used to verify the time marches in Section 5.5.5, and the model that will be used to compute the simple Jacobian presented in Section 5.5.4.

Using this algebraic model as the closure for the Boussinesq-forced Burgers' problem results in the set of solutions and statistics presented in Fig. 5.17b. The figure demonstrates that while such models can almost exactly reproduce the DNS statistics of the problem up to  $\frac{h}{h_{DNS}} = 3$ , linearised Green's function approximations increasingly break down as the scales of unresolved turbulence become increasingly large. Addressing these aspects is the VMM-ANN's aim.

Finally, the VMM-ANN would ideally be compared against SP-like simulations, to assess the potential of scale-consistent unresolved scales models with respect to models that introduce explicit scale breaks. However, the scope of implementing such a SP falls outside this work. The focus will rather lie with the performance of the model within the spectrum of the VMS framework, before extending the analyses.

### 5.5.7. Verification of full VMM-ANN

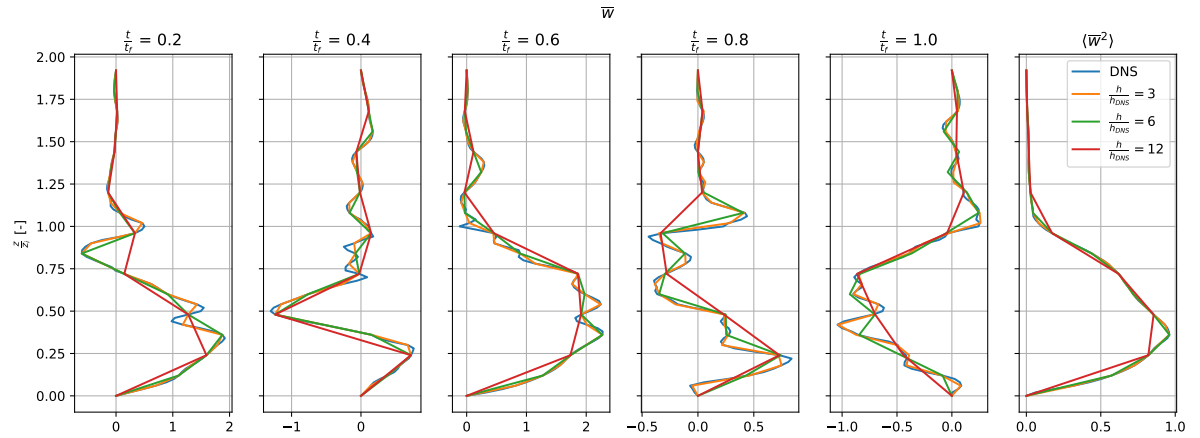
With all individual modules of the forward simulation explained and verified, it is possible to verify the complete model. This will be done in this section, using the manufactured solution problem. If the near-perfect ANN presented in Section 5.4.5 is employed to predict  $\hat{I}$  for a forward problem with the same discretisation as it was trained on, and the ANN implementation is correct, it can be expected to return very close to nodally exact representations of the solution. This must again be treated only as a verification and says nothing about ANN's ability to generalise to other problems. Space-time plots of the forward problem's predictions of  $\overline{w}$  and the interaction terms that underpin it are shown in Fig. 5.18, with measures of absolute ( $E_{L_2}$ ) and relative ( $1 - R^2$ ) error of the quantities compared to offline predictions included in Table 5.6.

Table 5.6 shows that in terms of the average  $L_2$  error  $E_{L_2}$  and  $R^2$ , the forward, "online" predictions of the interaction terms are nearly as good as their "offline" counterparts presented in Section 5.4.5. This results in impressively small errors in the predicted  $\overline{w}$ , verifying the ability of the VMM-ANN to predict  $\hat{I}$  and  $\overline{w}$  for this simple problem.

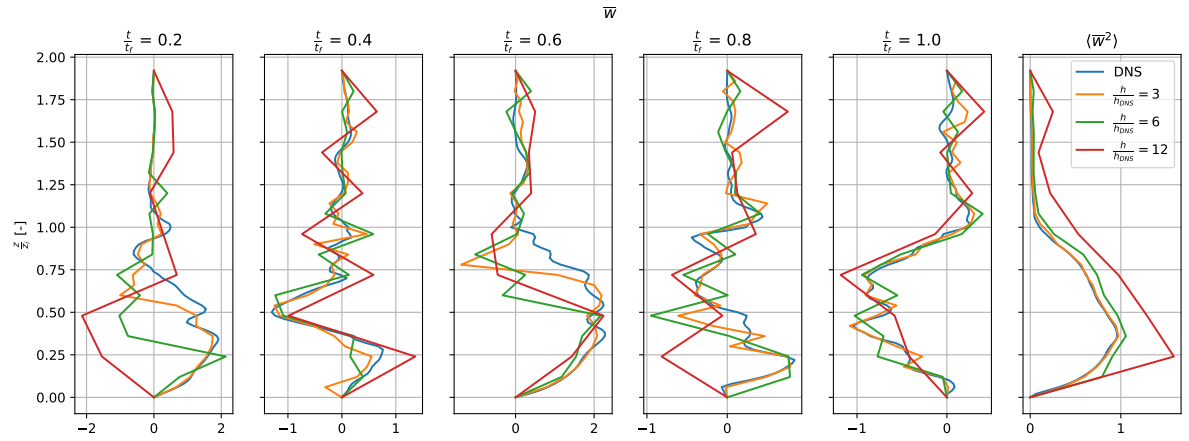
This is visually corroborated by Fig. 5.18; it shows how the oscillating solutions of the problem can be faithfully reproduced. The small errors that do occur manifest themselves around the extrema of the solution, where the ANNs are often operating in a range where they have little data to interpolate on. However, they almost always recover in a subsequent time step. This error mode will be revisited in Section 8.2.

This confirms Robijns' finding that near-perfect ANN predictions of the interaction terms in an offline sense are capable of navigating the dynamic, iterative time march in which it is let loose here [209], at least for simple problems where the ANN is mostly required to interpolate in its training space. It maintains this skill over 120 time steps, yielding a promising point of departure for the relatively long turbulence simulations in upcoming chapters.

This concludes the methodology that underpins the VMM-ANN modelling framework and finally allows assessments to be made on its ability in the context of the research questions. This will be therefore be the topic of the last four chapters of this thesis.



(a) Exact interaction terms



(b) Interaction terms from algebraic model.

Figure 5.17: Discrete, instantaneous solutions of the Boussinesq-forced Burgers' problem at  $\frac{h}{h_{DNS}} = [3, 6, 12]$  and single-column time-averaged statistics. All runs are with  $\frac{\Delta t}{\Delta t_{DNS}} = 2$ ,  $t_f = 6$  hr and averaging is only over the last 5 hrs.

Term	Online		Offline	
	$1 - R^2$	$E_{L_2}$	$1 - R^2$	$E_{L_2}$
$\left(\bar{\psi}, \frac{\partial w'}{\partial t}\right)$	$2.28 \cdot 10^{-5}$	$6.58 \cdot 10^{-6}$	$4.78 \cdot 10^{-6}$	$3.16 \cdot 10^{-6}$
$\left(\frac{\partial \bar{\psi}}{\partial z}, 2\bar{w}w'\right)$	$2.55 \cdot 10^{-5}$	$2.08 \cdot 10^{-6}$	$6.40 \cdot 10^{-6}$	$2.58 \cdot 10^{-6}$
$\left(\frac{\partial \bar{\psi}}{\partial z}, w'^2\right)$	$4.07 \cdot 10^{-5}$	$3.87 \cdot 10^{-8}$	$8.87 \cdot 10^{-6}$	$2.75 \cdot 10^{-8}$
$\bar{w}$	$5.38 \cdot 10^{-6}$	$5.47 \cdot 10^{-5}$	-	-

Table 5.6:  $R^2$  coefficient of determination and  $E_{L_2}$  for online VMM-ANN predictions of the components of  $\hat{I}$  and  $\bar{w}$ , compared to their offline counterparts.

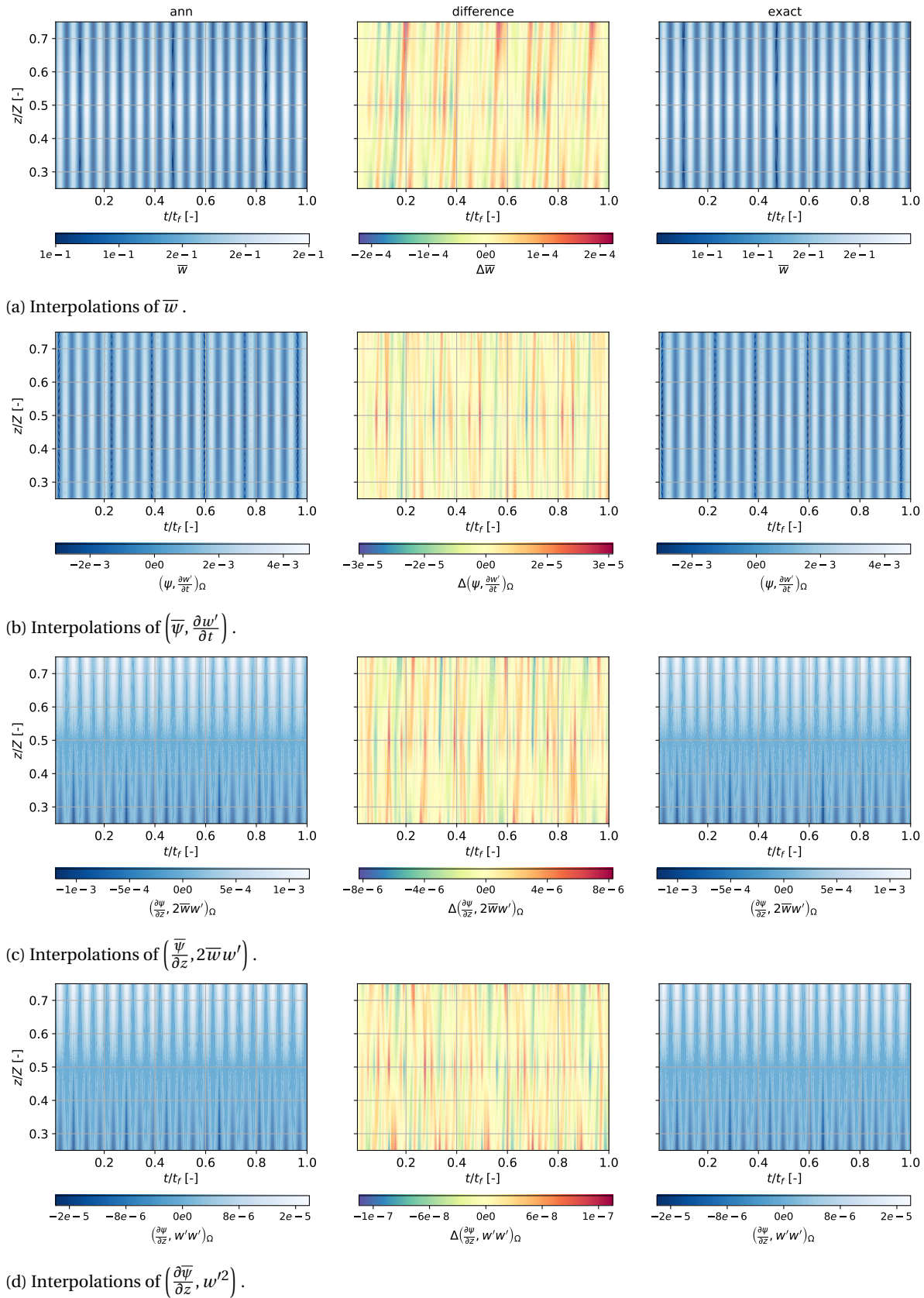


Figure 5.18: Space-time plots of the manufactured problem's solution and interaction terms predicted by the VMM-ANN (left), the exact model (right) and their difference (centre), for simulations where  $h = 0.25$ ,  $\Delta t = 1$ .



# 6

## Exact Projections of Interaction Terms

A rather uncommon feature of the developed framework is that it starts with a post-processing step of a high-fidelity simulation: Solving an identification problem for the interaction terms (see Section 5.3). In a broad sense, this allows visualising and analysing “exact” versions of these numerical constructions. While turbulent transfer decompositions in a multiscale sense have received plenty of attention in literature (see e.g. [108]), these numerical interaction terms have not. Therefore, their analysis might be interesting in its own right.

However, here the primary motivation for studying the interaction terms is to characterise their contributions to the resolved scales. This facilitates an assessment of the spatial distribution of the Galerkin and interaction terms, how the terms balance the momentum at various levels of discretisation, which scales in the problem define the unresolved scales projections and how the assumptions of traditional VMS and SP models hold up for the model problem. From these results, the study will establish the relevance of the model problem to the global problem and determine the discretisations where the relevance is most distinct. The analysis is conducted over the spatial dimension in Section 6.2 and in the spatial and temporal frequency domains in Section 6.3. The chapter starts, however, with a quick look at the energy spectra of the problem in Section 6.1.

### 6.1. Energy Spectra of the Model Problem

Section 2.1.2 showed that atmospheric turbulence at the resolution of a GCM is not associated with an inertial subrange in horizontal wavenumbers. In contrast, the model problem’s turbulence is in vertical wavenumbers of scales that are much smaller than those in Fig. 2.1. Therefore this model problem is expected to contain relatively few characteristics that translate directly to the richness of the Nastrom-Gage spectrum.

To investigate the model problem’s 1D spectrum, its distribution of turbulence kinetic energy  $E$  is computed through Eq. (2.2), by employing an energy-neutral Fourier transform<sup>1</sup> and plotted in Fig. 6.1 at different discretisation levels against spatial wavenumbers  $k_z$  and temporal wavenumbers  $k_t$ .

Since the vertical turbulence is anisotropic (as shown in Fig. 4.1), energy spectra of the atmospheric boundary layer with vertical wavenumbers are rather uncommon [43]. However, the spectrum’s upper end in Fig. 6.1a still decays with a  $-5/3$  exponent. It is tempting to note the similarity of this number to the Nastrom-Gage spectrum’s lower end, which similarly decays with this exponent. However, while that spectrum emerged in spite of significant anisotropy and a non-existent inertial range, the 3D boundary layer turbulence that underpins Fig. 6.1a’s distribution does contain an inertial range in the horizontal dimension [177], which is seen to transfer to the weakly anisotropic vertical dimension of this problem [195]. Hence, Fig. 6.1a appears to be much more in line with a traditional 1D instance of a Kolmogorov spectrum.

This is further illustrated by the second portion of the model problem’s spectrum, which decays rapidly. Rather than being a significant expression of anisotropy, such as the  $k^{-3}$  range in Fig. 2.1, this is a range where the velocity field becomes increasingly smooth, as energy is dissipated from its modes. There are

<sup>1</sup>By the application of Parseval’s theorem to the Discrete Fourier Transform (DFT),  $\sum_{n=0}^{N-1} (x(n))^2 = \frac{1}{N} \sum_{k=0}^{N-1} (X(k))^2$ , where  $X(k)$  is the Fourier transform of  $x(n)$  for a signal with length  $N$ . As  $N$  changes between discretisation levels, a consistent comparison of energy in equal modes at different discretisation will require energy to be conserved in the forward transform, and therefore scaling by  $\frac{1}{N}$  during this stage.

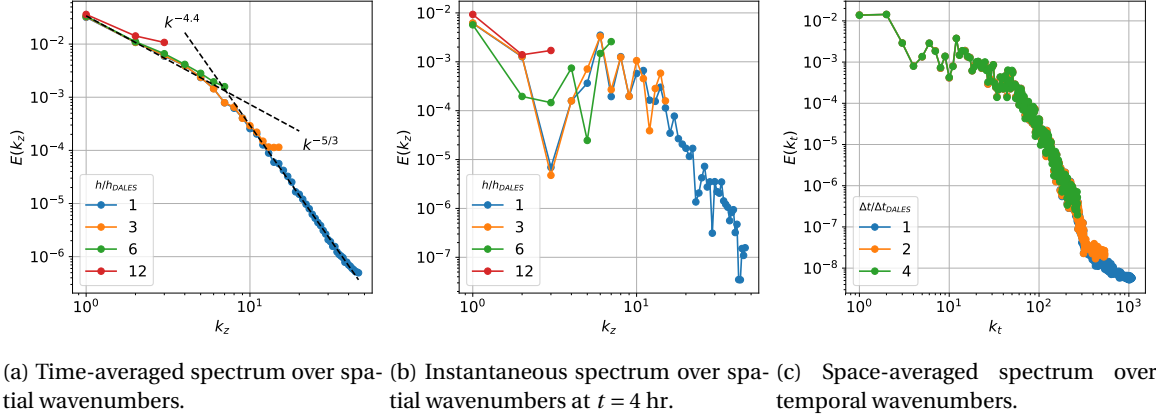


Figure 6.1: Discrete, averaged energy spectra of a single column of the forced Boussinesq problem for projections on grids that are 3, 6 and 12 times the vertical spacing of the DALES simulation and 2 and 4 times the time step of the DALES simulation. Note that increasingly coarse discretisations of the same DALES solution do not reproduce the same resolved Fourier modes, since the problem is not periodic.

two possible explanations for this. First, this could be a physical indication that the Kolmogorov scales are being approached at high resolution, which would yield spectra of similar shape [236]. However, because the data that constructs this spectrum derives from an LES run with an artificial viscosity closure, it is in fact much more likely a reflection of that model’s overambitious dissipation in its quest for stability [195, 229], and therefore not necessarily physical.

In all, this yields a spectrum that is not as shallow as other 1D tests commonly devised for testing prototype unresolved scales models for atmospheric motion [88, 160] and is therefore a kind first test. However, the test is still considered appropriate, as instantaneous snapshots of the flowfield, such as that presented in Fig. 6.1b do intermittently contain highly energetic, unresolved scales, which are seen to have an impact on the resolved scales. Such features do in fact translate to the larger-scale problem.

Hence, while conclusions based on this study’s model problem can clearly not be directly extrapolated to global, atmospheric turbulence, the simple problem does begin to capture several aspects that are relevant to the global problem. Therefore, this model problem is still considered an appropriate first test.

Based on these remarks, an interval of relevant scales is identified at which the ANNs should still proficiently learn the interaction terms and VMM-ANNs still successfully predict the solution from them: To be of any interest for physical turbulence-resolving models at large scale, discretisations that are cut off above the range of rapidly decaying energy must be considered. Spatial resolutions that are six times as coarse as the original DALES simulation begin meeting this criterion. Therefore, this discretisation will be considered the default test in the following chapters; it is the definition of a “coarse” discretisation promised in Section 3.6.

The temporal spectrum in Fig. 6.1c similarly consists of a relatively low number of large modes and a steep slope. However, as will be discussed in Chapter 8, there is no interesting scenario in which a discretisation coarser than four times the sampled DALES time step remains well-posed. While time discretisations that are at least another four times coarser are desired to begin approaching the energy plateau seen in Fig. 6.1c and mimic the more challenging situation faced by a GCM, this study employs time steps for which an appreciable range of the temporal spectrum remains resolved.

## 6.2. Time-Averaged Spatial Profiles of Exact Interaction Terms

Fig. 6.2 and Fig. 6.3 show time-averaged profiles of the  $L_2$  norms of the Galerkin and interaction terms at various levels of spatial and temporal discretisation, respectively. The terms have not been normalised by a convective velocity scale [236], as the illustration here is numerically oriented, rather than physical. This is also the rationale for plotting these somewhat unconventional quantities: They are the direct terms that participate in the simulations considered here, rather than more common representations of the turbulent fluxes discussed in Section 4.2.2. At coarser  $h$ , the individual weak form terms are integrals over increasingly large areas. However, the force term scales accordingly, such that the momentum budget remains exactly closed. Hence, although they show norms of the terms and not the terms themselves, the plots in essence illustrate how momentum is on average spatially redistributed among the terms as the discretisation changes.

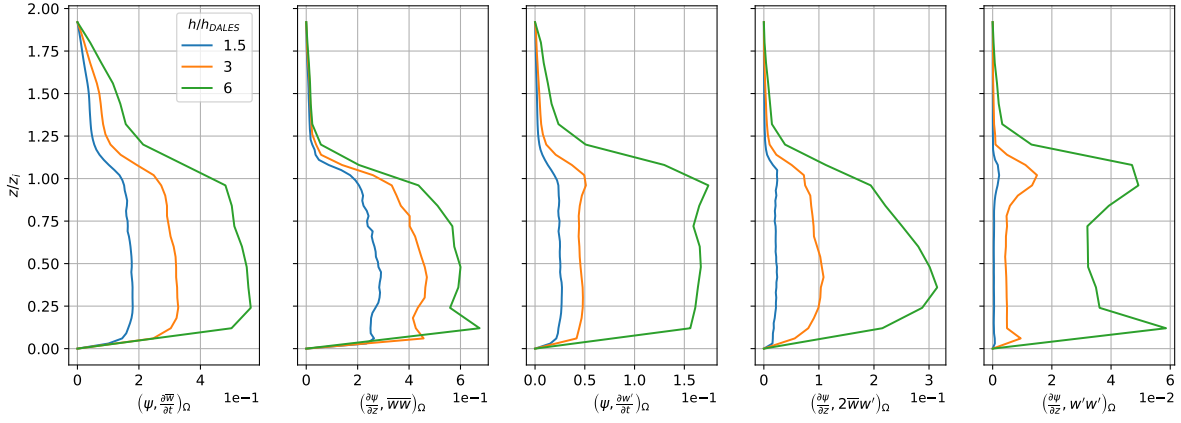


Figure 6.2: Spatial profiles of the squared weak form terms, averaged over 16 randomly sampled columns, varying with spatial discretisation  $h/h_{DALES}$ , at  $\Delta t/\Delta t_{DALES} = 2$ .

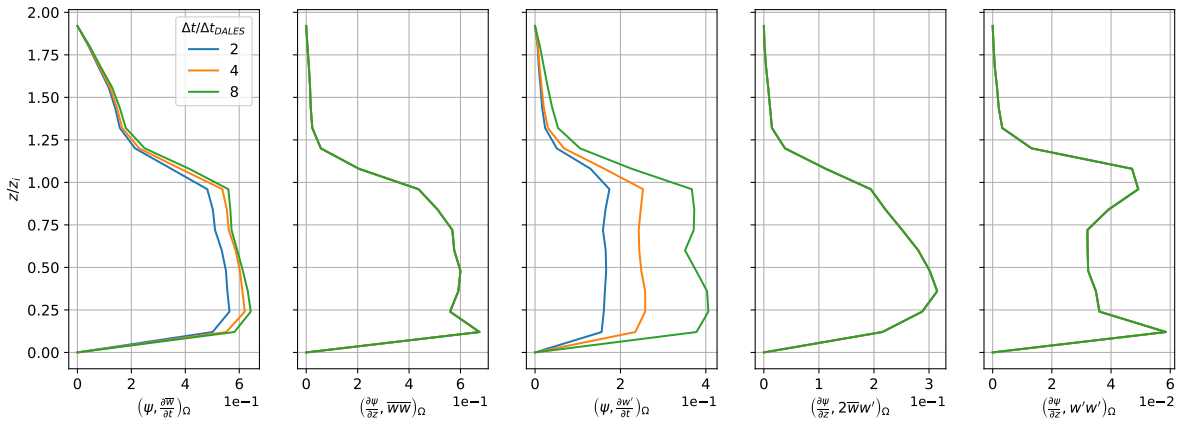


Figure 6.3: Spatial profiles of the squared weak form terms, averaged over 16 randomly sampled columns, varying with temporal discretisation  $\Delta t/\Delta t_{DALES}$ , at  $h/h_{DALES} = 6$ .

These profiles reveal several interesting characteristics of the various terms' roles in the simulation, that are instructive to ANN formulations for the interaction terms. Hence, they are all reviewed in this light in the following.

$\left(\overline{\psi}, \frac{\partial \overline{w}}{\partial t}\right)_{\Omega}$  This term contains a little less than half of the Galerkin terms' total amplitude at these discretisations. It represents the spatial projection of the evolution of resolved turbulent modes. As these are large modes, they are generally produced by the surface flux and dissipated only at the inversion. Hence, their time evolution's distribution is relatively constant throughout the mixed layer, only decaying a little throughout it. The term increases somewhat in magnitude as the spatial and temporal resolutions reduce, as its increased local integral width outweighs that a number of modes is cut from its resolved scales space.

$\left(\frac{\partial \overline{\psi}}{\partial z}, \overline{w}^2\right)_{\Omega}$  This term somewhat resembles term V in Eq. (4.3), if it is interpreted as a spatial redistribution operator of resolved  $\overline{w}$  with characteristic speed  $\overline{w}$ . Its magnitude profile does not follow the classical distribution of such terms, with a well-rounded shape and a distinct peak at  $\frac{z}{z_i} \approx 0.3$  [236]. This is because the term only contains resolved modes, leaving an increasingly significant portion of the spatial turbulent transfer in the layer's middle portion to the projection of the unresolved scales model at coarser  $h$ , which will be essential to capture to reproduce correct statistics of  $\overline{w}$ . Since it is not a function of the temporal discretisation, the term is unchanged as the time discretisation changes, as are the cross and Reynolds terms.

$\left(\overline{\psi}, \frac{\partial w'}{\partial t}\right)_\Omega$  This term expresses time changes in the unresolved scales that only exist on the resolved scales due the non-orthogonal nature of the scale decomposition (see Section 3.2.2 and Section 4.3.2). It is most active where the smallest scales in the simulation change and bears resemblance to its resolved-scales counterpart. At high spatial resolution, this does not have a distinct spatial structure; the term is relatively constant throughout the turbulent portion of the domain. As the simulation becomes coarser, however, it must recapture some of its Galerkin term's dropoff near the inversion, where small scales evolution matters [236]. This is in line with the general challenge of predicting inversions dominated by small scales at coarse resolution, of which Section 2.5.2 established the relevance to GCMs. The term also rapidly gains prominence as the time discretisation coarsens. In such situations, the assumptions that underpin non-dynamic VMS break down, and dynamic subscales methods must be considered. This is the case here and for GCMs, motivating the term's inclusion in the ANN model.

$\left(\frac{\partial \overline{\psi}}{\partial z}, 2\overline{w}w'\right)_\Omega$  The cross term constitutes the largest unresolved scales contribution to the budget at all discretisations considered here. Its role in the layer increases and changes as the spatial discretisation becomes increasingly coarse. It must then compensate for the resolved nonlinear term, which is limited to represent an increasingly narrow range of mode interactions. In particular, the cross term must capture direct interactions between modes above and below the grid cutoff. At large  $h$ , the magnitude of these interactions increase throughout the domain and especially in its lower third, yielding an increasingly full profile. This assigns a relatively substantial responsibility to the term to ensure the correct distribution of turbulence away from the wall.

$\left(\frac{\partial \overline{\psi}}{\partial z}, w'^2\right)_\Omega$  While being comparatively small throughout the domain, the Reynolds term has two interesting characteristics. First, it confirms the expectation that the resolved-scales projections of purely unresolved, small scales are most active at the turbulent boundaries [195, 236]: Most turbulent dissipation is expected to take place here, which in the presence of a net forward cascade of turbulent energy requires the smallest scales in the simulation to do this work. Second, as the smallest scales that drive this behaviour progressively live in the unresolved scales space as  $h$  increases, these contributions very rapidly become more substantial; they cannot be trivialised for accurate calculations at low resolution.

### 6.3. Averaged Distributions of Interaction Terms

While Fig. 6.2 and Fig. 6.3 provide insight into the terms' average spatial magnitudes, they do not say anything about their composition. Hence, their amplitudes' distribution over modes will be considered in this section. Fig. 6.4 and Fig. 6.5 show time-averaged spectral decompositions with  $k_z$  at various  $h$  and space-averaged spectral decompositions with  $k_t$  at various  $\Delta t$  of the terms, respectively. These decompositions are referred to here and in the following chapter as "distributions", to clarify that they arise from a discrete solution, rather than a continuous spectrum. They have been computed with an energy-conserving Fourier transform of the interaction terms, to again remain comparable at various levels of discretisation.

When plotted on the same amplitude scale, Fig. 6.4 shows that at all levels of discretisation, the majority of the budget's magnitude resides in the Galerkin terms: Their modal amplitudes are on average an order of magnitude larger than the interaction terms. The figure thus provides an illustration of the widely appreciated fact that most of the problem's energy can be captured on the resolved scales when the problem's energy spectrum is truncated in a rapidly decaying inertial range [195], such as that presented in Fig. 6.1a.

$\left(\overline{\psi}, \frac{\partial \overline{w}}{\partial t}\right)_\Omega$  This term's amplitudes are dominated by low spatial wavenumbers. As the term is intimately linked to  $\overline{w}$ , its distribution over spatial wavenumbers somewhat resembles Fig. 6.1a. It displays that large changes in  $\overline{w}$  in time are primarily driven by large, spatial structures in the flow, with the term dropping off quickly as  $k_z$  increases. At the highest spatial resolution considered, comparatively little amplitude is carried by the term's small, resolved scales. If like scales are most prone to interaction, this would suggest that the term experiences relatively little interaction with the unresolved scales. In other words, the resolved and unresolved scales are well-separated, and scale separation arguments could underpin models for the unresolved scales' impact on the term at this level of discretisation. For instance, doubling  $\frac{h}{h_{DALES}}$  from 1.5 to 3 merely increases  $\left(\overline{\psi}, \frac{\partial w'}{\partial t}\right)_\Omega$  by a factor 2.39 on average. This is mostly a reflection of the inte-

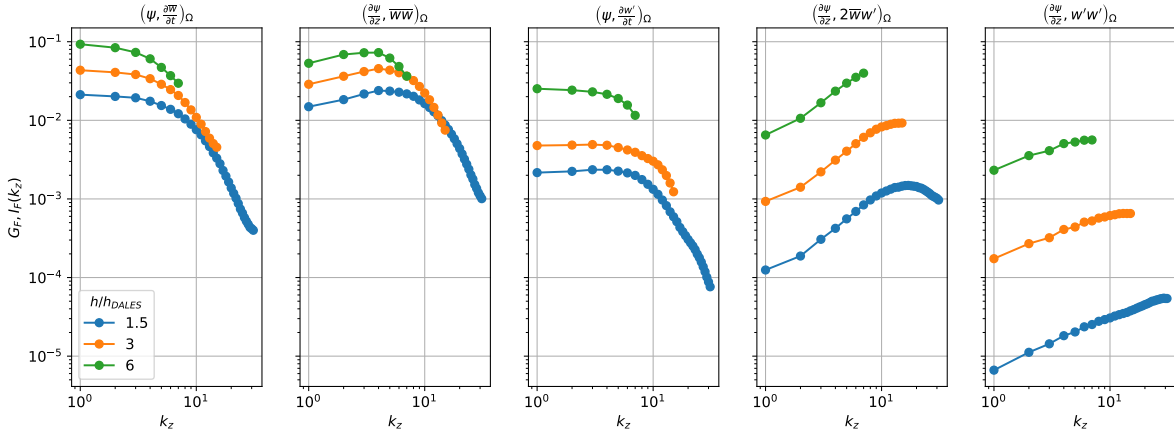


Figure 6.4: Temporally averaged modal decomposition of amplitudes of the Fourier-transformed Galerkin terms  $G_F$  and Interaction terms  $I_F$  over spatial wavenumbers, over the same number of columns as Fig. 6.2.

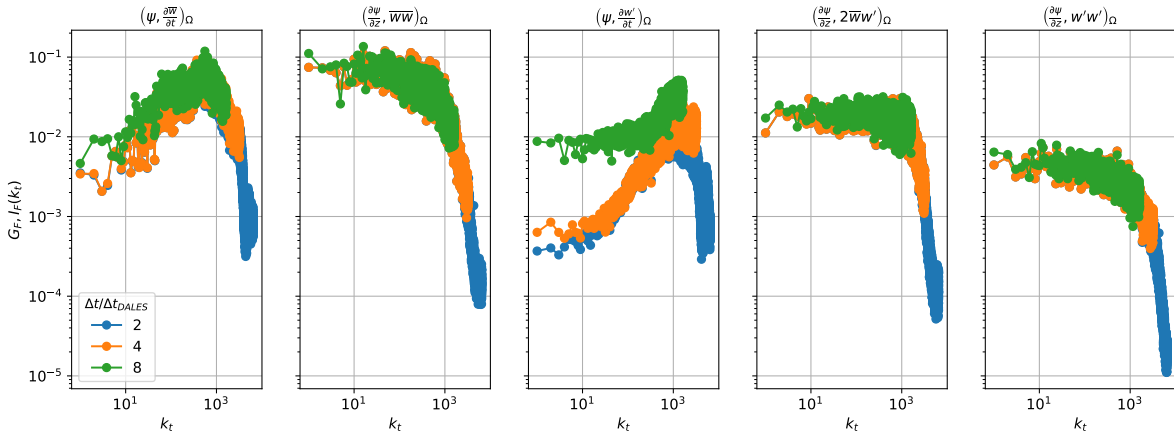


Figure 6.5: Spatially averaged modal decomposition of the amplitudes of the Fourier-transformed Galerkin terms  $G_F$  and interaction terms  $I_F$  over temporal wavenumbers, over the same number of columns as Fig. 6.3.

grals being evaluated over spatial domains that are twice their original size, and thus shows that not much of  $(\overline{\psi}, \frac{\partial \overline{w}}{\partial t})_\Omega$ 's amplitude is lost. However, further doubling  $h$  to a level at the top end of the rapidly energy-decaying range once again has a much larger impact (a factor of 4.49), as small resolved and large resolved modes are of more equal importance.

In the distribution over  $k_t$ , the term's role is much more significant at higher wavenumbers, before rapidly dropping off. As for the spectra in Section 6.1, this dropoff might indicate that they approach temporal scales that are so small that they physically begin dissipating energy into heat. However, it is more likely a numerical artefact, due to the necessity of sampling DALES data at 6 times its original time step ( $\Delta t_{DALES} = 6\Delta t_{DNS}$ ), and artificially smoothening the data with splines beyond this point. Hence, once the resolution approaches  $\Delta t_{DALES}$ , high wavenumber amplitudes will no longer have a turbulent set of scales to interact with. This identifies that running forward problems with temporal discretisations in the low end of the plotted interval is likely an overly kind representation of the true fluctuations in the boundary layer. Nevertheless, Section 8.2 will show that even at such artificially smooth levels, the numerical model encounters problems.

$(\frac{\partial \overline{\psi}}{\partial z}, \overline{w^2})_\Omega$  In contrast to the time derivative projection, this term peaks at intermediate  $k_z$ , with its peak shifting to ever lower wavenumbers as the discretisation becomes coarser. Hence, the term is more prone to spatial unresolved scales interactions than the time derivative projection, and is also modified somewhat more significantly as the spatial discretisation changes.

$\left(\overline{\psi}, \frac{\partial w'}{\partial t}\right)_\Omega$  As its resolved counterpart, low  $k_z$  modes dominate this term, making it the prevailing unresolved scales term in this wavenumber regime. The term is therefore relatively non-local in space. Its distribution over  $k_t$  shows that it is the primary vehicle for interaction of resolved and unresolved time scales. The unresolved time scales interact most strongly with the small, resolved time scales, resulting in a peak at intermediate  $k_t$ . Similar to its resolved-scales counterpart, the term drops off at even higher  $k_t$ , again showing that once  $\Delta t$  approaches  $\Delta t_{DALES}$ , the unresolved scales space is largely smooth.

$\left(\frac{\partial \overline{\psi}}{\partial z}, 2\overline{w}w'\right)_\Omega$  The cross-term is dominated by high-frequency spatial content. At these high  $k_z$ , its magnitude outweighs that of the other interaction terms, characterised by a distinct peak at the resolved scales space's cutoff wavenumber  $k_c$ . These observations indicate that i) the term's main role is to represent turbulent transfer of momentum between the portions of  $\overline{w}$  and  $w'$  around  $k_c$ , and that ii) this transfer is the most important interaction between resolved and unresolved scales at the discretisations in this study. These are common characteristics of LES with  $k_c$  in the inertial range, where turbulent transfer is dominated by a forward cascade of energy between like scales. In time, the term is dominated by a plateau over low wavenumbers, before dropping steeply.

Since the cross term is linear in  $w'$ , it is captured by the first of the infinite cascade of unresolved scales problems (see Eq. (3.13) and Eq. (3.14)). When it dominates the unresolved scales contribution, this motivates the use of linear unresolved scales models, such as the algebraic model [222]. Fig. 6.4 shows that this would have been a good assumption for most of the discretisations considered here and explains the relatively proficient performance of the algebraic model in Fig. 5.17b, even at  $\frac{h}{h_{DALES}} = 6$ . For a VMM-ANN, its direct dependence on  $\overline{w}$  is likely to make it the most tractable term to learn for an ANN model. Again, the term dips at the very smallest resolved scales, at high resolution. As in the above two instances, this is likely an artefact of the LES discretisation, such that high resolution simulations here should be treated with care.

$\left(\frac{\partial \overline{\psi}}{\partial z}, w'^2\right)_\Omega$  Finally, the Reynolds term is an order of magnitude less than the other terms at all discretisations, though it rapidly becomes more important at larger  $h$ . This is also in line with the theory discussed in Section 3.2.3: The term's nonlinearity in  $w'$  formally requires the infinite cascade of linear problems Eq. (3.13) to be posed. As the discretisation becomes coarser and the unresolved scales space becomes larger, an increasing number of the problems in this cascade becomes non-trivial, resulting in the higher-order terms of the asymptotic series for  $w'$  carrying an increasing amount of energy, until a level is reached where the asymptotic series can no longer be expected to converge [222].

For the range of discretisations of the problem considered here this is never the case, which further justifies the use of algebraic unresolved scales models in the context of VMS. However, it is a regime in which the original SP formulation is largely invalid. Its asymptotic derivation requires the time-averaged unresolved scales' momentum fluxes that are present on the resolved scales to be of order  $\varepsilon$  compared to the resolved scales' contribution (see Eq. (2.15)). If  $\varepsilon \approx 10^{-1}$ , Fig. 6.4 shows that these fluxes are dominated by the cross term, while the Reynolds term is mostly of  $O(\varepsilon^2)$ . Since  $\overline{w}$  appears explicitly in the cross term, this is incommensurate with fully separating the resolved and unresolved scales equations, as assumed by Eq. (2.9). As captured by requirement 3 in Section 2.6, this is why one would consider fully coupled equations, such as those that follow from asymptotic analysis (as in Section 2.5.1) or the VMS formulation, once GCM grid resolutions become so fine that the cross term's dynamics begin playing a significant role.

The lack of coarse resolutions where the Reynolds term's nonlinear dynamics dominate the model problem also clearly illustrates the limit of this study's applicability. Even at very high GCM resolutions, the Reynolds term (and other pure unresolved scales interactions) are expected to remain the largest unresolved scales contribution [88, 160]. For the discretisations considered here, they never are. Hence, the VMM-ANN cannot be fully tested on the scales that are most relevant to its potential use as a GCM. This confirms Section 6.1's observation that the tests here are a "kind" introduction of the model that can be considered a lower bound of its necessary capability.

## 6.4. Conclusions

The characteristic scales of the interaction terms to be predicted by the ANN are dominated by the model problem's relatively steep spectrum over spatial and temporal wavenumbers.  $\frac{h}{h_{DALES}} = 6$  is required to introduce modes above the rapidly decaying range of turbulence to the unresolved scales space, while no time discretisation considered here achieves this. Finer space and time discretisations suffer from approaching the DALES data's cutoff wavenumber and the associated, likely artificial, drop in turbulence. Therefore, the spatial discretisations of  $\frac{h}{h_{DALES}} = 6$  will be the default test case for the model in online settings, while the relatively fine time discretisations that will be used are likely artificially kind.

Even at coarse  $h$ , the Galerkin terms remain an order of magnitude more significant than the interaction terms. Hence, standard LES observations remain relatively valid: The linear cross term dominates the nonlinear Reynolds term in the transfer of turbulence between the resolved and unresolved scales spaces. However, the latter rises rapidly in prominence at coarser  $h$ , especially at the boundary and the inversion, and therefore begins resembling the strong, nonlinear backscatter that large-scale atmospheric models must negotiate. Both terms are dominated by high  $k_z$  modes and low  $k_t$  modes, such that they are relatively local in space and non-local in time. Conversely, the unresolved scales time derivative projection is dominated by low  $k_z$  modes and higher  $k_t$  modes. The impact of these characteristics on the predictive ability of ANNs that operate on feature sets that are local both in space and time will be extensively discussed in the following chapter.



# Machine Learning

Chapter 6 characterised several dimensions of the exact interaction terms of the model problem. This chapter will determine the extent to which these characteristics can be learned by the ANNs proposed in Chapter 5, when they are trained and evaluated offline on error-free data. After a note on dataset size in Section 7.1, the chapter discusses the predictive ability and generalisability of ANNs with various feature sets and architecture combinations in Section 7.2, to answer RQ2.1. Subsequently, Section 7.3 assesses the performance of one of these models at various levels of discretisation, to answer RQ2.2, before the most important findings are summarised in Section 7.4.

## 7.1. Dataset size

Broadly speaking, ANN unresolved scales and turbulence models tend to keep improving as the number of examples they face is increased, even at very large dataset sizes [21, 205, 255]. The obvious drawback associated with training on increasingly large datasets, however, is the computational cost penalty it imposes. Although the cost of ANN training might only have to be incurred once if the network is sufficiently well-trained to generalise to any situation one may wish to deploy it in, this may not be useful once the total simulation time of training the networks begins to approach the time required for running an appreciable number of DNSs. Therefore, a brief assessment is made here to gauge how an ANN's accuracy per unit computational time for this problem scales with the available dataset's size. This assessment is based on runs with FS2 and hand-tuned hyperparameters. It is conducted at the default discretisation of  $\frac{h}{h_{DNS}} = 6$  and  $\Delta t = 2\Delta t_{DNS}$ .

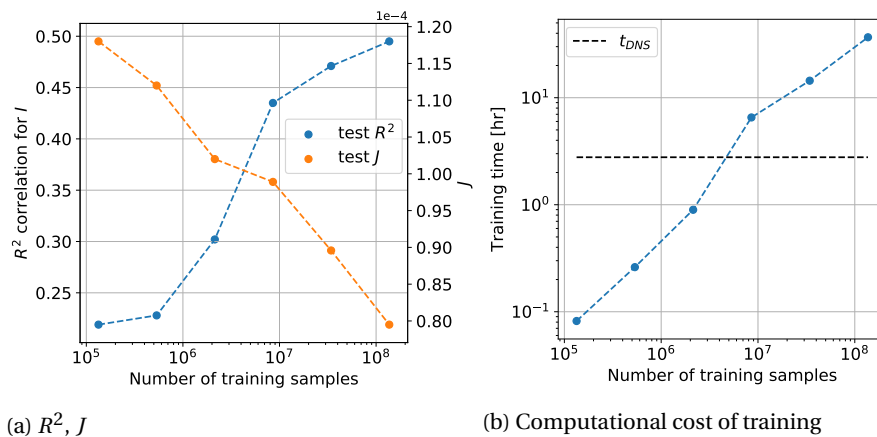


Figure 7.1: Scaling of predictive ability (Summed  $R^2$  over  $\hat{I}$  and  $J$ ) and training time as a function of the number of samples used for ANN training, for FS2. For the present problem, the time cost of running a forward problem with 1024 elements is included as a dashed line.

Fig. 7.1a shows that the prediction metric very roughly follows a linear trend throughout the range of samples that can be included from a single DALES simulation. Sequentially quadrupling the number of columns

that participate in the dataset from 2x2 (lower end of the figure) up to 64x64 (upper end of the figure) roughly keeps adding and subtracting proportional increments to  $R^2$  and  $J$ , respectively, with sublinear scaling at small and large dataset sizes. The training time, however, also scales approximately linearly and rapidly reaches the order of days. This computational cost is contextualised by running a DNS of the forward problem with  $h = 0.09375h_{DALES}$ ,  $\Delta t = 0.02\Delta t_{DALES}$  and an algebraic unresolved scales model. Without activating any of the code’s speedup settings, this simulation achieves a final, average  $L_2$  error of the solution of  $2.1 \cdot 10^{-4}$  at the cost of running approximately 3 hours. This simulation time is drawn as a dashed line in Fig. 7.1b.

In this light, several dataset sizes will be considered in this chapter. Grids of 8x8 columns, spaced by 16 columns in each dimension, span a sufficient spatial width to encounter most of the uncorrelated turbulence in the domain and offer some improvements in learning with respect to the lowest number of samples. Yet, their training costs are approximately an hour, which is less than merely running a DNS for this problem and facilitates turning the models around relatively quickly. The latter is essential in the following section, which treats the sensitivity and “optimisation” of ANN performance to the various input feature sets and architectural parameters and requires many ANNs to be trained. The optimised models that emerge from this section are then trained on the largest grid of 64x64 columns from a single DALES simulation, and must therefore be tested on a different simulation (see Section 5.4.4).

## 7.2. Input Features and Architecture

The feature sets in Table 5.2 span a wide set of candidate inputs. Hence, to fairly compare them, they are each subjected to a hyperparameter optimisation. Each individual training session in these optimisations employs the grid of 8x8 columns and the same  $z - t$  discretisation as in Section 7.1. The ANNs are judged in terms of  $J$  on a held out set of 16 columns from the same DALES simulation that generated the training data. These columns are located more than one correlation length away from any training column, and from each other.

For each feature set, three sweeps of training sessions are conducted to gauge the influence of the ANN hyperparameters. In the first, hand-based iterations are performed to identify orders of magnitude of learning rate,  $\lambda_{L_2}$ , dropout fraction and layer construction that function relatively well (an example combination from this phase was used to generate Fig. 7.1). 5% of the possible permutations of these ranges, reported in Table 7.1, are subsequently sampled with a random search, resulting in 984 individual training sessions. These yield the correlations in Table 7.2 and set the stage for a discussion on hyperparameter sensitivity. Finally, the models are scanned with a full grid search over the most promising parameter ranges, from which the best model configuration can be identified and conclusions can be drawn.

Parameter	Sampling range
Hidden layers	[1, 2, 3]
Neurons/layer	[64, 256, 512]
$\alpha_1$	$[1 \cdot 10^{-4}, 2.25 \cdot 10^{-3}, 5.00 \cdot 10^{-3}]$
$L_2$ weight regularisation $\lambda_{L_2}$	$[1 \cdot 10^{-6}, 1 \cdot 10^{-5}, 1 \cdot 10^{-4}]$
Dropout probability	[0.0, 0.125, 0.25]
Optimiser	[Adam, NAdam, RMSProp]
Activation	[ReLU, ELU, Sigmoid]
Batch size/Total number of samples	[0.25, 0.5, 1.0]
Epochs	[1000, 2500, 5000]

Table 7.1: Ranges of free hyperparameters sampled by random grid search, resulting in a total of 984 combinations.

### 7.2.1. Hyperparameter Sensitivity

By necessity, a discussion on hyperparameter sensitivity based on strongly downsampled data is somewhat incomplete and requires subjective judgement, a clear drawback of ANN modelling. However, within these limits, the relative impact of all hyperparameters on  $J$  are quantified in Table 7.2, Fig. 7.2 and Fig. 7.3.

All feature sets display similar trends in Table 7.2, albeit with different magnitudes. This allows decoupling the hyperparameter sensitivity study from the feature set sensitivity study. The former is treated first, with FS3 as the running example. Deviations from the trends between feature sets are mentioned where relevant.

Table 7.2 shows that  $J$  is insensitive to network depth and  $\lambda_{L_2}$ . Hence, these parameters are neglected for now. Next, small batch sizes are generally favourable. This is a positive finding, since only approximately 8 columns of data fits on the Graphical Processing Units (GPUs) at any instant, requiring small batch sizes for GPU-accelerated training. A large number of maximum epochs, 5000, is set, as many of the runs otherwise

Hyperparameter	FS1	FS2	FS3	FS4
$\alpha_l$	-0.719	-0.0790	-0.265	-0.527
Neurons/layer	-0.314	-0.0749	-0.115	-0.168
Epochs	-0.121	-0.120	-0.101	-0.163
Hidden layers	-0.079	0.0303	0.0329	-0.190
$\lambda_{L_2}$	0.00102	-0.0102	0.00390	0.00532
Dropout	0.0503	0.0294	0.150	0.0806
Batch size	0.376	0.0241	0.0165	0.432

Table 7.2: Pearson correlation ( $R$ ) of hyperparameters to  $J$  on the 16 validation columns, ranked in terms of positive to negative impact on reducing  $J$  over the ranges reported in Table 7.1.

reach the maximum number of epochs while still making progress. In practice, however, this limit is not often reached for well-trained models, which exit on early stopping (see, for instance, Fig. 7.4).

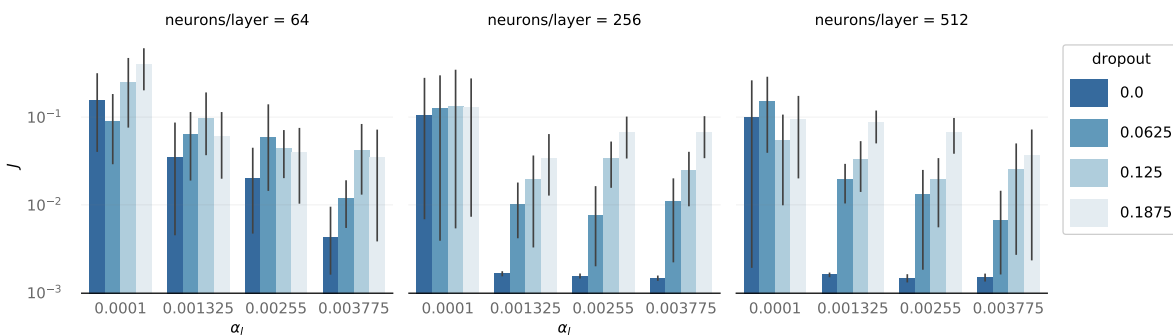


Figure 7.2: Average impact on  $J$  on the validation columns of varying the neurons/layer (subplots), learning rate (bar assemblies) and dropout (hue) in the ranges reported in Table 7.1. The extent of black bars denotes bootstrapped 95% confidence intervals, though the sampling rate is sufficiently low that these should be treated with care.

The three remaining impactful hyperparameters,  $\alpha_l$ , the number of neurons per layer and dropout probability, are plotted in Fig. 7.2, which illustrates three trends. First, the higher selected learning rates are favoured for minimising  $J$ . Second, dropout adversely impacts the loss, especially when combined with the higher learning rates. Finally, “wider” networks with more neurons per layer seem beneficial, though this trend stagnates at 512 neurons per layer. These tendencies broadly mirror Robijns’ optimised architecture, which also did not require dropout or weight regularisation, and employed few layers with many neurons per layer [209]. It is encouraging that these results translate to this study’s more realistic turbulence dataset.

The impact of optimiser and activation function choice is presented in Fig. 7.3. ReLUs and ELUs, with their non-saturating gradients, minimise  $J$  an order of magnitude better than standard sigmoid activations for the present problem. ELUs were considered for their ability to carry non-zero negative activations, which improves learning in several settings [46]. However, Fig. 7.3 finds that the biased ReLUs actually yield further improvements. Hence, all further nonlinear ANNs in this study employ such activation functions.

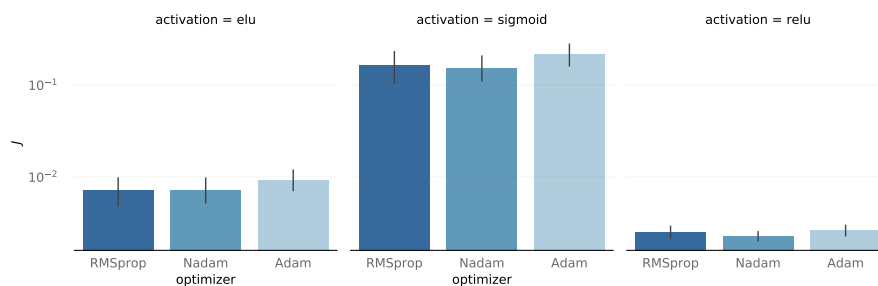


Figure 7.3: Average impact on  $J$  on the validation columns of varying the optimiser between RMSProp, NAdam and Adam, for ReLU, ELU and Sigmoid activation functions. The black bars denotes bootstrapped 95% confidence intervals.

The impact of the optimisation algorithm choice is much less pronounced, though a trend emerges here also: The Adam loss function is consistently outperformed by RMSprop loss and even further by its Nesterov momentum-augmented version, NAdam. While the difference is statistically insignificant when considering the variability in the results, this falls in line with the theoretical observation that Nesterov momentum should yield superior gradient direction improvements than its classical momentum counterpart [65]. It also matches recent empirical observations that the use of Nesterov momentum can translate to improved learning when combined with RMSProp methods that limit how far each parameter may proceed along the found direction [237]. For this dataset, Adam’s purely history-based momentum update to the gradient actually upsets the learning in comparison to RMSProp, which does not incorporate momentum. Hence, the results suggest that incorporating the gradients from the most recent step in the momentum update, as done in NAdam optimisation, helps to determine the correct gradient directions. Therefore, a NAdam optimiser will be considered in the remainder of this work, although its impact is small.

In conclusion,  $J$  is sensitive to batch size, learning rate, the number of neurons per layer and dropout, for all considered feature sets. Fig. 7.2 shows that ANN architectures of relatively shallow, “wide” networks, trained without regularisation or dropout at learning rates in the upper interval of the considered range perform best in these tests. Finally, Fig. 7.3 reveals that ANNs with ReLU activation functions and a NAdam optimiser yield the best performance, motivating their choice in the rest of this study.

### 7.2.2. Optimised Architecture and Feature Sets

With this sensitivity established, the second phase of optimisation consists of a full scan of parameter combinations in a reduced space around the best values from the first stage, along with some manual tests, for all feature sets. For FS3, the results are illustrated by Fig. 7.4.

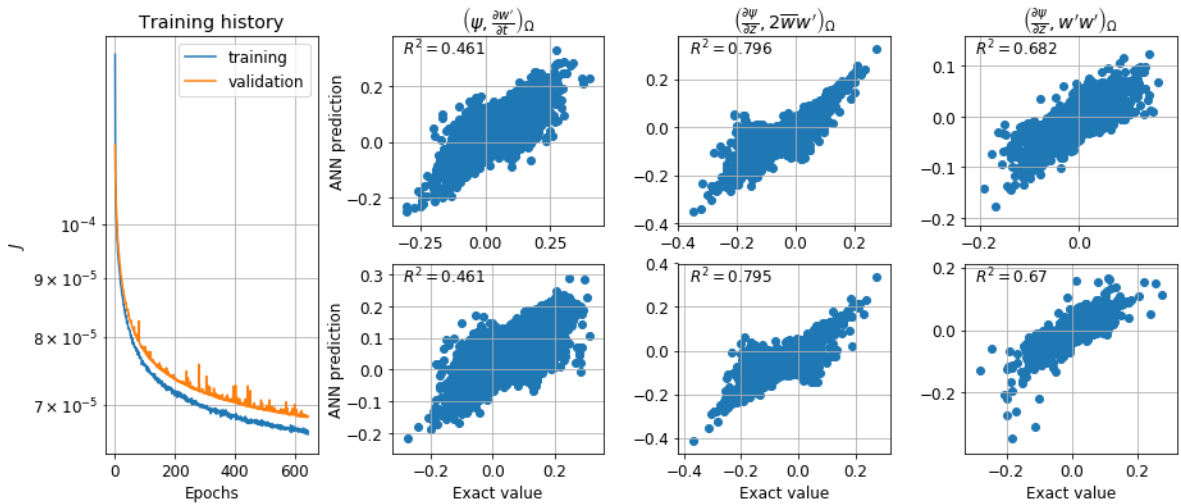


Figure 7.4: Training history on training and validation data and  $R^2$  correlation on validation data (upper row) and test data (lower row) of each of the three interaction terms for the best set of hyperparameters, with FS3 as input.

Trained on a grid of 64x64 columns, from which 16 validation columns are held out to assess early stopping, Fig. 7.4 shows that  $J$  converges similarly on both training and validation sets. This is encouraging, since many of the validation columns are new to the model. Fig. 7.4 further shows  $R^2$  from evaluations of the trained model on both the validation columns (upper row) as well as 16 uncorrelated columns of turbulence from a different DALES simulation (lower row). This latter, held-out set of data is also uncorrelated from any examples encountered in the hyperparameter optimisation and has remained hidden until now. It can thus be considered a “test” set in the traditional sense of the term [211]. The computed  $R^2$  measures on this test set are at most 0.01 lower than on the validation data, confirming that the ANN has generalised very well.

A pattern emerges from this figure that broadly transfers to all feature sets: In general, the cross term, which is linear in  $w'$ , is the easiest to learn, the nonlinear Reynolds term is more challenging and the unresolved scales’ time derivative projection is in most settings the most difficult term to learn.

The remaining feature sets’ best configurations and performance are listed in Table 7.3. For FS3 and FS4, larger, 1024 neuron layers increment the performance slightly compared to the previously considered

Hyperparameter	FS1	FS2	FS3	FS4	Algebraic
Hidden layers	3	2	2	2	
Neurons/layer	1024	512	512	512	
$\alpha_l$	$1 \cdot 10^{-4}$	$1 \cdot 10^{-4}$	$1 \cdot 10^{-4}$	$1 \cdot 10^{-4}$	
$\lambda_{L_2}$	0.0	0.0	0.0	0.0	
Dropout	0.01	0.0	0.0	0.0	
Optimiser	NAdam	NAdam	NAdam	NAdam	
Activation	ReLU	ReLU	ReLU	ReLU	
Relative batch size	0.125	0.5	0.5	0.125	
<hr/>					
$\bar{R}^2$ on test data					
$\left(\overline{\psi}, \frac{\partial w'}{\partial t}\right)_\Omega$	0.191	0.402	0.461	0.738	-
$\left(\frac{\partial \overline{\psi}}{\partial z}, 2\overline{w}w'\right)_\Omega$	0.637	0.602	0.795	0.926	0.267
$\left(\frac{\partial \overline{\psi}}{\partial z}, w'^2\right)_\Omega$	0.531	0.562	0.670	0.589	0.016
$J$ on test data	$6.31 \cdot 10^{-4}$	$7.95 \cdot 10^{-5}$	$7.46 \cdot 10^{-5}$	$1.62 \cdot 10^{-5}$	$5.58 \cdot 10^{-3}$

Table 7.3: Set of ANN architectures and hyperparameters that yield the best performance on all considered feature sets.  $R^2$  and  $J$  are listed on a test dataset of 16 columns from a different DALES dataset than was trained on.

512-neuron layers. This motivates choosing the much cheaper 512 neuron configuration (see Section 9.4 for the impact on the forward model's cost). For FS1, the improvement is considered substantial enough to incorporate wider layers, while this feature set also benefits from another hidden layer.

Despite these differences, the feature sets generally respond well to very similar architecture, mirroring Section 7.2.1. However, their performance differs considerably. FS1 does not include a time history, and is unable to represent  $\left(\overline{\psi}, \frac{\partial w'}{\partial t}\right)_\Omega$  well as a result. FS2 includes a history of two time levels, strongly improving the term's representation. However, this feature set does not depend on the current time level solution, curtailing its ability to predict the cross and Reynolds terms. FS3 combines the two first feature sets and improves the prediction further. Finally, including the Galerkin terms from the current time level gives a further improvement, reflected in FS4's high proficiency in the skill metrics. The improvement is only in terms of the linear terms in the budget, making the non-linear Reynolds term the hardest to predict for FS4.

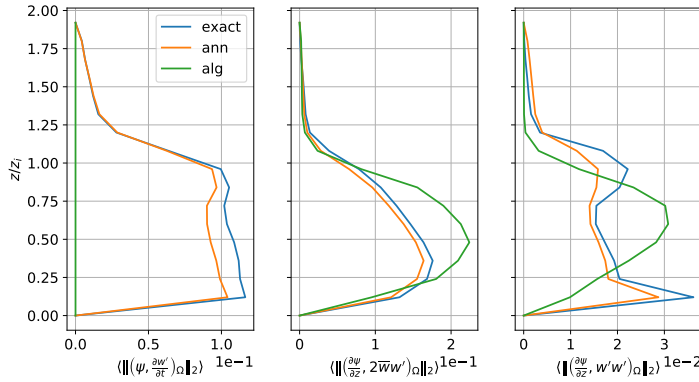


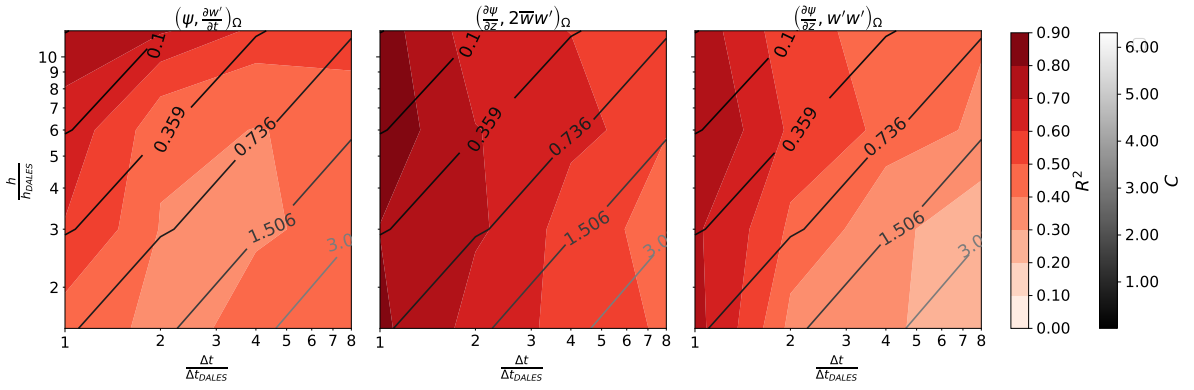
Figure 7.5: Comparison of time-averaged spatial distributions of the  $L_2$  norms of the interaction terms, as predicted by exact, ANN and algebraic models, at  $h/h_{DALES} = 6$  and  $\Delta t/\Delta t_{DALES} = 2$ , over 16 columns from a different DALES simulation than was trained on. The ANN is the best FS3 model in Table 7.3.

To judge the merit of these results, they can be compared to the algebraic model. As shown in Fig. 5.17b and discussed in Section 6.3, this model reproduces  $\overline{w}$  and its statistics well, even at the coarse discretisation considered here. However, Fig. 7.5 shows that the accuracy of the terms dramatically improves when they are predicted by the ANN. In terms of  $R^2$  and  $J$ , Table 7.3's right-most column further supports this observation. As expected from the discussion in Section 6.3, the linear, algebraic model reasonably predicts the cross term's statistics, but bears almost no resemblance to the non-linear Reynolds term; it is much better predicted by the ANN. The algebraic model does not account for  $\left(\overline{\psi}, \frac{\partial w'}{\partial t}\right)_\Omega$ . The ANN also predicts this term well.

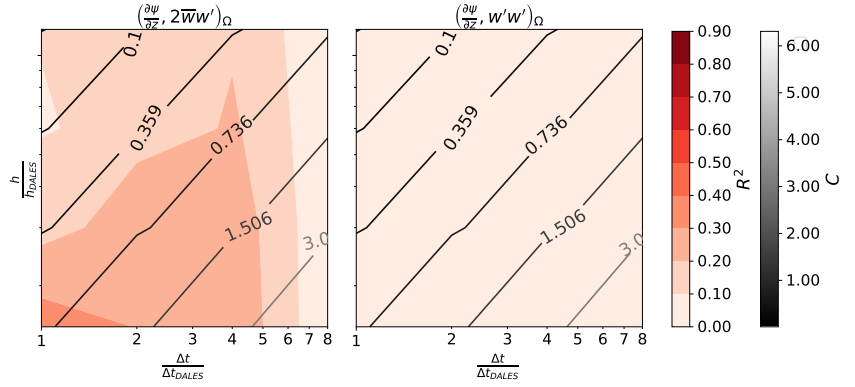
In conclusion, the optimal sets of hyperparameters ensure that all interaction terms can be learned with an accuracy that is much higher than that of the algebraic model at the considered resolution. This accuracy generalises very well outside the model's training envelope to cases where the turbulence is statistically equivalent. The skill displayed by the models is remarkable, since the individual turbulent realisations of the interaction terms that the ANN must predict here are uncorrelated to what it was trained upon.

### 7.3. Predictability as a Function of Discretisation Level

The best ANN configuration that emerges from Section 7.2 is now ready to be subjected to a number of tests to assess its ability to learn the interaction terms in several settings, in alignment with Majda's proposed systematic assessment of novel multiscale models (see Section 2.5.1 and Section 2.6). As proposed in Section 3.6, the first of these tests should be to which extent the ANNs can still predict the interaction terms as a function of resolved-scale parameters when the discretisation becomes increasingly coarse. In particular, to be promising unresolved scales models in practical situations, they must still accurately predict the terms once the discretisation's cutoff wavenumber  $k_c$  falls in the more shallow  $k^{-5/3}$  range of the model problem's energy spectrum, as established in Chapter 6. Fig. 7.6 aids in the assessment hereof.



(a) ANN



(b) Algebraic

Figure 7.6: Contours of  $R^2$  of an array of ANNs (top) and algebraic models (bottom) over a range of  $h$  and  $\Delta t$ . The ANNs use FS4 and the hyperparameters from Table 7.3, each trained and tested on data sampled with a different combination of  $h$  and  $\Delta t$ . All ANNs are trained on an equal number of samples, corresponding to the dimensions of the coarsest discretisation, randomly selected from 8x8 columns. They are evaluated on 16 different, full, uncorrelated columns from the same DALES simulation. Contour lines of constant Courant number  $C$  are superimposed.

Fig. 7.6a shows  $R^2$  of ANNs that take FS4 as input, use the hyperparameters from Fig. 7.4, and are trained on 8x8 column datasets generated with different, single combinations of the discretisation parameters  $h$  and  $\Delta t$ . Their  $R^2$  is evaluated on 16 corresponding, uncorrelated and previously hidden columns from the same DALES simulation. The figure furthermore draws iso-lines of constant Courant number  $C$ :

$$C = \frac{w^* \Delta t}{h} \quad (7.1)$$

Where  $w^*$  is a characteristic velocity. In this work, it is the maximum velocity encountered in a simulation.

The first observation that follows from Fig. 7.6 is that the ANN model's superiority over the algebraic model extends to any combination of  $h$  and  $\Delta t$  tested here. The algebraic model's cross term prediction only becomes somewhat satisfying at the finest resolutions in space and time, while its Reynolds term predictions are practically uncorrelated from the exact values at any resolution. This clearly shows that the algebraic model would be insufficient at the coarser scales required for atmospheric simulation where the Reynolds term dominates, as discussed in Section 6.3. The outlook for the ANNs, however, appears more promising.

For these ANNs, three observations follow from Fig. 7.6a. First, the prediction of the interaction terms generally improves as  $C$  becomes smaller. In particular, the unresolved scales time derivative prediction and Reynolds term display this trend, while all terms reach their highest predictive skill at the lowest  $C$ . Second, the improvement generally manifests itself more strongly when  $\Delta t$  reduces than when  $h$  increases. Hence, the terms' predictability does not appreciably appear to drop off as the resolved-scales turbulence departs the range of rapidly decaying turbulence. Finally, while the cross and Reynolds terms vary monotonically, the unresolved scales time derivative projection displays a distinct area in which its skill drops off. Hence, the trends observed here cannot be explained solely in terms of  $C$ .

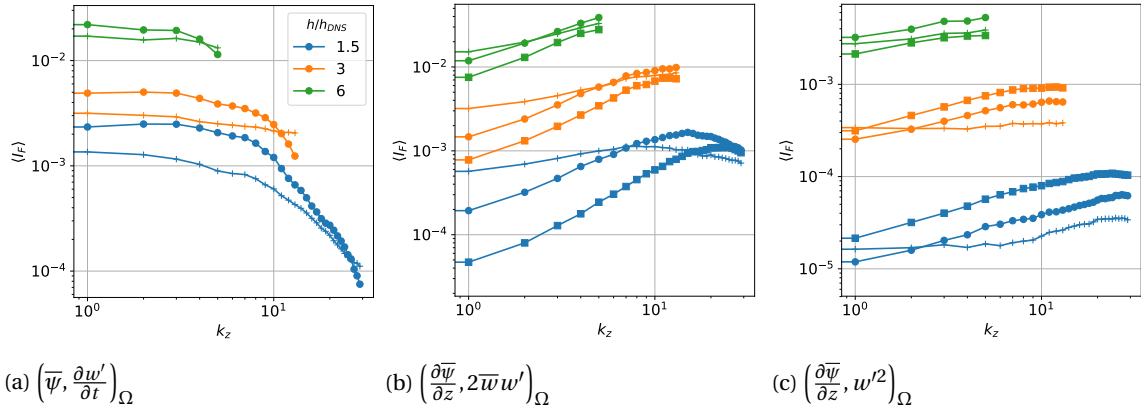


Figure 7.7: Amplitude distribution with  $k_z$  of exact (circles), algebraic (squares) and ANN (pluses) predictions of the interaction terms at three levels of spatial discretisation, averaged over time, for a test column.  $\Delta t/\Delta t_{DALES} = 2$ .

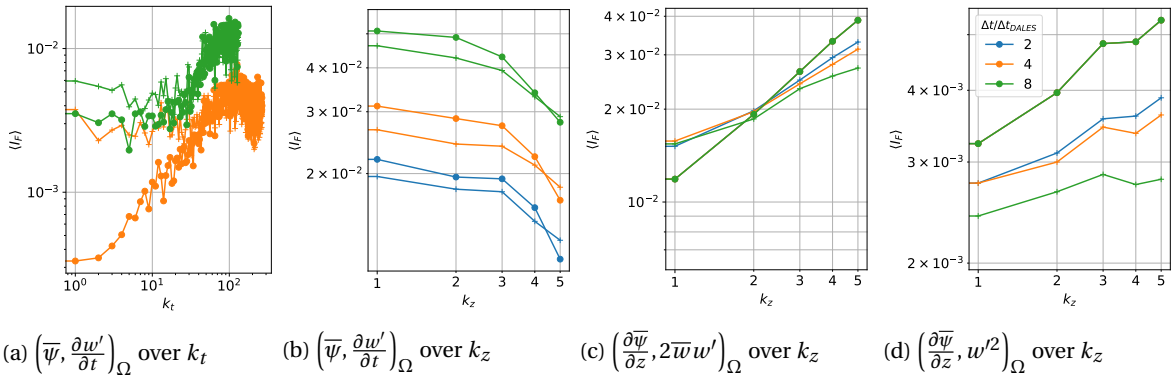


Figure 7.8: Amplitude distribution with  $k_z$  of exact (filled circles) and ANN (pluses) predictions of the interaction terms at three levels of temporal discretisation, averaged over space for a test column, and with  $k_t$  of the time derivative term at the two coarsest levels of  $\Delta t$ .  $h/h_{DALES} = 6$ .

To shed more light on these three observations, the amplitudes of the interaction terms are decomposed into Fourier modes of spatial wavenumber ( $k_z$ ) and temporal wavenumber ( $k_t$ ). The resulting distributions with  $k_z$  and  $k_t$  of these amplitudes are plotted in Fig. 7.7 and Fig. 7.8 for exact (circles), algebraic (squares) and ANN (pluses) interaction term predictions. These distributions mirror those presented in Section 6.3. Fig. 7.7 shows discretisations over three levels of  $h$ , but constant  $\Delta t$ , while Fig. 7.8 considers the influence of changing  $\Delta t$  at a constant  $h$ . The distributions are evaluated only for a single test column, but tests on different test columns were not found to display very different trends.

Fig. 7.7 shows two interesting facets of the algebraic model. First, despite being unable to predict where in

the spatial domain large-scale and small-scale variations in the interaction terms should appear (see Fig. 7.5), the model does predict reasonable averaged amplitudes distributed over  $k_z$  modes. Hence, if the turbulence were isotropic, the model might have predicted these terms quite well. Second, despite predicting increasingly deficient amplitude distributions at coarser  $h$ , the general shapes of these distributions are often better than those of the ANNs. Nevertheless, the errors of the algebraic model remain consistently larger than those of the ANNs, especially at coarser  $h$ .

Three factors appear to play a role in how the ANN predictions of the interaction terms evolve with discretisation and how they end up displaying the trends seen in Fig. 7.6a: i) The ANN input stencil's relation to the terms' dominant scales, ii) the ANN's structural errors and iii) the inherent predictability of the terms as a function of their resolved-scales input. The following paragraphs aim to discuss how each of these factors could affect the interaction terms, to separate the notion of "predictability" into two components: The predictability that results from the local stencils considered by Robijns and in this study, and the inherent predictability that remains when the impact of these stencils is accounted for.

### 7.3.1. Influence of the Stencil

The ANNs are trained to minimise the interaction terms' error in a global norm, perhaps leading one to hope that the ANNs will be equally proficient at predicting both the small and large scales of the interaction terms, at a specified  $h$  and  $\Delta t$ . However, the ANNs' input feature sets introduced in Section 5.4.2 are all defined on stencils that are quite local in space and time compared to the  $k_z$  and  $k_t$  modes that dominate the amplitude distributions of several terms in Figs. 7.7 and 7.8. The impact this has can be discussed on the basis of Fig. 7.9.

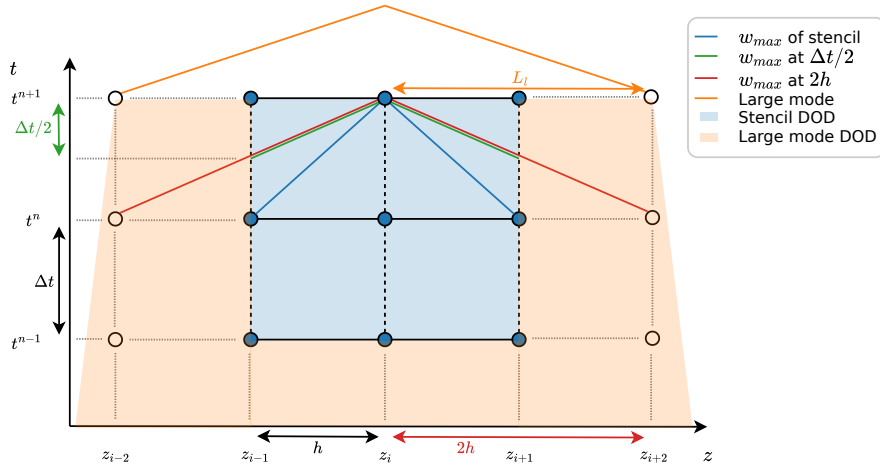


Figure 7.9: Highest  $w$  ( $w_{max}$ ) that can impact  $\hat{I}_i^{n+1}$  on the stencil from Fig. 5.9 at a chosen combination of  $\Delta t$  and  $h$  (blue line), at  $\Delta t/2$  (green line) and at  $2h$  (red line), compared to a larger mode of length  $L_l$  (orange line). The domains of dependence (DOD) of the stencil and the  $L_l$  mode are shaded blue and orange, respectively.

Fig. 7.9 depicts the space-time stencil of FS3 and FS4, which both include a two-level time history. The Domain of Dependence (DOD) of this stencil at a certain time step is shaded blue. For the nonlinear convection problem at hand,  $w$  is both the solution and the local convection velocity. The blue lines in the figure show the highest convective velocity that can be represented by such a stencil,  $w_{max}$ . If  $w > w_{max}$ , information locally travels faster than what the stencil can detect. One can recapture this information by reducing  $C$ , through either a reduction in  $\Delta t$  (green lines) or an increase in  $h$  (red lines), or by widening the stencil. Both lowering  $C$  and widening the stencil are expected to favourably impact  $k_z$  modes close to the domain of dependence of the stencil.

However, the nonlinearity of the problem makes it considerably more challenging to predict how  $k_z$  modes that are much more non-local than the stencil will respond to either of the above strategies. For instance, lowering  $C$  for an unchanged, local stencil might only benefit the  $k_z$  modes close to the  $2h$  cut-off wavenumber,  $k_c$ . These are the modes that can (almost) be resolved by the stencil. Hence, their well-posedness is expected to directly increase from reductions in  $C$ . However, if one assumes that the nonlinear mode interaction is the strongest between modes with similar  $k_z$ , the improvement in the predictability of these high  $k_z$  modes may not be felt by the lower  $k_z$  modes. Fig. 7.9 shows that even at very small  $\Delta t$ , the stencil would remain too local to directly cover the DOD of a larger spatial mode of characteristic length  $L_l$

and spatial wavenumber  $k_L \propto \frac{1}{L_l}$ , schematically illustrated with orange shading. Hence, these larger modes rely on such nonlinear scale transfer of information from the high  $k_z$  modes around  $k_c$  to be well-predicted. However, if the prediction of low  $k_z$  modes is truly separated from the high  $k_z$  stencil, which one would expect if  $k_L \ll k_c$ , improving the prediction of such modes might require explicitly including information of modes of lower  $k_z$ , closer to the scales of  $L_l$ , on the stencil.

Alternatively, one could view the inclusion of such non-local, low  $k_z$  information as better constraints on the high  $k_z$  modes' consistency with the larger  $k_z$  modes of which they are a part. Since all these high  $k_z$  modes are individually predicted, such consistency could benefit the lower  $k_z$  modes' consistency. Regardless of the exact explanation, this raises the expectation that including more non-local information on the ANN input stencil will aid its predictive ability of the interaction terms.

This can be achieved in two ways. First, increasing  $h$  means that  $k_c$  approaches  $k_L$ , such that more non-local, relevant information is available for the ANN to correctly predict the larger mode. However, the ANN must obviously account for the projection of increasingly many modes that begin to fall below the lower  $k_c$  of such coarser  $h$ , such that it remains interesting to see the extent to which the overall predictions drop off. Second, at a given  $h$ , the prediction of low  $k_z$  modes might benefit from increasing the stencil width to approach  $L_l$ . If its prediction truly requires non-local data, one would expect improvements from such wider stencils to continue to materialise for these modes until the stencil width approaches the correlation length of the turbulence  $L_c$ .

These conjectures could explain some behaviour of the unresolved scales' time derivative projection in Fig. 7.7a. The high  $k_z$  modes of this term are accurately predicted, while the low  $k_z$  that are much larger than what the stencil can cover suffer from systematic underprediction. The low  $k_z$  modes dominate the amplitude of the unresolved scales' time derivative projection. Hence, this offers an explanation for why it is so challenging to learn: The ANNs are unaware of the non-local features that drive the term.

Therefore, the unresolved scales' time derivative projection would likely benefit from non-local modelling. Such non-locality is added to the ANNs' input stencils in Fig. 7.10, which shows tests conducted with ANNs trained on FS4 input with stencils of width  $L_s = h$  to  $L_s = 4h$  in both directions from the equation of interest. Fig. 7.10a shows that as increasingly non-local data is accounted for, the prediction of progressively lower  $k_z$  modes substantially improves, while the high  $k_z$  modes remain rather unaffected. This does not immediately appear to reflect that the low  $k_z$  modes do not feel the influence of the high  $k_z$  modes, since *all* low  $k_z$  modes benefit from added non-locality. In fact, one could conjecture that the high  $k_z$  modes are the beneficiary from the added non-locality, while the nonlinear scale interaction in fact is strong and responsible for translating this improvement to the much lower  $k_z$ . Such a view is actually not so different from the alternative argument based on the stencil: Including information of the lower  $k_z$  features of the flow explicitly might improve the high  $k_z$  modes' consistency with these large phenomena in the ANN prediction.

Regardless of the exact underlying dynamics, the improved prediction of high-amplitude, low  $k_z$  modes substantially enhances the unresolved scales's time derivative projection's overall prediction. Such extensions are much more challenging to impose on SP formulations, which confine the unresolved scales to periodic domains embedded in a single element. Hence, SP would likely be limited in its ability to predict this term.

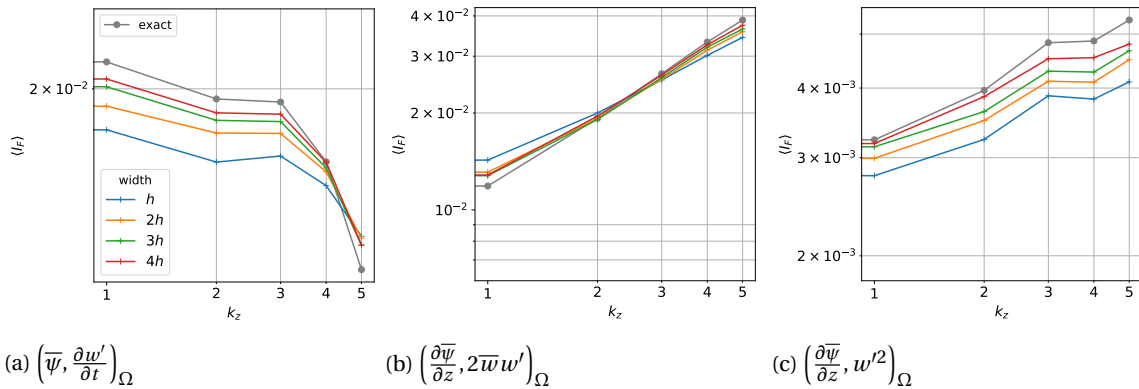


Figure 7.10: Amplitude distributions with  $k_z$  of the three interaction terms, predicted by ANNs with input stencil widths of 1-4h (pluses) compared to exact values (filled circles), averaged over the time dimension of a test column.  $h/h_{DALES} = 3$  and  $\Delta t/\Delta t_{DALES} = 2$ .

Fig. 7.7a also shows that the relative error in the unresolved scales' time derivative projection's low  $k_z$

modes reduces as  $h$  increases. As these modes dominate the term's amplitude, this improvement likely drives the increase in  $R^2$  for the term at larger  $h$ , observed in Fig. 7.6a. Based on the above discussion, this appears to show that the term's prediction benefits more from having non-local input available than it suffers from having to account for the projections of an increasing number of unresolved  $k_z$  modes as  $h$  increases. This trend is expected to continue as long as  $h < L_c$ . However, should  $h$  become so large that it exceeds the correlation length of the turbulence, it is unlikely that adding further non-locality to the stencil will aid the prediction further. For such cases, the unresolved scales' time derivative projection's predictability might begin to suffer as  $h$  becomes even larger.

As for the unresolved scales' time derivative projection, the cross term's prediction error is mostly concentrated at low  $k_z$ , far from the ANN's domain of dependence. Fig. 7.7b shows that at coarser  $h$ , the relative error of these modes again reduces, as  $k_c$  approaches them. Similarly, Fig. 7.10b displays small improvements in these modes as the stencil becomes increasingly non-local. In contrast to the time derivative term, however, high  $k_z$  modes that lie close to the local ANN stencil dominate the cross term's amplitude. This means the term suffers the least of any from the local stencil, explaining why it is i) insensitive to adding non-local input in Fig. 7.10b and ii) the most predictable of any of the terms in Table 7.3. As  $C$  reduces through either coarsening  $h$  (Fig. 7.7b) or refining  $\Delta t$  (Fig. 7.8c), especially the high-amplitude modes of high  $k_z$  increasingly enter the local DOD of the ANN in Fig. 7.9. This may explain why the cross term also benefits especially strongly from reductions in  $C$ , as seen in Fig. 7.6a. The Reynolds term responds somewhat differently; it is treated on its own in Section 7.3.3.

The paragraphs above show that increasing the non-locality of the input stencils presented in Fig. 7.10 improves the ANN's predictive ability. Their use is therefore recommended in future work. However, they do not feature in simulations of the forward problem, as they are unlikely to impact the answers to RQ3.

With respect to the temporal dimension, FS3 and FS4's stencils are also rather local: They only include the smallest,  $2\Delta t$   $k_t$  mode. This is very general for problems with rapidly changing statistical states, but may prevent the ANN from appropriately predicting the lower  $k_t$  modes of the problem. The ANN's knowledge of these modes would be even less if  $\Delta t$  reduces further and the stencil becomes even more local. However, reducing  $\Delta t$  also reduces  $C$ , such that high  $k_z$  modes around the cutoff wavenumber become better-posed. This actually results in improvements in the predictions of especially these modes in Fig. 7.8c and Fig. 7.8d (the unresolved-scales time derivative projection is considered in the next subsection). Furthermore, increasing the time history of the stencil from no history (FS1) to the  $2\Delta t$  history of FS3 and FS4, actually has little influence on the low  $k_t$  modes, as evidenced by Fig. 7.11. This may be because the stencil is still almost a decade of  $k_t$  removed from the scales that matter to the terms' predictions, which would prevent their accurate prediction under a similar assumption of scale separation as discussed for the spatial modes above. If this conjecture is true, these terms would likely require ANNs with very long-term input stencils, or statistics of their history, for their prediction to meaningfully improve at the time resolutions considered here. Such time histories have the added benefit of grounding the ANN predictions in long-term dynamics in online settings, which could prevent them from suddenly digressing the solutions of such problems from physical regimes. This will be shown in Section 8.3.4 and considered further in Section 9.1.

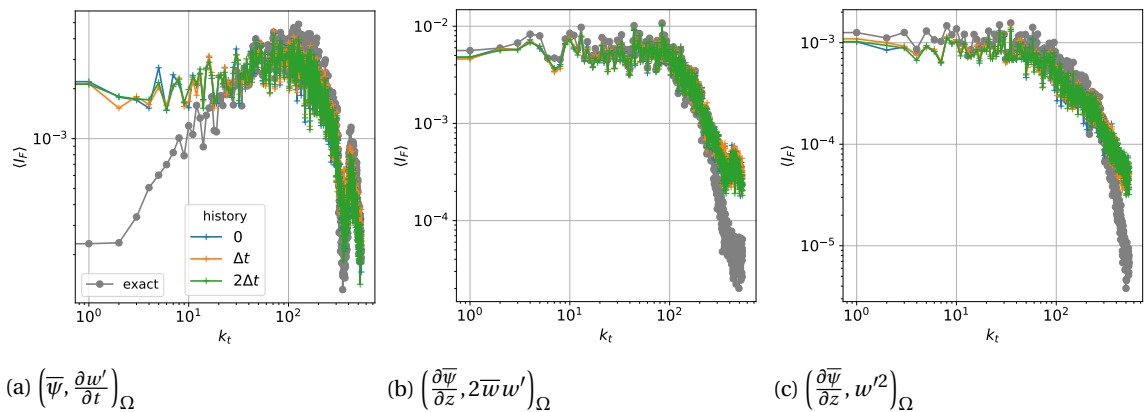


Figure 7.11: Amplitude distributions of the three interaction terms with  $k_t$ , predicted by ANNs with 0- $2\Delta t$  input history stencils (pluses) compared to exact values (filled circles), averaged over the space dimension of a test column.  $h/h_{DALES} = 3$  and  $\Delta t/\Delta t_{DALES} = 2$ .

### 7.3.2. Influence of Structural Errors

The time-discretisation trend of the unresolved scales time derivative projection cannot be immediately explained by the stencil. As seen in an integral sense in Fig. 7.6a and in the modal decompositions in Fig. 7.8b, its error is small at both large and small  $\Delta t$ , and larger at the intermediate discretisation level. Fig. 7.8a suggests that this may be due to the combination of two factors.

First, all the predicted amplitude distributions are without exception overly “shallow”: The ANNs structurally tend to underestimate how much the terms’ amplitudes change over their  $k_z$  and  $k_t$  modes, resulting in rather “flat” distributions. The terms’ total time-averaged amplitudes are also generally underpredicted, as can also be seen in Fig. 7.5. Such systematic ANN error in problems with multiple active scales is commonly associated with improper normalisation of their input data or lack of statistical generalisation. However, these ANNs’ inputs have been appropriately normalised (see Section 5.4.1), while the study has attempted to be rather careful not to fall in a biased generalisation trap. Furthermore, switching to a standardisation scheme, removing the normalisation entirely or testing on a larger set of columns has not been found to affect this underprediction. Hence, it appears to be a feature of the ANNs trained here.

This is a concerning observation, since ANNs generally derive their strength from their ability to extract multiscale features from a problem. In fact, this is one of the stronger arguments for their use as turbulence models [139]. However, even this could be due to stencil locality: The ANN’s weights and biases might be optimised only for the local features that can be represented on a narrow stencil. In support of this hypothesis, Fig. 7.10 shows that when increasingly non-local features are included, the shallowness is largely remedied. This conjecture is also in line with recent attempts to reconstruct full energy spectra from only large-scale variables with CNNs [76]. These distributions are also overly shallow and biased towards the magnitudes of the scales they were taught by.

The shallowness of the amplitude distributions has an interesting impact on the prediction of the low  $k_t$  modes of the unresolved scales’ time derivative projection when  $\Delta t/\Delta t_{DALES}$  increases from 4 to 8. Fig. 7.8a shows that at  $\Delta t/\Delta t_{DALES} = 4$ , the model overpredicts the long-term  $k_t$  modes of the term, possibly due to a lack of history in the stencil. However, hiking  $\Delta t/\Delta t_{DALES}$  to 8 raises the amplitudes of the exact low  $k_t$  modes to the same order of magnitude as the remainder of the unresolved scales’ time derivative projection’s scales. This somewhat luckily positions them at the order where the ANN already guessed they should be, based on its high  $k_t$  stencil. In turn, this suddenly improves the term’s correlation in a rather unexpected manner. Similar unexpected responses could of course occur in different regimes of the turbulence and the discretisation, even though they are not observed elsewhere in this study. Hence, the trends observed here and the conclusions drawn from them should be treated with the care that a system with such nonlinear behaviour demands.

### 7.3.3. Inherent Predictability

The importance of correlation to the resolved-scales input can be appreciated by considering the Reynolds term’s distribution with  $k_z$  in Fig. 7.7c. In similar fashion to the cross term, the Reynolds term’s amplitude peaks at the cutoff wavenumber, where the ANN stencil operates. However, this term is the pure product of unresolved scales interactions and is therefore in general less dependent on the resolved scales variables that live close to the grid cutoff than the linear cross and time derivative terms. This might be the reason why its high  $k_z$  modes are worse-predicted than its low  $k_z$  modes, and why it displays a more uniform error distribution over  $k_z$  that constantly improves as the input stencils are widened in Fig. 7.10c. As shown in Fig. 7.8d, reducing the time step again positively impacts especially the high-amplitude  $k_z$  modes.

In contrast, the error does *not* worsen at increasingly coarse spatial resolution, despite the rising prominence of higher-order contributions from the infinite cascade of linear problems that result from the unresolved scales’ nonlinearity. This is very encouraging, because as  $h$  increases i) the nonlinearity traditionally makes the Reynolds term increasingly ill-posed, but ii) the term also becomes progressively more important and would be the dominant contribution at the unresolved scales of a much larger scale model [222]. However, since Fig. 7.10c shows how the Reynolds term benefits from added non-local input, the addition of such input as  $h$  increases may outweigh a loss in inherent predictability, in similar fashion as what was observed for the unresolved scales time derivative projection. Once  $h > L_c$ , the term might therefore start to become worse predicted. Hence, tests on datasets with a range of  $k_z$  modes larger than the turbulence’s correlation length should be carried out to confirm whether the predictability of the Reynolds term remains high even at the scales of larger-scale atmospheric models.

### 7.3.4. Outlook

Summarising, the ANN predictions of the interaction terms remain dramatically better than those of algebraic models at all the levels of discretisation that have been considered in this study. This improvement in predictability remains regardless of which stencils are chosen. The local input stencil appears to facilitate decent predictions of the smallest scales of the interaction terms, which does not harm the cross term prediction, but is detrimental to the unresolved scales' time derivative projection. In contrast, the Reynolds term appears to be more directly dominated by its weaker relation to the small, resolved scales. All terms respond favourably to reductions in  $C$ , which improve the well-posedness of the high  $k_z$  modes of the terms. The exception is the non-monotonic region in  $\left(\overline{\psi \frac{\partial w'}{\partial t}}\right)_\Omega$ , which should serve as a cautionary note on the generality of these trends and their explanations.

In all, the individual terms' predictability does not appear to suffer inherently from coarser discretisation. However, this might change once  $h > L_c$ . Furthermore, as the magnitude of the unresolved scales projections is redistributed from the well-predicted cross term to the worse-predicted Reynolds term at coarser  $h$ , the overall error in the unresolved scales' projections does in fact increase when  $h$  increases. As the contributions of the interaction terms relative to the Galerkin terms will also only increase at larger  $h$ , this does mean that the overall model error rises and that forward simulations may increasingly fall prey to those errors.

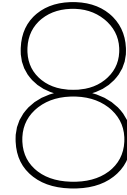
Robijns operated ANNs with local stencils that trained at  $C$  an order of magnitude less than the smallest numbers presented in Fig. 7.6a and ran simulations on problems with a much narrower range of scales than those considered here [209]. Therefore, while displaying considerable success in simple settings, Robijns' architectures are unlikely to be fully adequate to the model turbulence problem.

Finally, note that no tests have been conducted in this section to establish whether the ANN predictions of the interaction terms generalise with respect to different  $h$  and  $\Delta t$  combinations. Robijns showed results where the ANNs do appear to generalise with respect to  $h$  and  $\text{Re}$  [209]. It is obviously interesting to see whether this translates to the more realistic turbulence problem considered here. However, it is considered a second priority in this study, behind ensuring that the offline results presented in this section translate to online simulations. Therefore, such tests will not be carried out.

## 7.4. Conclusions

This chapter has ventured to answer RQ2. RQ2.1 is dealt with in Section 7.2, which finds that wide, shallow ANN architectures with ReLU activation, trained to minimise  $J$  without weight regularisation or dropout are beneficial for learning the interaction terms of the model problem in a priori simulations. Adding a time history to the feature set strongly improves the prediction of the unresolved scales' time derivative projection, while including the Galerkin terms as input features further improves both the prediction of this projection and that of the cross term. The models are relatively proficient at reproducing the exact statistics of the interaction terms outside their training envelope and significantly outperform their algebraic counterparts. However, the terms are less impressively learned than for Robijns' simple problem and systematically err on the low side, with potential implications for the forward problem.

In answer to RQ2.2, the interaction term predictions considered here do not display a significant dropoff in predictability when they must account for an increasing number of increasingly energetic spatial or temporal unresolved scales, outside their training envelope. Rather, the observed predictability changes in the terms are ascertained to depend on the stencil of an ANN input's relation to the scales of the problem: The local stencil facilitates good prediction of the smallest resolved scales on the grid, favouring the cross term's modal distributions. All terms but the unresolved scales' time derivative projection's response to  $\Delta t$  improve with lower  $C$ , as the stencil's domain of dependence encapsulates an increasing number of high  $k_z$  modes. In spite of the individual terms remaining well-predicted, the inherently more ill-posed and worse-predicted Reynolds term will increasingly dominate the interaction terms' contribution at lower  $h$ , which itself will begin dominating the resolved scales terms. Therefore, the modelling error associated with the term could eventually become sufficiently substantial that it may overshadow forward simulations of the resulting numerical model.



## Properties of VMM-ANNs: Simple Problem

The previous chapter ascertained that relatively simple ANN architectures based on local data stencils of the resolved scales possess considerable skill in learning the interaction terms of a VMM for the Boussinesq-forced test case, and that the potential for the resulting VMM-ANN models to improve state of the art algebraic models and possibly SP is therefore vast. However, for this potential to materialise, the models must translate their skill to forward problem simulations. This is the topic of RQ3, which is answered in the upcoming two chapters.

The forward problem introduces two additional dimensions of which the ANNs trained on error-free data in offline settings are unaware and to which the field has paid relatively little attention so far. First, the nonlinear nature of the problem requires the iterative Newton procedure outlined in Section 5.5.1 to be carried out in each time step. To consistently couple the resolved and unresolved scales, the ANNs are here included in this procedure, although it is a dimension that the ANN never encountered in generating the results in Chapter 7. Second, the ANNs will inevitably introduce modelling errors, which means that their input in online simulations will become polluted by the errors they themselves induce. However, the ANNs have only been trained on exact data from the statistical envelope of the DALES-generated turbulence. One might therefore expect these two dimensions to introduce new and interesting hurdles for the models to clear, which in turn might have contributed to the lack of generalisation and stability observed in previous ANN unresolved scales models (these were discussed in Section 3.5.3).

The following two chapters will answer the three subquestions of RQ3. First, they will confirm that the added, unknown dimensions of the forward problem render the simple ANNs from the previous chapter insufficiently informed to capitalise on their considerable promise. They will show that this results in the VMM-ANNs missing two fundamental prerequisites of numerical models, as presented in Section 3.5.3: A unique solution is not always attainable, and even when it is, the model does not continuously find the unique solution throughout its running, yielding instability. This answers RQ3.1. The chapters will furthermore show that traditional approaches to improve the forward simulations are insufficient to remedy these fundamental flaws, suggesting that the added dimensions of the forward problem must be addressed at their root for the encouraging results from Chapter 7 to translate to online running. This answers RQ3.2. Finally, the models' computational cost is considered, in answer to RQ3.3.

Uniqueness and stability are properties that the model should possess independently of an ANN's prediction accuracy. Hence, this chapter first eliminates the prediction error and focusses on the impact of the iterative procedure. It returns to the manufactured solution problem, for which the terms are predicted close to perfection and the solution can be almost perfectly attained, as shown in Section 5.5.7. This also allows analysing the model's properties in a setting where they can be understood.

This chapter considers RQ3.1 and RQ3.2, beginning with an assessment of the model's uniqueness and stability characteristics in Section 8.1 and Section 8.2 over much more conventional levels of discretisation and Courant number  $C$  than considered in [209]. These sections identify two main failure modes of the model and suggest underlying causes, while Section 8.3 investigates which parameters of the simulations do and do not affect these properties.

## 8.1. Uniqueness

Section 5.5.1 introduced the nonlinear nature of the weak residual  $\mathcal{R}_{w_i}$  and the corresponding necessity to solve for the degrees of freedom that minimise its  $L_2$  norm iteratively. Assuming the ANN were a linear operator  $\mathcal{L}$ ,  $\mathcal{R}_{w_i}$  would be a coupled set of quadratics in  $[a_{i-1}, a_i, a_{i+1}]$  for the chosen basis, where each quadratic is a function of three unknown amplitudes:

$$\mathcal{R}_{w_i}^{n+1} = \left( \bar{\psi}_i, c_{t,1} \sum_{j=i-1}^{i+1} \bar{\psi}_j a_j^{n+1} \right)_{\Omega} - \left( \frac{\partial \bar{\psi}_i}{\partial z}, \sum_{j=i-1}^{i+1} (\bar{\psi}_j a_j^{n+1})^2 \right)_{\Omega} + \mathcal{L} \left[ \sum_{j=i-1}^{i+1} \bar{\psi}_j a_j^{n+1}, \sum_{j=i-1}^{i+1} \bar{\psi}_j (\bar{\psi}_j a_j^{n+1})^2, K \right] - (\bar{\psi}_i, F_i)_{\Omega} \quad (8.1a)$$

$$F_i = c_{t_2} a_i^n + c_{t_3} a_i^{n-1} - f \quad (8.1b)$$

$$K = K(a_i^n, a_i^{n-1}, \dots) \quad (8.1c)$$

Where  $K$  contains all ANN input features that are not functions of the unknown amplitudes, such as information from previous time steps (e.g.  $a_i^n$  and  $a_i^{n-1}$ ). The uniqueness of any  $\bar{w}^{n+1}$  hinges on the number of real roots that Eq. (8.1) prescribes for  $\mathcal{R}_{w_i}$ . Bézout's theorem limits how many such roots there can be [225]. In its base form, this theorem states that a pair of polynomials  $X_1$  and  $X_2$  of degrees  $d_1$  and  $d_2$  that have less than infinitely many common points has a number of intersections equal to the product of their degrees  $d_1 d_2$ , if one counts intersections at infinity, in the complex plane and of higher multiplicity than 1. This may be generalised to higher dimensional systems: Assume one has  $n$  homogeneous polynomials in  $n+1$  variables of degrees  $d_1, \dots, d_n$ . These polynomials form  $n$  "hypersurfaces" in a projective space of dimension  $n$ . If a finite number of hypersurface intersections exists within a "ground field" that is algebraically closed, the exact number of intersections is  $d_1 \cdot d_2 \cdots d_n$ , if one again counts intersections at infinity, in the complex plane and of higher multiplicity than 1. In this context, Bézout's theorem provides an upper bound to the amount of real roots that  $\|\mathcal{R}_{w_i}\|_2$  might have in terms of the number of elements of a discretisation  $n_{el}$ :  $2^{n_{el}-1}$ .

While the number of solutions to Eq. (8.1) is therefore exponential in its number of spatial degrees of freedom, this often has no practical implications. There are two reasons for this. First, infinity and complex roots occur often, but are also often excluded from the numerical method's possible solution set. Multiplicity roots are practically speaking of no concern. Second, even when multiple roots materialise in the numerical method's solution space, the problem can remain practically unique if the spurious roots are sufficiently far removed from the physical basin of attraction that a well-initialised problem never encounters it.

To analyse the uniqueness of the VMM-ANN in particular and the Newton procedure it must negotiate in every time step in general, it is instructive to map the response of  $\|\mathcal{R}_{w_i}\|_2$  to two degrees of freedom. Hence, the problem is reduced to three-element discretisations with two fixed boundary nodes and two degrees of freedom  $a_1$  and  $a_2$ . These amplitudes are illustrated at an instance in time in Fig. 8.1, along with the piecewise linear bases  $\bar{\psi}$  that weight them, the resulting  $\bar{w}$ , the continuous solution  $w$  and the  $w'$  that results.

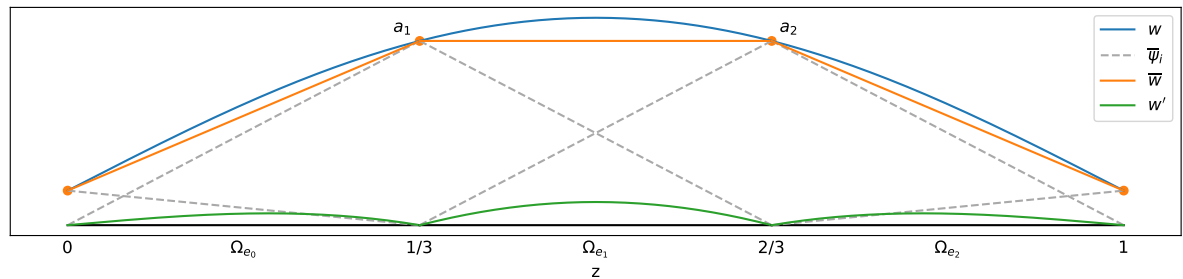


Figure 8.1: Finite element discretisation of the manufactured solution problem with two degrees of freedom.

This discretisation gives rise to response surfaces of  $\|\mathcal{R}_{w_i}\|_2$  in  $a_1$  and  $a_2$  at each time step, such as those presented in Fig. 8.2. The ANNs trained to close this model display the near-perfect learning behaviour presented in Fig. 5.13. Hence, these ANNs are expected to predict  $\mathcal{R}_{w_i}$ 's roots nearly perfectly if they are given correct input and remain within the confines of the manufactured solution that the model was trained on.

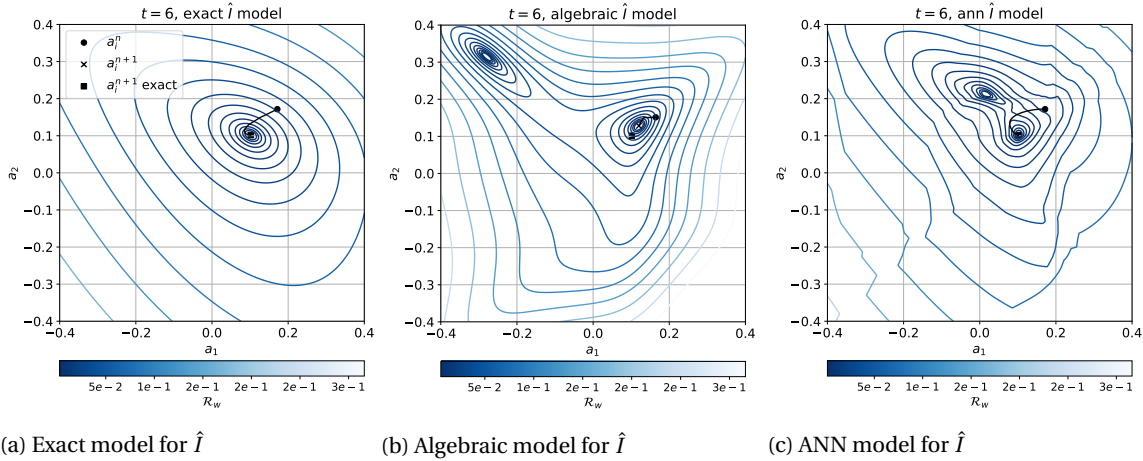


Figure 8.2: Response surfaces of  $\|\mathcal{R}_{w_i}\|_2$  for a manufactured solution problem with two degrees of freedom  $a_1$  and  $a_2$ . They derive from simulations where  $\Delta t = 2$ ,  $h = \frac{1}{3}$  and  $C = 1.2$ . The ANN's structure is the same as that of the FS3 model in Table 7.3.

Fig. 8.2 shows  $\|\mathcal{R}_{w_i}\|_2(a_1, a_2)$  when exact, algebraic and ANN models predict the interaction terms. The responses are displayed for the first time step at which the unresolved scales model is active<sup>1</sup>, such that the plotted convergence paths of each simulation originate from the same initial condition and can be compared.

Fig. 8.2a shows that the exact model has a single, well-defined root. This may be understood by returning to Eq. (8.1). When an exact model for  $\hat{I}$  is prescribed, it exactly specifies what the terms should be and is not a function of the problem's degrees of freedom. Therefore, it does not affect the problem's order, but interestingly also does not display more than the single, correct root, to which the solution converges. It is an example of a situation where only a single root appears in the real, finite space of solutions to Eq. (8.1).

In contrast, the algebraic model's input depends on  $a_i^{n+1}$  through  $\overline{\mathcal{R}}_s$  and  $\tau$  (see Eq. (5.30)). Furthermore, it does so in a nonlinear manner, by multiplying  $\overline{\mathcal{R}}_s$  with a nonlinear  $\tau$ . This allows the model to affect the problem's roots more profoundly, illustrated by the appearance of a second root of  $\|\mathcal{R}_{w_i}\|_2$  in Fig. 8.2b. Practically speaking, however, this is not of much concern, for the following three reasons. First, the spurious root and its attractor boundary are situated relatively far from the domain where the model operates; in the language of complex systems, the model is relatively resilient [216]. Second, the gradients of  $\|\mathcal{R}_{w_i}\|_2$  remain smooth, such that it is unlikely that the model's Jacobian will induce large, unexpected excursions that might cross the attractor basin's boundary. Finally, the model's Jacobian is highly commensurate with its predicted space of  $\|\mathcal{R}_{w_i}\|_2$ , such that up-to-date Jacobian guesses direct the model very proficiently towards its root from any initial condition. This yields rapid convergence, and makes attractor switches due to bad gradient predictions very unlikely. Hence, the algebraic model remains practically unique.

Despite these attractive characteristics, the algebraic model mispredicts the root of  $\|\mathcal{R}_{w_i}\|_2$  with respect to the exact model (indicated by a black square in the response surfaces in this chapter). The ANN estimate of  $\hat{I}$  returns a much better guess of the position of the root with respect to the exact solution. Fig. 8.2c shows that this estimate nearly coincides with the root, as the near-perfect training of the model would lead one to expect. However, the figure also displays the model's adverse characteristics in the same three categories that left the algebraic model practically unique. First, it shows the appearance of a second root. However, in contrast to the algebraic model, this root's attractor boundary lies much closer to the correct root, making it likelier for the model to converge to the spurious solution. Second, its  $\mathcal{R}_{w_i}$  space is highly nonlinear, with strong, local gradient changes and even discontinuities appearing. This makes converging the model a highly challenging procedure, where sudden, large mispredictions of the Jacobian that could drive the model far from its desired root are likely. Finally, the model's algebraic Jacobian does not match this distorted  $\mathcal{R}_{w_i}$  space well, orienting the iterative increments to  $a_1$  and  $a_2$  in the wrong direction. In Fig. 8.2c, this brings the solution very close to spilling over into the wrong attractor and converging to the spurious root. Hence, this direct ANN model for the interaction terms does not appear to be practically unique.

One may identify two facets of the VMM-ANNs' non-uniqueness. The first is laid bare by reducing the ANN to a linear operator, as assumed in Eq. (8.1), and simplifying the ANNs' architecture. This can be done

<sup>1</sup>This is the third time step. Exact closure terms are employed in the first two time steps, see Section 5.5.5

by replacing their non-linear ReLU activation functions with linear transformations from layer  $n$  to  $n + 1$ :

$$x_i^{n+1} = \omega_{ij}^n x_j^n + b_i^{n+1} \quad (8.2)$$

The simplest ANN model for such a situation consists of a single hidden layer with a single node that linearly transforms a sum of the input features to the output features. Such a model is illustrated in Fig. 8.3a.

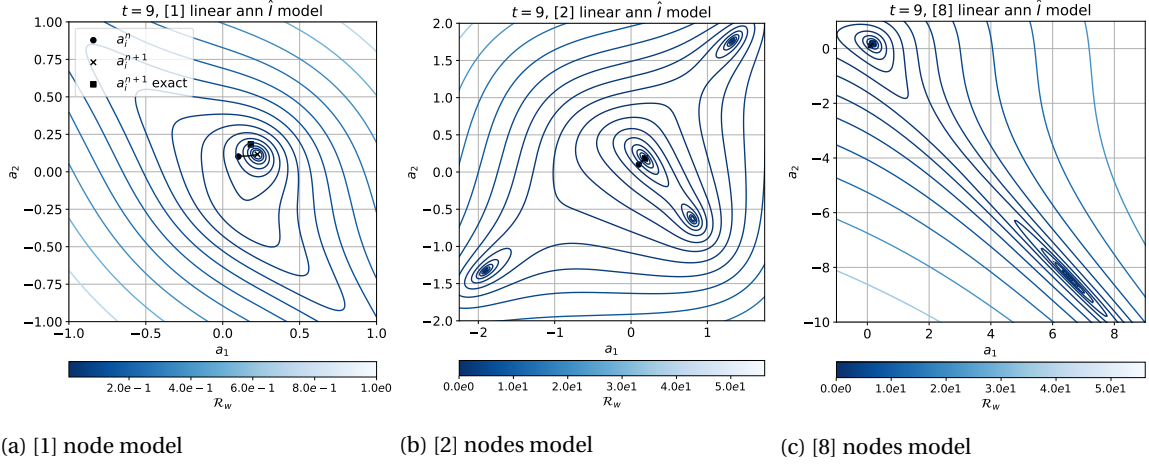


Figure 8.3: Response surfaces of  $\|\mathcal{R}_{w_i}\|_2$  for a manufactured solution problem with two degrees of freedom  $a_1$  and  $a_2$  for ANN models with a linear activation function. They derive from simulations where  $\Delta t = 3$ ,  $h = \frac{1}{3}$  and  $C = 1.8$ . The ANNs have a single layer with varying numbers of neurons and take FS3 as input.

A single-neuron, linear model is incapable of good predictions, as one might expect. However, it also possesses only a single root, likely because the ANN is unable to add much complexity to  $\|\mathcal{R}_{w_i}\|_2$ . However, adding a second neuron to this model's hidden layer is already sufficient to make Bézout's upper bound of four roots spread out into the real space that the VMM-ANN might converge to. For this simple problem, they are well-spaced and adding further neurons to the layer tends to spread the roots farther apart, as shown in Fig. 8.3c. However, such "root spreading" is concerning and has real implications, as seen later in this chapter.

The second aspect of the VMM-ANN's non-uniqueness is introduced by restoring the nonlinearity to the ANN. Since ANNs commonly derive their strength from being a highly nonlinear map from their input to their output and Section 3.3.4 and Section 6.1 established that linearised models of the unresolved scales of the turbulence problem at coarse discretisation will not suffice, the model must likely possess such nonlinearity to be useful. However, the implications of sequentially reintroducing the nonlinearity are illustrated in Fig. 8.4, which considers a simplified model architecture of two neurons in two hidden layers ([2, 2]).

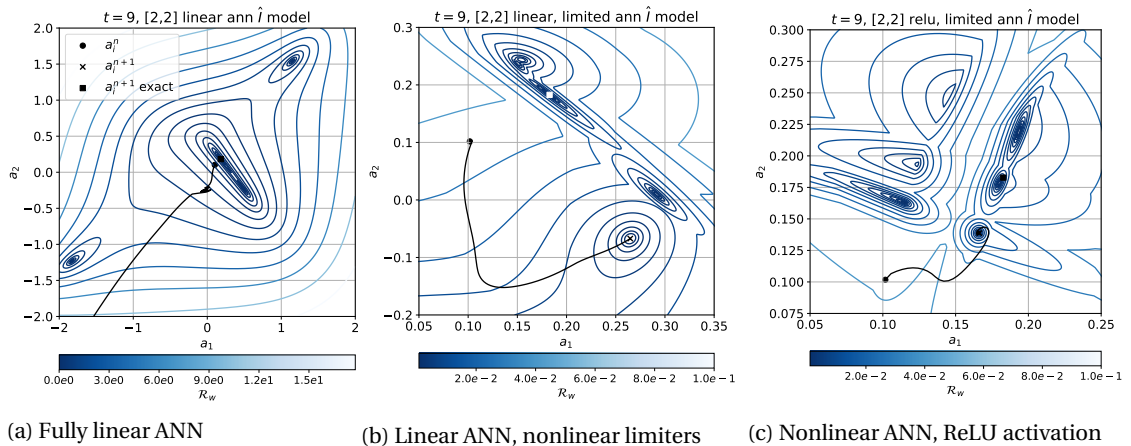


Figure 8.4: Response surfaces of  $\|\mathcal{R}_{w_i}\|_2$  for a manufactured solution problem with two degrees of freedom  $a_1$  and  $a_2$  for [2, 2] ANN models with various degrees of nonlinearity. They derive from simulations where  $\Delta t = 3$ ,  $h = \frac{1}{3}$  and  $C = 1.8$ . The ANNs take FS3 as input.

Fig. 8.4a illustrates the fully linear model, which still displays 4 roots. As will be discussed in Section 8.3.3, Robijns found that limiting the ANN predictions to the maximum and minimum values of their training dataset may aid the convergence of the nonlinear procedure. However, Fig. 8.4b illustrates that adding such nonlinear limiters to the linear ANN completely distorts the  $\mathcal{R}_{w_i}$  space and in fact adds a root. Finally, Fig. 8.4c shows that substituting the linear activation functions for ReLUs again further complicates the  $\mathcal{R}_{w_i}$  space and that another root is added.

These simple networks illustrate that once the model for  $\hat{I}$  is left to ANNs of much higher nonlinearity than the second order polynomials in  $a_i^{n+1}$  that predict the Galerkin terms, Bézout's theorem no longer bounds the maximum number of roots of  $\|\mathcal{R}_{w_i}\|_2$ . Even though these ANNs predict the correct root well, they can and do introduce more roots. More worryingly, more roots appear as the model's nonlinearity increases, and they often cluster increasingly closely together (pay particular attention to the comparative axis scales in Fig. 8.4). In Fig. 8.4c, this would require the solution to travel across an attractor with a spurious root to arrive at the correct solution, an obvious impossibility for Newton methods. Finally, the added nonlinearity highly distorts the gradients and distribution of attractors in the  $\mathcal{R}_{w_i}$  space. Therefore, the solution in Fig. 8.4b converges to a spurious root, despite being initialised closest in Euclidian distance to its correct root. Even the linear model's weak residual space presented in Fig. 8.4a is sufficiently incommensurate with the model's Jacobian that the solution is driven to infinity, instead of converging to the correct root.

If the spurious roots would appear very close to the correct solution, even this non-uniqueness might not have been too concerning to a pragmatist if the solution prediction remains adequate. However, even for Fig. 8.4c, where the spurious root is not overly far removed from the correct root, the wrong prediction is damaging enough for the next time step to no longer represent anything close to the correct roots. This leads both the limited linear and fully nonlinear ANNs to diverge in the time step after that plotted in Fig. 8.4.

In all, direct VMM-ANNs as considered by Robijns [209] are non-unique in very problematic ways. Linear ANNs already tend to bring out the maximum number of roots of the nonlinear problem, while further roots beyond the Bézout bound are introduced as the ANNs' nonlinearity is restored and extended. The roots are often closely clustered and their surrounding attractors highly distorted, leading to attractor switches and consequent divergence of the models.

This will not have shown up in Robijns' studies of the model's sensitivity to noisy and biased predictions of the interaction terms, as these cases still employed an exact model for the terms with only a single root [209]. However, it does not explain why the model often remained stable and successful in that study or in Section 5.5.7. This will be addressed next.

## 8.2. Stability

Stable simulations should be continuous and well-defined, in the sense that small perturbations to the input data should only yield small perturbations to the output data [111]. Given that all input to the models is finite, this definition encompasses divergence of the model to infinity. In this light, the weak residual spaces of the VMM-ANNs presented above are clearly not stable. This is due to the large number of attractors that present themselves in the VMM-ANN's weak residual space and the model's inability to successfully navigate such a space, leading to wildly different outcomes of the models if they are pushed over the boundary of a basin of attraction. As soon as such an attractor switch occurs, the models tend to wander off in unpredictable directions and rapidly grow to infinity. Therefore, the traits that give the mode its non-unique character are also factors driving its instability.

The simulation results presented in Section 5.5.7, however, were exceptionally proficient, leading one to question what else governs the stability of the VMM-ANNs. An answer to this question would also answer RQ3.1 more comprehensively. The question is therefore treated at present. For linear models, one could analyse stability analytically by means of a Von Neumann analysis [111]. A more common approach for nonlinear problems, such as the problem at hand, is to evaluate the energy balance of the model. However, as explained in Section 5.3.1, it is not in general possible to evaluate the contribution to the resolved-scales energy balance when the interaction terms' sum over elements is predicted by the ANN, rather than their element contribution. Therefore, this section limits itself to a direct analysis of the problem, presented in Fig. 8.5 and Fig. 8.6, while Section 8.3.3 gives an interpretation of the energy evolution for the simple problem. This still creates a window through which the inner workings of the instability may be seen, though follow-up work should ideally conduct the analysis in terms of the energy balance directly.

A primary driver of when instability manifests itself appears to be  $C$ . Fig. 8.5 shows the temporal evolution of the three degrees of freedom that were predicted well at the end of Section 5.5.7, at three increasingly

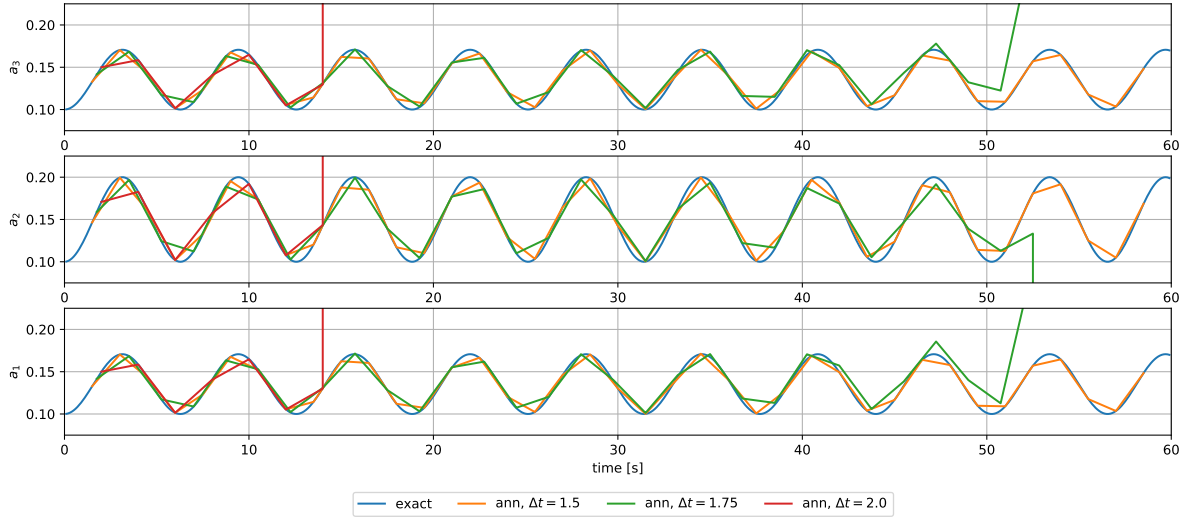


Figure 8.5: Temporal evolution of the three degrees of freedom  $a_1$ ,  $a_2$  and  $a_3$  at increasing  $\Delta t$  of simulations with  $h = 0.25$ , closed by ANNs of shape  $[512, 512]$  taking FS3 as input.  $C = [1.2, 1.4, 1.6]$  for  $\Delta t = [1.50, 1.75, 2.00]$ .

coarse time discretisations. As  $C$  increases through increments to  $\Delta t$ , the models start to diverge, and do so progressively early in the simulation. At  $\Delta t = 1.5$  ( $C = 1.4$ ), divergence occurs in the  $2h$  mode: After a period of several time steps in which  $a_2$  is slightly mispredicted, the error carries over to the neighbouring modes and the solution is driven to  $\pm\infty$ . The model that runs with the largest time step,  $\Delta t = 2$ , has  $C = 1.6$  and diverges straight to infinity from a seemingly well-predicted state.

Hence, there are two distinct versions of the instability; both are presented below with the aid of Fig. 8.6. This figure yet again shows  $\|\mathcal{R}_{w_i}\|_2(a_1, a_2)$  for a problem with two degrees of freedom, where  $C$  varies between 0.6, 1.2 and 1.8 in its three windows, i.e. it is a different problem than presented in Fig. 8.5. Fig. 8.6 shows the first time step,  $n_e$ , in which the models' prediction error exceeds  $1 \cdot 10^{-4}$ , an order of magnitude larger than the largest error observed in the near-perfect cases in Section 5.5.7. Note that similar to the time at which instability sets in,  $n_e$  reduces as  $\Delta t$  rises: From 120 time steps for the fine model, through 21 steps for the intermediate model, to only 13 steps for the coarsest model.

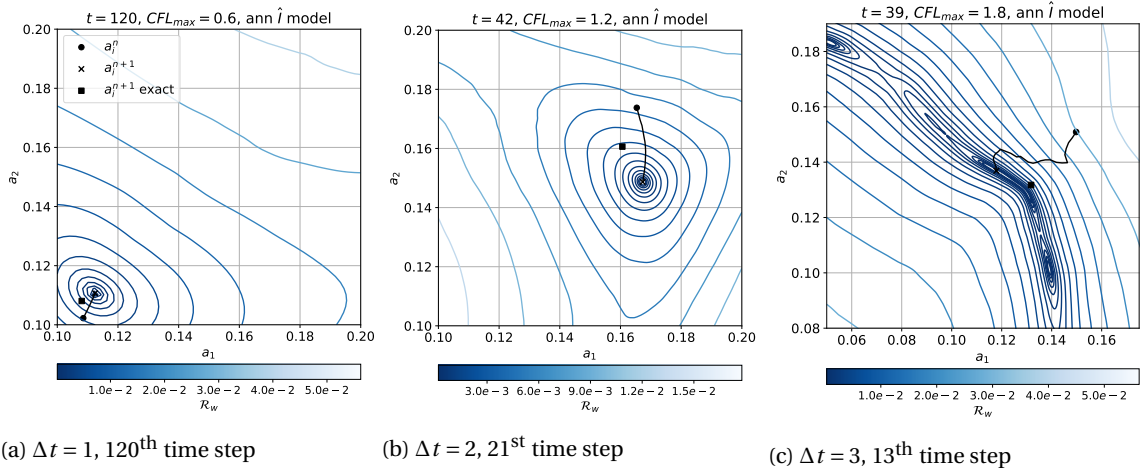


Figure 8.6: Response surfaces of  $\|\mathcal{R}_{w_i}\|_2$  at the time step  $n_e$ , when the solution's  $E_{L_2} > 10^{-4}$  for the first time, for three increasing  $\Delta t$ . The spatial grid spacing is  $h = \frac{1}{3}$ , while the ANNs take FS3 as input and have a  $[512, 512]$  structure.

The first version of the instability is directly associated with the nonlinearity of the weak residual space. It is illustrated in Fig. 8.6c. Within a full period  $T$  of the sine wave, the problem becomes increasingly ill-posed as  $\Delta t$  increases (when  $\Delta t > T$ , this perfectly periodic problem is identical to one with a time step of  $\Delta t - T$  and

should therefore behave similarly as when  $\Delta t < T$ ). In particular, for increasing  $\Delta t$ , the initial prediction of  $a_1$  and  $a_2$  will on average be farther from its correct solution, requiring the model to traverse progressively long distances through the weak residual space to find a root. This makes it much more likely that a spurious root is encountered along the way, or that the model comes across regions where bad gradient predictions drive it to infinity. This is exacerbated by the weak residual space, which itself becomes less workable at larger  $\Delta t$ : In Fig. 8.6c, multiple, clustered roots again appear and the gradient predictions become increasingly erratic. Given that the largest  $\Delta t$  model presented in Fig. 8.5 departed from a near-perfect initial condition, but diverges in the time step after that plotted here, it is conjectured that an ill-posed weak residual space is the primary driver behind the direct divergence to infinity of that simulation also.

The second version of instability is the unstable propagation and accumulation of errors. This instability makes single modes in the intermediate-level discretisation in Fig. 8.5 grow, leading them to diverge the Newton procedure. Fig. 8.6a and Fig. 8.6b show the response surfaces associated with the onset of such instabilities. They are not related to the ANN's distortion of the weak residual, as the models converge well to the prescribed root. However, the figures show that the root itself is wrongly positioned. These appear to be "genuine" model errors. Although they initially quite small, these errors increase over several time steps: The ANN makes an error, this feeds lower quality input back to the ANN in the next time step and further deteriorates the predictions. A point is then quickly reached where the initial condition for a time step is sufficiently far removed from the training space of this non-generalised model that no roots can be found and the simulation diverges.

While erratic behaviour is expected of the model once the solution leaves the region of data where the model was trained, it remains unclear why the model, which is excellent when operating inside the training space, begins displaying errors at all. In fact, avoiding modelling error was a primary driver for considering the near-perfect, simple manufactured solution problem in this chapter. It is therefore interesting that the onset of instability appears to potentially result from very small errors, and that it grows in a fashion reminiscent of classical small-scale mode growth associated with unstabilised finite element methods [34]. However, consider that the problem has no mechanism of dissipating energy from such modes other than the interaction terms themselves. This means that any error in the terms on the overly energetic side must be compensated by an equal error on the dissipative side for the simulation to remain stable. Instead, as will be discussed in Section 8.3, the errors tend to reinforce themselves due to the nature of the problem and the interaction terms. Without the explicit inclusion of an operator that dampens the rising modes, the model has no way of remaining stable and has no choice but to blow up.

In summary and in the context of RQ3.1, the two dimensions of the forward problem that are added to the offline problem in this chapter are observed to correspond to two sources of instability: Those engendered by an ANN-induced, ill-posed weak residual space and those driven by self-reinforcing error accumulation. These sources explain the instabilities observed by Robijns, and suggest why that study by and large managed to run stable calculations at very low  $C$  for very well-trained ANNs in the context of a simple problem. To simulate more complex turbulence at higher  $C$ , these instabilities must be addressed. This is the topic of RQ3.2, whose study begins in the next section.

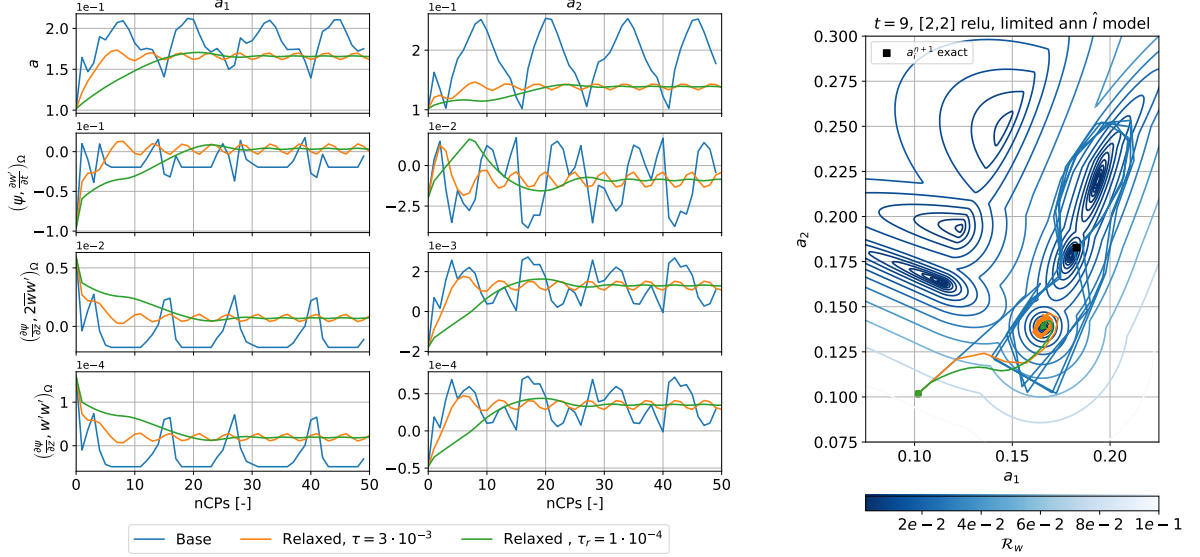
## 8.3. Improvement Attempts

To address the characteristics found and the concerns raised by the two previous sections, the following sections focus on several strategies that attempt to improve the identified drawbacks of the model, concentrating on RQ3.2. They assess which modified VMM-ANN architectures constitute better platforms to translate the offline performance to online simulations, and which do not. Sections 8.3.1 to 8.3.3 first focus on whether it is possible to improve the forward simulation's architecture somewhat to better navigate the nonlinear weak residual space, through the introduction of adaptive relaxation, a better Jacobian and limiting schemes. Next, Sections 8.3.4 to 8.3.7 consider the influence of the ANN's design within the model, by gauging the influence of different time stencils, by including the nonlinear procedure in the ANNs' training space and even by replacing the direct ANN with an explicit, order-controlled scheme, which can also be posed as a hybrid formulation with the algebraic model.

### 8.3.1. Adaptive Relaxation

The VMM-ANNs in the previous sections often diverged due to overambitious steps along a predicted gradient direction, which landed the models in regimes where they converged to spurious roots or directly diverged. Another, somewhat related failure that is often encountered is shown in Fig. 8.7. Here, the model

previously considered in Fig. 8.4c oscillates around three of its roots, without ever converging to any of them. Fig. 8.7a shows that the strong oscillations of the solution are reflected in the interaction terms. These change strongly between single CPs for both degrees of freedom, which induces large, sudden changes in the magnitude and direction of the CP solution vector  $\Delta a_i$ . These consequently fail to drive the solution towards any root.



(a) Convergence traces of the solution  $a$  and the components of  $\hat{I}$  for the weak forms for  $a_1$  and  $a_2$ .

(b) Response surfaces of  $\|\mathcal{R}_{w_i}\|_2(a_1, a_2)$  and convergence paths of  $a_1$  and  $a_2$ .

Figure 8.7: The impact of adaptive relaxation on convergence of  $\mathcal{R}_w$  for a [2,2] ANN model for  $\hat{I}$  with ReLU activation functions and FS3 as input. Blue lines signify convergence without any relaxation, orange lines are adaptively relaxed with  $\tau_r = 1 \cdot 10^{-3}$  and green lines with  $\tau_r = 1 \cdot 10^{-4}$ . The simulations are run with  $\Delta t = 3$ ,  $h = \frac{1}{3}$ ,  $C = 1.8$ , and the algebraic Jacobian.

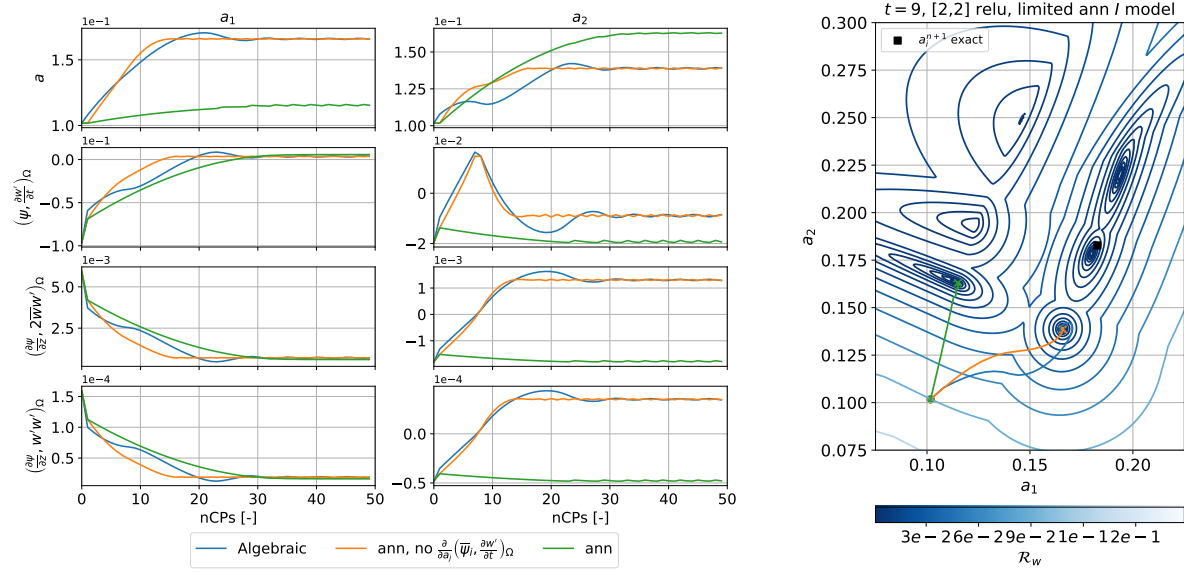
If one consults Appendix C.3, one will see that the iterative Newton procedure can be understood as a forward Euler discretisation of a continuous problem that should monotonically decay the weak residual to the root of the basin of attraction in which it is initialised. This stands clearly in contrast with the oscillating convergence paths in Fig. 8.7. In Appendix C.3, adaptive relaxation of the Newton procedure is identified as an interesting solution. Such relaxation prevents large, uncontrolled steps in the highly nonlinear portions of the space, where monotonic convergence towards the nearest root is desired. At the same time, it allows large steps once the model approaches a root. The effects of adaptive relaxation with two different scales of its free parameter  $\tau_r$  are shown in Fig. 8.7.

For the displayed case, adding increasing levels of adaptive relaxation progressively manages to rid the Newton procedure of its oscillating behaviour. Smaller allowed deviations from the continuous convergence path yield more monotonic behaviour, despite requiring more CPs to converge the model. However, Fig. 8.7 also shows that adaptive relaxation i) still cannot guarantee convergence to the correct root and ii) cannot even guarantee convergence to the root of the attractor in which the time step is initialised, the lower left root in Fig. 8.7b.

### 8.3.2. ANN Jacobian

The second of the drawbacks that remain when running with relaxation can be amended by addressing the Jacobian prediction. In the above sections, many cases could have continued converging to correct roots for several time steps if they were correctly steered. However, because the weak residual spaces of ANN-closed models differ so substantially from those predicted by algebraic models, the algebraic Jacobian cannot faithfully represent the gradients of the ANN-closed model, leading the simulations into spurious attractors or even to infinity. Therefore, the ANN Jacobian elaborated on in Section 5.5.4 is introduced to the model here. Its effects are illustrated by Fig. 8.8.

The figure displays relaxed convergence for the same case as in the previous section, with three different



(a) Convergence traces of the solution  $a$  and the components of  $\hat{I}$  for the weak forms for  $a_1$  and  $a_2$

(b) Response surface of  $\|\mathcal{R}_w\|_2(a_1, a_2)$  and convergence paths of  $a_1$  and  $a_2$

Figure 8.8: The impact of the Jacobian implementation on convergence of  $\mathcal{R}_w$  for a [2,2] ANN model for  $\hat{I}$  with ReLU activation functions and FS3 as input. Blue lines signify convergence with an algebraic Jacobian (Eq. (5.28)), orange lines a ANN-based Jacobian that ignores the unresolved scales' time derivative and green lines the full ANN Jacobian. The simulations are run with  $\Delta t = 3$ ,  $h = \frac{1}{3}$ ,  $C = 1.8$ , and  $\tau_r = 10 \cdot 10^{-4}$ .

Jacobians. Substituting the algebraic Jacobian's cross and Reynolds term contributions for their ANN counterparts (blue and orange lines) improves the convergence, highlighting the extent to which these terms are differently predicted when an ANN is embedded in the model. However, this is still insufficient to restrain the model from proceeding into the wrong attractor.

The prevention of an attractor switch is only achieved once the model employs the full ANN Jacobian, including the unsteady unresolved scales projection's contribution (green line). Once this is included, the model converges to the root of its initial attractor along a relatively straight convergence path. This suggests that directly embedding ANNs in the Newton procedure requires employing relatively high-fidelity versions of the Jacobian that must be continuously updated within a time step. Note that in achieving the correct convergence, the interaction terms related to  $a_1$  have not changed; the only change is in the prediction of the interaction terms to  $a_2$ . This shows how the misprediction of a single mode's interaction term is in fact sufficient to drive the entire solution to the wrong root.

In general, including the ANN Jacobian often helps preventing spillover into wrong attractors and divergence of the Newton procedure, though it cannot guarantee this. It yields better guesses for  $\Delta a_i$ , such that less relaxation is required for convergence. The combined effect reduces the number of CPs required to converge the model at any time step. However, as will be discussed in Section 9.4, its net effect is still an increase in computation time, as it requires four additional ANN evaluations per element.

While this section shows the ANN Jacobian's proficiency, it also immediately highlights its limits. While helping the model converge to the nearest root of the weak residual, this is still not the correct root. The inability of any Newton method to deal with this situation in the presence of an ANN closure therefore remains a fundamental flaw that simple fixes to the traditional numerical model's architecture cannot solve.

### 8.3.3. Limiting schemes

One way of deterring the ANNs from sabotaging the iterative Newton procedure was suggested by Robijns: He found that limiting ANNs to their training domain with nonlinear cutoffs was beneficial to bound the ANN predictions of the interaction terms during the iterative procedure [209]. When normalised, this study's training domain's limits are  $-0.5$  and  $0.5$  (see Section 5.4.1). However, the limited ANN prediction  $I_i$  could be cut off at any  $[I_{min}, I_{max}]$ :

$$\hat{I}_i = \begin{cases} I_{min}, & \hat{I}_i \leq I_{min} \\ \hat{I}_i, & I_{min} < \hat{I}_i < I_{max} \\ I_{max}, & \hat{I}_i \geq I_{max} \end{cases}$$

Such cutoffs were only intended to constrain the CP sequence and not to affect the roots of the residual. However, Fig. 8.4 showed that they have the potential to strongly distort the entire weak residual space and exacerbate the non-uniqueness problem as a result. Nevertheless, they are gauged here because they do appear to influence the stability problem in an interesting manner.

Their effect is illustrated by Fig. 8.9. This figure displays the time evolution of the three modes of a 4 element discretisation, along with their predicted interaction terms, for three simulations that are relaxed and use the ANN Jacobian. The first of these does not employ limiters and diverges after 7 time steps.

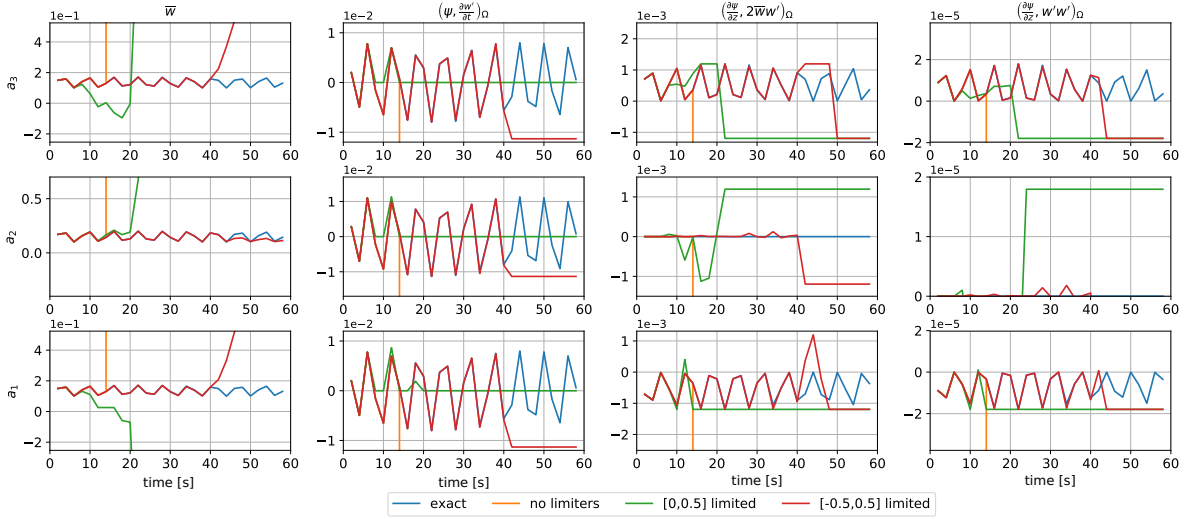


Figure 8.9: Temporal evolution of the three degrees of freedom  $a_1$ ,  $a_2$  and  $a_3$  when the components of  $\hat{I}$  are nonlinearly limited, for simulations run with  $h = 0.25$ ,  $\Delta t = 2$ ,  $C = 1.6$ .  $\hat{I}$  is predicted by an ANNs of shape  $[512, 512]$ , taking FS3 as input.

The second is limited to only allow normalised ANN predictions of the unsteady unresolved scales projection between  $[0.0, 0.5]$ . This is an interesting case, because for the manufactured sine problem considered here (Eq. (4.9)),  $w$  is strictly positive and  $\frac{\partial w}{\partial t}$  is in direct opposite phase to  $w$ . This latter observation can be seen in Fig. 8.9, where  $(\bar{\psi}, \frac{\partial w'}{\partial t})_{\Omega}$ , which follows  $\frac{\partial w}{\partial t}$ , is in opposite phase to  $\bar{w}$ . For each mode,  $(\bar{\psi}, \frac{\partial w'}{\partial t})_{\Omega}$ 's contribution to the problem's resolved-scale energy balance is  $-(\bar{w}, \frac{\partial w'}{\partial t})_{\Omega}$  (see e.g. Appendix B of [209] for an elaboration). Hence, in Fig. 8.9 the term will add energy when it is negative and subtract energy when it is positive. One may hypothesise that restricting the model to only positive predictions of the term prevents it from adding energy to the simulation, which potentially could prevent the unstable error accumulation discussed in Section 8.2.

In practice, however, this type of term-biasing yields a much too dissipative solution. The first time when the term should have become negative, but is limited at 0,  $\bar{w}$  already begins decaying rapidly. While the other terms initially compensate somewhat to keep the signal alive, the solution quickly reduces to around zero and even becomes negative. Once  $\bar{w} < 0$ , positive instances of  $(\bar{\psi}, \frac{\partial w'}{\partial t})_{\Omega}$  will actually add energy to the simulation, and its magnitude is expected to increase. However, the model is already sufficiently far removed from its functioning space that it switches attractors and diverges the Newton iterations. This illustrates the importance of including backscattering energy in the simulation: Neglecting it is here almost equally detrimental as including it. Less extreme positive limiting of the term is observed to decay  $\bar{w}$  somewhat slower, but it cannot prevent it.

Finally, limiting the solution to the ANN's full training domain  $[-0.5, 0.5]$  in similar fashion to what was done by Robijns does interestingly allow the simulation to hold on significantly longer than if no limiters

are used. Hence, while it distorts the weak residual space, including these limiters does discourage large excursions during the Newton iterations for this problem, similarly to what is reported by Robijns [209].

However, even this simulation also eventually diverges in a problematic way. Different modes do eventually begin growing a little, as evidenced by small errors in  $a_2$  of the cross and Reynolds terms around 30 s into the simulation. Eventually, this is enough to push the model to converge to a spurious root where all interaction terms are stuck in their limiters, at  $t = 42$  s. It is particularly instructive to consider  $\left(\overline{\psi}, \frac{\partial w'}{\partial t}\right)_\Omega$ . It gets stuck in its lower limiter, leading it to add energy to  $\overline{w}$ , which grows as a consequence. However, because  $\overline{w}$  was already close to the maximum of the physical signal, it now grows beyond this maximum value. Since  $\overline{w}$  and  $\left(\overline{\psi}, \frac{\partial w'}{\partial t}\right)_\Omega$  are exactly out of phase, this leads the ANN to believe that the term should be even more negative. However, the limiter disallows this. The result is that the term adds a constant amount of energy to the simulation every subsequent time step while  $\overline{w}$ 's amplitude grows exponentially larger: The rapid divergence has been replaced with a slow divergence.

The cross and Reynolds terms can also contribute to the instability. Depending on the sign of the solution's local gradient, these terms can be both positive and negative. Once the solution is sufficiently far from a physical situation, the terms can abruptly flip signs, suddenly beginning to add or subtract energy. This sometimes stabilises the simulation; in Fig. 8.9 it causes divergence even quicker.

The interesting thing to note here is that this confirms that the instabilities in the simulation can be self-reinforcing. If the ANN were not limited, but for instance linearly extrapolating outside its trained range, it would keep predicting larger values of  $\left(\overline{\psi}, \frac{\partial w'}{\partial t}\right)_\Omega$ , adding energy during the nonlinear iterations and immediately diverge, if there is no mechanism in the simulation that contains the energy. Even if a root to the solution does happen to exist in this direction, it will be one that adds energy.

Once the terms are stuck in their limiters, the iterative Newton procedure often fails to find any root, even with ANN Jacobians and high values of relaxation. Given how important it is that the Jacobian matches the space in which the ANN operates, this is not unsurprising, especially when considering that when the ANN is limited, the ANN Jacobian is undefined at the discontinuity. This ‘‘stagnating’’ failure mode leads to low-progress CPs or the slow divergence of the simulation over several time steps. It is revisited in Section 9.1.

In all, despite worsening the non-uniqueness problem, limiting is observed to help in delaying error introduction, although it does not possess the ability to eliminate error accumulation and the associated instability. This could potentially be improved somewhat by making the limiter continuous, or by making its extrapolating value penalise growth in energy-inducing terms. However, its formulation remains inherently opposed to the idea that well-generalised ANNs should also perform well outside their training space and be tested and confirmed to operate well there. Hence, the ANN should know of energy conservation and physics by itself. Therefore, the next two sections focus on such improvements.

### 8.3.4. Longer Temporal Input Stencils

As  $\Delta t$  increases within a period of the sinusoidal manufactured solution, almost all resolved, temporal variation is in the  $2\Delta t$  wave. This stands in contrast to the temporal resolutions considered for Boussinesq-forced model problem in Section 6.3, at which the terms are dominated by intermediate  $k_t$  modes that lie far from the  $2\Delta t$  wave. Hence, while increasing the local stencil to include the  $2\Delta t$  wave did not improve the prediction of the interaction terms for the Boussinesq-forced problem in Section 7.3, it may have a more favourable impact on this much more local manufactured solution. Contrary to targeting improved offline predictions of the interaction terms, the incentive for using longer input stencils in online simulations is their potential to ground the dominating  $k_t$  modes of the ANN in reality longer: If the prediction is conditioned on a time history, i) at least part of its input remains stationary throughout an iterative solution procedure, which keeps at least some of the ANN inputs reasonable, and ii) roots that would lie far from the history's tendency could be penalised.

The benefits of including two time levels to the ANN's input stencil are confirmed by Fig. 8.10. It shows the time-evolution of the problem with three degrees of freedom, closed by ANNs that are fed FS1 (information at time levels  $t^{n+1}$  only), FS3 (information at  $t^{n+1}$ ,  $t^n$  and  $t^{n-1}$ ) and an in-between feature set named FS1.1, which includes the solution at time levels  $t^n$  and  $t^{n+1}$ , at a simulation with  $C = 1.2$ . While the FS3 simulation remains stable and accurate throughout the simulated time domain, the FS1.1 simulation diverges, and the FS1 simulation diverges even earlier, even when the limiters are included in the models. Hence, the inclusion of longer time stencils is indeed a stabilising force, such that FS3 will be the default feature set for the Boussinesq-forced problem. However, given that much lower  $k_t$  modes dominate that problem's time history, it may require much longer time history stencils than considered in this work for these benefits to materialise.

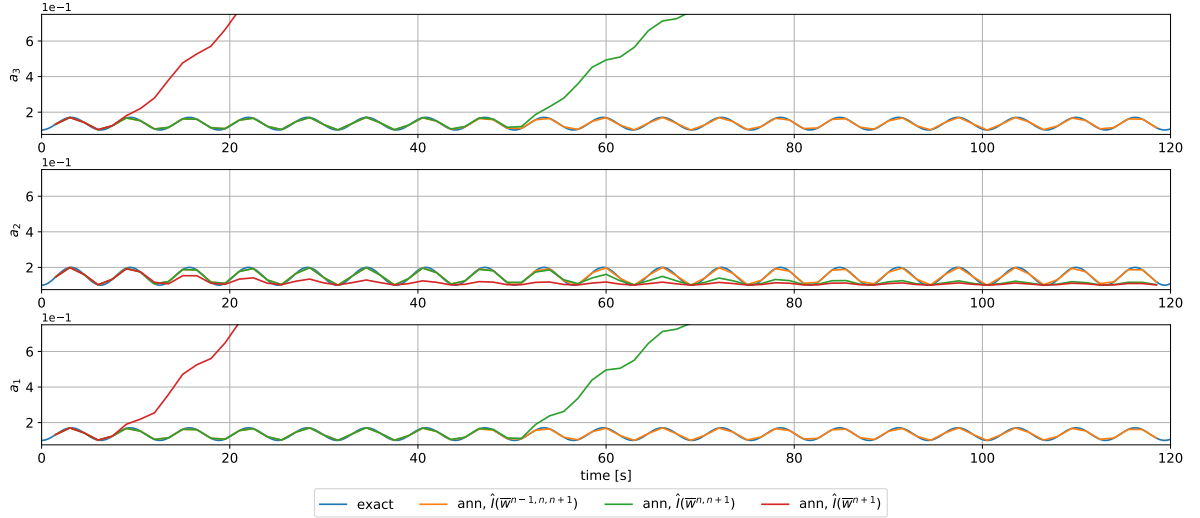


Figure 8.10: Temporal evolution of the three degrees of freedom  $a_1$ ,  $a_2$  and  $a_3$  of simulations with  $h = 0.25$ ,  $\Delta t = 1.5$ ,  $C = 1.2$ , closed by ANNs of shape  $[512, 512]$  that depend on  $\bar{w}^{n+1,n,n+1}$ ,  $\bar{w}^{n+1,n}$  and  $\bar{w}^n$  respectively.

### 8.3.5. Training on CP Data

The treacherous appearance of the  $\mathcal{R}_{w_i}$  space most likely reflects that the ANNs considered thus far are not familiar with the existence of such a space. They have only been trained on correct data that assume the models have already survived the nonlinear solution procedure's journey on this manifold. However, mapping out and training on  $m$  samples in each of the  $n_{el} - 1$  degrees of freedom of  $\mathcal{R}_{w_i}$  would require  $m^{n_{el}-1}$  samples to be taken and trained on at each time step, which rapidly becomes intractable.

A compromise might be to only train on data in the weak residual space that is relevant. Such data may be found in the convergence paths that are traced in the space when exact versions of the interaction terms are included in the simulations, as illustrated in Fig. 8.2a. Sampling such data at intermediate stages of the CPs may help to teach the ANN to follow these convergence paths.

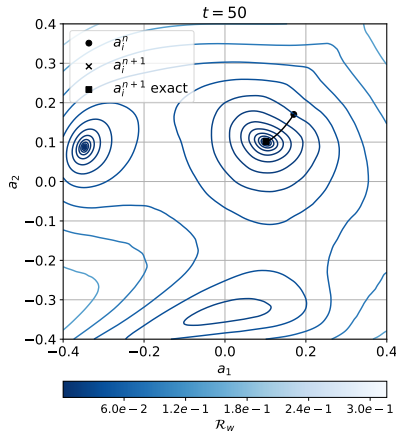


Figure 8.11: Response surface of  $\|\mathcal{R}_{w_i}\|_2$  for the ANN model trained on CP sequence data, for  $\hat{I}$  at  $t = 50$  s for a simulation with  $\Delta t = 2$ ,  $h = 0.333$ ,  $C = 1.2$ .

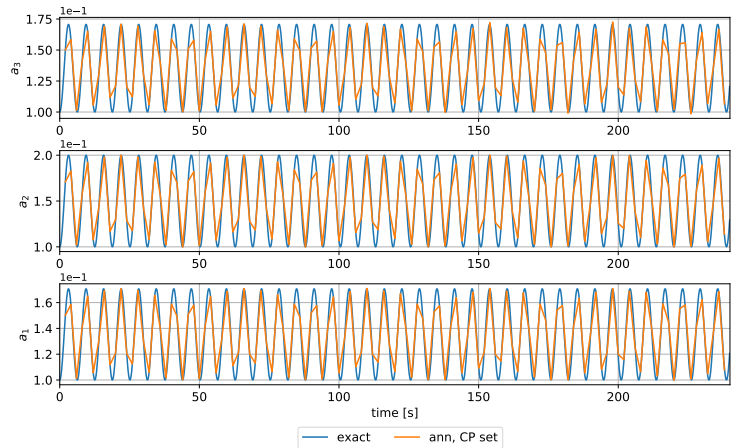


Figure 8.12: Temporal evolution of the three degrees of freedom  $a_1$ ,  $a_2$  and  $a_3$  of simulations with  $h = 0.25$ ,  $\Delta t = [1, 2]$ ,  $C = [0.8, 1.6]$ , for an ANN trained on data from the nonlinear Newton sequence of an exact-model forward problem

Fig. 8.11 shows that the model's weak residual space can indeed be considerably improved by including CP data in the ANN's training. While two other attractor basins can be identified for a 2 degree of freedom model after 50 time steps, these are similarly far removed as they are for the algebraic model, while the basin the ANN operates in is both relatively smooth and wide. This facilitates much better convergence behaviour, requiring significantly less iterations than direct approaches (see Table 8.1). Fig. 8.12 shows that at high  $C$ , the model

remains stable when a third degree of freedom is introduced, in contrast to any of the other configurations. This supports the hypothesis that informing the ANNs of the existence of the weak residual space, rather than merely the weak residual's root, will improve the model's behaviour in that space.

The drawback to this approach is that it still adds a dimension that the ANN must learn to generalise over. Here, it means that what was previously a dataset of 2,400 examples turned into one with 99,400 samples. While one could subsample the CPs and not include every point the exact solution procedure visits, this was found in the above tests to be significantly less effective. However, when more degrees of freedom are introduced and the problem becomes more complex, one might need to resort to such subsampling to contain training times. Furthermore, it is unclear whether knowledge of weak residual hypersurfaces is something that generalises. Hence, the final judgement of the model is postponed until the following chapter, where it will be subjected to a more challenging test case outside its training envelope.

### 8.3.6. A Quadratic Coefficient ANN Model

Another approach to solving the problems encountered in the previous sections is to prevent the ANNs from influencing  $\mathcal{R}_{w_i}$  at all. Such a model is proposed here as a larger departure from the original framework, to assess whether this would restore practical uniqueness and stability of the model.

Rather than letting the ANN predict the interaction terms directly, this model only lets the ANN predict the coefficients  $c_k$ ,  $k = 0, \dots, 8$  of a general quadratic in the same three degrees of freedom that affect a mode:

$$\hat{I} = c_k P(a)_k \quad (8.3a)$$

$$P(a) = [a_{i-1}^2, a_i^2, a_{i+1}^2, a_{i-1}a_i, a_{i-1}a_{i+1}, a_i a_{i+1}, a_{i-1}, a_i, a_{i+1}] \quad (8.3b)$$

If  $c_k$  is no longer a function of the degrees of freedom  $a_i$ , this means that  $\mathcal{R}_{w_i}$ 's order is restored to two, again containing the number of possible roots. Hence, this simulation turns to the explicit input stencil FS2 as its ANN inputs, despite this yielding worse-trained models for the actual turbulence problem.

The model predicts the coefficients once at the start of each time step, and keeps them constant throughout the iterative solution procedure that follows. These coefficients can then be used to find the model's Jacobian contribution. This can now be derived analytically, by differentiating  $\hat{I}$  to its appropriate  $a_i$ . This allows the construction of each of the terms in an element's Jacobian (see Appendix C.2 for an elaboration):

$$\frac{\partial}{\partial a_i} (\hat{I}_i) = 2c_1 a_i + c_3 a_{i-1} + c_5 a_{i+1} + c_7 \quad (8.4a)$$

$$\frac{\partial}{\partial a_{i+1}} (\hat{I}_i) = 2c_2 a_{i+1} + c_4 a_{i-1} + c_5 a_i + c_8 \quad (8.4b)$$

$$\frac{\partial}{\partial a_i} (\hat{I}_{i+1}) = 2c_1 a_i + c_3 a_{i+1} + c_4 a_{i+2} + c_6 \quad (8.4c)$$

Which are added in the same manner as the traditional ANN Jacobian (see Algorithm 4 in Appendix C.2). This gives the model two further distinct advantages over the direct models: First, the model only requires five expensive ANN evaluations per degree of freedom at the outset of a time step, with cheap evaluations of the quadratic evaluating  $\hat{I}$  and  $\frac{\partial \hat{I}}{\partial a_j}$  at every following corrector pass. Second, since the weak residual space is again quadratic, the model requires little relaxation and only a few CPs to converge.

This is illustrated by Fig. 8.13. It shows the convergence paths from the same initial condition of the same discretisation with direct and quadratic coefficient models. The direct models display their typically erratic behaviour, converging to a spurious root in few iterations if running unrelaxed with an ANN Jacobian, in many iterations if relaxed and running with the algebraic Jacobian, and diverging when running with an ANN Jacobian and relaxation. The quadratic coefficient model, however, converges to the correct root in 4 iterations, on par with the algebraic model's convergence.  $\mathcal{R}_{w_i}$  is again quadratic, smooth and contains only a single root, seemingly solving the non-uniqueness problem.

However, even this model suffers from the ANN. As  $\mathcal{R}_{w_i}$  remains a quadratic, its maximum number of roots might still appear. All four of these are brought out already in the very next time step, illustrated in Fig. 8.14. This figure also illustrates that the model can still suffer from instabilities: The model already displays convergence to a slightly wrong prediction of the root. When another degree of freedom is introduced, Fig. 8.15 confirms that the model quickly diverges. At reduced  $C$ , the model again holds on longer. However, error propagation eventually spills that simulation over into a different attractor at  $t = 39$  s, where it remains.

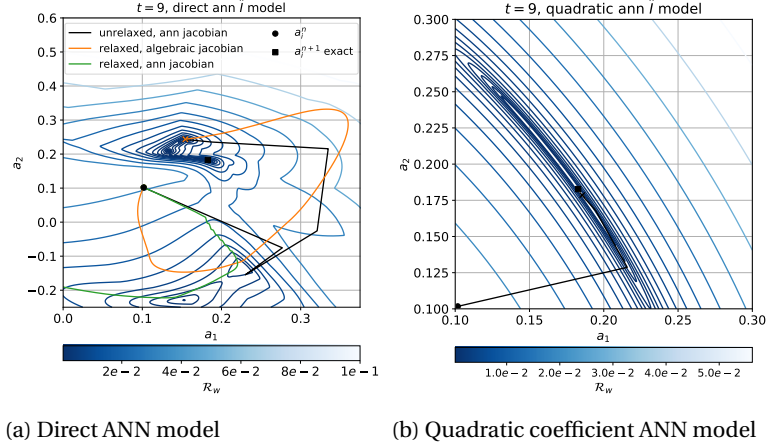


Figure 8.13: Response surfaces of  $\|\mathcal{R}_{w_i}\|_2$  for the direct (FS3 input, nonlinearly limited) and quadratic coefficient (FS2 input) ANN models for  $\hat{I}$ . Black lines signify unrelaxed convergence with an ANN Jacobian (Eq. (5.28)), orange lines relaxed convergence ( $\tau_r = 1 \cdot 10^{-4}$ ) with an algebraic Jacobian, and green lines relaxed convergence ( $\tau_r = 1 \cdot 10^{-4}$ ) with an ANN Jacobian. The simulations are run with  $\Delta t = 3$ ,  $h = \frac{1}{3}$ ,  $C = 1.8$ .

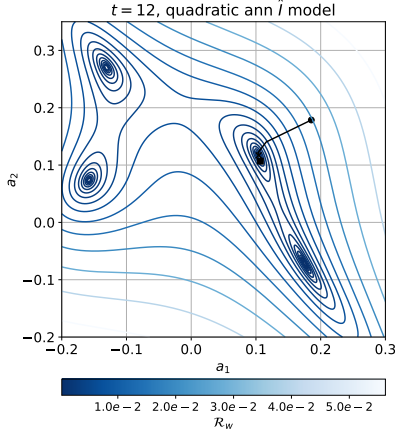


Figure 8.14: Response surface of  $\|\mathcal{R}_{w_i}\|_2$  for the quadratic coefficient ANN model for  $\hat{I}$  at  $t = 12$  s for a simulation with  $\Delta t = 3$ ,  $h = 0.333$ ,  $C = 1.8$ .

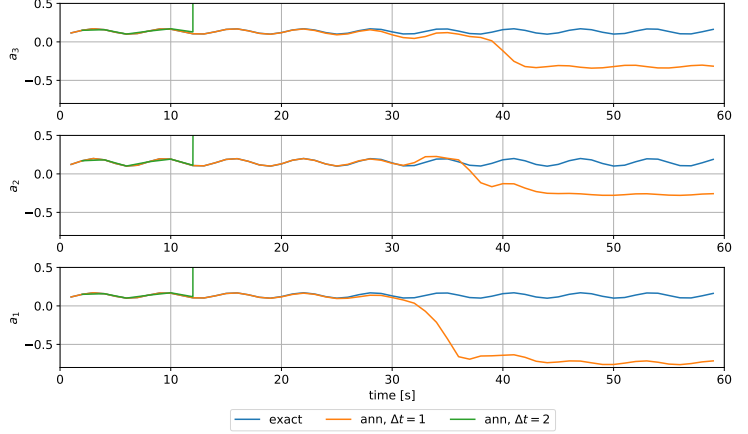


Figure 8.15: Temporal evolution of the three degrees of freedom  $a_1$ ,  $a_2$  and  $a_3$  of simulations with  $h = 0.25$ ,  $\Delta t = [1, 2]$ ,  $C = [0.8, 1.6]$ , for the quadratic coefficient ANN model for  $\hat{I}$ .

Hence, even retooling the model to eliminate part of the ANN's detrimental characteristics is found to be insufficient to guarantee its uniqueness and stability. The only manner in which the ANNs' influence over the weak residual space could be fully eliminated is likely through the use of explicit time marches, where the ANNs only predict a single value at the outset of a time step and no minimisation of the weak residual based on the unknown degrees of freedom is carried out.

Such explicit time marches might avoid the weak residual-related problems encountered here. However, they can also no longer guarantee the minimisation of the weak residual. Furthermore, they can only access a history of information, resulting in worse-trained ANNs. Finally, they must likely operate at much smaller  $\Delta t$  to avoid the second mode of instability encountered here, as they remain explicit. Therefore, although their investigation would certainly be interesting, translating the models to fully explicit configurations is not necessarily a primary recommendation.

### 8.3.7. Hybrid Algebraic-ANN Model

A final approach to improved navigation of the weak residual space for problems that operate at traditional LES discretisation level may be to leverage the algebraic model. These models are cheap, in certain situations provably unconditionally stable [226] and generally practically unique. Hence, one could first converge the

nonlinear problem in a time step with this model, and use that guess as an initial condition from which the ANN can attempt to find a better solution. This is illustrated in Fig. 8.16, where an ANN converges the simulation from the algebraic model's guess to the exact root. For this case, the algebraic model's prediction is decent, reducing the distance the ANN would have to move the model through the nonlinear space and aiding its convergence to the physical root as a result. It additionally allows using up-to-date input features of the algebraic model's prediction of the cross and Reynolds terms,  $\left(\frac{\partial \bar{\psi}}{\partial z}, -2\bar{w}\tau\bar{\mathcal{R}}_s\right)_\Omega$  and  $\left(\frac{\partial \bar{\psi}}{\partial z}, \left(\tau\bar{\mathcal{R}}_s\right)^2\right)_\Omega$ , as input features to the ANN.

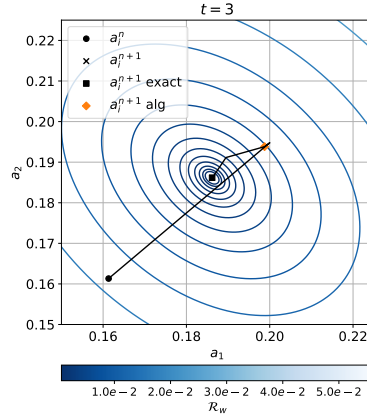


Figure 8.16: Response surface of  $\|\mathcal{R}_w\|_2$  for the hybrid algebraic-ANN formulation, for simulations where  $\Delta t = 1$ , at  $t = 3$ . The ANNs are conditioned on input from the converged algebraic model (at the orange diamond).

Here, the model is embedded in the quadratic coefficient model. Perhaps unsurprisingly, it therefore fails in exactly the same manner as the quadratic coefficient model: Its divergence patterns follow those presented in Fig. 8.15. This suggests that the reduced distance the model must traverse in the weak residual space does not necessarily aid its stability. Also, this method has the potential to break down when the algebraic model exits its domain of validity at large  $h$ , or when strong nonlinearities remain in the weak residual space between the converged algebraic model and the correct root of the ANN model. However, this model is also not designed to improve the second type of instability that dominates the quadratic ANN failures observed here. Rather, it could aid in keeping the more challenging turbulence problem unique.

## 8.4. Conclusions

The direct VMM-ANNs considered by Robijns are here found to be practically non-unique when ANNs that are unaware of the weak residual space are asked to traverse it. Linear ANNs bring out the maximum number of real roots of the second-order problem, and the introduction of nonlinearity to the networks makes them increasingly ill-posed. This sources instability when  $C$  is much higher than considered by Robijns, as navigating the distorted and nonlinear space leads the model into spurious attractors or prevents it from converging. Furthermore, instability at large  $C$  is observed even when the nonlinear space is successfully traversed, as small errors tend to accumulate and lead single modes to suddenly diverge. These two modes of instability are hypothesised to result from the ANNs' lack of knowledge of weak residual spaces and erroneous input data, answering RQ3.1.

In support of this hypothesis, this chapter does not find alternative configurations of the VMM-ANN model that fully abate stability issues at the levels of temporal discretisation desired to run large calculations. Their various architectures, maximum  $C$ , cost and failure properties are summarised in Table 8.1. Relaxation and an ANN Jacobian increase the likelihood that the model will converge smoothly to the nearest root, but still cannot guarantee this is the physical root and prevent the first mode of instability. Robijns' limiting schemes and longer temporal input stencils are capable of postponing the second mode of instability, but cannot prevent it. However, modifying the ANN's training to actually include knowledge of the  $\mathcal{R}_{w_i}$  space improves its stability. Similarly, completely preventing it from partaking in the convergence in this space by only letting it predict the coefficients to a general quadratic in the degrees of freedom returns a bound to the model's non-uniqueness. While the second mode of instability manifests itself even for these model architectures once  $C$  becomes sufficiently large, these models do provide an initial outlook for what might be needed

Type	C	FS	Limits	$\tau_r$	Jacobian	$\frac{\text{cPs}}{\text{step}}$	$\frac{t}{\text{step}}$	nD	Fail.
Direct	1.8	3	-	$1 \cdot 10^{-4}$	Algebraic	250	0.0863	0	WR
Direct	1.8	3	-	$1 \cdot 10^{-4}$	ANN	250	0.131	0	Div
Direct	1.8	3	-	-	ANN	10	0.0123	0	WR
Direct	1.2	3	-	$1 \cdot 10^{-4}$	ANN	131	0.0604	-	-
Direct	1.4	3	-	$1 \cdot 10^{-4}$	ANN	165	0.0734	28	Div
Direct	1.6	3	-	$1 \cdot 10^{-4}$	ANN	239	0.0835	5	Div
Direct	1.6	3	[0.0,0.5]	$1 \cdot 10^{-4}$	ANN	152	0.0763	2	Stag
Direct	1.6	3	[-0.5,0.5]	$1 \cdot 10^{-4}$	ANN	240	0.105	23	Stag
Direct	1.2	1	[-0.5,0.5]	$1 \cdot 10^{-4}$	ANN	192	0.0955	4	Stag
Direct	1.2	1.1	[-0.5,0.5]	$1 \cdot 10^{-4}$	ANN	148	0.0665	36	Stag
CP Set	1.6	3	-	$1 \cdot 10^{-4}$	ANN	40.1	0.0674	-	-
Quadratic	1.8	2	-	-	ANN	7	0.00135	4	MG
Quadratic	2	0.8	-	-	ANN	5.73	0.00272	32	WR
Quadratic	2	1.6	-	-	ANN	6.75	0.00204	4	Div
Hybrid	2	1.6	-	-	Alg/ANN	10.0	0.00255	4	Div

Table 8.1: Characteristics of computational cost, accuracy and stability of direct and quadratic ANNs for simulations with ANNs of shape [512,512]. nD is the number of successfully completed time steps without simulation divergence. The failure modes WR, Div, MG and Stag refer to wrong root prediction, divergence of the iterative procedure, mispredicted root growth, and stagnation of the Newton iterations.

to translate the ANNs' offline promise to online performance.

This discussion answers RQ3.2 in the context of the manufactured solution problem. However, it should be further investigated in the context of the model problem, to establish the extent to which the characteristics observed here translate to more realistic simulations, how these change once substantial model error is introduced and whether the conjectured directions for improving forward simulations of VMM-ANNs also apply to this problem. This will be the topic of Chapter 9.

## Properties of VMM-ANNs: 1D Turbulence

Chapter 8 established two modes of instability that prevent the sizeable promise of ANN unresolved scales models to translate to forward simulations of VMM-ANNs: Those associated with ill-posed weak residual spaces and those that follow from error accumulation over several time steps. While the former could already be realistically assessed in the context of the highly accurate manufactured solution problem, the latter will presently be addressed for the more realistic Boussinesq-forced Burgers' problem, where substantial ANN model error enters the simulation. Hence, to fully answer RQ3, this chapter will consider the VMM-ANN for the more realistic model problem.

First, Section 9.1 gauges the extent to which the stability characteristics identified for the manufactured solution translate to a case with significant model error. While it will identify the same two modes of instability that plagued the manufactured solution, it will conclude that none of the configurations from the previous chapter that attempted to address the weak residual's ill-posedness hold up when model errors are large. Section 9.2 will subsequently confirm that the impact of these errors escalates as the resolution of the model reduces and the ANN's role widens, as would be required by GCMs.

In this context, Section 9.3 will investigate the apparently dominating second mode of instability in more detail. By preventing the instability through the introduction of an artificial viscosity operator, it will gather evidence to support the hypothesis that the instability arises partially due to a lack of knowledge on how the ANNs trained on error-free data deal with inexact inputs engendered by their own prediction errors. This will allow RQ3.2 to be finally answered, leading to recommendations on new directions that could potentially allow the ANNs' offline skill to translate to online simulations, as well as the implications this might carry for the models' costliness. Finally, Section 9.4 studies the model's computational cost, to answer RQ3.3 and complete the study.

### 9.1. Stability

Section 8.2 highlighted that the models are most likely to function at low Courant number  $C$ . Also, Section 7.3 indicated that the interaction terms are better predicted at low  $C$ . Hence, to provide the model with optimal preconditions for its successful operation, the following tests are run at only twice the DALES-sampled time step, where very little temporal fluctuation remains under the grid cutoff. However, the defining criterion of success for the model would be its ability to simulate turbulence once the cutoff wavenumber of the simulation lies largely outside the rapidly energy-decaying range. Hence, based on the analysis from Section 6.3,  $h = 6h_{DALES}$  is chosen. For an exact Burgers' problem, this yields a maximum  $C$  around 0.4, which is significantly lower than where the simple cases listed in Table 8.1 still converged. This discretisation level allows directly accessing the ANN models listed in Table 7.3. Hence, they are models that trained on a set of 64x64 DALES columns, and are tested here on a single, randomly selected column of data from a different simulation.

Table 9.1 lists a number of model configurations run at this discretisation, when they are closed by an ANN with the architectures listed in Table 7.3. These models sequentially introduce the improvement strategies suggested in Section 8.3, and are listed alongside their offline and online  $R^2$  correlation of instantaneous samples of the three interaction terms. This facilitates a direct comparison between the ANN's online and offline trends.

Type	FS	Limits	$\tau_r$	Jac.	Offline $R^2$	Online $R^2$	nD	Fail
Direct	3	-	-	Alg.	[0.461,0.795,0.670]	[0.071,0.615,0.434]	22	MG
Direct	3	-	$1 \cdot 10^{-4}$	Alg.	[0.461,0.795,0.670]	[0.071,0.615,0.434]	22	MG
Direct	3	-	$1 \cdot 10^{-4}$	ANN	[0.461,0.795,0.670]	[0.071,0.615,0.434]	22	MG
Direct	3	[-0.5,0.5]	$1 \cdot 10^{-4}$	ANN	[0.461,0.795,0.670]	[0.071,0.615,0.434]	22	Stag
Direct	3	[-0.5,0.5]	$1 \cdot 10^{-4}$	Alg.	[0.461,0.795,0.670]	[0.021,0.144,0.207]	40	Stag
Direct	3	[0.0,0.5]	$1 \cdot 10^{-4}$	ANN	[0.461,0.795,0.670]	[0.000,0.674,0.427]	25	Stag
Direct	1	[-0.5,0.5]	$1 \cdot 10^{-4}$	ANN	[0.191,0.637,0.531]	[0.018,0.108,0.004]	22	MG
Direct	4	-	$1 \cdot 10^{-4}$	Alg.	[0.738,0.926,0.589]	[0.001,0.009,0.029]	1	Stag
CP set	3	[-0.5,0.5]	0.01	Alg.	[0.532,0.777,0.701]	[0.012,0.419,0.005]	28	MG
Hybrid	H	-	0.01	ANN	0.845	0.027	164	MG
Quad.	2	-	$1 \cdot 10^{-4}$	ANN	0.638	0.509	54	MG
None	-	-	$1 \cdot 10^{-4}$	Alg.	-	-	-	No

Table 9.1: Characteristics of accuracy and stability of direct and quadratic ANNs for simulations with  $h = 6h_{DALES}$ ,  $\Delta t = 2\Delta t_{DALES}$ ,  $C \approx 0.417$  and ANNs from Table 7.3. “CP set” refers to ANNs trained on an exact model’s convergence and hybrid refers to the algebraic-ANN models. nD is the number of successfully completed time steps without simulation divergence. The failure modes MG and Stag refer to mode growth-driven divergence and stagnated convergence of the iterative solution procedure.

It is acknowledged that  $R^2$  is a somewhat deficient yardstick. The ANN will inevitably introduce errors to the simulation that will push the instantaneous solution trace of the chaotic problem away from the exact solution and reduce  $R^2$ . However, perturbing the initial problem might not prevent reproducing the problem’s statistics appropriately [150, 177], which is all one would hope to achieve. Hence, the  $R^2$  metrics in Table 9.1 and later in this chapter overestimate the extent of the miscorrelation in online simulations. Still, the metric will be used within these limits, because the trends it displays are still indicative of the phenomena that are encountered.

All cases in Table 9.1 diverge. Hence, they are listed alongside the number of time steps they successfully complete until they fail, as well as their failure modes. Also, the online  $R^2$  is computed over the time interval before the predicted  $\bar{w}$  first exceeds the maximum magnitude encountered in the exact simulation.

While instabilities arise in many different locations, all these cases diverge due to the uncontrolled growth of one or several modes of the lowest resolved wavenumber,  $2h$ , very similarly to what was observed for the simple models in Section 8.2. Hence, it is not so difficult to imagine that the problems of those simulations are also encountered here, but that they are compounded by the relatively large modelling errors of the ANNs for the Boussinesq-forced problem. The following paragraphs attempt to ascertain this hypothesis for the models listed in Table 9.1, by i) characterising the typical instability development of these models, ii) identifying the occurrence of problems associated with ill-posed weak residual spaces and iii) discussing the instabilities that still remain.

The mode growth underpinning the failure is exemplified by Fig. 9.1. This figure shows the spatial distributions of the solution and the interaction terms over four time steps from the first simulation listed in Table 9.1. Its instability is due to an excited mode adjacent to the boundary. As displayed in Fig. 6.2, this mode often features large unresolved scales projections, making such relatively highly excited boundary modes a relatively common situation.

In the first plotted time step, excessive energy is added to the mode, as the ANN predicts  $\left(\bar{\psi}, \frac{\partial w'}{\partial t}\right)_\Omega$  to be negative when it should be positive, and underpredicts  $\left(\frac{\partial \bar{\psi}}{\partial z}, w'^2\right)_\Omega$ . The excitement of this mode is not damped, as the ANN predictions remain poor and continue adding energy to the mode as a history of increasingly large  $\bar{w}$  is developed. When unchecked, this quickly causes the mode to grow until the predictions of the other terms begin failing at  $nDt = 21$ , and the iterative procedure is driven to infinity at  $nDt = 23$ . This diverging path of the Newton iterations is illustrated by the red line in Fig. 9.3.

One may read from Table 9.1’s online  $R^2$  that  $\left(\bar{\psi}, \frac{\partial w'}{\partial t}\right)_\Omega$  is generally mispredicted in the simulation that gives rise to Fig. 9.1, compared to that model’s offline  $R^2$ . Fig. 7.7 showed that in such offline settings, the smallest, resolved scales of  $\left(\bar{\psi}, \frac{\partial w'}{\partial t}\right)_\Omega$  are particularly well-predicted. Therefore, it is surprising that these modes of the term give rise to the instability of the forward simulation. This could therefore be an indication of an early root switch.

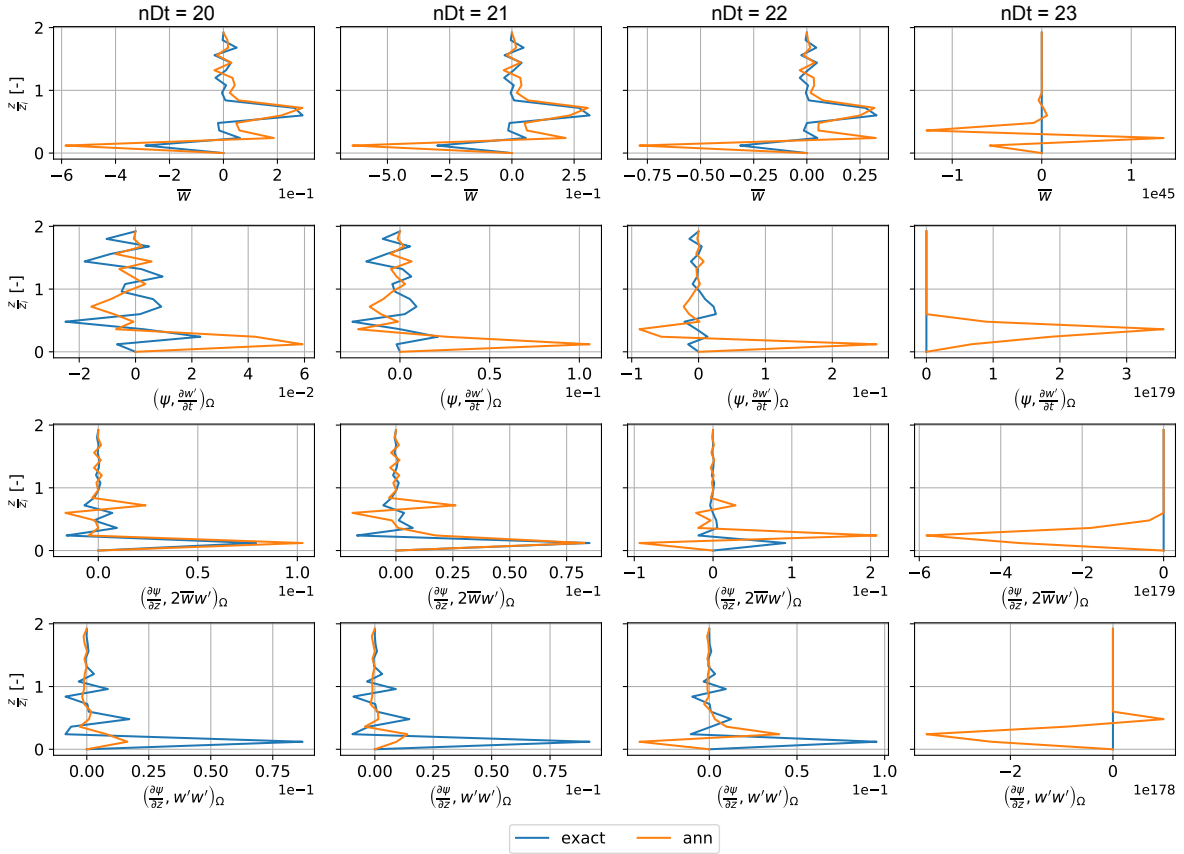


Figure 9.1: Evolution of instability in  $\bar{w}$  for the first model listed in Table 9.1, over four consecutive time steps due to subsequent mispredictions of the three, plotted interaction terms, for an excitation of the boundary-adjacent mode at  $nDt = 20, 21$ , sudden growth of the mode at  $nDt = 22$  and divergence at  $nDt = 23$ .

Sections 8.3.1 and 8.3.2 showed that helping the model with relaxation or an improved Jacobian could cure the problem. Furthermore, Section 8.3.3 showed that nonlinear limiting of the interaction terms could postpone divergence. However, with the former two additions, the model still diverges in similar fashion at the same time step. Adding the nonlinear limiters, however, does prevent the Newton iterations from diverging at  $nDt = 20$ . Unfortunately, it also prevents the procedure from converging at this time step, resulting in the stagnating failure mode discussed in Section 8.3.3 as the models remain stuck in the limiters.

Table 9.1 shows that several other cases also become unstable in this manner. For instance, term biasing to prevent the simulation from adding energy to the boundary mode is only marginally more successful. It allows the simulation to live an additional 3 time steps, before the Newton iterations for this model also stagnate.

Interestingly, when the nonlinear limiters are combined with an algebraic Jacobian, rather than the ANN Jacobian, the model continues to find roots for more time steps. This simulation also fails due to the boundary mode growth, but does so somewhat more slowly than the other simulations. Hence, while all cases display somewhat similar behaviour, the evolution of this case's energy spectrum, plotted in Fig. 9.2, is a particularly clear illustration of the problem. At  $nDt = 15$ , the simulation predicts all modes relatively well, with the exception of the boundary mode, which causes the energy in the  $2h$  mode to perk up. With the lack of a dissipative operator, the energy proceeds to spread to more of the small, resolved modes at  $nDt = 20$ . At  $nDt = 25$ , the increasing energy in the mode has begun to influence all other modes, and the convergence of the Newton procedure stagnates shortly after this instance.

The only change in the architecture of this model with respect to models that diverge after 22 time steps is the changed Jacobian. This suggests that the boundary mode may have undergone an attractor switch. Indeed, Fig. 9.3 provides evidence for such a switch. It depicts the convergence traces of the Newton iterations for the first two degrees of freedom from the lower boundary,  $a_1$  and  $a_2$ , for models with an algebraic (orange) and an ANN (green) Jacobian. Despite originating from an almost identical  $\bar{w}$  prediction, the simulation

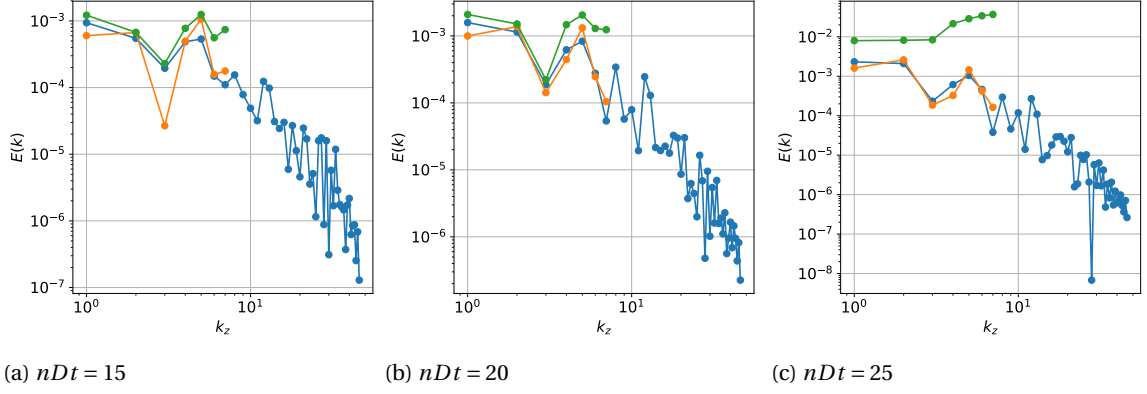


Figure 9.2: Three instantaneous energy spectra corresponding to  $w$  (blue), exact  $\bar{w}$  (orange) and VMM-ANN predictions of  $\bar{w}$  (green), separated by 5 time steps, over a period where energy accumulates in the smallest resolved modes of the VMM-ANN, run with the FS3 ANN from Table 7.3, on a discretisation with  $h = 6h_{DALES}$ ,  $\Delta t = 2\Delta t_{DALES}$  and  $C \approx 0.417$ .

with the ANN Jacobian does not find a root. The algebraic Jacobian simulation, however, rapidly increases the interaction terms until they hit the limiters. The simulation then proceeds to converge  $\bar{w}$  to a root that exists with the interaction terms on their limiters. However, the profiles in Fig. 9.3 show that this converged solution has already travelled an appreciable distance from its correct position and still adds energy to  $a_1$  and  $a_2$ . Therefore, adding the nonlinear limiters merely slows the divergence of the mode, just as for the simple problems.

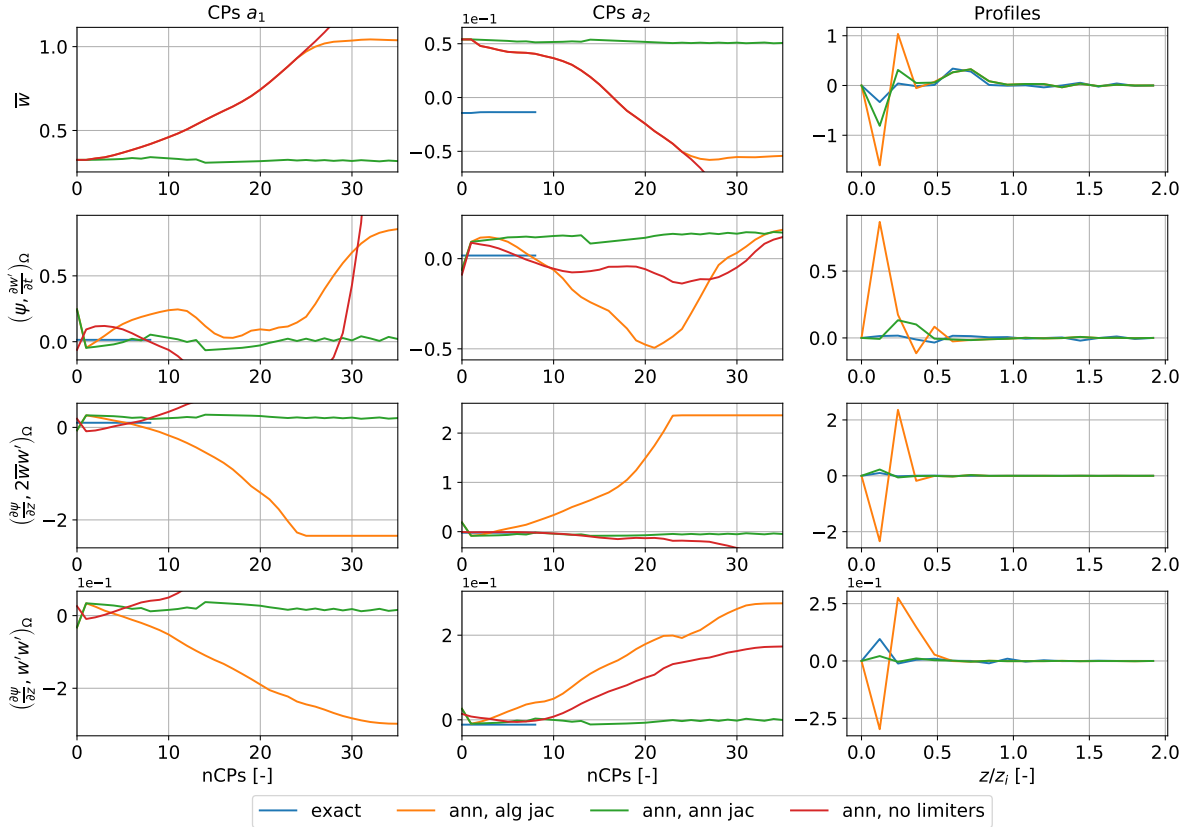


Figure 9.3: Convergence paths of the first two modes and final profiles of the solution and interaction terms at  $nDt = 23$  (failure) for simulations closed by exact and ANN predictions of the interaction terms. The models employ ANN and algebraic Jacobians (orange, green lines respectively) with nonlinear limiters active, and algebraic Jacobian without nonlinear limiting (red line). Note that the latter simulation diverges, such that its final profiles are not plotted.

Table 9.1 shows several other models that also are unstable. In particular, all feature sets diverge, ranging from the low-correlating FS1 to the high-correlating FS4. The failure of FS1 and FS3 after an equal number of time steps indicates that the improvement seen in the simple problem when including a time history to the input stencil does not translate to the Boussinesq-forced problem. This could be an indication that the input stencils are too local in time for the ANN to understand that the local predictions must also be consistent with the high-amplitude, long-term dynamics of the turbulence, as hypothesised in Section 7.3. The failure of FS4, however, is especially notable: Despite clearly being the best-performing feature set in offline evaluation, it diverges much earlier than the other models, after only a single time step. This cannot be well explained within the current analysis. It does, however, reinforce the observation that good offline predictions do not necessarily translate to online performance.

Training the ANNs on samples from the nonlinear iteration space substantially improved the predictions in Section 8.3.5. However, this strategy also does not offer much improvement for the more realistic model problem. While this simulation survives the initial mode growth, it soon destabilises elsewhere, as illustrated by the CP set entry in Table 9.1.

The quadratic coefficient model holds on somewhat longer. It does not excite the boundary mode and does not display the symptoms of attractor switches. However, the model disturbs a different, single mode somewhat later, still leading to divergence of the Newton iterations. While one might expect that this model would suffer from having to use the lower-correlating FS2 as input, it rather has relatively high-correlating online predictions of the terms, showing once again that very different characteristics are demanded of the models in an online setting than in an offline setting. No configuration of the model holds on longer than what is reported in Table 9.1. This suggests that even models with better-posed weak residual spaces fall prey to instability, just as was observed for the simple case. However, as will be discussed in Section 9.2, it is the only model that manages to remain stable in online running at finer discretisation, albeit with unimpressive results.

Finally, the hybrid model holds on longest of any configuration. Its training results in relatively high correlation on its offline predictions of the interaction term. Even for this model, however, the story remains unchanged: Despite the fact that it presumably must traverse a much shorter distance in the Newton iterations, it is sufficient to prevent the ANNs from remaining stable. With very low online correlation on the interaction term, it fails after 164 time steps due to the divergence of a different, single mode.

From these results, one can conclude that the models are insufficiently general to translate their dramatic improvement over algebraic models in offline settings to online simulations for the Boussinesq-forced test case, in a similar manner as observed in the simple test case in Chapter 8. The same two modes of instability as observed in Section 8.2 occur: In some cases, divergence is provably due to the ill-posed weak residual space, which still leads single modes to switch attractors. However, for this more complicated problem, the second version of instability appears to be further compounded by the ANN's imperfect offline predictions of the interaction terms, which do not translate to good online performance. As a consequence, errors accumulate in the small scales of the simulations, which with or without attractor switches induce instabilities. This increased model error appears to diverge the calculations earlier than was observed for their simple counterparts, even at much lower  $C$ . Little to no improvement in the model's stability is observed for this problem when strategies are deployed that result in much better-posed weak residual spaces in Section 8.3. Therefore, the second mode of instability might be the most far-reaching problem of the method, which may require very different remedies than examined so far in this work. This instability is therefore further discussed in Section 9.3. First, however, the severeness of the instability's impact is assessed by gauging how the model's behaviour changes as a function of the discretisation level.

## 9.2. Influence of Discretisation

RQ3 concerns the transfer of the ANNs' predictive ability from offline to online simulations of turbulence on grids that directly resolve phenomena down to the upper end of the range of rapidly energy-decaying scales. The previous section shows that none of the configurations considered here successfully achieve this, even at relatively low  $C$  ( $< 0.5$ ). Section 7.3 showed that there is no strong dropoff in the ANNs' ability to predict the interaction terms at coarser  $h$ , which might lead one to think that the instabilities observed in forward simulations are relatively independent of  $h$ . However, Section 7.3 also hypothesised that this might be another feature of online simulations that offline tests cannot appropriately capture: At finer resolution, the ANNs' negative influence over the model is likely to be less, potentially leading to better stability characteristics. This was already observed by reducing  $\Delta t$  for the manufactured solution problem in Section 8.2.

Hence, this section considers runs of the direct and quadratic coefficient model with considerably refined discretisations for the Boussinesq-forced Burgers' problem. It reexamines the range of spatial discretisations encountered in Section 7.3, but refines the time direction further, below the sampling interval of DALES. In these cases, almost no unresolved scales fluctuation remaining in the signal, such that the unresolved scales' time derivative projection merely interpolates a spline. The smoothness of the signal in time should then make the problem as well-posed as one can imagine.

Type	$\Delta t/\Delta t_{DALES}$	$h/h_{DALES}$	Offline $R^2$	Online $R^2$ before MG	nD	Failure	
Direct	2	6	[0.461,0.795,0.670]	[0.021,0.615,0.434]	22	MG	
	2	3	[0.394,0.703,0.479]	[0.031,0.109,0.137]	62	Stag	
	2	1.5	[0.360,0.654,0.370]	[0.097,0.205,0.176]	55	Stag	
	1	6	[0.656,0.850,0.787]	[0.201,0.112,0.183]	106	Stag	
	1	3	[0.595,0.798,0.714]	[0.212,0.367,0.178]	115	Stag	
	1	1.5	[0.463,0.816,0.731]	[0.242,0.478,0.203]	154	Stag	
	0.5	6	[0.702,0.861,0.805]	[0.286,0.197,0.221]	100	MG	
	0.5	3	[0.612,0.804,0.754]	[0.261,0.178,0.243]	280	Stag	
	0.5	1.5	[0.530,0.822,0.701]	[0.275,0.189,0.217]	329	Stag	
	Quadratic	2	6	0.536	0.612	47	MG
		2	3	0.249	0.029	-	-
		2	1.5	0.359	0.016	-	-
1		6	0.556	0.363	111	MG	
1		3	0.305	0.521	201	Stag	
1		1.5	0.279	0.034	-	-	
0.5		6	0.604	0.178	211	Stag	
0.5		3	0.208	0.179	571	Stag	
0.5		1.5	0.274	0.007	-	-	

Table 9.2: Characteristics stability of simulations closed by direct and quadratic coefficient ANN models. The direct models down to  $\Delta t/\Delta t_{DALES} = 1$  correspond to those in Fig. 7.6a, while the quadratic models, closed by FS2, are trained on the same dataset as the direct models. The simulations run with  $\tau_r = 0.01$ , an ANN Jacobian and nonlinear limiting to  $[-0.5, 0.5]$  (only for direct models). Online  $R^2$  before mode growth is measured until the first instance where  $\bar{w}$  in the domain exceeds the maximum value encountered in the exact simulation, and nD is the number of successfully completed time steps without simulation divergence. The failure modes Stag and MG refer to stagnation and mode-growth-driven divergence of the Newton scheme.

Table 9.2 illustrates that the  $R^2$  of the direct model's interaction terms is somewhat restored to their offline performance as both temporal and spatial discretisation come down one level. The trend stagnates beyond this single step for the cross and Reynolds terms. This is likely because all solutions eventually depart reality and fail. Hence, their skill should be compared in conjunction with the number of time steps until failure. The nD column in Table 9.2 confirms what was hypothesised in Section 7.3: Despite the offline ANN predictions being relatively insensitive to coarser  $h$ , the ANN's model error is less impactful as the resolution increases and the ANN's role diminishes. Here, this translates to simulations that remain stable longer.

The quadratic coefficient model remains fully stable for several cases. However, it is not yet particularly accurate. While the instantaneous  $R^2$  of the interaction terms listed in Table 9.2 over-exaggerates the lack of accuracy of the model, Fig. 9.5c shows it cannot yet reproduce the model's statistics. This implies that even when stable, the models are not yet capable of handling the errors they have induced well. However, this may merely be another feature of the same, underlying problem and not an additional dimension of deficiency. Furthermore, restoring the smoothness of and removing roots from the weak residual space has seemed to return stability to this model. While no proof can be offered that these theoretical improvements are the direct cause of the enhanced stability, they will certainly will not have hurt.

In all, the lack of generalisability from offline to online simulations appears to be exacerbated at coarser resolution, where the ANNs' increasing, unconstrained model error plays a progressively large role. In spite of impressive performance at coarse resolutions in offline simulations, they fail earlier when they must carry an increasing burden in the forward simulation. Without further constraints, this likely makes their current formulation a rather ineffective unresolved scales model for a GCM, where their impact would often be even more substantial than here [160]. Therefore, a direction one might look in to find such constraints is discussed in the following section.

### 9.3. Aspects of Stability

The introduction of significant model error with the Boussinesq-forced problem demands a closer look at the second mode of instability: The accumulation of energetic errors in the smallest, resolved scales. Section 8.3 showed that strategies that ease the travel through the numerical weak residual space can somewhat cure the first type of instability. In particular, training the ANNs on data from this space yielded much better results. Given that instabilities still quickly materialise for such CP-trained models in Section 9.1, one might hypothesise that a similar lack of generalisation lies at the foundation of the second mode of instability: The ANNs appear to suffer when they leave the safe haven of perfect physical data input and are cast into the storm of an online simulation where they are continuously subjected to the product that their own errors create. This will be investigated in two stages below. First, artificial viscosity will be introduced to the simulations to i) ascertain that excessive energy accumulation lies at the foundation of the problems encountered here, ii) assess how much dissipation is required to re-establish reasonable simulations and iii) judge whether the ANNs' offline performance returns if the simulation is kept close to physical solutions. Second, their sensitivity to having to generalise outside their training data is analysed. From this analysis, an improvement direction for curing the instabilities is suggested.

#### 9.3.1. Artificial Viscosity Stabilisation

Section 8.2 showed that all simulations considered thus far destabilise due to accumulating energy in their smallest resolved modes, leading to the above suggestion that this might be driven by a lack of a rigorous method that constrains the unresolved scales' energy. Because the developed framework is not conducive to straightforward online evaluation of the problem's large-scale energy balance, the evidence to support this hypothesis can be delivered by reintroducing an operator to the model that attempts to stabilise the calculation by inherently working to restore the energy balance.

The classical formulation for such stabilisation is an artificial viscosity model [229]. The introduction of such a model is clearly inconsistent with the idea of attempting to represent the unresolved scales terms exactly. Furthermore, adding it on top of the interaction terms models essentially "double-counts" the turbulence. However, perhaps a small amount of artificial viscosity is already sufficient to cap the sudden mode growths that destabilise the calculation. If this is all that is required to return the solution to reasonable regimes, this would indicate energy conservation as a clear improvement avenue for the ANN unresolved scales models. If these regimes are additionally well-handled by the ANN, it would furthermore show that one might not have to wander far down that avenue to arrive at a decent model. Therefore, an artificial viscosity term  $V$  is added to simulations of the direct and quadratic coefficient models, according to Eq. (9.1):

$$V = 2\nu_a \left( \frac{\partial \bar{\psi}}{\partial z}, \frac{\partial \bar{w}}{\partial z} \right)_{\Omega} \quad (9.1a)$$

$$\nu_a = c_{a,1} \bar{w} \frac{\partial \bar{w}}{\partial t} + c_{a,2} h^2 \frac{\partial \bar{w}}{\partial z} \quad (9.1b)$$

This definition is inspired by Scovazzi's shock-capturing scheme [223], and is intended to increase the diffusion in the presence of i) strong gradients and ii) rapid, large increases in the resolved-scale energy associated with single-mode instability. However, when added to the coarsely resolved test cases in Table 9.1, the model still does not converge. This is only achieved once the spatial resolution is doubled. These first results of a converging, direct ANN mode are presented in Fig. 9.4.

Three observations can be made from this figure. First, the instantaneous snapshots of the turbulence in this figure reveal that the artificial viscosity term is often concerned with negating the effects of the larger contributions of the ANN-predicted interaction terms. Second, the time-averaged profiles of the interaction terms of such a converged simulation, plotted in the right-most window of the figure, show that the dominating cross term (full line) is significantly overpredicted with respect to its exact equivalent (dashed line), despite Section 7.2.2 showing that the ANN predictions tended to underpredict the terms' influence in offline settings. Finally, despite the ANN still dominating the overall unresolved scales predictions, the viscosity term's impact here already outweighs that of the unresolved scales' time derivative projection and the Reynolds term. In combination, these observations broadly appear to confirm the unstable nature of the model: Its offline characteristics do not translate to online simulations, requiring significant levels of opposite effects from a dissipative operator to remain stable. A strategy to ensure energy conservation will therefore be required to address the instability problem.

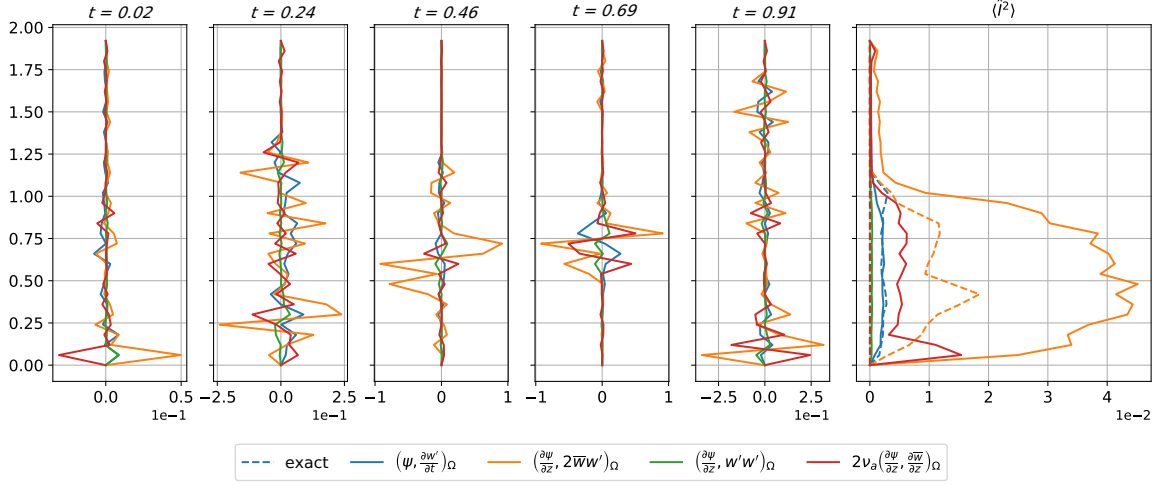


Figure 9.4: Profiles of instantaneous and time-averaged norms of the interaction terms of a VMM-ANN run stabilised with additional artificial viscosity,  $c_{a,1} = 1 \cdot 10^{-3}$ ,  $c_{a,2} = 1 \cdot 10^{-2}$ . The simulation runs at  $\Delta t = 2\Delta t_{DALES}$ ,  $h = 3h_{DALES}$ ,  $C \approx 0.33$ , with a direct FS3 ANN interaction term model, using the hyperparameters from Table 7.3.

As shown in Section 9.2, the quadratic coefficient model can also remain stable at finer levels of discretisation. This is not yet attributable to any model skill: Fig. 9.5c displays that a large amount of energy still accumulates in this model's smallest, resolved scales. The predicted  $\langle \overline{w}^2 \rangle$  profile is in turn much too energetic. However, this model provides a good starting point for a heuristic assessment of how much artificial viscosity would be necessary to return the statistics to a reasonable level. Two such tests are shown in Fig. 9.5, labelled “low  $\nu_a$ ” ( $c_{a,1} = 1 \cdot 10^{-4}$ ,  $c_{a,2} = 1 \cdot 10^{-3}$ ) and “high  $\nu_a$ ” ( $c_{a,1} = 1 \cdot 10^{-3}$ ,  $c_{a,2} = 1 \cdot 10^{-2}$ ). They illustrate that the ANN prediction of the interaction term and the velocity statistics can only be reproduced faithfully for the “high  $\nu_a$ ” case, where the artificial viscosity begins relieving the ANN as the major unresolved scales stable. Hence, they confirm that the current form of the model has a long way to go before it can be labelled stable.

The results also support the hypothesis posed at the outset of this section. The ANN’s average predictive performance can be somewhat restored when the solution’s statistics are confined by the artificial viscosity. Hence, this suggests that their lack of knowledge of where their errors drive the solution may be fundamental to their lack of online performance.

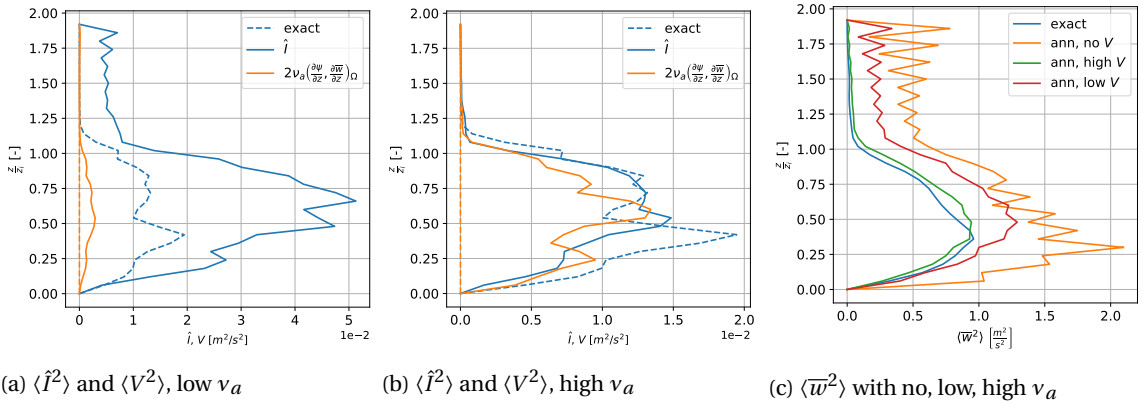


Figure 9.5: Time-averaged profiles of the  $L_2$  norms of the sum of ANN-predicted interaction terms and “low” ( $c_{a,1} = 1 \cdot 10^{-4}$ ,  $c_{a,2} = 1 \cdot 10^{-3}$ ) and “high” ( $c_{a,1} = 1 \cdot 10^{-3}$ ,  $c_{a,2} = 1 \cdot 10^{-2}$ ) artificial viscosity terms, with their resulting vertical velocity statistics. Simulations are with the quadratic coefficient model at  $\Delta t = 2\Delta t_{DALES}$ ,  $n_{el} = 32$ ,  $C = 0.33$ , closed by a [512,512] ANN, taking FS2 as input.

### 9.3.2. Dataset Dependence

However, one might also hypothesise that training the ANNs on larger datasets with more examples would already provide them with a broader basis on which they could handle incorrect guesses. This is unlikely to be true, as the ANNs considered here have been subjected to  $O(10^4)$  times as many examples as what is present in a single-column forward simulation during training. Also, even larger training runs than reported here very rapidly become impractically expensive. Finally, the model seems to misbehave not because it is unaware of different realisations of the same statistical turbulence; Section 7.2.2 showed that it generalises fairly well to those. Rather, it struggles with the statistically different situations that it creates for itself through error propagation.

In a similar vein, however, one might argue that the models tested in Section 9.1 are merely insufficiently general to run on columns outside their sphere of training examples, or that the models are unlucky and have been tested on a particularly challenging column. To tie up these loose ends, several tests have been conducted on different columns both inside and outside the model's training set. Furthermore, tests have been conducted with ANNs that have been trained only on a single column of data, and subsequently tested only on that column of data.

Training set	Testing column	Offline $R^2$	Online $R^2$	nD	Fail
8x8	Outside	[0.461,0.795,0.670]	[0.071,0.615,0.434]	22	MG
8x8	Inside	[0.461,0.795,0.670]	[0.009,0.267,0.279]	34	MG
1	Outside	[0.236,0.585,0.596]	[0.175,0.023,0.059]	28	MG
1	Inside	[0.236,0.585,0.596]	[0.071,0.053,0.263]	33	MG

Table 9.3: Characteristics of stability of direct ANNs with FS3 input and hyperparameters from Table 7.3 for simulations with  $h = 6h_{DALES}$ ,  $\Delta t = 2\Delta t_{DALES}$ ,  $C \approx 0.417$ . The training sets are the default 8x8 set and a single, randomly chosen column, while inside and outside refer to whether they have been tested on a column that belongs to or is uncorrelated from their training set, respectively. nD is the number of successfully completed time steps without simulation divergence. The failure mode MG denotes mode growth-driven divergence of the iterative solution procedure.

However, Table 9.3 shows that these tests do not produce results of note. All models still fail relatively early, excited by different single modes that diverge the calculations. Even training and running on the exact same column does not improve matters. This strengthens the hypothesis that rather than due to a lack of generalisability of the ANNs to offline tests outside their training envelope, it is their lack of generalisability from offline to online simulations that curtails their stability and consequently, their accuracy.

### 9.3.3. Outlook

In particular, the observations in this section support the conjecture posed at the outset of Chapter 8: It might be the lack of the offline-trained ANNs' knowledge on how to handle the errors they themselves induce in forward simulations that lies at the heart of the instabilities observed in Section 9.1. More generally, this hypothesis falls in line with very recent research on ANN predictions of HIT [21] and on Lorenz attractors [217], where strong offline performance could not generalise to physical realisations of temporal trajectories of deterministic chaos in previously unseen spaces, once an imperfect history had to be considered. This suggests that the issue may be relatively broad.

In this light, the stability issues encountered in this work are unlikely to be curable by any straightforward extensions of the VMM-ANN model, providing a definite answer to RQ3.2. Rather, the observations suggest that one might need to extend the training space of the ANNs to cover the currently ignored difference between offline and online simulation. Hence, this motivates one to consider training strategies that inform the ANNs of their errors. This could be achieved through offline training on datasets that have been augmented with erroneous input examples. This data could for instance be created artificially, or by unstable forward problem simulations with a pre-trained ANN model embedded. Going further, one might reconsider the merits of online training, discussed in Section 5.4. For such training, one could run a VMM-ANN with a pre-trained ANN in parallel with a high-fidelity model. Every  $n$  time steps, one could compute a loss function based on the VMM-ANN's performance with respect to the high-fidelity simulation and update the ANN's weights and biases according to the standard backpropagation algorithms outlined in Section 3.5.1 and Section 5.4 before the next time step. Rasp suggests in a publication that emerged weeks before this thesis was finalised [204] that such online training strongly aids the energy instabilities of his original study of ANN-closed SP [205]. Hence, this surfaces as an interesting pathway also for the prediction of interaction terms.

In contrast to the studies quoted above, however, the framework proposed here consistently steps the interaction terms and discretised resolved scales through an iterative procedure, yielding a second dimension of difference between offline and online simulation. Knowledge of several points in this space was found to improve the ANN predictions of the weak residual spaces in Section 8.3.5 for simple problems, similar to what Rasp finds for the physical problem [204]. Hence, any of these error-augmented learning strategies require another dimension for the method considered in this work: Offline training would have to consider data from the CP sequence *and* from erroneous examples, while online training would have to be embedded *within* the iterative schemes that are used to solve the nonlinear, discrete problem, for the ANN training to be conditioned on both i) the numerics of the weak residual and ii) the statistically different physical states its errors lead it to see. In all, both strategies are therefore likely to substantially increase the computational cost of training, since they both add a dimension to the training space that potentially contains many degrees of freedom. Therefore, even if such strategies do succeed in translating the offline promise of ANN-predicted interaction terms to online simulations, it is unclear whether their accuracy per degree of freedom can still outperform that of traditional parameterisation. That would in turn pose serious questions to studies that have contended that ANNs represent a pathway to higher accuracy per degree of freedom [79, 139]. These conjectures should therefore be investigated in more detail.

## 9.4. Computational Cost

RQ3.3 treats the final, vital aspect of the performance of VMM-ANNs covered by this study: The model's computational cost. In fact, as discussed in Section 2.2.4, the main driver for the development and investigation of these models is the allure of reproducing the problem's large-scale behaviour accurately with a reduced number of degrees of freedom with respect to what its physics demand of direct computational methods. While the previous sections have discussed several aspects of the model that at present curtail their accuracy, these sections have not discussed at what computational cost. This was also not treated by Robijns [209]. Therefore, this section reviews the computational cost of each of the model's stages, contrasts the cost to the algebraic model and a DNS of the problem, and discusses scalability in the problem's number of degrees of freedom and dimensionality.

The columns of Table 9.4 report the results that are treated in the following subsections: Cost of ANN training  $t_{train}$  (Section 9.4.1), weak residual assembly  $t_{\mathcal{R}_w}$  (Section 9.4.2), Jacobian assembly  $t_{jac}$  (Section 9.4.3), Newton iterations  $\frac{n_{CPS}}{step}$  (Section 9.4.4) and overall cost  $\frac{t}{step}$  (Section 9.4.5), for selected cases from Table 9.1. These cases were run with similar levels of computational background activity, such that the presented results are expected to roughly indicate the relative performance of the configurations they reflect. The discussions do not concern the solution of linear systems at each step of the CPs, which are observed to be similarly expensive for ANNs and algebraic models here.

Type	FS	$\tau_r$	Jac.	$t_{\mathcal{R}_w} [\cdot 10^{-4}]$	$t_{jac} [\cdot 10^{-4}]$	$\frac{t_{train}}{t_{alg}}$	$\frac{cPs}{step}$	$\frac{t}{step} [\cdot 10^{-3}]$	$\frac{\frac{t}{step}}{\frac{t}{step}_{alg}}$
Alg.	-	-	Alg.	$5.05 \pm 0.102$	$5.38 \pm 2.70$	-	$6.05 \pm 1.25$	$4.71 \pm 0.654$	1
DNS	-	-	Alg.	$5.01 \pm 3.17$	$5.12 \pm 0.101$	-	$110 \pm 22.4$	$690 \pm 52.5$	-
Direct	3	-	Alg.	$22.1 \pm 0.505$	$3.53 \pm 1.78$	7.88	$33.2 \pm 11.2$	$86.2 \pm 6.67$	14.1
Direct	3	$10^{-4}$	Alg.	$21.2 \pm 0.512$	$3.34 \pm 1.54$	7.88	$58.2 \pm 12.1$	$149 \pm 6.19$	24.3
Direct	3	$10^{-4}$	ANN	$22.1 \pm 0.496$	$70.3 \pm 12.4$	7.88	$34.2 \pm 8.42$	$292 \pm 8.37$	47.7
Quad.	2	-	ANN	$5.42 \pm 0.217$	$5.89 \pm 1.72$	9.86	$5.03 \pm 1.02$	$8.89 \pm 0.432$	1.45
CP set	3	0.01	Alg.	$22.0 \pm 0.554$	$3.41 \pm 1.12$	79.4	$4.13 \pm 0.921$	$75.4 \pm 0.149$	12.32
Hyb.	H	0.01	ANN	$5.24 \pm 0.092$	$5.64 \pm 1.62$	9.21	$36.4 \pm 7.85$	$15.2 \pm 0.175$	3.22

Table 9.4: Characteristics of computational cost of direct and quadratic ANNs for simulations corresponding to selected runs from Table 9.1. All time units are in seconds. The listed values are a run's mean  $\pm$  its standard deviation

### 9.4.1. ANN Training

The first aspect of the simulation cost is training the ANNs. Although this would be a one-off investment if the model is sufficiently general, the previous two chapters show that such generalisability is not achieved here, nor is it in any other studies on atmospheric unresolved scales modelling conducted so far [79, 205]. Given this lack of generalisability, it is instructive to retain the training cost of a single ANN as a fraction of a single forward problem simulation's total cost.

Referring back to Fig. 7.1b, the cost of training an ANN for this one-dimensional test problem rapidly surpasses that of running a DNS without any stabilisation of the forward problem. As an extension of this comparison, Table 9.4 considers the cost of training as a fraction of the total runtime of a decently performing algebraic model,  $\frac{t_{train}}{t_{alg}}$ . The training times of the various ANN models are obviously influenced by numerous factors that are unaccounted for in this comparison, such as the ANN hyperparameters, number of inputs, weight initialisation and ability to quickly find a good optimum. However, despite these differences, the table ascertains that even when training on the standard, 8x8 column sets considered in Chapter 7, all ANN configurations are already consistently almost an order of magnitude more expensive than a full forward pass of an algebraic model.

Hence, even if the ANNs significant improvement in accuracy over the algebraic model could be translated to online simulations, they might still struggle to outperform the simpler model in terms of accuracy per unit of computational cost. This might improve as the simulations scale, however, as will be discussed next.

### 9.4.2. Weak Residual Assembly

During weak residual assembly of a direct version of the ANN, one forward pass of the network is required per element. Under the assumption that the ANNs will have an equal number of nodes  $n_{neur}$  in each of its  $n_{lyr}$  dense layers (as here), the computational cost of the weak residual assembly, in terms of number of operations, scales with a leading order of  $n_{el}n_{lyr}n_{neur}^2$ . This derives from having to compute  $n_{lyr}$  dense matrix-vector products of  $O(n_{neur}^2)$ , while activation function evaluations only scale with  $n_{neur}$ . Hence, an ANN's evaluation cost scales linearly in the numerical problem's degrees of freedom, but quadratically in the ANN's complexity. However,  $n_{neur}$  might in turn scale with  $n_{el}$  if new phenomena must be learned in larger problems, such that this is not necessarily universal.

The algebraic model, on the other hand, primarily scales with  $n_{el}n_{ip}n_{alg}$ , having to solve a single equation of cost  $n_{alg}$  at each integration point. Hence, as long as  $n_{ip}n_{alg} < n_{lyr}n_{neur}^2$ , it is cheaper than the ANN. For the problems listed in Table 9.4, this is certainly the case: Evaluating the weak residual with an ANN embedded is around 4 times as expensive when an algebraic model is used.

This balance is expected to be somewhat modified if the problem's two remaining dimensional degrees of freedom are added. In such cases, the ANN complexity would presumably increase, requiring a higher  $n_{neur}$ . However, its cost would still merely scale with  $n_{el}$ , while the algebraic model would require tensor grids of integration points, resulting in a scaling of  $n_{el}n_{ip}^3n_{alg}$ . This might give situations where weak residual assembly with ANNs is cheaper than with the algebraic model, although tests that realistically investigate this would require the extension of the test case considered here to 3D.

The improved scaling will almost certainly have a tangible impact when using a quadratic coefficient model, which only evaluates the ANN *once* per weak residual assembly in a time step. Therefore, this model's weak residual assembly cost is on average comparable to that of the algebraic model. As it also avoids an integration point loop, it will scale the best of all models considered here.

### 9.4.3. Jacobian Assembly

The scaling of the ANN Jacobian assembly is very similar to that of the weak residual, although the finite difference technique used in this work requires four forward passes of the ANN per element instead of one. As shown in Table 9.4, the ANN Jacobian evaluation is therefore roughly four times as costly as the ANN weak residual evaluation. The cost could be reduced to the levels of weak residual assembly if automatic differentiation techniques estimate the Jacobian entries. These techniques would require only a single backwards pass per element if the ANN is a function of all degrees of freedom of a weak form. The cost of a backwards pass through the network is similar as a forward pass, as its matrices merely need to be transposed to carry out such an operation [211].

Assembling the Jacobian based on the algebraic model incurs only a marginally higher computational cost than the algebraic model weak residual assembly: The current implementation only requires the evaluation of a single  $\tau$  per element ( $\frac{\partial r_i}{\partial a_j}$  components are neglected, as discussed in Section 5.5.4). Hence, the overall difference in cost between the ANN and algebraic Jacobian assembly in Table 9.4 exceeds an order of magnitude. However, note that the quadratic coefficient model's ANN Jacobian assembly cost changes similarly little as the algebraic Jacobian, compared to their weak residual assembly cost. This is because the quadratic coefficient model also merely requires a single forward pass of the ANN per element for the Jacobian assembly, from which the Jacobian contributions in Eq. (8.4) can be evaluated.

The same discussion on scaling as for the weak residual assembly applies to the Jacobian assembly. How-

ever, given its added comparative cost, the potential improvements of the ANN Jacobian might only materialise on very large grids with many integration points.

#### 9.4.4. Newton Iterations

Several of the parameters discussed in the previous sections also affect the number of Newton iterations that are on average required to converge the problem to a root. Section 8.3.1 showed that relaxation can aid convergence in certain cases. However, Table 9.4 demonstrates that this on average requires 1.76 times as many CPs, making a time step almost twice as expensive to take.

Furthermore, Section 8.3.2 showed that an improved ANN Jacobian reduces the number of CPs required to converge the model per time step, which might weigh up somewhat for its added cost per evaluation. Unfortunately, this reduction is generally much less than the added evaluation cost, a cost that must additionally be incurred at every CP to retain the benefits of the model. This makes simulations with an ANN Jacobian approximately 3 times as expensive to advance in time as simulations with an algebraic Jacobian. More broadly, all the direct ANN models in Table 9.4 still have weak residual spaces that are challenging for the Newton procedure to navigate. These require more than five times as many iterations to converge in a time step than algebraic models do, further exacerbating the costliness of direct, implicit ANN unresolved scales models.

In Section 8.3.5, employing ANNs trained on data from the Newton iterations improves the smoothness and convexity of the weak residual space. Here, this is paired with a large reduction in the number CPs required per time step. Similarly, the quadratic coefficient model, with its quadratic weak residual space, is easy to converge in few CPs: Even less CPs are commonly required than for the algebraic model. Finally, hybrid algebraic-quadratic coefficient models require around three times as many iterations per time step ( $36.4 \pm 7.85$ ) than the sum of an algebraic and quadratic coefficient model ( $6.05 \pm 1.25 + 5.03 \pm 1.02$ ). Hence, the cheapness of these individual models cannot be leveraged in a combined model.

#### 9.4.5. Overall Cost

These sections have highlighted that to minimise computational cost, the ANNs should be embedded in the models in such a way that they ensure cheap weak residual and Jacobian assembly, with approximately quadratic weak residual spaces that do not require relaxation and facilitate rapid convergence in every time step. While cheaper weak residual and Jacobian assembly might be achieved by leveraging parallel architecture to conduct forward passes of the ANNs, the ill-posed weak residual spaces are an inherent deficiency of the direct models in Table 9.4. Overall, this generally results in costs per time step that are an order of magnitude higher than that of the algebraic model. This adds another dimension to the model's current deficiency. However, the models remain an order of magnitude cheaper than having to run a DNS. Hence, they could still be relatively proficient in terms of accuracy per unit computational cost, if their dramatic improvement in offline prediction accuracy with respect to the algebraic model can be translated to online performance at lower cost than a DNS. The quadratic ANN model further lightens the perspective: Its weak residual and Jacobian assemblies are cheap and its weak residual space is well-posed, such that it can compete with the cost of the algebraic model at the considered level of discretisation. If it had immediate potential as a predictive model, its scaling would make it very attractive indeed.

### 9.5. Conclusions

This chapter concludes the present study on VMM-ANNs by assessing their performance in forward simulations of 1D statistically stationary boundary layer turbulence outside the models' training envelope, compared to both the ground truth high-fidelity DALES simulation and algebraic approximations of the interaction terms.

For direct ANN models, no unequivocally stable regime of the model has been identified at coarse discretisation, even at very low  $C$ . Relaxation, ANN Jacobians, training with data from the CP sequences, different feature sets, algebraic-ANN hybrids and various training sets all fail to remedy the occurrence of single modes diverging. The failure modes appear to somewhat reflect those encountered in simple problems: Attractor switches have been identified, while considerable model error now accumulates quickly over several time steps. These errors add energy to single modes and introduce the models to regimes where they suddenly drive the weak residual to infinity, or prevent it from converging.

The instabilities are postponed and even disappear for several configurations of the quadratic coefficient model at finer resolution. This confirms that while the interaction terms' predictability might not drop off at coarse resolution, the forward simulation's error suffers significantly when the ANNs' role is expanded, as

would have to be the case for larger-scale models.

The addition of an explicitly dissipative artificial viscosity operator remedies the instabilities, confirming that the lack of energy conservation lies at the root of the second mode of instability in online simulations. Furthermore, the ANN predictions of the interaction terms recover once a sufficient amount of artificial viscosity returns the simulations to physical regimes. This provides evidence that it is the models' lack of exposure to the regions their errors make them enter that lies at the foundation of their failure in this study. It is suggested that including these regions in the training of the ANNs, either in offline or online settings, could amend the failure. However, this might come at a significant additional computational cost.

This would be non-trivial, because embedding direct ANN architectures in the forward problem already strongly increases the computational cost of weak residual assembly, Jacobian assembly and the nonlinear solution procedure, in addition to their training cost. While likely scaling somewhat better than the algebraic model, this highlights that most of the ANNs' offline performance must be regained in online simulations if ANN unresolved scales models are to remain competitive with algebraic or DNS models in terms of accuracy per degree of freedom. In turn, this imposes limits on the computational cost that can be invested in strategies that attempt to regain the models' offline performance in online settings.



# 10

## Conclusions and Recommendations

In this work, a data-driven unresolved scales model for a consistent multiscale modelling framework is proposed that in theory could meet four requirements for future General Circulation Models (GCMs), identified in Chapter 2. The framework i) makes no assumptions on the unresolved scales model's form, ii) fully and consistently couples the resolved and unresolved scales models, iii) explicitly handles intermittent, energetic backscatter to the resolved scales and iv) as a result could improve the prediction of low, stratocumulus clouds if the projection of unresolved scales onto the resolved scales can be inferred when only informed by the resolved scales.

In Chapter 3, Artificial Neural Networks (ANNs) are identified as models with particularly high potential to meet these criteria, leading to the development of a Variational Multiscale Method (VMM)-ANN modelling framework. The framework is tested in the context of a highly simplified, one-dimensionalised inviscid Burgers' problem, forced by a genuinely turbulent term that derives from statistically stationary Large Eddy Simulation (LES) simulations of a Convective Boundary Layer (CBL) with the Boussinesq equations, as outlined in Chapter 4. This model problem is proposed as a stepping stone to actual turbulence simulations. In conjunction with the methodology outlined in Chapter 5, this forms the basis for answering the study's research questions.

### 10.1. Conclusions

#### RQ1

*What are the characteristic scales, spatial distributions and relevance to the global problem of the amplitudes of the interaction terms of a VMS formulation for the model problem, over a range of time and space discretisation levels?*

The turbulence of the model problem features a net-forward scattering cascade, with a short range of  $-5/3$  decay followed by a more rapidly decaying range, such that the interaction terms remain smaller than the Galerkin terms at any level of discretisation. Nevertheless, their amplitude content is significant, especially at high spatial wavenumbers of the cross and Reynolds stresses and high temporal wavenumbers of the unresolved scales time derivative projection, at reduced spatial grid resolution. At reduced temporal resolution, the latter term also becomes increasingly significant. The cross term is especially important for redistribution in the lower third of the domain, while the Reynolds term matters most at the turbulent boundaries. While the phenomena that drive the model problem's turbulence are very different from those that are faced by global models, they are judged to provide a suitable platform for a primary assessment of the developed model.

#### RQ2

*What is the ability of feed-forward ANNs trained on error-free data to make generalised offline predictions of the model problem's exact interaction terms, compared to state-of-the-art models?*

Training ANNs to represent the interaction terms of the model problem on error-free data in offline settings yields promising results when the models are evaluated in uncorrelated, offline settings. This can be observed through the answers that Chapter 7 provides to RQ2's two sub-questions.

**RQ2.1**

*Which combinations of ANN input variables, output variables and architecture ensure that the ANN accurately represents the interaction terms?*

The interaction terms can be learnt successfully by employing shallow, wide ANNs trained with learning rates in the high end of the considered range, without weight regularisation or dropout. The unresolved scales' time derivative projection benefits from the inclusion of a time history in its input feature set; including the Galerkin terms in the feature set further improves both the time derivative term and the cross term. The models dramatically improve the offline representation of the exact spatial statistics of the interaction terms in comparison to simple, algebraic, state of the art unresolved scales models, when evaluated on unseen, uncorrelated examples of the statistical turbulence that they were trained on. However, they are less well-predicted than in the simple problems encountered in [209], which is partially attributable to the input stencil's relation to the turbulence: While the stencil is local in space and time, the unresolved scales' time derivative projection's amplitude is dominated by large, non-local spatial modes and the cross- and Reynolds terms by long-term temporal modes. Including information on larger spatial modes in the input stencils of the ANNs improves their representation.

**RQ2.2**

*To what extent can an ANN predict the interaction terms over a range of increasingly coarse space and time discretisations?*

The interaction terms remain well-predicted by the ANNs over a range of grid resolutions that require them to represent the effects of inertial range turbulence. All terms but the unresolved scales' time derivative projection improve monotonically with reducing Courant number  $C$ . This is conjectured to be due to increasing overlap between the spatio-temporal domain covered by the stencil and the domain of dependence of the large, non-local modes. In spite of remaining well-predicted, the overall ANN model error is observed to rise at coarser spatial discretisation, as the interaction terms' amplitudes are progressively redistributed from the well-predicted cross term towards the worse-predicted Reynolds term. In total, this will increase the presence of model error in increasingly coarse online simulations that themselves require larger unresolved scales contributions.

**RQ3**

*To what extent does an ANN's generalised offline predictive ability at coarse resolutions translate to online simulations?*

Chapters 8 and 9 extensively demonstrate that the promising results in offline settings shown by ANNs that are trained on error-free data outside the numerical procedures of a forward problem do not translate directly to such forward simulations. The models are unstable, especially at coarser levels of discretisation. The model's failure in this simple test case provides a problematic starting point for its extension to larger-scale simulations. However, the answers to RQ3.1-RQ3.3 give some perspective to this conclusion.

**RQ3.1**

*What are sources of the stability issues encountered by Robijns in [209]?*

Investigations of a simple sine wave in 2 and 3 degrees of freedom reveal that the VMM-ANN models have two modes of instability, associated with two dimensions of the forward problem that offline model evaluations do not need to consider. The first of these results from the ANNs' impact on the nonlinear weak residual, which must be minimised to solve for the problem's degrees of freedom during every time step. The nonlinear ANNs i) introduce an unbounded number of roots to the weak residual when they depend on the problem's unknowns and ii) tend to cluster the nonlinear problem's roots in a space where they may be encountered even when the ANNs do not increase the order of the problem's nonlinearity in the degrees of freedom. This makes the VMM-ANNs practically non-unique and the problems they attempt to solve ill-posed. Instability arises from attractor switches and divergence that occur in the nonlinear Newton procedure that attempts to negotiate the distorted weak residual space that the ANNs engender. It is exacerbated at large time steps, where the models must travel far through the space.

A second mode of instability is observed even when the VMM-ANNs' weak residual spaces are well-posed: Once a small error is made, the ANNs appear insufficiently general to retain the statistical properties of the offline problem they were trained on and quickly become nonsensical. This is the second dimension that distinguishes online evaluation from error-free offline training.

Both modes of instability are also observed in forward simulations of the more realistic Boussinesq-forced Burgers' problem, where single modes accumulate energy and diverge. Attractor switches have been iden-

tified to play a part in this and it is hypothesised that distorted weak residual spaces do as well. However, instabilities of the second mode, driven by ANN-induced model errors, appear to dominate.

### RQ3.2

*To what extent can stability issues be abated by alternative formulations of the VMM-ANN model?*

No simple modifications of the VMM-ANN have been found that unconditionally remedy these two modes of instability. For the manufactured solution problem, it is shown that the first mode cannot be treated by relaxation or an improved Jacobian, which fail to guarantee the model's uniqueness. In contrast, models that limit the order of the weak residual or are trained on data sampled from trajectories through the weak residual space remedy the space's distorted appearance and non-uniqueness. From this, it is concluded that to simulate forward problems successfully, training ANNs to reproduce the correct solution of a weak form is insufficient: The network cannot generalise this knowledge to construct smooth and convex hypersurfaces *around* their correct solutions. Hence, accounting for this dimension of online running in the ANN training or model formulation substantially helps abating the first mode of instability. However, even models with better-posed weak residual spaces still fall prey to the second mode of instability.

Robijns' limiting, which keeps the predicted interaction terms close to their physical training regime, and longer temporal input stencils, which ground the ANN predictions in a temporal history, both postpone the second mode of instability somewhat, but also cannot prevent its occurrence.

The instability of each of these configurations translates to simulations of the Boussinesq-forced Burgers' problem. For this problem, the only models that remain stable are examples of a quadratic coefficient ANN model that bounds the weak residual order, when they are run at finer resolutions than what is relevant for the turbulence of the model problem. This links back to RQ2.2's answer: While the offline predictive ability of the ANNs does not drop off at increasingly coarse resolution, their model error holds the online simulations hostage when their role is expanded.

The only formulation of the VMM-ANN that consistently abates the stability issues contain an artificial viscosity, which returns excellent solution statistics and reestablishes some of the ANNs' performance from offline simulations. The latter observation suggests that the ANNs are also insufficiently generalised to handle the errors they impose on the solution they drive, when these errors eventually feed back statistically different states to their input than they were trained upon.

In summary, it appears that the two dimensions of online simulations that were insufficiently accounted for in offline training on error-free data are the reason why no stable alternative formulations of the VMM-ANN could be found: The ANNs' lacking knowledge on how to handle i) the weak residual space and ii) errors they themselves induce.

### RQ3.3

*What is the model's computational cost compared to higher-fidelity simulations and algebraically stabilised VMM?*

Finally, direct ANN architectures steeply increase the computational cost of weak residual assembly, Jacobian assembly and the Newton procedure, in addition to an appreciable training cost, when compared to algebraic VMM closures. However, they might scale somewhat better than the algebraic models, while the explicit quadratic coefficient model is already competitively cheap, albeit at the sacrifice of some offline performance.

In all, this study poses serious questions to the view that ANNs might be the silver bullet of unresolved scales models. More broadly, it questions whether numerical procedures, which pose very stringent and precise requirements on the models they successfully co-operate with, are commensurable with the unconstrained manner in which the ANNs have been treated in this study. As mentioned at the outset of the document, problems observed in this work are likely to translate to other multiscale problems that one might be tempted to solve with ANN unresolved scales models, and to other numerical frameworks in which they could be embedded in this context. Yet, these conclusions also identify several immediate improvement directions for future work, such that the overall outlook is not as bleak as they suggest, but actually still full of potential.

## 10.2. Recommendations

### Neural Network Structure

Section 7.3 showed that the offline predictions of the ANNs are limited by the input stencil, which is rather local in comparison to the dominant spatial and temporal scales of several of the terms. This was amended

by considering wider spatial input stencil, although they were not considered in forward simulations of the problem. Such stencils would inform the simulation of larger scales, and discourage the excitement of single, local modes to unreasonable amplitudes if the rest of the domain remains well-predicted. In a similar vein, tailoring the locality of feature interaction in a problem is already well-described by Convolutional Neural Networks (CNNs). Their convolutional layers can be set with strides that would control the non-locality of the problem in a more global, spatial sense [21]. Such parameters can be related to features such as the correlation length of the turbulence. Since CNNs commonly open the door to strong performance increases in problems with many, varying features, it is recommended to abandon the dense local architectures considered here for CNNs that are evaluated once for the entire spatial domain, with the feature extraction at all scales in the domain embedded in the architecture.

Similarly, one might incorporate longer temporal histories or statistics thereof as input to the ANNs. These histories may prevent nonphysical time-step level fluctuations, by removing spurious roots that do not mesh with the longer-term behaviour of the problem. They may also restrain the model from migrating into statistically different regimes that do not agree with the problem's long-term dynamics. However, ANN architectures that cover long-term behaviour already exist: Several sophisticated architectures of Recurrent Neural Networks (RNNs) are already somewhat capable of successfully incorporating long- and short-term histories into their predictions in fluid flow problems [255]. These architectures might therefore be leveraged to keep the models better in check with their important, longer-term dynamics.

### Weak Boundary Conditions

The mode that destabilises the forward problem is frequently the mode directly adjacent to the boundary. This is because the strong, homogeneous Dirichlet boundary condition requires very large gradients in the solution from the wall in the first element. This requirement may be relaxed by substituting the strong conditions for their weak counterparts, which is often observed to aid stability of the wall-layer in traditional LES [112]. Weak formulations would also naturally handle the heat flux boundary conditions of 3D simulations, should follow-up studies get to those. Hence, it is recommended to incorporate such interpretations of the boundary condition in following work.

### Enforcement of Energy Conservation

The implementation of the method considered here precluded a proper analysis of the evolution of energy in the resolved flow. While this did not curtail the identification of the phenomena driving the instability of the 1D Boussinesq-forced problem, it should ideally be more fully conducted in the online simulations of future work. Additionally, the evaluation of such balances could be used as online constraints on how rapidly energy is allowed to accumulate in the scales that are normally associated with instability. While constraining the evolution of energy comes dangerously close to imposing a prediction on the model instead of the model giving the prediction, the cutoffs of such models could likely already be set at relatively high values, as clearly nonphysical behaviour is here seen to emerge on very short time scales, driven by the potential of the non-linear Newton procedure to rapidly drive the solution to nonsensical regimes. In an offline sense, the models could be informed of the energy balance during training, where one can add the energy evolution of each interaction term to the cost function. Finally, one might return to a framework that is slightly less ambitious than what is studied here, where energy conservation is enforced explicitly by the model form (e.g. [226]), and only predict the coefficients of such models. This line of research is gaining traction in the atmospheric modelling community [220]. While such frameworks are less general than what is considered here, they are much better positioned to leverage prior knowledge of how the unresolved scales should behave, even if this knowledge is put forward through phenomenological models.

### Training for the online problem

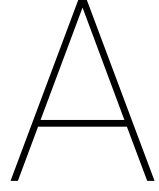
The most profound limit of the ANNs considered here, however, appears to be their lack of generalisability from offline settings to online simulations. The evidence presented in Section 8.3.5 and Section 9.3 suggests that this might be due to lacking knowledge of both the iterative solution procedure and the physical regimes the model error drives it to. Two general strategies might be targeted to amend this, as outlined at the end of Section 9.3.

First, one may attempt to add the weak residual and model-induced error dimensions to an offline training set. For such training, a single training example of an error-free set of inputs and an interaction term output would be enriched with input data from i) the weak residual space and ii) errors the ANNs could have induced, for instance from an earlier online simulation.

---

Second, Rasp's recent study suggests training the ANNs online might improve how the ANNs are taught to deal with the errors they themselves induce [204]. As noted in Section 9.3, both strategies likely rapidly scale the expense of the training, such that detailed studies are recommended to gauge their effectiveness in generalising the ANNs to online simulations and the resulting accuracy per unit computational cost.





# Atmospheric Scale Ranges and Models

Despite the lacking evidence for its general validity [153], global atmospheric models traditionally rely on scale separation to contain their computational cost. When formulating a mathematical model, this is done by manipulating the Navier-Stokes equations (Eq. (2.1)) to isolate the scale ranges that one is interested in [130, 202]. Self-contained, distinct scale ranges, as opposed to continuous, strongly interacting spectra, would allow mathematical models to be unambiguously posed for the dominating phenomena over a given range of scales without worrying whether this will interact with different sets of scales. This allows the focus to be placed only on the phenomena that are predominantly associated with the scales one is interested in. As these models appear in several discussions in this report, the following paragraphs aim to provide the background and reasoning that leads to their formulation.

Klein presents a framework of multiscale asymptotics that allows the identification of the distinguished scale-specific asymptotic limits of Eq. (2.1) [130, 131]. He departs from eight universal characteristics that define atmospheric motion, presented in Table A.1.

Characteristic	Symbol	Order of magnitude [unit]
Earth radius	$R_e$ [m]	$6 \cdot 10^6$
Earth rotation rate	$\Omega_e$ [ $s^{-1}$ ]	$10^{-4}$
Gravitational acceleration	$g$ [ $ms^{-2}$ ]	$10^1$
Sea-level surface pressure	$p_0$ [ $Nm^{-2}$ ]	$10^5$
Freezing temperature of H <sub>2</sub> O	$T_0$ [K]	$3 \cdot 10^2$
Equator-pole and vertical tropospheric potential temperature difference	$\Delta \theta_0$ [K]	$4 \cdot 10^1$
Dry gas constant	$R_g$ [ $m^2s^{-2}K^{-1}$ ]	$3 \cdot 10^2$
Dry ratio of specific heats	$\gamma$ [-]	$10^1$

Table A.1: Universal characteristics of atmospheric motion, adopted from Klein [131]

The seven dimensional characteristics in Table A.1 allow construction of auxiliary quantities, typically referred to in literature as sea-level air density  $\rho_0 \sim 1.25 \text{ kgm}^{-3}$  and density scale height  $h_{sc} \sim 11 \text{ km}$ , as well as three distinct signal speeds: sea-level speed of sound  $c_s \sim 330 \text{ ms}^{-1}$ , “internal wave speed”  $c_{int} \sim 110 \text{ ms}^{-1}$  and “thermal wind velocity”  $u_{th} \sim 12 \text{ ms}^{-1}$ . Internal waves refer to oscillations that are balanced by gravity, while thermal winds pertain to the motion induced by potential temperature gradients under hydrostatic and geostrophic balance. With these quantities, one may construct three independent, nondimensional  $\Pi$  parameters. While not very rigorously confined by Klein, it can be instructive to relate these  $\Pi$  parameters to a single small parameter  $\varepsilon \sim O(10^{-1})$ , which allows them to refer to ratios between the different characteristic speeds [131]:

$$\Pi_1 = \frac{h_{sc}}{R_e} \approx 1.6 \cdot 10^{-3} = c_1 \varepsilon^3 \sim \frac{u_{th}}{c_s} \quad (\text{A.1a})$$

$$\Pi_2 = \frac{\Delta \Theta_{ref}}{T_{ref}} \approx 1.5 \cdot 10^{-1} = c_2 \varepsilon \sim \frac{u_{th}}{c_{int}} \quad (\text{A.1b})$$

$$\Pi_1 = \frac{c_s}{\Omega_e R_e} \approx 4.7 \cdot 10^{-1} = c_3 \sqrt{\varepsilon} \sim \frac{c_{int}}{c_s} \quad (\text{A.1c})$$

In combination with  $h_{sc}$  and  $R_e$ , the length scales that correspond to the three characteristic signal speeds then give rise to five discernible spatial scales from the initial characteristics. Table A.2 presents these with typical nomenclature, and links their relative scaling to  $h_{sc}$  in terms of  $\varepsilon$  to indicate their distinct scale association:

Characteristic length	Symbol	$\varepsilon$ scaling	Value [unit]
Planetary scale	$L_p = \frac{\pi}{2} R_e$	$\varepsilon^{-3} h_{sc}$	$10^4$ km
Obukhov radius / External Rossby radius	$L_{ob} = \frac{c_{ref}}{\Omega_e}$	$\varepsilon^{-\frac{5}{2}} h_{sc}$	$3.3 \cdot 10^3$ km
Synoptic scale / Rossby radius	$L_{ro} = \frac{c_{int}}{\Omega_e}$	$\varepsilon^{-2} h_{sc}$	$1.1 \cdot 10^3$ km
Meso- $\beta$ scale	$L_{meso} = \frac{u_{th}}{\Omega_e}$	$\varepsilon^{-1} h_{sc}$	$1.5 \cdot 10^2$ km
Meso- $\gamma$ scale / density scale height	$h_{sc} = \frac{\gamma p_0}{g \rho_0}$	$\varepsilon^0 h_{sc}$	$1.1 \cdot 10^1$ km

Table A.2: Discernible length scales of atmospheric motion, adopted from Klein [131]

At each of these length scales, different terms in Eq. (2.1) have different magnitudes, as illustrated by the definitions of their non-dimensional scaling parameters in Eq. (A.2). Two notes should be taken from these definitions: First, at the characteristic velocity and length scales presented above,  $Re$  is always very large, such that the viscous term in Eq. (2.1b) is commonly neglected at the mathematical modelling stage to reduce Eq. (2.1) to the Euler equations [169, 236]. This is the reason why no reference dynamic viscosity  $\mu_d$  is included in Table A.1. Second, the non-dimensional numbers are interdependent and can be re-expressed in terms of  $\varepsilon$ . For instance, if  $l_{ref} = h_{sc}$ ,  $u_{ref} = u_{th}$  and  $t_{ref} = \frac{h_{sc}}{u_{th}}$ :

$$Fr = \frac{u_0}{\sqrt{g l_0}} = \frac{u_{th}}{R_g T_{ref}} = \frac{u_{th}}{c_s} = \varepsilon^3 \quad (\text{A.2a})$$

$$Ma = \frac{u_0}{\sqrt{p_0 / \rho_0}} = \frac{u_{th}}{c_s} = \varepsilon^3 \quad (\text{A.2b})$$

$$Ro = \frac{u_0}{2 \Omega_e l_0} = \frac{1}{2} \frac{L_{meso}}{h_{sc}} = \frac{1}{2} \varepsilon \quad (\text{A.2c})$$

$$St = \frac{l_0}{t_0 u_0} = 1 \quad (\text{A.2d})$$

$$Re = \frac{\rho_0 u_0 l_0}{\mu} = \frac{\rho_0 u_{th} h_{sc}}{\mu_d} \sim O(10^{10}) \quad (\text{A.2e})$$

Carrying out a similar interpretation at the other main discernible length scales, maintaining  $u_0 = u_{th}$  and  $t_0 = \frac{l_0}{u_0}$ , shows how the different terms scale differently as the characteristic length scale increases:

Non-dimensional parameter	Definition	$h_{sc}$	$L_{meso}$	$L_{Ro}$	$L_p$
Froude number	$Fr = \frac{u_0}{\sqrt{g l_0}}$	$\varepsilon^3$	$\varepsilon^{\frac{7}{2}}$	$\varepsilon^4$	$\varepsilon^{\frac{9}{2}}$
Mach number	$Ma = \frac{u_0}{\sqrt{p_0 / \rho_0}}$	$\varepsilon^3$	$\varepsilon^3$	$\varepsilon^3$	$\varepsilon^3$
Rossby number	$Ro = \frac{u_0}{2 \Omega_e l_0}$	$\frac{1}{2} \varepsilon$	$\frac{1}{2} \varepsilon^2$	$\frac{1}{2} \varepsilon^3$	$\frac{1}{2} \varepsilon^4$
Strouhal number	$St = \frac{l_0}{t_0 u_0}$	1	1	1	1

Table A.3: Non-dimensional parameters in Eq. (2.1) and their value in terms of  $\varepsilon$  at the discernible reference lengths of Table A.2, when  $u_0 = u_{th}$  and  $t_0 = \frac{l_0}{u_0}$

If one then assumes that solutions to Eq. (2.1) can depend on only a single temporal scale, vertical length scale and horizontal length scale, all appropriate to the phenomenon under consideration, a hierarchy of asymptotic “single-regime” models may be constructed in terms of scalings with  $\varepsilon$  when  $\varepsilon \rightarrow 0$ . These models are the most frequently encountered mathematical interpretations of atmospheric motion. When  $\varepsilon$  is compared to  $h_{sc}$  and  $t_0 = \frac{h_{sc}}{u_0}$ , these models may be summarised by Fig. A.1.

Particularly useful models for time-dependent, advective processes arise when  $t_0$  and  $l_0$  are of the same order (internal waves are better described when a timescale is constructed with  $c_{int}$  and  $l_0$ ). These are the

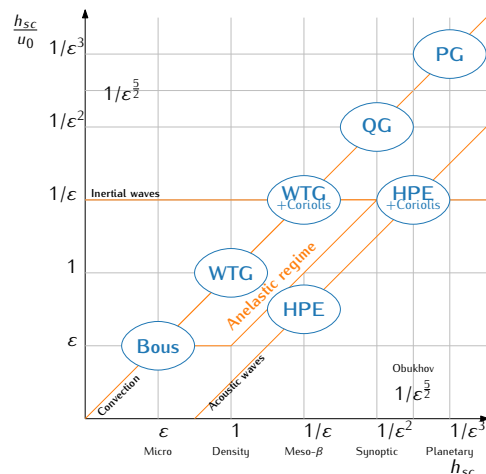


Figure A.1: Particular mathematical models at various ranges of length and time scales compared to  $h_{sc}$  and  $u_0 = u_{th}$ . WTG is the weak temperature gradient model, HPE are the hydrostatic primitive equations, QG is quasi-geostrophic motion and PG is planetary geostrophic motion

combinations on the diagonal of Fig. A.1 that correspond to the non-dimensional parameters in Table A.3. An example is the set of Weak Temperature Gradient (WTG) models, which arise in the asymptotic limit of Eq. (2.1) when  $\epsilon^0 - \epsilon^{-1}$  is introduced. WTG models are often used for analyses in tropical meteorology [162].

When  $l_0$  and  $u_0$  increase, different balances begin dominating. In particular,  $Ro$  reduces such that Earth-rotational effects become increasingly important in the horizontal momentum equations. This results in the quasi-geostrophic models on the synoptic scales and planetary geostrophic models on the planetary scales [259]. As Table A.3 shows, the balance at leading order for these models is increasingly between global-scale pressure gradients and Coriolis forces as  $Ma$  and  $Ro$  attain the same order at the scale of  $L_{Ro}$ .

### A.1. The Anelastic and Boussinesq Equations

The anelastic equations have two attractive characteristics: First, they identify a flow regime in which not a single timescale needs to be chosen, but a range of timescales remains valid [189]. Second, they prohibit the acoustic wave solutions allowed by Eq. (2.1).

Acoustic waves are broadly considered insignificant for meteorological or climatological phenomena at the global scale [130, 189, 202]. Yet, their discretised representation obliges high temporal resolutions to guarantee the stability of most numerical methods [230]. To save computational cost, it is therefore common to filter acoustic waves from the equations [85]. This yields analogous situations to classic incompressible flow regimes, although they are explicitly required to still describe phenomena associated with moist convection, stratification and rotational effects when applied for atmospheric simulation [131].

The anelastic approximation achieves this by assuming that sound speed  $c_s \rightarrow \infty$ , such that linear pressure wave solutions to Eq. (2.1) are prohibited and such information travels throughout the domain instantaneously [202]. This can be achieved by setting  $\frac{\partial \rho}{\partial t}$  in Eq. (2.1a) to 0, proposing that the velocity field is divergence-free.

The anelastic assumption is valid when four conditions are met [202]. First, all thermodynamic variables may only deviate slightly from their reference values, such that density and pressure perturbations  $\rho''$  and  $p''$  from a reference state  $\rho_0$  and  $p_0$ , defined as  $\rho'' = \rho - \rho_0$  and  $p'' = p - p_0$ , are relevant unknowns. Second, processes associated with advection ( $O(u_{th})$ ) and internal waves ( $O(c_{int})$ ) must be of sufficiently low frequency, or large time scale, that they are far removed from processes at the time scales of the speed of sound ( $c_s$ ). Third, the advective and internal wave dynamics must be of similar time scales. This statement means that the frequency of the internal waves, the Brunt-Väisälä frequency, is of similar order as the inertial scale frequency  $t_0^{-1} = \frac{u_0}{l_0}$ . In terms of the analysis above, it demands that  $c_{int} = O(u_{th})$  when  $\epsilon \rightarrow 0$  [131]. Finally, the ‘‘aspect ratio’’ of the motions, or the ratio of characteristic vertical and horizontal length scales, must be sufficiently small. This justifies neglect of time-variations in the density perturbations in Eq. (2.1a), while maintaining their influence in the  $Ma$  and  $Fr$  terms in Eq. (2.1b), where they influence pressure and potential

temperature perturbations. In dimensional flux form, this leads to Eq. (A.3):

$$\frac{\partial}{\partial x_j} (\rho u_j) = 0 \quad (\text{A.3a})$$

$$\frac{\partial}{\partial t} (\rho u_i) + \frac{\partial}{\partial x_j} (\rho u_j u_i) + 2\varepsilon_{ijk} \Omega_{ej} \rho u_k + \frac{\partial p}{\partial x_i} + g \rho \delta_{i3} = 0 \quad (\text{A.3b})$$

$$\frac{\partial}{\partial t} (\rho \theta) + \frac{\partial}{\partial x_j} (\rho \theta u_j) = S_\theta \quad (\text{A.3c})$$

The anelastic system can reduce pressure prediction to solving a diagnostic Poisson equation, similar to what can be done for incompressible flow [92, 202]. However, in combination with the numerical challenges of solving pressure Poisson equations, it has two important drawbacks. First, it only remains accurate for small variations in  $\theta$  with respect to the reference state, which does not hold across the troposphere [69]. Second, it does not conserve energy [13] unless the reference state is isentropic [202]. Therefore, more general versions of the anelastic equations [149], or extensions such as the pseudo-incompressible equations [69, 130], have been developed.

The Boussinesq equations result from further reducing the scales of the motion considered in the problem. In particular, when the motion's depth in  $z$  becomes of  $O(\varepsilon)$ , Fr and gravity will become increasingly dominant, such that the motion is comparatively less influenced by fluctuations in pressure with respect to the reference state. Pressure fluctuations are then much smaller than density or temperature fluctuations, such that by the ideal gas law:

$$\frac{\theta''}{\theta_0} = -\frac{\rho''}{\rho_0} \quad (\text{A.4})$$

This allows the removal of density fluctuations from the equations of motion, expressing them only in terms of pressure fluctuations  $\pi = \frac{p''}{\rho_0}$  and temperature fluctuations  $\theta'' = \theta - \theta_0$ :

$$\frac{\partial u_j}{\partial x_j} = 0 \quad (\text{A.5a})$$

$$\frac{\partial u_i}{\partial t} + u_j \frac{\partial u_i}{\partial x_j} + 2\varepsilon_{ijk} \Omega_{ej} u_k + \frac{\partial \pi}{\partial x_i} + g \frac{\theta''}{\theta_0} \delta_{i3} = 0 \quad (\text{A.5b})$$

$$\frac{\partial \theta}{\partial t} + \frac{\partial}{\partial x_j} (\theta u_j) = S_\theta \quad (\text{A.5c})$$

The Boussinesq equations are frequently employed for atmospheric boundary layer computations of shallow convection. While they can result in satisfactory analyses of processes at these scales, the discussion above aims to highlight that they are not valid at much larger scales, where different processes dominate the motion. Nevertheless, since these scales are meaningful for climate-scale predictions satisfactorily described in global-scale models, they are considered a suitable place to begin developing new models.

## A.2. The hydrostatic primitive equations

At larger scales, a fluid flow model must remain valid across the globe. This yields significant challenges for posing mathematical models that exploit scale-specific phenomena, neglect acoustic waves, but remain consistent with the original equation set.

Therefore, it is generally considered necessary to retain fully compressible equations in the horizontal for length scales larger than  $h_{sc}$  [131], while approximations are often introduced through the vertical momentum equation [253]. The most common approximation is to consider that this equation reduces to hydrostatic balance. This is justified by recognising that a characteristic vertical length scale is  $h_{sc}$ , while the planetary length scale  $L_p = \varepsilon^{-3} h_{sc}$ . This is the shallow-atmosphere approximation [253, 254]. It forms the grounds for omitting the time-varying component of vertical velocity  $w$ , by pointing out that  $t_0 = \frac{L_p}{u_{th}} = \varepsilon^{-3} \gg \frac{L_{Ro}}{u_{th}} = \varepsilon^{-2}$ , such that internal gravity waves, which are fluctuations of  $w$  associated with  $c_{int} \propto L_{Ro}$  are neglected. This is the quasi-steady approximation [171, 202].

Hydrostatic balance therefore explicitly filters both vertical acoustic and internal waves by ignoring vertical mean velocity, while allowing horizontally propagating acoustic waves such as Lamb waves [131]. This

is problematic for direct modelling of small scale behaviour, because the horizontal perturbation pressure force is not hydrostatically balanced by the perturbation density field, leading to spurious, unstable modes [202]. However, as discussed in Section 2.2, global-scale discretised models commonly employ grid resolutions that are too large to simulate these scales, deferring this problem to the higher-resolution models that are expected to emerge over the coming decade.

### A.3. The Superparameterisation (SP) Equations

Grabowski's original proposal for SP departs from the anelastic equations Eq. (A.3) and casts them on the general SP form Eq. (2.9). This results in seven large scale and small scale anelastic equations for moist dynamics, such that in the terminology of Eq. (2.9),  $\chi = [u_i, \theta, q_v, q_c, q_p]^T$ , where  $q_v$ ,  $q_c$  and  $q_p$  are the mixing ratios of water vapour, condensed water and precipitation (condensed water that falls relative to the flow) [83]. All assumed small-scale effects are included in the small-scale equations. Only large-scale advection, buoyancy (as denoted with reference to the ambient state  $\theta_e$  and the reference potential temperature profile  $\bar{\theta}_0$ ), Coriolis forcing and optional gravity wave absorbers (subsumed under the optional source terms  $f$ ) and pressure perturbations with respect to a geostrophically balanced ambient condition normalised with the anelastic reference density  $\rho_0$  remain in the large-scale equations.  $\kappa = \frac{R_v}{R_g} - 1$  ( $R_v$  is the gas constant of water vapour) and  $\bar{\xi} = [\bar{\theta}, \bar{q}_v, \bar{q}_c, \bar{q}_p]$ , while the total derivative  $\frac{D}{Dt}$  subsumes the steady and unsteady inertial terms.

$$\frac{\partial(\rho_0 \bar{u}_j)}{\partial x_j} = 0 \quad (\text{A.6a})$$

$$\frac{D\bar{u}_i}{Dt} = -\frac{\partial\bar{\pi}}{\partial x_i} + \delta_{i,3}g \left( \frac{\bar{\theta} - \bar{\theta}_e}{\bar{\theta}_0} + \kappa(\bar{q}_v - \bar{q}_{v,e}) - \bar{q}_c - \bar{q}_p \right) + F_{SS}^{\bar{u}_i} + f_{\bar{u}_i} \quad (\text{A.6b})$$

$$\frac{D\bar{\xi}}{Dt} = F_{SS}^{\bar{\xi}} + f_{\bar{\xi}} \quad (\text{A.6c})$$

The small-scale anelastic equations take on a similar form:

$$\frac{\partial(\rho_0 u'_j)}{\partial x_j} = 0 \quad (\text{A.7a})$$

$$\frac{Du'_i}{Dt} = -\frac{\partial\pi'}{\partial x_i} + \delta_{i,3}g \left( \frac{\theta' - \theta'_e}{\theta'_0} + \kappa(q'_v - q'_{v,e}) - q'_c - q'_p \right) - F_{SS}^{u'_i} + f_{u'_i} \quad (\text{A.7b})$$

$$\frac{D\theta'}{Dt} = \frac{\theta_e}{T_0} \left[ \frac{L_v}{c_p} (\text{CON} + \text{DEP}) + r_f \right] + S_{\theta'} - F_{SS}^{\theta'} + f_{\theta'} \quad (\text{A.7c})$$

$$\frac{Dq'_v}{Dt} = -\text{CON} - \text{DEP} + s_{q_{v'}} - F_{SS}^{q'_{v'}} + f_{q'_{v'}} \quad (\text{A.7d})$$

$$\frac{Dq'_c}{Dt} = \text{CON} - \text{ACC} - \text{AUT} - F_{SS}^{q'_{c'}} + f_{q'_{c'}} \quad (\text{A.7e})$$

$$\frac{Dq'_p}{Dt} = \frac{1}{\rho_0} \frac{\partial}{\partial z} (\rho_0 v_t q'_p) + \text{ACC} + \text{AUT} + \text{DEP} - F_{SS}^{q'_{p'}} + f_{q'_{p'}} \quad (\text{A.7f})$$

Where  $r_f$  is the temperature influence due to radiative flux divergence,  $L_v$  is the latent heat of evaporation or condensation of water,  $c_p$  is the specific heat of air at constant pressure and  $v_t$  is the sedimentation velocity of precipitation water. Cloud condensation from water vapour CON, autoconversion of condensate into precipitation AUT, condensate accretion through precipitation ACC and the precipitation source or sink through deposition or evaporation of water vapour DEP are all modelled on the small scales only, originally through Grabowski's own simple scheme [82].



# B

## A Bulk Model for the Statistically Stationary Convective Boundary Layer

Van Driel and Jonker consider a bulk model of the CBL [247]. This model reduces the problem to a 1D situation with constant  $\theta$  and exactly linearly reducing  $\langle w''\theta'' \rangle$  in the mixed layer. The temperature inversion  $\Delta\langle\theta\rangle$  is a discontinuity.

These assumptions simplify the problem greatly. Consider first continuity in its conservative form over the layer, which simplifies to indicating that  $z_i$  varies in time only with the net vertical velocity  $w_e - w_s$ ,  $w_e$  denoting the entrainment velocity directed upwards and  $w_s$  denoting a possible subsidence velocity oriented downwards:

$$\frac{\partial z_i}{\partial t} = w_e - w_s \quad (\text{B.1})$$

Hence, if one is to prevent the layer from growing in time, one must know what drives  $w_e$  and subsequently balance it with a subsidence. [247] proposes to achieve this with a radiative sink,  $S_\theta \propto w_s$ . The study proceeds to derive a bulk model for the CBL that can be subjected to analytical stability analysis, to find a suitable choice for  $S_\theta$  that ensures that  $\frac{\partial z_i}{\partial t} = 0$ . This choice informs the governing inputs of the high-fidelity statistically stationary LES simulation of this study. Therefore, the approach is briefly described below.

To be solved, Eq. (B.1) requires an approximation for  $w_e$ . For this purpose, consider the conservation equation for potential temperature within the CBL, represented here in its integral form also.  $\langle\theta\rangle$ , constant in space, varies in time only as a balance of turbulence-induced flux at the vertical domain boundaries, the surface and the inversion height, or through any source term in the layer. This is where the radiative source  $S_\theta$  is introduced.

$$z_i \frac{\partial \langle\theta\rangle}{\partial t} = -S_\theta + \langle w''\theta'' \rangle_s - \langle w''\theta'' \rangle_{z_i} \quad (\text{B.2})$$

In addition, potential temperature is conserved over the temperature discontinuity, which requires slightly more analysis. Consider, for the 1D problem, this sudden jump in  $\langle\theta\rangle$  over  $z_i$  ( $z_l$  denotes any  $z$  within the convective layer, whereas  $z$  is a location above it):

$$\frac{\partial}{\partial t} \left[ \int_{z_l}^{z_i^-} \langle\theta\rangle dz + \int_{z_i^+}^z \langle\theta\rangle dz \right] = \langle w''\theta'' \rangle_{z_l} - \langle w''\theta'' \rangle_z - \int_{z_l}^z S_\theta dz \quad (\text{B.3})$$

$\langle w''\theta'' \rangle_z = 0$ , as the layer above the inversion is assumed to be a stable stratification, with no turbulence. As the temperature inversion may change over time, Leibniz' rule must be invoked to carry out the integration:

$$\frac{\partial z_i}{\partial t} \langle\theta\rangle_{z_i^-} + \int_{z_l}^{z_i^-} \frac{\partial \langle\theta\rangle}{\partial t} dz - \frac{\partial z_i}{\partial t} \langle\theta\rangle_{z_i^+} + \int_{z_i^+}^z \frac{\partial \langle\theta\rangle}{\partial t} dz = \langle w''\theta'' \rangle_{z_l} - \int_{z_l}^z S_\theta dz \quad (\text{B.4})$$

Defining the temperature discontinuity is  $\Delta\langle\theta\rangle = \langle\theta\rangle_{z_i^+} - \langle\theta\rangle_{z_i^-}$  and recognising that the remaining integrals of  $\frac{\partial\langle\theta\rangle}{\partial t}$  merely represent new flux and radiation balances such as Eq. (B.2) in the respective domains below and above the discontinuity, this can be rewritten as:

$$-\frac{\partial z_i}{\partial t}\Delta\langle\theta\rangle + \langle w''\theta''\rangle_{z_i} - \langle w''\theta''\rangle_{z_i^-} - \int_{z_i}^{z_i^-} S_\theta dz + \langle w''\theta''\rangle_{z_i^+} - \langle w''\theta''\rangle_z - \int_{z_i^+}^z S_\theta dz = \langle w''\theta''\rangle_{z_i} - \int_{z_i}^z S_\theta dz \quad (\text{B.5})$$

Again invoking the argument that all turbulent fluxes above the discontinuity are 0, while cancelling the fluxes at  $z_i$  and radiation terms under the assumption that  $S_\theta$  is a time-independent constant yields an expression relating the entrainment flux to the inversion strength:

$$\frac{\partial z_i}{\partial t}\Delta\langle\theta\rangle = -\langle w''\theta''\rangle_{z_i^-} = -\langle w''\theta''\rangle_{z_i} \quad (\text{B.6})$$

[247] proposes to simplify Eq. (B.6) through Lilly's zeroth-order model [146], by setting  $\frac{\partial z_i}{\partial t} \approx w_e$  under the assumption that layer growth is locally driven:

$$\langle w''\theta''\rangle_{z_i} \approx -w_e\Delta\langle\theta\rangle \quad (\text{B.7})$$

This is obviously inconsistent with Eqs. (B.1) and (B.2). Nevertheless, it is adopted here to illustrate a more important point: The layer's growth is related to the inversion strength  $\Delta\langle\theta\rangle$ . Hence, to ensure the stability of the layer, one must analyse the evolution of  $\Delta\langle\theta\rangle$  in addition to that of  $z_i$ . An evolution equation for  $\Delta\langle\theta\rangle$  is easily posed by applying the assumptions of the simplified model [240]:

$$\frac{\partial\Delta\langle\theta\rangle}{\partial t} = \frac{\partial\langle\theta\rangle_{z_i^+}}{\partial t} - \frac{\partial\langle\theta\rangle_{z_i^-}}{\partial t} \quad (\text{B.8a})$$

$$\frac{\partial\langle\theta\rangle_{z_i^-}}{\partial t} = \frac{\partial\langle\theta\rangle}{\partial t} \quad (\text{B.8b})$$

$$\frac{\partial\langle\theta\rangle_{z_i^+}}{\partial t} = \frac{\partial\langle\theta\rangle_{z_i^+}}{\partial z_i} \frac{\partial z_i}{\partial t} = \Gamma \frac{\partial z_i}{\partial t} \quad (\text{B.8c})$$

$$\frac{\partial\Delta\langle\theta\rangle}{\partial t} = \Gamma \frac{\partial z_i}{\partial t} - \frac{\partial\langle\theta\rangle}{\partial t} \quad (\text{B.8d})$$

Where  $\Gamma = \frac{\partial\langle\theta\rangle}{\partial z}$ . This is considered a constant at any location above  $z_i$ . If one then chooses  $S_\theta$ 's proportionality constant such that  $S_\theta = w_s\Gamma$ , this can be rewritten, using the reduced continuity equation to:

$$\frac{\partial\Delta\langle\theta\rangle}{\partial t} = \Gamma w_e - \frac{\partial\langle\theta\rangle}{\partial t} - S_\theta \quad (\text{B.9})$$

Assuming  $\langle w''\theta''\rangle_s$  will be specified as a boundary condition and is known, this leaves four equations (Eqs. (B.1), (B.2), (B.7) and (B.9)) for five unknowns ( $w_e$ ,  $w_s$ ,  $\langle\theta\rangle$ ,  $\Delta\langle\theta\rangle$  and  $\langle w''\theta''\rangle_{z_i}$ ). To evaluate  $\langle w''\theta''\rangle_{z_i}$  and close the model, an estimate must be made of the transport of turbulent flux from the surface to the inversion altitude, often achieved through further simplification of Eq. (4.4). Common options are to assume that vertical redistribution is instantaneous through only term V in Eq. (4.3) [18, 240], that only the vertical velocity component matters for this transport and that it is directly driven by the surface heat flux. This yields:

$$-\langle w''\theta''\rangle_{z_i} \approx C'' \frac{\partial}{\partial z} \langle kw' \rangle \approx C' w''^3 \approx C \langle w''\theta'' \rangle_s \quad (\text{B.10})$$

Van Driel and Jonker point out that making this assumption breaks down when the convective timescales in the layer are short, because it assumes that term i in Eq. (4.3) is 0, which is unreasonable [247]. This is improved by posing a transport equation for  $E$  (as proposed in [184]).

Regardless of which closure model is employed, the model is tractable for analytical fixed point and linear fluctuation analysis to ascertain that statistically stable situations can be reached [247]. The former is done by rewriting Eqs. (B.1), (B.2), (B.7), (B.9) and (B.10) to two evolution equations for  $z_i$  and  $\Delta\langle\theta\rangle$ :

$$\frac{\partial z_i}{\partial t} = \frac{C \langle w''\theta'' \rangle_s}{\Delta\langle\theta\rangle} - w_s \quad (\text{B.11a})$$

$$\frac{\partial \Delta \langle \theta \rangle_i}{\partial t} = \langle w'' \theta'' \rangle_s \left( \frac{C\Gamma}{\Delta \langle \theta \rangle} + \frac{1+C}{z_i} \right) \quad (\text{B.11b})$$

And subsequently setting the time derivatives in Eq. (B.11) to 0. This returns a single fixed-point solution,  $z_{i_0}, \Delta \langle \theta \rangle_0$ :

$$\Delta \langle \theta \rangle_0 = \frac{C \langle w'' \theta'' \rangle_s}{w_s} \quad (\text{B.12a})$$

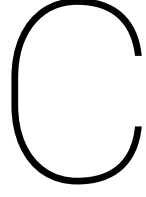
$$z_{i_0} = \frac{(1+C) \langle w'' \theta'' \rangle_s}{S_\theta} \quad (\text{B.12b})$$

The leading order time-derivatives of linear fluctuations to these fixed points are summarised in a Jacobian matrix, which has eigenvalues with ever negative real parts, revealing that the fixed points are unconditionally stable:

$$\lambda_{1,2} = -\frac{1 \pm \sqrt{\frac{1-3C}{1+C}}}{2C} \frac{\Gamma w_s^2}{\langle w'' \theta'' \rangle_s} \quad (\text{B.13})$$

Hence, this analysis informs that the choice of  $S_\theta = \Gamma w_s$  is suitable to ensure that a statistically stationary situation can be maintained as long as  $\langle w'' \theta'' \rangle_s > \text{const} > 0$  and its fluctuations are not overly large.





## Methodology Details

Several details of the methodology that is broadly outlined in Chapter 5 are further exhibited in this appendix. While these details distract from the higher-level discussion in the main text, they are included here to ensure the completeness of the study's documentation.

### C.1. Bi-Cubic Interpolation of DALES Data

To construct the forcing anywhere in the spatio-temporal 1D domain of the Boussinesq-forced Burgers' problem, the discrete, sampled  $w$  in any column of the Dutch Atmospheric Large Eddy Simulation (DALES) data must be made a continuous function of  $z$  and  $t$  from its nodal definition  $z_i$  and  $t^n$ :

$$w_i^n \rightarrow w(z, t) \quad (\text{C.1})$$

To achieve this,  $w(z, t)$  is defined as a set of bi-cubic Hermite splines. Given  $z_i < z < z_{i+1}$  and  $t^n < t < t^{n+1}$ , four such 1D splines are constructed along the time direction at  $z_{i+j}$ ,  $j = [-1, 0, 1, 2]$ , assuming the grid spacing  $h$  and time step  $\Delta t$  are constant:

$$w(z_{i+j}, t) = \sum_{k=0}^3 c_{jk} t^k \quad (\text{C.2})$$

Where  $c_{jk}$  is the  $4 \times 4$  matrix that ensures the satisfaction of:

$$w(z_{i+j}, t^n) = w_{i+j}^n \quad (\text{C.3})$$

$$w(z_{i+j}, t^{n+1}) = w_{i+j}^{n+1} \quad (\text{C.4})$$

$$\frac{\partial w(z_{i+j}, t^n)}{\partial t} = \frac{w_{i+j}^{n+1} - w_{i+j}^{n-1}}{2\Delta t} \quad (\text{C.5})$$

$$\frac{\partial w(z_{i+j}, t^{n+1})}{\partial t} = \frac{w_{i+j}^{n+2} - w_{i+j}^n}{2\Delta t} \quad (\text{C.6})$$

Such that they may be written as:

$$c_{jk} = \begin{bmatrix} -\frac{1}{2} & \frac{3}{2} & -\frac{3}{2} & \frac{1}{2} \\ 1 & -\frac{5}{2} & 2 & -\frac{1}{2} \\ -\frac{1}{2} & 0 & \frac{1}{2} & 0 \\ 0 & 1 & 0 & 0 \end{bmatrix} \left[ w_{i+j}^{n-1}, w_{i+j}^n, w_{i+j}^{n+1}, w_{i+j}^{n+2} \right]^T \quad (\text{C.7})$$

Using the four  $w(z_{i+j}, t)$  that can be computed in this fashion, a final cubic Hermite spline is constructed along the  $z$ -direction to estimate  $w(z, t)$ . It is also designed according to the above methodology, needing to satisfy  $C^0$  continuity and the finite difference approximation for  $C^1$  continuity at  $z_i$  and  $z_{i+1}$ .

The use of central differences to approximate the derivatives at the four boundaries of  $[t^n, t^{n+1}] \times [z_i, z_{i+1}]$  ensures a  $C^1$  continuous representation of  $w$  throughout the domain, with exception of nodes that require interpolations across a boundary. These must be handled with one-sided finite differences to let the spline be drawn. The zero-time boundary is made entirely homogeneous. As no higher order derivatives in  $z$  and  $t$  will be taken of this function, the above approach ensures that also  $f$  is  $C^1$  continuous, such that no unphysical discontinuities are introduced.

## C.2. Finite Difference ANN Jacobian Assembly

In the  $i + 1^{\text{st}}$  element, the approach to assembling the Jacobian from ANN predictions of  $\hat{I}$  aims to add the following element matrix to the global system:

$$\frac{\partial \hat{I}_i}{\partial a_j} = \begin{bmatrix} \frac{\partial}{\partial a_i} (\hat{I}_i) & \frac{\partial}{\partial a_{i+1}} (\hat{I}_i) \\ \frac{\partial}{\partial a_i} (\hat{I}_{i+1}) & 0 \end{bmatrix} \approx \begin{bmatrix} \frac{\hat{I}_i(a_{i-1}, a_i + \delta a, a_{i+1}) - \hat{I}_i(a_{i-1}, a_i, a_{i+1})}{\delta a} & \frac{\hat{I}_i(a_{i-1}, a_i, a_{i+1} + \delta a) - \hat{I}_i(a_{i-1}, a_i, a_{i+1})}{\delta a} \\ \frac{\hat{I}_{i+1}(a_i + \delta a, a_{i+1}, a_{i+2}) - \hat{I}_{i+1}(a_i, a_{i+1}, a_{i+2})}{\delta a} & 0 \end{bmatrix} \quad (\text{C.8})$$

Section 8.3.2 only features three non-zero terms, since terms that overlap elements need not be computed when full interaction terms, rather than their element contributions, are computed. Each of the three derivative terms in Eq. (C.8) are approximated with a simple first order finite difference in which ANN-predicted interaction terms appear with perturbed  $a_j$ -dependent inputs. These perturbed features are summarised in Table C.1.

Function of $a$	$\frac{\partial}{\partial a_i} (\hat{\mathbf{I}}_i)$	$\frac{\partial}{\partial a_{i+1}} (\hat{\mathbf{I}}_i)$	$\frac{\partial}{\partial a_i} (\hat{\mathbf{I}}_{i+1})$
$a_{i-1}$	1	1	0
$a_i$	$1 + \delta a$	1	$1 + \delta a$
$a_{i+1}$	1	$1 + \delta a$	1
$a_{i+2}$	0	0	1
$\frac{\partial a}{\partial t} i-1$	1	1	0
$\frac{\partial a}{\partial t} i$	$1 + c_{t,1} \delta a$	1	$1 + c_{t,1} \delta a$
$\frac{\partial a}{\partial t} i+1$	1	$1 + c_{t,1} \delta a$	1
$\frac{\partial a}{\partial t} i+2$	0	0	1
$\overline{\mathcal{R}}_{s,I,i}(a_{i-1}, a_i, a_{i+1})$	$(1, 1 + \delta a, 0)$	$(1, 1, 0)$	$(0, 1 + \delta a, 1)$
$\overline{\mathcal{R}}_{s,I,i+1}(a_i, a_{i+1}, a_{i+2})$	$(1 + \delta a, 1, 0)$	$(1, 1 + \delta a, 0)$	$(0, 1, 1)$

Table C.1: Perturbations of the amplitudes  $a$  for the unknown input features of the ANN, used to construct finite difference approximations to the Jacobian contributions in the left column.  $c_{t,1}$  is a factor for the time derivative's finite difference approximation (see Section 5.5.5).

The factor  $c_{t,1}$  in this table is the factor that multiplies the terms proportional to  $\overline{w}^{n+1}$  in the finite difference time marches Eq. (5.26) and Eq. (5.29). Hence, it represents the unknowns at  $t^{n+1}$  in the time stepping scheme.

The direct perturbations to  $a$  and  $\frac{\partial a}{\partial t}$  in Table C.1 are straightforward to compute. Strong residual terms, however, must be assembled with the correct perturbations in the loop over Integration Point (IP)s.  $\frac{\partial \hat{I}_i}{\partial a_j}$  is added only after that loop. The base  $\hat{I}$  is updated each time a new weak form is reached, while the perturbed  $\hat{I}$  and the resulting finite differences are computed and added in internal loops over active weak forms (*eqs*) and active weighting functions (*wfs*).

The full implementation of the ANN-Jacobian is summarised by Algorithm 4.

**Algorithm 4** ANN-Jacobian Assembly

---

```

1: for i=0,1,...,nel do ▷ Element loop
2:   if i=0 then
3:     Assemble global strong residual vector  $\mathcal{R}_{s,I,i}$ 
4:   for ip=0,1,...,nIP do ▷ Integration point loop
5:     Load current guess of  $\bar{w}$ ,  $\frac{\partial \bar{w}}{\partial t}$  and known  $f$ 
6:     for eq=0,1 do ▷ Active weak forms in element
7:       for wf=0,1 do ▷ Active amplitudes in element
8:         Add IP contribution to Galerkin terms of  $\frac{\partial \mathcal{R}_{w,eq}}{\partial a_{wf}}$  in element  $i$ 
9:         if sgsType=Algebraic then
10:          Add IP contribution to algebraic unresolved scales terms of  $\frac{\partial \mathcal{R}_{w,eq}}{\partial a_{wf}}$  in element  $i$ 
11:         else if sgsType=ANN then
12:          Compute  $\left[ \bar{\mathcal{R}}_{s,I,i}(a_{i-1}, a_i + \delta a), \bar{\mathcal{R}}_{s,I,i+1}(a_i + \delta a, a_{i+1}), \bar{\mathcal{R}}_{s,i+1}(a_i, a_{i+1} + \delta a) \right]^T$ 
13:         if sgsType=ANN then
14:           for eq=0,1 do ▷ Active weak forms in element
15:             if eq=1 then
16:               Update  $\hat{I}_i$ 
17:             for wf=0,1 do ▷ Active amplitudes in element
18:               Compute  $\hat{I}_{eq,wf}^P$ 
19:               Compute and add  $\frac{\partial \hat{I}_i}{\partial a_j}$ 

```

---

### C.3. Adaptive Relaxation Scheme for Newton's Method

An adaptive relaxation scheme has been implemented to improve convergence behaviour. It is based on rewriting the Taylor expansion Eq. (5.24) that results in the iterative Newton scheme Eq. (5.25) as an explicit Euler discretisation with a step size equal to the relaxation factor  $\lambda_r$  (which is 1 in Eq. (5.25b):

$$\frac{a_i^{p+1} - a_i^p}{\lambda} = - \left( \frac{\partial \mathcal{R}_{w_i}}{\partial a_j} \right)^{-1} \mathcal{R}_{w_i}, \quad a_i^0 = a_i^n \quad (\text{C.9})$$

This can be interpreted as a discretisation of the non-linear system of coupled Ordinary Differential Equation (ODE)s:

$$\frac{\partial a_i}{\partial \lambda_r} = - \left( \frac{\partial \mathcal{R}_{w_i}}{\partial a_j} \right)^{-1} \mathcal{R}_{w_i}, \quad a(\lambda_r = 0) = a_i^0 \quad (\text{C.10})$$

Assuming the parameters in Eq. (C.10) are continuous and exact and the coupled ODEs are diagonalised, each decoupled equation can be solved for  $\mathcal{R}_w$ :

$$\mathcal{R}_w = \mathcal{R}_0 e^{-\lambda_r} \quad (\text{C.11})$$

Which describes convergence to the nearest root of  $\mathcal{R}_w$  as  $\lambda_r \rightarrow \infty$  along a monotonic, exponential path. In reality, however,  $\frac{\partial a_i}{\partial \lambda_r}$  is not continuous,  $\frac{\partial \mathcal{R}_{w_i}}{\partial a_j}$  is not exact and the system of equations is not decoupled. Therefore, deviations from the exponential convergence path will occur. These can manifest themselves as oscillating convergence behaviour [140] or even divergence [219] of the Newton procedure. Therefore, an adaptive procedure is employed here that constrains  $\lambda_r$  with a free parameter that controls the  $L_2$  norm of the leading order error between the exponential convergence path  $a(\lambda_r)$  and a linearised explicit Euler convergence path  $\hat{a}(\lambda_r)$  in every Corrector Pass (CP) (see [11] for a derivation):

$$\tau_r^p = \|a(\lambda_r^p) - \hat{a}(\lambda_r^p)\|_2 \approx \frac{\lambda_r^p}{2} \left\| \left( \frac{\partial \mathcal{R}_{w_i}}{\partial a_j} \right) \right\|_2 \quad (\text{C.12})$$

Setting  $\tau_r^p = 0$  renders an infinitely long convergence path in line with Eq. (C.11). Large values of  $\tau$  allow large excursions from the exponential path, yielding faster convergence but higher risk of oscillations or

divergence. However, Eq. (C.12) indicates that the error becomes increasingly small close to roots of  $\mathcal{R}_{w_i}$ , where  $\left\| \left( \frac{\partial \mathcal{R}_{w_i}}{\partial a_j} \right) \right\|_2, \|\Delta a_i\|_2 \rightarrow 0$ . Hence, with a fixed, preset  $\tau_r^p$ , Eq. (C.12) can be leveraged to construct an adaptive scheme for  $\lambda_r^p$  that minimises oscillations and other deviations induced by taking large steps from bad initial guesses in a space with large gradients of  $a_i$ , while reducing to an unrelaxed scheme ( $\lambda_r = 1$ ) when it approaches a root:

$$\lambda_r^p = \min \left( \sqrt{\frac{2\tau_r}{\|\Delta a_i^p\|}}, 1 \right) \quad (\text{C.13})$$

A second order scheme for  $\lambda$  that extends Eq. (C.12) to a second order approximation of the error [11] is also implemented and tested. However, this is not found to have significant improvement over Eq. (C.13) on oscillating convergence cases, even though it requires an additional linear system solve per CP. It is therefore not considered further here.

# Bibliography

- [1] HYPRE: Scalable linear solvers and multigrid methods. <https://computation.llnl.gov/projects/hypre-scalable-linear-solvers-multigrid-methods>, 2008.
- [2] MFEM: Modular finite element methods library. [mfem.org](http://mfem.org), 2010.
- [3] Frugally deep. <https://github.com/Dobiasd/frugally-deep>, 2019.
- [4] Opennn: Neural networks. <http://www.opennn.net/>, 2019.
- [5] Autonomio talos. <https://github.com/autonomio/talos>, 2019.
- [6] Martín Abadi, Paul Barham, Jianmin Chen, Zhifeng Chen, Andy Davis, Jeffrey Dean, Matthieu Devin, Sanjay Ghemawat, Geoffrey Irving, Michael Isard, et al. Tensorflow: a system for large-scale machine learning. In *OSDI*, volume 16, pages 265–283, 2016.
- [7] Daniel S Abdi, Lucas C Wilcox, Timothy C Warburton, and Francis X Giraldo. A gpu-accelerated continuous and discontinuous galerkin non-hydrostatic atmospheric model. *The International Journal of High Performance Computing Applications*, page 1094342017694427, 2017.
- [8] Assyr Abdulle, E Weinan, Björn Engquist, and Eric Vanden-Eijnden. The heterogeneous multiscale method. *Acta Numerica*, 21:1–87, 2012.
- [9] Nash’at Ahmad and John Lindeman. Euler solutions using flux-based wave decomposition. *International Journal for Numerical Methods in Fluids*, 54(1):47–72, 2007.
- [10] Ido Akkerman, Jurijs Bazilevs, VM Calo, Thomas Hughes, and Steven Hulshoff. The role of continuity in residual-based variational multiscale modeling of turbulence. *Computational Mechanics*, 41(3):371–378, 2008.
- [11] Mario Amrein and Thomas P Wihler. Fully adaptive newton–galerkin methods for semilinear elliptic partial differential equations. *SIAM Journal on Scientific Computing*, 37(4):A1637–A1657, 2015.
- [12] Akio Arakawa. The cumulus parameterization problem: Past, present, and future. *Journal of Climate*, 17(13):2493–2525, 2004.
- [13] Akio Arakawa and Celal S Konor. Unification of the anelastic and quasi-hydrostatic systems of equations. *Monthly Weather Review*, 137(2):710–726, 2009.
- [14] Akio Arakawa and Wayne Howard Schubert. Interaction of a cumulus cloud ensemble with the large-scale environment, part i. *Journal of the Atmospheric Sciences*, 31(3):674–701, 1974.
- [15] Nathan P Arnold, Mark Branson, Zhiming Kuang, David A Randall, and Eli Tziperman. Mjo intensification with warming in the superparameterized cesm. *Journal of Climate*, 28(7):2706–2724, 2015.
- [16] Claudio Baiocchi, Franco Brezzi, and Leopoldo Franca. Virtual bubbles and the galerkin-least-squares method. *Comput. Methods Appl. Mech. Engrg*, 10(5), 1993.
- [17] Pierre Baldi and Kurt Hornik. Neural networks and principal component analysis: Learning from examples without local minima. *Neural networks*, 2(1):53–58, 1989.
- [18] F Keith Ball. Control of inversion height by surface heating. *Quarterly Journal of the Royal Meteorological Society*, 86(370):483–494, 1960.
- [19] Saulo R. M. Barros, David Dent, Lars Isaksen, G Robinson, G Mozdzyński, and F Wollenweber. The ifs model: A parallel production weather code. *Parallel Computing*, 21(10):1621–1638, 1995.

- [20] Atilim Gunes Baydin, Barak A Pearlmutter, Alexey Andreyevich Radul, and Jeffrey Mark Siskind. Automatic differentiation in machine learning: a survey. *Journal of Machine Learning Research*, 18(153):1–153, 2017.
- [21] Andrea D Beck, David G Flad, and Claus-Dieter Munz. Deep neural networks for data-driven turbulence models. *arXiv*, 2018.
- [22] Marijn Beekman. Using artificial neural networks as unresolved-scale models for the burgers equation, 2016.
- [23] Gal Berkooz, Philip Holmes, and John L Lumley. The proper orthogonal decomposition in the analysis of turbulent flows. *Annual review of fluid mechanics*, 25(1):539–575, 1993.
- [24] Tyrus Berry, Dimitrios Giannakis, and John Harlim. Nonparametric forecasting of low-dimensional dynamical systems. *Physical Review E*, 91(3):032915, 2015.
- [25] Tom Beucler, Stephan Rasp, Michael Pritchard, and Pierre Gentine. Achieving conservation of energy in neural network emulators for climate modeling. *arXiv preprint arXiv:1906.06622*, 2019.
- [26] Christopher M Bishop et al. *Neural networks for pattern recognition*. Oxford university press, 1995.
- [27] Olivier Boucher, David Randall, Paulo Artaxo, Christopher Bretherton, Graham Feingold, Piers Forster, V-M Kerminen, Yutaka Kondo, Hong Liao, Ulrike Lohmann, et al. Clouds and aerosols. In *Climate change 2013: the physical science basis. Contribution of Working Group I to the Fifth Assessment Report of the Intergovernmental Panel on Climate Change*, pages 571–657. Cambridge University Press, 2013.
- [28] Leo Breiman. Random forests. *Machine learning*, 45(1):5–32, 2001.
- [29] Noah D Brenowitz and Christopher S Bretherton. Prognostic validation of a neural network unified physics parameterization. *Geophysical Research Letters*, 2015.
- [30] Christopher S Bretherton. Insights into low-latitude cloud feedbacks from high-resolution models. *Phil. Trans. R. Soc. A*, 373(2054):20140415, 2015.
- [31] Christopher S Bretherton, Malcolm K MacVean, Peter Bechtold, Andreas Chlond, William R Cotton, Joan Cuxart, Hans Cuijpers, Marat Khairoutdinov, Bronko Kosovic, Dave Lewellen, et al. An intercomparison of radiatively driven entrainment and turbulence in a smoke cloud, as simulated by different numerical models. *Quarterly Journal of the Royal Meteorological Society*, 125(554):391–423, 1999.
- [32] Christopher S Bretherton, Peter N Blossey, and Cristiana Stan. Cloud feedbacks on greenhouse warming in the superparameterized climate model sp-ccsm4. *Journal of Advances in Modeling Earth Systems*, 6(4):1185–1204, 2014.
- [33] Florent Briant and Tapio Schneider. Constraints on climate sensitivity from space-based measurements of low-cloud reflection. *Journal of Climate*, 29(16):5821–5835, 2016.
- [34] Alexander N Brooks and Thomas JR Hughes. Streamline upwind/petrov-galerkin formulations for convection dominated flows with particular emphasis on the incompressible navier-stokes equations. *Computer methods in applied mechanics and engineering*, 32(1-3):199–259, 1982.
- [35] Tan Bui-Thanh, Karen Willcox, Omar Ghattas, and Bart van Bloemen Waanders. Goal-oriented, model-constrained optimization for reduction of large-scale systems. *Journal of Computational Physics*, 224(2):880–896, 2007.
- [36] Horace Robert Byers and Roscoe R Braham. *The thunderstorm: report of the Thunderstorm Project*. US Government Printing Office, 1949.
- [37] RIKEN Next-Generation Supercomputer R&D Center. K-computer took first place in the world. Retrieved from: [http://www.nsc.riken.jp/K/diary\\_eng.html](http://www.nsc.riken.jp/K/diary_eng.html). Accessed: 14/11/2018, 2011.
- [38] Jule G Charney. Geostrophic turbulence. *Journal of the Atmospheric Sciences*, 28(6):1087–1095, 1971.

- [39] Lingfen Chen. *Aspects of POD-based wall-layer modeling for the variational multiscale method*. PhD thesis, TU Delft, 2015.
- [40] Lingfen Chen, Wouter Edeling, and Steven Hulshoff. Pod enriched boundary models and their optimal stabilisation. *International Journal for Numerical Methods in Fluids*, 77(2):92–107, 2015.
- [41] Anning Cheng and Kuan-Man Xu. Improved low-cloud simulation from a multiscale modeling framework with a third-order turbulence closure in its cloud-resolving model component. *Journal of Geophysical Research: Atmospheres*, 116(D14), 2011.
- [42] Lei Cheng, Stefano Mattei, Peter W Fick, and Steven J Hulshoff. A semi-continuous formulation for goal-oriented reduced-order models. In *Proceedings-WCCM XI: 11th World Congress on Computational Mechanics; ECCM V: 5th European Conference on Computational Mechanics; ECFD VI: 6th European Conference on Computational Fluid Dynamics, Barcelona, Spain, 20-25 July 2014*. CIMNE, 2014.
- [43] Yu Cheng, Qi Li, Stefania Argentini, Chadi Sayde, and Pierre Gentine. Turbulence spectra in the stable atmospheric boundary layer. *arXiv preprint arXiv:1801.05847*, 2018.
- [44] François Chollet et al. Keras. <https://keras.io>, 2015.
- [45] Jintai Chung and GM Hulbert. A time integration algorithm for structural dynamics with improved numerical dissipation: the generalized- $\alpha$  method. *Journal of applied mechanics*, 60(2):371–375, 1993.
- [46] Djork-Arné Clevert, Thomas Unterthiner, and Sepp Hochreiter. Fast and accurate deep network learning by exponential linear units (elus). *arXiv preprint arXiv:1511.07289*, 2015.
- [47] Ramon Codina. Comparison of some finite element methods for solving the diffusion-convection-reaction equation. *Computer Methods in Applied Mechanics and Engineering*, 156(1-4):185–210, 1998.
- [48] Ramon Codina. Stabilization of incompressibility and convection through orthogonal sub-scales in finite element methods. *Computer methods in applied mechanics and engineering*, 190(13-14):1579–1599, 2000.
- [49] Ramon Codina. Stabilized finite element approximation of transient incompressible flows using orthogonal subscales. *Computer Methods in Applied Mechanics and Engineering*, 191(39-40):4295–4321, 2002.
- [50] Ramon Codina and Jordi Blasco. A finite element formulation for the stokes problem allowing equal velocity-pressure interpolation. *Computer Methods in Applied Mechanics and Engineering*, 143(3-4):373–391, 1997.
- [51] Ramon Codina and Javier Principe. Dynamic subscales in the finite element approximation of thermally coupled incompressible flows. *International journal for numerical methods in fluids*, 54(6-8):707–730, 2007.
- [52] Ramon Codina, Javier Principe, Oriol Guasch, and Santiago Badia. Time dependent subscales in the stabilized finite element approximation of incompressible flow problems. *Computer Methods in Applied Mechanics and Engineering*, 196(21-24):2413–2430, 2007.
- [53] Ramon Codina, Santiago Badia, Joan Baiges, and Javier Principe. Variational multiscale methods in computational fluid dynamics. *Encyclopedia of Computational Mechanics Second Edition*, pages 1–28, 2018.
- [54] Ronald R Coifman and Stéphane Lafon. Diffusion maps. *Applied and computational harmonic analysis*, 21(1):5–30, 2006.
- [55] Daan Crommelin and Eric Vanden-Eijnden. Subgrid-scale parameterization with conditional markov chains. *Journal of the Atmospheric Sciences*, 65(8):2661–2675, 2008.
- [56] Dacian Daescu and Michael Navon. A dual-weighted approach to order reduction in 4dvar data assimilation. *Monthly Weather Review*, 136(3):1026–1041, 2008.

- [57] Stephan R de Roode and Peter G Duynkerke. Observed lagrangian transition of stratocumulus into cumulus during astex: Mean state and turbulence structure. *Journal of the atmospheric sciences*, 54(17):2157–2173, 1997.
- [58] James W Deardorff. Numerical study of heat transport by internal gravity waves above a growing unstable layer. *The Physics of Fluids*, 12(12):II–184, 1969.
- [59] James W Deardorff. Stratocumulus-capped mixed layers derived from a three-dimensional model. *Boundary-Layer Meteorology*, 18(4):495–527, 1980.
- [60] Willem Deconinck, Peter Bauer, Michail Diamantakis, Mats Hamrud, Christian Kühnlein, Pedro Maciel, Gianmarco Mengaldo, Tiago Quintino, Baudouin Raoult, Piotr K Smolarkiewicz, et al. Atlas: A library for numerical weather prediction and climate modelling. *Computer Physics Communications*, 220:188–204, 2017.
- [61] Jesse Dorrestijn. *Stochastic convection parameterization*. PhD thesis, TU Delft, 2016.
- [62] Jesse Dorrestijn, Daan Crommelin, JA Biello, and SJ Böing. A data-driven multi-cloud model for stochastic parametrization of deep convection. *Phil. Trans. R. Soc. A*, 371(1991):20120374, 2013.
- [63] Jesse Dorrestijn, Daan T Crommelin, A Pier Siebesma, and Harm JJ Jonker. Stochastic parameterization of shallow cumulus convection estimated from high-resolution model data. *Theoretical and Computational Fluid Dynamics*, 27(1-2):133–148, 2013.
- [64] Jesse Dorrestijn, Daan T Crommelin, A Pier Siebesma, Harmen JJ Jonker, and Frank Selten. Stochastic convection parameterization with markov chains in an intermediate-complexity gcm. *Journal of the Atmospheric Sciences*, 73(3):1367–1382, 2016.
- [65] Timothy Dozat. Incorporating nesterov momentum into adam, 2016.
- [66] Peter D Dueben and Peter Bauer. Challenges and design choices for global weather and climate models based on machine learning. *Geoscientific Model Development*, 11(10):3999–4009, 2018.
- [67] Jean-Louis Dufresne and Sandrine Bony. An assessment of the primary sources of spread of global warming estimates from coupled atmosphere–ocean models. *Journal of Climate*, 21(19):5135–5144, 2008.
- [68] Thomas Durieux. Exploring the use of artificial neural network based subgrid scale models in a variational multiscale formulation, 2015.
- [69] Dale R Durran. Improving the anelastic approximation. *Journal of the atmospheric sciences*, 46(11):1453–1461, 1989.
- [70] JJ Dussen, Stephan R Roode, Andrew S Ackerman, Peter N Blossey, Christopher S Bretherton, Marcin J Kurowski, Adrian P Lock, Roel AJ Neggers, Irina Sandu, and Pier A Siebesma. The gass/euclipse model intercomparison of the stratocumulus transition as observed during astex: Les results. *Journal of Advances in Modeling Earth Systems*, 5(3):483–499, 2013.
- [71] Kerry Emanuel. Quasi-equilibrium thinking. *INTERNATIONAL GEOPHYSICS SERIES*, 70:225–256, 2000.
- [72] F Fang, CC Pain, IM Navon, MD Piggott, GJ Gorman, PE Farrell, PA Allison, and AJH Goddard. A pod reduced-order 4d-var adaptive mesh ocean modelling approach. *International Journal for Numerical Methods in Fluids*, 60(7):709–732, 2009.
- [73] Ibrahim Fatkullin and Eric Vanden-Eijnden. A computational strategy for multiscale systems with applications to lorenz 96 model. *Journal of Computational Physics*, 200(2):605–638, 2004.
- [74] European Centre for Medium-Range Weather Forecasts (ECWMF). *IFS Documentation: Part III: Dynamics and Numerical Procedures (CY43R3)*. ECWMF, 2017.
- [75] Leopoldo P Franca and F Valentin. On an improved unusual stabilized finite element method for the advective–reactive–diffusive equation. *Computer Methods in Applied Mechanics and Engineering*, 190(13-14):1785–1800, 2000.

- [76] Kai Fukami, Koji Fukagata, and Kunihiko Taira. Super-resolution reconstruction of turbulent flows with machine learning. *Journal of Fluid Mechanics*, 870:106–120, 2019.
- [77] Kunihiko Fukushima and Sei Miyake. Neocognitron: A self-organizing neural network model for a mechanism of visual pattern recognition. In *Competition and cooperation in neural nets*, pages 267–285. Springer, 1982.
- [78] Yarin Gal and Zoubin Ghahramani. Dropout as a bayesian approximation: Representing model uncertainty in deep learning. In *international conference on machine learning*, pages 1050–1059, 2016.
- [79] Pierre Gentine, Mike Pritchard, Stephan Rasp, Gael Reinaudi, and Galen Yacalis. Could machine learning break the convection parameterization deadlock? *Geophysical Research Letters*, 45(11):5742–5751, 2018.
- [80] Luis Gimeno. Grand challenges in atmospheric science. *Frontiers in Earth Science*, 1:1, 2013.
- [81] Ian Goodfellow, Yoshua Bengio, and Aaron Courville. *Deep learning*. MIT press, 2016.
- [82] Wojciech W Grabowski. Toward cloud resolving modeling of large-scale tropical circulations: A simple cloud microphysics parameterization. *Journal of the atmospheric sciences*, 55(21):3283–3298, 1998.
- [83] Wojciech W Grabowski. Coupling cloud processes with the large-scale dynamics using the cloud-resolving convection parameterization (crp). *Journal of the Atmospheric Sciences*, 58(9):978–997, 2001.
- [84] Wojciech W Grabowski. Comments on “preliminary tests of multiscale modeling with a two-dimensional framework: sensitivity to coupling methods”. *Monthly Weather Review*, 134(7):2021–2026, 2006.
- [85] Wojciech W Grabowski. Towards global large eddy simulation: super-parameterization revisited. *Journal of the Meteorological Society of Japan. Ser. II*, 94(4):327–344, 2016.
- [86] Wojciech W Grabowski and Piotr K Smolarkiewicz. Crp: A cloud resolving convection parameterization for modeling the tropical convecting atmosphere. *Physica D: Nonlinear Phenomena*, 133(1-4):171–178, 1999.
- [87] Wojciech W Grabowski, Xiaoqing Wu, and Mitchell W Moncrieff. Cloud-resolving modeling of tropical cloud systems during phase iii of gate. part i: Two-dimensional experiments. *Journal of the atmospheric sciences*, 53(24):3684–3709, 1996.
- [88] Ian Grooms and Andrew J Majda. Efficient stochastic superparameterization for geophysical turbulence. *Proceedings of the National Academy of Sciences*, 2013.
- [89] Ian Grooms and Andrew J Majda. Stochastic superparameterization in a one-dimensional model for wave turbulence. *Commun. Math. Sci*, 12(3):509–525, 2014.
- [90] Ian Grooms, K Shafer Smith, and Andrew J Majda. Multiscale models for synoptic–mesoscale interactions in the ocean. *Dynamics of Atmospheres and Oceans*, 58:95–107, 2012.
- [91] Ian Grooms, Yoonsang Lee, and Andrew J Majda. Ensemble kalman filters for dynamical systems with unresolved turbulence. *Journal of Computational Physics*, 273:435–452, 2014.
- [92] Françoise Guichard and Fleur Couvreur. A short review of numerical cloud-resolving models. *Tellus A: Dynamic Meteorology and Oceanography*, 69(1):1373578, 2017.
- [93] Richard Haberman. *Applied Partial Differential Equations with Fourier Series and Boundary Value Problems: Pearson New International Edition*. Pearson Education Limited, 2013.
- [94] John Harlim. Data-driven computational methods: Parameter and operator estimations (chapter 1). *arXiv preprint arXiv:1803.07711*, 2018.
- [95] Dennis L Hartmann. *Global physical climatology*, volume 103. Newnes, 2015.
- [96] Trevor Hastie, Jerome Friedman, and Robert Tibshirani. *The elements of statistical learning*. Springer series in statistics New York, NY, USA:, 2001.

- [97] Thijs Heus, Chiel C van Heerwaarden, Harm JJ Jonker, A Pier Siebesma, Steffen Axelsen, Karel van den Dries, Olivier Geoffroy, Alfred F Moene, David Pino, Stephan S de Roode, et al. Formulation of and numerical studies with the dutch atmospheric large-eddy simulation (dales). *Geosci. Model Dev*, 3: 415–444, 2010.
- [98] Matthew D Hoffman, David M Blei, Chong Wang, and John Paisley. Stochastic variational inference. *The Journal of Machine Learning Research*, 14(1):1303–1347, 2013.
- [99] Chris Hope. The \$10 trillion value of better information about the transient climate response. *Phil. Trans. R. Soc. A*, 373(2054), 2015.
- [100] Kurt Hornik, Maxwell Stinchcombe, and Halbert White. Multilayer feedforward networks are universal approximators. *Neural networks*, 2(5):359–366, 1989.
- [101] Frédéric Hourdin, Thorsten Mauritsen, Andrew Gettelman, Jean-Christophe Golaz, Venkatramani Balaji, Qingyun Duan, Doris Folini, Duoying Ji, Daniel Klocke, Yun Qian, et al. The art and science of climate model tuning. *Bulletin of the American Meteorological Society*, 98(3):589–602, 2017.
- [102] Robert A Houze. Observed structure of mesoscale convective systems and implications for large-scale heating. *Quarterly Journal of the Royal Meteorological Society*, 115(487):425–461, 1989.
- [103] Guillaume Houzeaux, Beatriz Eguzkitza, and Mariano Vázquez. A variational multiscale model for the advection–diffusion–reaction equation. *Communications in Numerical Methods in Engineering*, 25(7): 787–809, 2009.
- [104] Thomas JR Hughes. A multidimensional upwind scheme with no crosswind diffusion. *Finite Element Methods for Convection Dominated Flows*, AMD 34, 1979.
- [105] Thomas JR Hughes. Multiscale phenomena: Green’s functions, the dirichlet-to-neumann formulation, subgrid scale models, bubbles and the origins of stabilized methods. *Computer methods in applied mechanics and engineering*, 127(1-4):387–401, 1995.
- [106] Thomas JR Hughes, Leopoldo P Franca, and Gregory M Hulbert. A new finite element formulation for computational fluid dynamics: Viii. the galerkin/least-squares method for advective-diffusive equations. *Computer methods in applied mechanics and engineering*, 73(2):173–189, 1989.
- [107] Thomas JR Hughes, Luca Mazzei, and Kenneth E Jansen. Large eddy simulation and the variational multiscale method. *Computing and visualization in science*, 3(1-2):47–59, 2000.
- [108] Thomas JR Hughes, Luca Mazzei, Assad A Oberai, and Alan A Wray. The multiscale formulation of large eddy simulation: Decay of homogeneous isotropic turbulence. *Physics of fluids*, 13(2):505–512, 2001.
- [109] Thomas JR Hughes, Guglielmo Scovazzi, and Leopoldo P Franca. Multiscale and stabilized methods. *Encyclopedia of Computational Mechanics Second Edition*, pages 1–64, 2018.
- [110] Steven Hulshoff. Variational multiscale methods. Unpublished lecture notes of AE4137 CFD 3: Large Eddy Simulation, 2017.
- [111] Steven Hulshoff. Lecture notes: Computational modelling ae2220 ii. Unpublished lecture notes, 2019.
- [112] Steven Hulshoff, EA Muntz, and J Labrujere. Wall-stress boundary conditions for variational-multiscale les. *International Journal for Numerical Methods in Fluids*, 66(11):1341–1353, 2011.
- [113] Christiane Jablonowski and David L Williamson. The pros and cons of diffusion, filters and fixers in atmospheric general circulation models. In *Numerical Techniques for Global Atmospheric Models*, pages 381–493. Springer, 2011.
- [114] Kenneth E Jansen, Christian H Whiting, and Gregory M Hulbert. A generalized- $\alpha$  method for integrating the filtered navier–stokes equations with a stabilized finite element method. *Computer methods in applied mechanics and engineering*, 190(3-4):305–319, 2000.

- [115] Fredrik Janson, Gijs van den Oord, Johanna Grönqvist, Inti Pelupessy, Maria Chertova, Pier Siebesma, and Daan Crommelin. Regional superparameterization of clouds and convection with 3d les models in openifs. Personal communication, 2019.
- [116] Claes Johnson. *Numerical Solution of Partial Differential Equations by the Finite Element Method*. Cambridge University Press, 1897.
- [117] CR Jones, Christopher Bretherton, and Michael Pritchard. Mean-state acceleration of cloud-resolving models and large eddy simulations. *Journal of Advances in Modeling Earth Systems*, 7(4):1643–1660, 2015.
- [118] Joon-Hee Jung and Akio Arakawa. The resolution dependence of model physics: Illustrations from nonhydrostatic model experiments. *Journal of the atmospheric sciences*, 61(1):88–102, 2004.
- [119] Joon-Hee Jung and Akio Arakawa. Preliminary tests of multiscale modeling with a two-dimensional framework: Sensitivity to coupling methods. *Monthly weather review*, 133(3):649–662, 2005.
- [120] Markos A Katsoulakis, Andrew J Majda, and Dionisios G Vlachos. Coarse-grained stochastic processes and monte carlo simulations in lattice systems. *Journal of Computational Physics*, 186(1):250–278, 2003.
- [121] James F Kelly and Francis X Giraldo. Continuous and discontinuous galerkin methods for a scalable three-dimensional nonhydrostatic atmospheric model: Limited-area mode. *Journal of Computational Physics*, 231(24):7988–8008, 2012.
- [122] Marat Khairoutdinov, David Randall, and Charlotte DeMott. Simulations of the atmospheric general circulation using a cloud-resolving model as a superparameterization of physical processes. *Journal of the Atmospheric Sciences*, 62(7):2136–2154, 2005.
- [123] Marat F Khairoutdinov and David A Randall. A cloud resolving model as a cloud parameterization in the ncar community climate system model: Preliminary results. *Geophysical Research Letters*, 28(18):3617–3620, 2001.
- [124] Marat F Khairoutdinov, Steve K Krueger, Chin-Hoh Moeng, Peter A Bogenschutz, and David A Randall. Large-eddy simulation of maritime deep tropical convection. *Journal of Advances in Modeling Earth Systems*, 1(4), 2009.
- [125] Boualem Khouider and Andrew J Majda. A simple multicloud parameterization for convectively coupled tropical waves. part i: Linear analysis. *Journal of the atmospheric sciences*, 63(4):1308–1323, 2006.
- [126] Boualem Khouider, Amik St-Cyr, Andrew J Majda, and Joseph Tribbia. The mjo and convectively coupled waves in a coarse-resolution gcm with a simple multicloud parameterization. *Journal of the Atmospheric Sciences*, 68(2):240–264, 2011.
- [127] Byungsoo Kim, Vinicius C Azevedo, Nils Thuerey, Theodore Kim, Markus Gross, and Barbara Söhlenthaler. Deep fluids: A generative network for parameterized fluid simulations. *arXiv preprint arXiv:1806.02071*, 2018.
- [128] Diederik P Kingma and Jimmy Ba. Adam: A method for stochastic optimization. *arXiv preprint arXiv:1412.6980*, 2014.
- [129] Diederik P Kingma and Max Welling. Auto-encoding variational bayes. *arXiv preprint arXiv:1312.6114*, 2013.
- [130] Rupert Klein. Asymptotic analyses for atmospheric flows and the construction of asymptotically adaptive numerical methods. *ZAMM-Journal of Applied Mathematics and Mechanics/Zeitschrift für Angewandte Mathematik und Mechanik: Applied Mathematics and Mechanics*, 80(11-12):765–777, 2000.
- [131] Rupert Klein. Scale-dependent models for atmospheric flows. *Annual review of fluid mechanics*, 42:249–274, 2010.

- [132] Wolfgang Knorr and Martin Heimann. Uncertainties in global terrestrial biosphere modeling: 1. a comprehensive sensitivity analysis with a new photosynthesis and energy balance scheme. *Global Biogeochemical Cycles*, 15(1):207–225, 2001.
- [133] Bruno Koobus and Charbel Farhat. A variational multiscale method for the large eddy simulation of compressible turbulent flows on unstructured meshes—application to vortex shedding. *Computer Methods in Applied Mechanics and Engineering*, 193(15–16):1367–1383, 2004.
- [134] Robert H Kraichnan. Inertial ranges in two-dimensional turbulence. *The Physics of Fluids*, 10(7):1417–1423, 1967.
- [135] Vladimir M Krasnopolsky, Michael S Fox-Rabinovitz, and Alexei A Belochitski. Using ensemble of neural networks to learn stochastic convection parameterizations for climate and numerical weather prediction models from data simulated by a cloud resolving model. *Advances in Artificial Neural Systems*, 2013:5, 2013.
- [136] Naina Kurian. Subgrid-scale model using artificial neural networks for wall-bounded turbulent flows, 2018.
- [137] Marcin J Kurowski, Wojciech W Grabowski, and Piotr K Smolarkiewicz. Anelastic and compressible simulation of moist deep convection. *Journal of the Atmospheric Sciences*, 71(10):3767–3787, 2014.
- [138] Marcin J Kurowski, Wojciech W Grabowski, and Piotr K Smolarkiewicz. Anelastic and compressible simulation of moist dynamics at planetary scales. *Journal of the Atmospheric Sciences*, 72(10):3975–3995, 2015.
- [139] J Nathan Kutz. Deep learning in fluid dynamics. *Journal of Fluid Mechanics*, 814:1–4, 2017.
- [140] Gangaram Ladde and BG Zhang. Oscillation and nonoscillation for systems of two first-order linear differential equations with delay. *Journal of mathematical analysis and applications*, 115(1):57–75, 1986.
- [141] Domenico Lahaye and Cees Vuik. Scientific computing. Unpublished lecture notes of WI4201: Scientific Computing, 2015.
- [142] Corentin J Lapeyre, Antony Misdariis, Nicolas Cazard, Denis Veynante, and Thierry Poinso. Training convolutional neural networks to estimate turbulent sub-grid scale reaction rates. *Combustion and Flame*, 203:255–264, 2019.
- [143] Yann LeCun, Yoshua Bengio, and Geoffrey Hinton. Deep learning. *nature*, 521(7553):436, 2015.
- [144] Tristan S LÉcuyer, Hiroko K Beaudoin, Matthew Rodell, et al. The observed state of the energy budget in the early twenty-first century. *Journal of Climate*, 28(21):8319–8346, 2015.
- [145] Douglas K Lilly. On the numerical simulation of buoyant convection. *Tellus*, 14(2):148–172, 1962.
- [146] Douglas K Lilly. Models of cloud-topped mixed layers under a strong inversion. *Quarterly Journal of the Royal Meteorological Society*, 94(401):292–309, 1968.
- [147] Erik Lindborg. The energy cascade in a strongly stratified fluid. *Journal of Fluid Mechanics*, 550:207–242, 2006.
- [148] Julia Ling, Andrew Kurzawski, and Jeremy Templeton. Reynolds averaged turbulence modelling using deep neural networks with embedded invariance. *Journal of Fluid Mechanics*, 807:155–166, 2016.
- [149] Franik B Lipps and Richard S Hemler. A scale analysis of deep moist convection and some related numerical calculations. *Journal of the Atmospheric Sciences*, 39(10):2192–2210, 1982.
- [150] Edward N Lorenz. Deterministic nonperiodic flow. *Journal of the atmospheric sciences*, 20(2):130–141, 1963.
- [151] Edward N Lorenz. The predictability of a flow which possesses many scales of motion. *Tellus*, 21(3):289–307, 1969.

- [152] Edward N Lorenz. Predictability: A problem partly solved. In *Proc. Seminar on predictability*, volume 1, 1996.
- [153] Sean Lovejoy, Adrian Tuck, Susan J Hovde, and Daniel Schertzer. Do stable atmospheric layers exist? *Geophysical Research Letters*, 35(1), 2008.
- [154] David J Lucia, Philip S Beran, and Walter A Silva. Reduced-order modeling: new approaches for computational physics. *Progress in Aerospace Sciences*, 40(1-2):51–117, 2004.
- [155] John Leask Lumley. The structure of inhomogeneous turbulent flows. *Atmospheric turbulence and radio wave propagation*, 1967.
- [156] Zhendong Luo, Jiang Zhu, Ruiwen Wang, and I Michael Navon. Proper orthogonal decomposition approach and error estimation of mixed finite element methods for the tropical pacific ocean reduced gravity model. *Computer Methods in Applied Mechanics and Engineering*, 196(41-44):4184–4195, 2007.
- [157] David JC MacKay. A practical bayesian framework for backpropagation networks. *Neural computation*, 4(3):448–472, 1992.
- [158] Andrew J Majda. Multiscale models with moisture and systematic strategies for superparameterization. *Journal of the Atmospheric Sciences*, 64(7):2726–2734, 2007.
- [159] Andrew J Majda. Challenges in climate science and contemporary applied mathematics. *Communications on Pure and Applied Mathematics*, 65(7):920–948, 2012.
- [160] Andrew J Majda and Ian Grooms. New perspectives on superparameterization for geophysical turbulence. *Journal of Computational Physics*, 271:60–77, 2014.
- [161] Andrew J Majda and Marcus J Grote. Mathematical test models for superparametrization in anisotropic turbulence. *Proceedings of the National Academy of Sciences*, 106(14):5470–5474, 2009.
- [162] Andrew J Majda and Rupert Klein. Systematic multiscale models for the tropics. *Journal of the Atmospheric Sciences*, 60(2):393–408, 2003.
- [163] Syukuro Manabe, Joseph Smagorinsky, and Robert F Strickler. Simulated climatology of a general circulation model with a hydrologic cycle. *Mon. Wea. Rev.*, 93(12):769–798, 1965.
- [164] Brian E Mapes. Equilibrium vs. activation control of large-scale variations of tropical deep convection. In *The physics and parameterization of moist atmospheric convection*, pages 321–358. Springer, 1997.
- [165] Simone Marras, James F Kelly, Frank X Giraldo, and Mariano Vázquez. Variational multiscale stabilization of high-order spectral elements for the advection–diffusion equation. *Journal of Computational Physics*, 231(21):7187–7213, 2012.
- [166] Simone Marras, Margarida Moragues, Mariano Vázquez, Oriol Jorba, and Guillaume Houzeaux. Simulations of moist convection by a variational multiscale stabilized finite element method. *Journal of Computational Physics*, 252:195–218, 2013.
- [167] Simone Marras, Margarida Moragues, Mariano Vázquez, Oriol Jorba, and Guillaume Houzeaux. A variational multiscale stabilized finite element method for the solution of the euler equations of nonhydrostatic stratified flows. *Journal of Computational Physics*, 236:380–407, 2013.
- [168] Simone Marras, Francis X Giraldo, and Andreas Müller. An les-like stabilization of the spectral element solution of the euler equations for atmospheric flows. *Dudley Knox Library*, 2014.
- [169] John Marshall and R Alan Plumb. *Atmosphere, ocean and climate dynamics: an introductory text*, volume 21. Academic Press, 2016.
- [170] Romit Maulik and Omer San. A neural network approach for the blind deconvolution of turbulent flows. *Journal of Fluid Mechanics*, 831:151–181, 2017.
- [171] Carlos R Mechoso and Akio Arakawa. Numerical models | general circulation models. *Encyclopedia of Atmospheric Sciences*, 2015.

- [172] Gerald A Meehl, Thomas Stocker, Pierre Friedlingstein, Jonathan M Gregory, Reto Knutti, et al. Global climate projections. in 'climate change 2007: the physical science basis. contribution of working group i to the fourth assessment report of the intergovernmental panel on climate change', 2007.
- [173] Fernando Menzaque, Rodolfo R Rosales, Esteban G Tabak, and Cristina V Turner. The forced inviscid burgers equation as a model for nonlinear interactions among dispersive waves. *work*, 465:99, 2001.
- [174] Michele Milano and Petros Koumoutsakos. Neural network modeling for near wall turbulent flow. *Journal of Computational Physics*, 182(1):1–26, 2002.
- [175] Michael J Mills, Anja Schmidt, Richard Easter, Susan Solomon, Douglas E Kinnison, Steven J Ghan, Ryan R Neely, Daniel R Marsh, Andrew Conley, Charles G Bardeen, et al. Global volcanic aerosol properties derived from emissions, 1990–2014, using cesm1 (waccm). *Journal of Geophysical Research: Atmospheres*, 121(5):2332–2348, 2016.
- [176] Yoshiaki Miyamoto, Yoshiyuki Kajikawa, Ryuji Yoshida, Tsuyoshi Yamaura, Hisashi Yashiro, and Hirofumi Tomita. Deep moist atmospheric convection in a subkilometer global simulation. *Geophysical Research Letters*, 40(18):4922–4926, 2013.
- [177] Siddhartha Mukherjee, Jérôme Schalkwijk, and Harmen JJ Jonker. Predictability of dry convective boundary layers: An les study. *Journal of the Atmospheric Sciences*, 73(7):2715–2727, 2016.
- [178] Johannes Mülmenstädt and Graham Feingold. The radiative forcing of aerosol–cloud interactions in liquid clouds: wrestling and embracing uncertainty. *Current Climate Change Reports*, 4(1):23–40, 2018.
- [179] Christine Nam, Sandrine Bony, J-L Dufresne, and H Chepfer. The 'too few, too bright' tropical low-cloud problem in cmip5 models. *Geophysical Research Letters*, 39(21), 2012.
- [180] Gregory Nastrom and K So Gage. A climatology of atmospheric wavenumber spectra of wind and temperature observed by commercial aircraft. *Journal of the atmospheric sciences*, 42(9):950–960, 1985.
- [181] Gregory Nastrom, K So Gage, and WH Jasperson. Kinetic energy spectrum of large-and mesoscale atmospheric processes. *Nature*, 310(5972):36, 1984.
- [182] Luis Carlos Navarro Hernandez. Design of residual-based unresolved-scale models using time-averaged solution data, 2015.
- [183] Michael A Nielsen. *Neural networks and deep learning*, volume 25. Determination press USA, 2015.
- [184] FTM Nieuwstadt and RA Brost. The decay of convective turbulence. *Journal of the atmospheric sciences*, 43(6):532–546, 1986.
- [185] Peter D Nooteboom, Qing Yi Feng, Cristóbal López, Emilio Hernández-García, and Henk A Dijkstra. Using network theory and machine learning to predict el niño. *arXiv preprint arXiv:1803.10076*, 2018.
- [186] Jan Martin Nordbotten. Variational and heterogeneous multiscale methods. In Karl Kunisch, Günther Of, and Olaf Steinbach, editors, *Numerical Mathematics and Advanced Applications*, pages 713–720. Springer, 2010.
- [187] Assad A Oberai and Thomas JR Hughes. A palette of fine-scale eddy viscosity and residual-based models for variational multiscale formulations of turbulence. *Computational Mechanics*, 57(4):629–635, 2016.
- [188] Paul A O’Gorman and John G Dwyer. Using machine learning to parameterize moist convection: Potential for modeling of climate, climate change and extreme events. *Journal of Advances in Modeling Earth Systems*, 2018.
- [189] Yoshimitsu Ogura and Norman A Phillips. Scale analysis of deep and shallow convection in the atmosphere. *Journal of the atmospheric sciences*, 19(2):173–179, 1962.
- [190] United Nations / Framework Convention on Climate Change. Adoption of the paris agreement. *21st Conference of the Parties, Paris*, 2015.

- [191] John Paisley, David Blei, and Michael Jordan. Variational bayesian inference with stochastic search. *arXiv preprint arXiv:1206.6430*, 2012.
- [192] Hossein Parishani, Michael S Pritchard, Christopher S Bretherton, Matthew C Wyant, and Marat Khairoutdinov. Toward low-cloud-permitting cloud superparameterization with explicit boundary layer turbulence. *Journal of Advances in Modeling Earth Systems*, 9(3):1542–1571, 2017.
- [193] Wendy S Parker. Predicting weather and climate: Uncertainty, ensembles and probability. *Studies in History and Philosophy of Science Part B: Studies in History and Philosophy of Modern Physics*, 41(3): 263–272, 2010.
- [194] Jeffrey R. Pierce, Debra Weisenstein, Patricia Heckendorn, Thomas Peter, and David W. Keith. Efficient formation of stratospheric aerosol for climate engineering by emission of condensable vapor from aircraft. *Geophysical Research Letters*, 37(18), 2010. doi: 10.1029/2010GL043975. L18805.
- [195] Stephen B Pope. *Turbulent Flows*. Cambridge University Press, 2000.
- [196] Rudolph W Preisendorfer and Mobley Curtis D. *Principal component analysis in meteorology and oceanography*. Elsevier Sci. Publ., 1988.
- [197] Javier Principe and Ramon Codina. On the stabilization parameter in the subgrid scale approximation of scalar convection–diffusion–reaction equations on distorted meshes. *Computer methods in applied mechanics and engineering*, 199(21-22):1386–1402, 2010.
- [198] Javier Principe, Ramon Codina, and Florian Henke. The dissipative structure of variational multiscale methods for incompressible flows. *Computer Methods in Applied Mechanics and Engineering*, 199(13-16):791–801, 2010.
- [199] Ronald G Prinn. Development and application of earth system models. *Proceedings of the National Academy of Sciences*, 110(Supplement 1):3673–3680, 2013.
- [200] Maziar Raissi, Paris Perdikaris, and George Em Karniadakis. Physics informed deep learning (part i): Data-driven solutions of nonlinear partial differential equations. *arXiv preprint arXiv:1711.10561*, 2017.
- [201] Maziar Raissi, Paris Perdikaris, and George Em Karniadakis. Physics informed deep learning (part ii): data-driven discovery of nonlinear partial differential equations. *arXiv preprint arXiv:1711.10566*, 2017.
- [202] David Randall. The anelastic and boussinesq approximations. *Published lecture notes*, 2010.
- [203] David Randall. The evolution of complexity in general circulation models. In Leo Donner, Wayne Schubert, and Richard Somerville, editors, *The Development of Atmospheric General Circulation Models. Complexity, Synthesis and Computation*. Cambridge University Press, 2010.
- [204] Stephan Rasp. Online learning as a way to tackle instabilities and biases in neural network parameterizations. *arXiv preprint arXiv:1907.01351*, 2019.
- [205] Stephan Rasp, Michael S Pritchard, and Pierre Gentine. Deep learning to represent sub-grid processes in climate models. *arXiv preprint arXiv:1806.04731*, 2018.
- [206] Franco Rispoli and GZ Rafael Saavedra. A stabilized finite element method based on sgs models for compressible flows. *Computer methods in applied mechanics and engineering*, 196(1-3):652–664, 2006.
- [207] Patrick J Roache. *Fundamentals of verification and validation*. Hermosa Publishers, 2009.
- [208] André Robert. Bubble convection experiments with a semi-implicit formulation of the euler equations. *Journal of the Atmospheric Sciences*, 50(13):1865–1873, 1993.
- [209] Michel Robijns. A machine learning approach to unresolved-scale modeling for burgers’ equation, 2019.
- [210] David E Rumelhart, Geoffrey E Hinton, and Ronald J Williams. Learning representations by back-propagating errors. *nature*, 323(6088):533, 1986.

- [211] Stuart J Russell and Peter Norvig. *Artificial intelligence: a modern approach*. Malaysia; Pearson Education Limited,, 2016.
- [212] Fabrizio Sarghini, G De Felice, and Stefania Santini. Neural networks based subgrid scale modeling in large eddy simulations. *Computers & fluids*, 32(1):97–108, 2003.
- [213] Masaki Satoh, Taro Matsuno, Hirofumi Tomita, Hiroaki Miura, Tomoe Nasuno, and Shin-ichi Iga. Non-hydrostatic icosahedral atmospheric model (nicam) for global cloud resolving simulations. *Journal of Computational Physics*, 227(7):3486–3514, 2008.
- [214] Masaki Satoh, Hirofumi Tomita, Hisashi Yashiro, Hiroaki Miura, Chihiro Kodama, Tatsuya Seiki, Akira T Noda, Yohei Yamada, Daisuke Goto, Masahiro Sawada, et al. The non-hydrostatic icosahedral atmospheric model: Description and development. *Progress in Earth and Planetary Science*, 1(1):18, 2014.
- [215] Jérôme Schalkwijk, Harmen JJ Jonker, A Pier Siebesma, and Erik Van Meijgaard. Weather forecasting using gpu-based large-eddy simulations. *Bulletin of the American Meteorological Society*, 96(5):715–723, 2015.
- [216] Marten Scheffer, Steve Carpenter, Jonathan A Foley, Carl Folke, and Brian Walker. Catastrophic shifts in ecosystems. *Nature*, 413(6856):591, 2001.
- [217] Sebastian Scher and Gabriele Messori. Preprint: Generalization properties of neural networks trained on lorenz systems. *Nonlinear Processes in Geophysics*, 2019.
- [218] Dominik Schillinger, John A Evans, Felix Frischmann, René R Hiemstra, Ming-Chen Hsu, and Thomas JR Hughes. A collocated c0 finite element method: Reduced quadrature perspective, cost comparison with standard finite elements, and explicit structural dynamics. *International Journal for Numerical Methods in Engineering*, 102(3-4):576–631, 2015.
- [219] Hans Rudolf Schneebeli and Thomas P Wihler. The newton–raphson method and adaptive ode solvers. *Fractals*, 19(01):87–99, 2011.
- [220] Tapio Schneider, Shiwei Lan, Andrew Stuart, and João Teixeira. Earth system modeling 2.0: A blueprint for models that learn from observations and targeted high-resolution simulations. *Geophysical Research Letters*, 44(24), 2017.
- [221] Tapio Schneider, João Teixeira, Christopher S Bretherton, Florent Brient, Kyle G Pressel, Christoph Schär, and A Pier Siebesma. Climate goals and computing the future of clouds. *Nature Climate Change*, 7(1):3, 2017.
- [222] Guglielmo Scovazzi. *Multiscale methods in science and engineering*. PhD thesis, stanford university Stanford, CA, 2004.
- [223] Guglielmo Scovazzi, Edward Love, and Mikhail Shashkov. A multi-scale q1/p0 approach to langrangian shock hydrodynamics. Technical report, Sandia National Laboratories, 2006.
- [224] Jongmin Seo, Daniele E Schiavazzi, and Alison L Marsden. Performance of preconditioned iterative linear solvers for cardiovascular simulations in rigid and deformable vessels. *Computational Mechanics*, pages 1–23, 2019.
- [225] Rob Séroul. The bézout theorem. In *Programming for Mathematicians*, chapter 2.4.1, page 10. Springer Verlag, Berlin, 2000.
- [226] Farzin Shakib, Thomas JR Hughes, and Zdeněk Johan. A new finite element formulation for computational fluid dynamics: X. the compressible euler and navier-stokes equations. *Computer Methods in Applied Mechanics and Engineering*, 89(1-3):141–219, 1991.
- [227] Pier A Siebesma and Albert AM Holtslag. Model impacts of entrainment and detrainment rates in shallow cumulus convection. *Journal of the atmospheric sciences*, 53(16):2354–2364, 1996.
- [228] Pier A Siebesma, Pedro MM Soares, and João Teixeira. A combined eddy-diffusivity mass-flux approach for the convective boundary layer. *Journal of the atmospheric sciences*, 64(4):1230–1248, 2007.

- [229] Joseph Smagorinsky. General circulation experiments with the primitive equations: I. the basic experiment. *Monthly weather review*, 91(3):99–164, 1963.
- [230] Piotr K Smolarkiewicz, Christian Kühnlein, and Nils P Wedi. A consistent framework for discrete integrations of soundproof and compressible pdes of atmospheric dynamics. *Journal of Computational Physics*, 263:185–205, 2014.
- [231] Zbigniew Sorbjan. Decay of convective turbulence revisited. *Boundary-Layer Meteorology*, 82(3):503–517, 1997.
- [232] PA Srinivasan, L Guastoni, Hossein Azizpour, Phillip Schlatter, and Ricardo Vinuesa. Predictions of turbulent shear flows using deep neural networks. *Physical Review Fluids*, 4(5):054603, 2019.
- [233] Nitish Srivastava, Geoffrey Hinton, Alex Krizhevsky, Ilya Sutskever, and Ruslan Salakhutdinov. Dropout: a simple way to prevent neural networks from overfitting. *The Journal of Machine Learning Research*, 15(1):1929–1958, 2014.
- [234] Cristiana Stan, Marat Khairoutdinov, Charlotte A DeMott, V Krishnamurthy, David M Straus, David A Randall, James L Kinter, and J Shukla. An ocean-atmosphere climate simulation with an embedded cloud resolving model. *Geophysical Research Letters*, 37(1), 2010.
- [235] Bjorn Stevens and Donald H Lenschow. Observations, experiments, and large eddy simulation. *Bulletin of the American Meteorological Society*, 82(2):283–294, 2001.
- [236] Roland B Stull. *An introduction to boundary layer meteorology*, volume 13. Springer Science & Business Media, 2012.
- [237] Ilya Sutskever, James Martens, George Dahl, and Geoffrey Hinton. On the importance of initialization and momentum in deep learning. In *International conference on machine learning*, pages 1139–1147, 2013.
- [238] Charles A Taylor, Thomas JR Hughes, and Christopher K Zarins. Finite element modeling of three-dimensional pulsatile flow in the abdominal aorta: relevance to atherosclerosis. *Annals of biomedical engineering*, 26(6):975–987, 1998.
- [239] Miguel A. C. Teixeira. The physics of orographic gravity wave drag. *Frontiers in Physics*, 2:43, 2014. ISSN 2296-424X. doi: 10.3389/fphy.2014.00043. URL <https://www.frontiersin.org/article/10.3389/fphy.2014.00043>.
- [240] Hendrik Tennekes. A model for the dynamics of the inversion above a convective boundary layer. *Journal of the atmospheric sciences*, 30(4):558–567, 1973.
- [241] Tijmen Tieleman and Geoffrey Hinton. Lecture 6.5-rmsprop: Divide the gradient by a running average of its recent magnitude. *COURSERA: Neural networks for machine learning*, 4(2):26–31, 2012.
- [242] Simone Tilmes, Jadwiga H Richter, Michael J Mills, Ben Kravitz, Douglas G MacMartin, Francis Vitt, Joseph J Tribbia, and Jean-Francois Lamarque. Sensitivity of aerosol distribution and climate response to stratospheric so2 injection locations. *Journal of Geophysical Research: Atmospheres*, 122(23), 2017.
- [243] Hirofumi Tomita, Hiroaki Miura, Shin-ichi Iga, Tomoe Nasuno, and Masaki Satoh. A global cloud-resolving simulation: Preliminary results from an aqua planet experiment. *Geophysical Research Letters*, 32(8), 2005.
- [244] Jonathan Tompson, Kristofer Schlachter, Pablo Sprechmann, and Ken Perlin. Accelerating eulerian fluid simulation with convolutional networks. *arXiv preprint arXiv:1607.03597*, 2016.
- [245] Ka Kit Tung and Wendell Welch Orlando. The k-3 and k-5/3 energy spectrum of atmospheric turbulence: Quasigeostrophic two-level model simulation. *Journal of the atmospheric sciences*, 60(6):824–835, 2003.
- [246] Kiwon Um, Xiangyu Hu, and Nils Thuerey. Liquid splash modeling with neural networks. *arXiv preprint arXiv:1704.04456*, 2017.

- [247] Robert van Driel and Harm JJ Jonker. Convective boundary layers driven by non-stationary surface heat fluxes. *Journal of the Atmospheric Sciences*, 68:272–738, 2010.
- [248] Nick Verheul and Daan Crommelin. Data-driven stochastic representations of unresolved features in multiscale models. *Commun. Math. Sci*, 14(5):1213–1236, 2016.
- [249] Albert W Vreman. The filtering analog of the variational multiscale method in large-eddy simulation. *Physics of fluids*, 15(8):L61–L64, 2003.
- [250] Zhu Wang, Imran Akhtar, Jeff Borggaard, and Traian Iliescu. Proper orthogonal decomposition closure models for turbulent flows: a numerical comparison. *Computer Methods in Applied Mechanics and Engineering*, 237:10–26, 2012.
- [251] E Weinan, Bjorn Engquist, Xiantao Li, Weiqing Ren, and Eric Vanden-Eijnden. Heterogeneous multi-scale methods: a review. *Commun. Comput. Phys*, 2(3):367–450, 2007.
- [252] Andy A White. A view of the equations of meteorological dynamics and various approximations. *Large-scale atmosphere–ocean dynamics*, 1:1–100, 2002.
- [253] Andy A White and N Wood. Dynamical meteorology | primitive equations. In *Encyclopedia of Atmospheric Sciences*. Elsevier, 2015.
- [254] Andy A White, Brian J Hoskins, Ian Roulstone, and Andrew Staniforth. Consistent approximate models of the global atmosphere: shallow, deep, hydrostatic, quasi-hydrostatic and non-hydrostatic. *Quarterly Journal of the Royal Meteorological Society*, 131(609):2081–2107, 2005.
- [255] Steffen Wiewel, Moritz Becher, and Nils Thuerey. Latent-space physics: Towards learning the temporal evolution of fluid flow. *arXiv preprint arXiv:1802.10123*, 2018.
- [256] Chenyue Xie, Jianchun Wang, Ke Li, and Chao Ma. Artificial neural network approach to large-eddy simulation of compressible isotropic turbulence. *Physical Review E*, 99(5):053113, 2019.
- [257] Yulong Xing, Andrew J Majda, and Wojciech W Grabowski. New efficient sparse space–time algorithms for superparameterization on mesoscales. *Monthly Weather Review*, 137(12):4307–4324, 2009.
- [258] Kuan-Man Xu and Anning Cheng. Evaluating low-cloud simulation from an upgraded multiscale modeling framework model. part i: Sensitivity to spatial resolution and climatology. *Journal of Climate*, 26(16):5717–5740, 2013.
- [259] Radyadour Kh Zeytounian. *Asymptotic modeling of atmospheric flows*. New York: Springer, 1990.
- [260] Dongkun Zhang, Lu Lu, Ling Guo, and George Em Karniadakis. Quantifying total uncertainty in physics-informed neural networks for solving forward and inverse stochastic problems. *arXiv preprint arXiv:1809.08327*, 2018.
- [261] Ming Zhao, J-C Golaz, IM Held, V Ramaswamy, S-J Lin, Y Ming, P Ginoux, B Wyman, LJ Donner, D Paynter, et al. Uncertainty in model climate sensitivity traced to representations of cumulus precipitation microphysics. *Journal of Climate*, 29(2):543–560, 2016.